

**Observations of Stratigraphy and Volcanism
from Guinevere and Sedna Planitiae, Venus**

**A thesis submitted for the Degree of Doctor of
Philosophy of the University of London**

By

Duncan L. Copp

**University of London Observatory
Planetary Image Centre
Department of Physics and Astronomy
University College London**

1997

ProQuest Number: 10105232

All rights reserved

INFORMATION TO ALL USERS

The quality of this reproduction is dependent upon the quality of the copy submitted.

In the unlikely event that the author did not send a complete manuscript and there are missing pages, these will be noted. Also, if material had to be removed, a note will indicate the deletion.



ProQuest 10105232

Published by ProQuest LLC(2016). Copyright of the Dissertation is held by the Author.

All rights reserved.

This work is protected against unauthorized copying under Title 17, United States Code.
Microform Edition © ProQuest LLC.

ProQuest LLC
789 East Eisenhower Parkway
P.O. Box 1346
Ann Arbor, MI 48106-1346

I dedicate my work to Jake - may his generation find answers to questions I'd never thought of asking.

The diversity of phenomena of nature is so great, and the treasures hidden in the heavens so rich, precisely in order that the human mind shall never be lacking in fresh nourishment.

- Johannes Kepler, *Mysterium Cosmographicum*

Acknowledgements

I owe many people a great deal. First and foremost, I would like to extend my thanks to Professor John Guest (who supervised my work), and Dr Ellen Stofan for their patience and constant encouragement. I'm very grateful to have had the opportunity to work with John and Ellen, I learnt a tremendous amount and had a great deal of fun; thank you again. My thanks also to my fellow research colleagues at Mill Hill and the Department of Geological Sciences: Dr Mike Lancaster, Dr Mark Biddiss, Dave Heather, Simon Tapper and Antony Brian. I also wish to thank Valerie Peerless and Maureen Evans for all the kindness they have shown me during my time at the Annexe, I'd never have completed without your help.

I've been very lucky in having the support of friends and family during my research. Thanks go to Melanie and Shirley Whittle, Dennis and Lisa Croxal, Sarah Holland, Dr Chris Riley, Robyn Dummer, Amanda Baraclough, Siri Wooster, Alan Dalmon, and Alan Gibson for their support. Particular thanks go to Martin Wooster for his help and encouragement. I'm grateful too for support from friends past and present at the BBC; Duncan Franklin, Nicole Abie, Phillip Henry, Sarah Langford and Susan Batson. In particular, I'd like to thank Stephen Holland for allowing me to continue my work at BSS while researching. Lastly, I thank my Mother, Father, Sarah and Martin, Linda and Phillippe for their kind words of support and encouragement, I'm very grateful to you all.

This work was supported by a Perrin studentship from the Department of Physics and Astronomy, University College London. Field work and conference expenses were funded by the Graduate School, University College London, (United States) and by The Central Research Council (Mt. Etna - Sicily). Further funding was gratefully received from the Hugh Westwood Educational Trust. All Magellan images are courtesy of NASA/JPL.

Abstract

Detailed mapping, using recently acquired full resolution photo-products and synthetic stereo data from the Magellan spacecraft, is used to investigate the stratigraphy and formation of landforms observed on Venus. The research focuses on two large contiguous plains, Guinevere and Sedna Planitiae. It has been suggested that distinct volcanic and deformational processes have operated throughout Venus within specific time periods. For example tesserae are considered to have only formed relatively early on in the visible venusian rock record. New observations of volcanic landforms within Guinevere and Sedna Planitia support a non-directional stratigraphy.

Contrary to earlier models for the evolution of coronae, those in the study area have had a protracted history. Both Idem-Kuva and Heng-o display multiple phases of annulus formation (previously thought to occur during a specific stage of corona formation). Furthermore, annulus formation and rim topography formation do not necessarily coincide in space and time, as seen at Idem-Kuva, indicating that both large and small-scale deformational processes at coronae can be protracted. The amount and style of volcanism associated with the coronae studied here varies considerably. Predicted early stage volcanism is not observed at Idem-Kuva, Nissaba or Silvia Coronae, while Benten Corona shows multiple phases of volcanism which decrease in volume over time.

A study of Sif and Gula Montes shows the two large shield volcanoes have a different overall morphology, summit structure and associated flow fields. Sif Mons is approximately circular in plan view, with a prominent summit caldera, with morphologically varying flow fields. In contrast, Gula Mons is elongate in plan view, surmounted by a rift joining two modified calderas, and is surrounded by more sinuous flows. Using terrestrial volcanoes as analogies, especially Mt. Etna, it is shown that the morphological differences between the two volcanoes may be a consequence of different internal and surrounding stress regimes.

Contents

1	Introduction	1
1.1	The Planet Venus	1
1.2	A Summary of Pre-Magellan Observations of Venus	3
1.2.1	Earth Based Observations	3
1.2.2	Pre-Magellan Space Missions	5
1.2.3	Observations from the Venusian Surface	5
1.2.4	Orbital Atmosphere Observations	11
1.2.5	Orbital Altimetric and Radar Observations	14
1.3	The Magellan Mission	17
1.3.1	The Aims of the Magellan Mission	17
1.3.2	Magellan Instrumentation and Operation	18
1.3.3	Mapping cycles	23
1.4	The Magellan Data Set	24
1.4.1	SAR Data	24
1.4.2	Altimetric and Radiometric Data	28
1.4.3	Synthetic Stereo Data	28
1.5	Implications of the new Magellan Data	29
1.5.1	The VMAP Project	30
1.6	Summary	31
2	Current Models of Stratigraphy and Volcanic Processes on Venus	33
2.1	Introduction	33
2.2	A Model of the Global Stratigraphy of Venus	33
2.2.1	The Pre-Fortunian Period	34
2.2.2	The Fortunian Period	36
2.2.3	The Guineverian Period	40
2.2.4	The Aurelian Period	42
2.3	A Sequence of Deformation within the Global Stratigraphy Model	42
2.4	Summarising the Global Stratigraphy Model	45

2.5 A Global Resurfacing Model (GRM) and Equilibrium Resurfacing Model (ERM): Two 'end member' Scenarios	46
2.6 Models of Evolution for Volcanic Landforms on Venus	51
2.6.1 A Model for Corona Evolution and Stratigraphic Significance	51
2.6.2 Large Shield Volcanoes	53
2.6.3 Pyroclastic Eruptions	62
2.7 Summary	64
3 Guinevere and Sedna Planitiae; Mapping, Description and Interpretation	66
3.1 Introduction	66
3.2 Geological Mapping of Venus	67
3.3 Geological Mapping using SAR Radar	72
3.3.1 Radar Interpretation	72
3.4 Unit Description and Interpretation	81
3.4.1 Tesserae - <i>t</i> , and Deformed Plains - <i>pd</i>	81
3.4.2 The Lineated and Mottled Plains - <i>gplm</i> and <i>splm</i>	87
3.4.3 The Regional Plains - <i>gpr</i> and <i>spr</i>	98
3.4.4 The Homogeneous Plains - <i>gph</i> and <i>sph</i>	106
3.4.5 Edifice Fields - <i>ef</i>	106
3.4.6 Isolated Flow - <i>f</i>	117
3.4.7 Volcanic Centres - <i>vc</i> , and Sif and Gula Materials	120
3.4.8 Coronae	122
3.4.9 Great Flow Fields	124
3.4.10 Impact and Surficial Crater Materials	128
3.5 A Quantitative Measure of the Amount of Materials Associated with an Identifiable Source	130
3.6 Stratigraphic Observations From Guinevere and Sedna Planitiae	135
3.7 Comparison of Stratigraphic Observations of Guinevere and Sedna Planitiae with the Global Stratigraphic Model	139
3.7.1 Evidence for Repeated Phases of Volcanism	139
3.7.2 Evidence for Repeated Phases of Deformation	144
3.8 Resurfacing Models and the Venusian Stratigraphy	146

3.9 Summary and Conclusions	147
4 New Insights into Corona Evolution and Stratigraphy	149
4.1 Introduction	149
4.2 Observation of Coronae in Guinevere and Sedna Planitia	151
4.2.1 Idem-Kuva Corona	151
4.2.2 Nissaba Corona	161
4.2.3 Benten Corona	165
4.2.4 Heng-o Corona	173
4.2.5 Silvia Corona	183
4.3 Implications for Corona Evolution	188
4.3.1 Stage 1: Uplift and Interior Deformation	188
4.3.2 Stage 2: Annulus Formation	189
4.3.3 Stage 3: Corona Relaxation and the Correlation of Coronae Relief with Age	190
4.4 Implications for Coronae Stratigraphy on Venus	192
4.4.1 Dating Coronae using Local Stratigraphic Relations	192
4.4.2 Dating Coronae using Crater Statistics	193
4.5 Summary and Conclusions	195
5 A Geological Interpretation of Sif and Gula Montes	196
5.1 Introduction	196
5.2 Constrains on the Identification and Interpretation of Volcanic Materials using Radar	198
5.2.1 Radar Instrument Constraints	200
5.2.2 Surficial Constrains	201
5.3 Description and Interpretation of Volcanic Units of Sif and Gula Montes	206
5.3.1 Sheet Flows	206
5.3.2 Compound Flow Fields of Sif and Gula Montes	217
5.3.3 Sif Mons	218
5.3.4 Gula Mons	222

5.3.5 Flank Eruptive Sites at Sif Mons	228
5.3.6 Diffuse Volcanic Materials near the Summits of Sif and Gula Montes	230
5.4 Comparison of Flow Materials at Sif and Gula Montes	233
5.5 Description and Comparison of the Gross Morphology and Summit Structure of Sif and Gula Montes	234
5.6 The Internal Dynamics and Evolution of Sif and Gula Montes	238
5.6.1 Edifice Morphology and Summit Structure	283
5.6.2 Comparative Flow Morphology	240
5.6.3 Internal Plumbing and Evolution	241
5.7 An Evolutionary Model for Sif and Gula	243
5.8 Implications for Models of Large Shield Volcanism on Venus	244
5.9 Summary and Conclusions	247
6 Conclusions	249
References	256
Appendices	286
I Magellan Radar Products: Acquisition and Reduction	286
II USGS Unit Descriptions for V31	294
III USGS Unit Descriptions for V19	301
Key to Mapping Symbols	308
IV SAR and Ancillary Radar Data for V31	310
V SAR and Ancillary Radar Data for V31	314

List of Tables

1.1	Physical properties of Venus compared with Earth and Mars	2
1.2	Chronology of venusian observations by spacecraft	6
1.3a	Venera measurements of radioactive elements	9
1.3b	Chemical measurements for Venera 13 and 14	9
1.4	Chronology of the Magellan Mission	19
1.5	Parameters of the Magellan SAR instrument	20
1.6	Other radar instruments in comparison with Magellan SAR	21
1.7	Magellan data products	27
2.1	Depths to magma chambers on Venus as a function of atmospheric pressure and magma volatile content	59
3.1	Variation of incidence angle against latitude	74
3.2	Percentage of materials associated with a volcanic landforms within Guinevere and Sedna Planitiae	132
3.3	Quantitative measure of materials within Guinevere and Sedna Planitiae	133
5.1	Comparison of SIR-C data for selected flows at Mt. Etna	203
5.2	Radar data for flow units at Sif Mons and Gula Montes	209

List of Figures

1.1	Location of Venera and Vega landing sites	7
1.2	Comparison of the vertical thermal structure of the atmospheres of Venus and Earth	12
1.3	Distribution of the low lying plains of Venus	15
1.4	Comparison of elevation for Earth, Venus and Mars	16
1.5	Magellan observing geometry in the SAR imaging, altimeter, and radiometer modes of operation	22
1.6	Magellan SAR data products	26
2.1	Proposed divisions for the Global Stratigraphy Model	35
2.2	Sinusoidal equal-area projection showing the sizes and distribution of craters on Venus	37
2.3	Comparison of a Monte Carlo simulation (Random) and the actual distribution of impact craters	38
2.4	Histogram showing the percentage of impact craters compared to surface area in 500 m elevation bins	39
2.5	Summary of the Global Stratigraphic Model	43
2.6	Block diagrams of Venus resurfacing models	47
2.7	Paradigms for models of geological formation evolution of Venus	48
2.8	The growth and development of oceanic terrestrial volcanoes	55
2.9	Volcano growth and migration of magma reservoirs on the Earth and Venus	57
2.10	Modelled effect of different surface elevations on the depth of magma reservoirs	58
2.11	Schematic illustration showing models of edifice and subsurface reservoir growth for Venus and Earth	61
3.1	Location of 62 quadrangles devised for the Venus Mapping Project (VMAP)	68
3.2	FMAP coverage for Sif Mons	69
3.3	FMAP coverage for Sedna Planitia	70
3.4	C1-MIDR coverage for the study area	71

3.5	Magellan SAR incidence angle as a function of latitude	73
3.6	Slant-range and ground-angle geometries	76
3.7	Illustration of geometry distortions in radar images: (a) radar image foreshortening (b) radar layover (c) radar shadowing	77
3.8	Radar backscatter as a function of incidence angle for representative surfaces	78
3.9	Surface roughness effects on radar backscatter	80
3.10	Location Map for named features in V31	82
3.11	Location Map for named features in V19	83
3.12	Plot of radar backscatter for units in V31	84
3.13	Plot of radar backscatter for units in V19	85
3.14	Southern portion of Manzan-Gurme Tessera	86
3.15	Guinevere regional plains and Guinevere lineated and mottled plains materials	88
3.16	Stratigraphic relations of Sedna plains materials	90
3.17	Zorile Dorsa	91
3.18	Minor ridge belt within the Guinevere and lineated mottled plains	92
3.19	Full resolution image showing structures associated with areas of the mottled and lineated plains	93
3.20	Small volcanic edifices and associated mantle deposits contained within the Guinevere lineated and mottled plains	95
3.21	Patch shield volcanism is seen to modify Sedna regional plains materials	97
3.22	Toci Tholus, an example of an intermediate volcano centre	99
3.23	Ridge belt cutting the regional plains	101
3.24	Stratigraphic relations between various plains units and structures seen in north central Guinevere Planitia	102
3.25	Bi-directional wrinkle ridge structures seen within Guinevere regional plains	103
3.26	Stealth volcanoes in Guinevere Planitia	104
3.27	Radar characteristics and relations of the Sedna regional, homogeneous, and mottled and lineated plains	107
3.28	An example of a relatively young edifice field situated in western Guinevere Planitia	109

3.29	Olosa Colles in Guinevere Planitia	110
3.30	Enlarged image of Olosa Colles	111
3.31	Enlarged view of the centre edifice field located at 13.5 ⁰ N, 314.5 ⁰ E	112
3.32	An example of a relatively old edifice field situated in lineated and mottled plains materials (V19)	114
3.33	An example of a relatively old edifice field situated in the Sedna lineated and mottled plains	115
3.34	Example of a Patch edifice field	116
3.35	Example of the Isolated flow unit	118
3.36	Isolated flow units seen superposed on plains materials of southern Guinevere Planitia	119
3.37	Different scales of melting and convection on Venus	123
3.38	Neago Fluctus superposed on northern Sedna regional plains	125
3.39	Wrinkle ridges cutting Neago Fluctus flow materials	126
3.40	Cunitz and Enid craters; V31	129
3.41	Graphs showing percentage of flow materials	134
3.42	Correlation chart for V31	136
3.43	Correlation chart for V19	137
3.44	Example of buried large edifice in Aino Planitia	141
3.45	Example of buried volcano in Ganiki Planitia	142
4.1	Location Map for the five coronae in V31	150
4.2	Magellan image of Idem-Kuva and Nissaba Coronae	152
4.3	Sketch map of Idem-Kuva and Nissaba Coronae	153
4.4	Topographic profiles of Idem-Kuva and Nissaba Coronae	155
4.5	Topographic map of Idem-Kuva Corona	156
4.6	Interior of Idem-Kuva	157
4.7	SW section of Idem-Kuva Corona	158
4.8	The northern section of Idem-Kuva Corona	159
4.9	Topographic map of Nissaba Corona	162
4.10	Central Nissaba Corona	163
4.11	Benten Corona and associated flow materials	166
4.12	Sketch map of Benten Corona	167
4.13	Topographic profiles of Benten Corona	169
4.14	Topographic map of Benten Corona	170

4.15	The interior of Benten Corona	171
4.16	Heng-o and Beltis Coronae	174
4.17	Sketch map of Heng-o and Beltis Coronae	175
4.18	Topographic profiles of Heng-o and Beltis Coronae	176
4.19	Topographic map of Heng-o and Beltis Coronae	177
4.20	The southern margin of Heng-o Corona	178
4.21	Two phases of annulus deformation seen at the SW rim of Heng-o Corona	179
4.22	The northern rim of Heng-o Corona	180
4.23	Silvia Corona	184
4.24	Sketch map of Silvia Corona	185
4.25	Topographic profile of Silvia Corona	186
4.26	Topographic map of Silvia Corona	187
5.1	Sif and Gula Montes location map	197
5.2	Sif and Gula Montes	199
5.3	Plot of radar backscatter for selected flow units at Mt. Etna	204
5.4	Sketch map of Sif Mons	207
5.5	Sketch map of Gula Mons	208
5.6	Plot of radar backscatter of flow units identified at Sif and Gula Montes	213
5.7	Unit 1 flow materials; Sif Mons	214
5.8	Unit 1 flow materials; Gula Mons	216
5.9	Flow units observed on the northern flank of Sif Mons	219
5.10	Controlled flows of Unit 3a; Sif Mons	220
5.11	Identification of a channel within the flow materials of Unit 3b; Sif Mons	221
5.12	The summit region of Sif Mons	223
5.13	Site of lava tube seen within Unit 5 of Sif Mons	224
5.14	Digitate flows located on the southern flank of Gula Mons	225
5.15	Unit 3 flow materials NE of Gula Mons	226
5.16	Location of interpreted flank eruptive sites on the eastern flank of Sif Mons	229
5.17	The summit region of Gula Mons	231

5.18	Topographic profiles of Sif Mons	235
5.19	Topographic profiles of Gula Mons	236
5.20	Gula Mons and Idem-Kuva Corona	239

Appendix

Figure 1	Burst mode method of data collection	287
Figure 2	Magellan mapping orbit profile	288
	Key to mapping symbols	308

Maps / Basemaps

Map 1	Geological Map of the USGS Sif Mons Mapping Quadrangle: Venus	Back Wallet
Map 2	Geological Map of the USGS Sedna Planitia Mapping Quadrangle: Venus	Back Wallet
Basemap 1	Sif Mons Quadrangle	Back Wallet
Basemap 2	Sedna Planitia Quadrangle	Back Wallet

Chapter 1

Introduction

1.1 The Planet Venus

A familiar friend to folk who rise just before dawn, or who stroll during twilight, Venus has always held a special place in the heavens. This beautiful celestial spectacle has been commented on since antiquity. The Babylonians called her Ishtar, 'the bright torch of the heavens', the Greeks and Romans knew her as the Goddess of Beauty, and the Chinese as Tai-pe, the 'Beautiful White One'.

Until the second half of the twentieth century, observations of Venus were limited to those made with telescopes. During the Renaissance period, Italian astronomer Galileo Galilei observed the phases of Venus, contributing to the theory that the Earth did not lie at the centre of the Universe. Interest in the planet grew during the centuries which followed, with history's most eminent astronomers, including Cassini, Herschel and Halley, each trying to unlock her secrets. The discovery that Venus was similar in size to the Earth, and had a substantial atmosphere resulted in some believing its surface may have been Earth-like.

Much has been learnt about Venus since these early observations. During the mid 1930s, spectroscopy and infrared radiometry measured the bulk atmospheric component as CO₂. Later, spectroscopic measurements showed the permanent clouds to consist of sulphuric acid droplets. By tracking cloud features, the upper atmosphere was seen to have a super-rotation of approximately 5 days. The surface heat flux was observed to equate to a ground temperature brightness of approximately 327⁰ C. The venusian day was found to be longer than the venusian year (Table 1.1). Furthermore, Venus was recognised as the only planet which has a retrograde rotation.

Physical property	Venus	Earth	Mars
Mass (Earth=1)	0.815	1.000	0.107
Mass (kg)	4.871×10^{24}	5.976×10^{24}	6.421×10^{23}
Equatorial radius (km)	6051.3	6378	3398
Equatorial radius (Earth=1)	0.949	1.000	0.532
Mean density (g/cm^3)	5.42	5.52	3.94
Equatorial gravity (ms^{-2})	8.87	9.78	3.72
Equatorial escape vel. (km s^{-1})	10.4	11.2	5.0
Oblateness	0.000	0.003	0.006
Orbital period	224.7	365.25	686.98
Sidereal rotation period	243.01 days	23.934 hr	24.622 hr
Obliquity	-2.6°	23.45°	23.98°
Mean surface temperature ($^\circ\text{C}$)	468	15	-55
Mean surface pressure (bar)	90	1	0.007
Atmosphere	CO_2	N_2, O_2	CO_2
Mean distance from Sun (km)	108.20×10^6	149.60×10^6	227.94×10^6

Table 1.1 Physical properties of Venus compared with Earth and Mars.

Only during the last 35 years has geological and geomorphological information of Venus been intermittently provided. The exploration of Venus by a flotilla of spacecraft has resulted in a new geological understanding, showing a complex and dynamic multitude of tectonic and volcanic processes.

The Magellan mission, launched in 1989, was designed to undertake further investigation and represents the culmination of venusian research to date. The purpose of this thesis is to forward the understanding of geological processes which have acted to form the surface of Venus observed today from radar images. In particular, the work focuses on refining venusian stratigraphy and the evolution of specific volcanic landforms. New observations are provided from the utilisation of various data sets and detailed geological mapping of specific areas of the surface.

Before presenting the observations and interpretations of the work, this introductory chapter provides a brief chronology of previous terrestrial and spacecraft observations of Venus, highlighting major findings which have contributed to understanding the planet. As the research presented in the following chapters is primarily based on observations from data returned by the Magellan mission, a summary of the data products from the mission are described. Finally, the implications of newly available data, and framework of the thesis are discussed.

1.2 A Summary of Pre-Magellan Observations of Venus

1.2.1 Earth Based Observations

Considerable investigation of Venus has been conducted via Earth based studies using data gathered by Doppler Radio Detection And Ranging (RADAR) techniques. Radar is the principal tool used when observing the surface of Venus as the planet is permanently shrouded by clouds which reside in the upper atmosphere which prevent optical observations of the surface.

Radar images from Earth are obtained principally from three United States radio telescope observatories: the 43 meter antenna at Haystack in Massachusetts, the 64 meter antenna located at Goldstone in the Mojave Desert, and the large 300 meter radio telescope at Arecibo in Puerto Rico. The telescopes operate at 3.8 cm, 12.6 cm, and 70 cm wavelengths respectively (*Goldstein et al.*, 1976; *Campbell and Burns*, 1980; *Cattermole*, 1994). Radar images are obtained during inferior conjunction when Venus lies between the Earth and the Sun. However, owing to the near resonance between the rotation of Venus and its closest approach to Earth, only one side of the planet can be mapped using Earth-based radar (*Campbell and Burns*, 1980). Image resolution is dependent on latitude, with equatorial regions having the greatest spatial resolution. Vertical resolution is typically 500 metres. Radar observations from Earth have resulted in approximately 25% surface coverage (*Campbell et al.*, 1976; *Goldstein et al.*, 1976, 1978; *Saunders and Malin*, 1977; *Campbell and Burns*, 1980).

Early radar observations had a spatial resolution of between 5 and 20 km (typically 10 km) and showed the motion of large radar-bright features as the planet rotated, interpreted as upland areas (*Goldstein*, 1965, 1967). Improved resolution during the 1980s, showed smaller surface features between 1.5 and 4 km in size from both northern and southern hemispheres (e.g. Ishtar Terra and the Themis-Alpha-Lada region respectively, *Campbell et al.*, 1991; *Senske et al.*, 1991a). The images provided important information on the surficial geology, for instance data from the upland area Beta Regio showed a large depression at the summit. The upland was subsequently interpreted as a large volcanic rise considered analogous to martian and terrestrial hotspot areas (*Senske et al.*, 1991b). Maxwell Montes and Ishtar Terra, described by *Campbell et al.* (1976), were interpreted to be a consequence of tectonic activity.

Further data obtained from the Arecibo station, with improved resolution (1.5-2.0 km), were used to map nine geological units from Beta Regio, Guinevere Planitia, Sedna Planitia (the planitiae studied in this thesis) and Western Eistla Regio. The

units were interpreted as volcanic in origin, based on radar backscatter values and areal extent. Many units showed structural modification inferred as tectonic processes (*Campbell et al.*, 1990; *Senske et al.*, 1991b).

A full treatment of observations and interpretations of linear deformation zones, volcanic edifices (including Sif and Gula Montes), and crater distribution acquired from Earth based radar are discussed in detail in the following papers: *Campbell et al.* (1989, 1990), *Arvidson et al.* (1990), *Ford and Senske* (1990) and *Senske et al.* (1991a, 1991b).

1.2.2 Pre-Magellan Space Missions

Information about the venusian environment and physical properties (Table 1.1) has been obtained by 21 spacecraft since 1962. Table 1.2 summarises the findings from spacecraft exploration of Venus. Described in more detail below are the results from the Russian Venera lander space missions. To date, the Venera landers provide the only direct chemical and photographic data on which to infer lithology, composition and rock type. A full discussion of the results from the Venera missions can be found in *Barsukov et al.* (1986, 1992).

1.2.3 Observations from the Venusian Surface

Detailed information of small-scale surface characteristics and rock composition of Venus has been established from data returned from 10 Russian Venera soft-lander spacecraft. (Figure 1.1) To date, the data represent the only *in situ* surficial investigations, providing chemical and erosional constraints. The data include spectroscopic measurements and panoramic images in black and white, and colour.

The first spacecraft to survive an atmospheric descent was Venera 7 in 1971. Instruments on board the craft confirmed a

Mission	Date	Country	Results
Mariner 2	27/08/62	USA	Close encounter - 34,745 km. Disclosed surface temperature at 468 C and absence of magnetic field.
Venera 4	12/06/67	USSR	Relayed atmospheric information for 93 minutes.
Mariner 5	14/06/67	USSR	Close encounter - 4023 km. Atmospheric data.
Venera 5	05/01/69	USSR	Aerodynamic parachute decent - confirmed high Co2 content and lack of water.
Venera 6	10/01/69	USSR	Similar probe as Venera 5 - similar results.
Venera 7	17/08/69	USSR	First probe to soft-land. Transmitted data for 23 minutes. Atmospheric data.
Venera 8	27/03/72	USSR	Radioed surface temperature and pressure after landing on the sunlit side of the planet.
Mariner 10	03/11/73	USA	Encountered Venus en route to Mercury, observed global atmospheric circulation in vis. & UV.
Venera 9	08/06/75	USSR	Orbiter-lander, similar to Venera 8. First black and white panoramic view of the surface.
Venera 10	14/06/75	USSR	Similar to Venera 9. Panoramic view of surface.
Pioneer 12	20/05/78	USSR	Venus orbiter, first Radar observations of surface.
Pioneer 13	08/08/78	USSR	Spacecraft carried 4 probes which entered the venusian atmosphere- temperature and pressure data and information on wind velocities.
Venera 11	09/09/78	USSR	Flyby - lander. Atmospheric data returned.
Venera 13	31/10/81	USSR	Orbiter - lander, relayed first colour images.
Venera 14	04/11/81	USSR	Orbiter - lander, returned colour imagery. Drilled soil samples and conducted seismic experiments.
Venera 15	02/06/83	USSR	Orbiter, radar mapping 2-4 km resolution.
Venera 16	07/06/83	USSR	Similar to Venera 15 - radar mapping.
Vega 1	15/12/84	USSR	Venus descent vehicle and atmospheric balloon.
Vega 2	21/12/84	USSR	Similar to Vega 1 spacecraft - same instruments.
Magellan	04/05/89	USA	Orbiter, radar mapping - 120m resolution. 98% of the planet imaged - altimetric, radiometric and gravity data gathered.

Table 1.2 Chronology of venusian observations by spacecraft. After Young (1990).

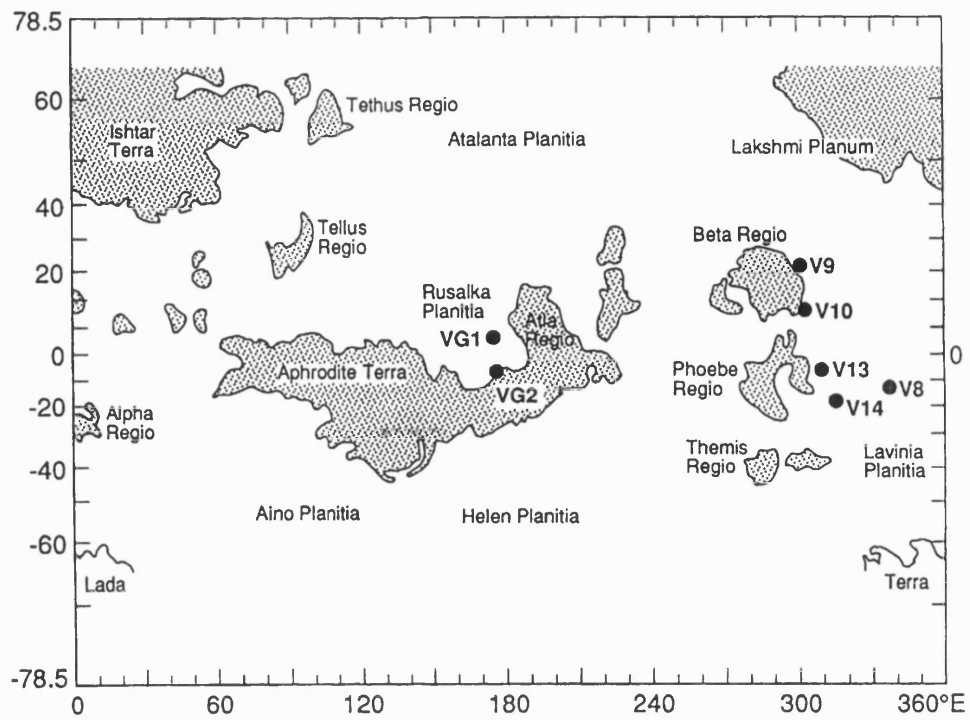


Figure 1.1 Location of Venera (V), and Vega (VG) landing sites. After Weitz and Basilevsky (1993).

surface temperature and pressure of approximately 470⁰ C and 90 bars respectively at the landing site. Veneras 8, 9 and 10 landers used gamma-ray spectroscopy to determine the content of K, U, Th at the surface beneath the lander. Veneras 13 and 14 used X-ray fluorescence spectroscopy to determine the abundance of Si, Ti, Al, Fe, Mg, Ca, K, S, and Cl in the top centimetre of the venusian surface. Broadly two divisions of rocks were interpreted from the spectroscopy. Veneras 9-14 returned data which showed a low isotopic (K, U and Th) abundance and elemental concentrations compatible with terrestrial tholeiitic basalts (*Florensky, 1977a*). Tables 1.3a and 1.3b summaries the results of chemical analysis measured by Venera 13 and 14. In contrast, measurements taken by Venera 8, situated on a small topographic rise east of Navka Planitia, showed greater concentrations of K, U and Th, indicative of a more evolved igneous rock.

Basilevsky et al. (1992) suggest the materials sampled at the Venera 8 site may have two possible terrestrial analogues: first, an igneous rock such as quartz monzonite, quartz syenite or andesite, possibly indicating the presence of terrestrial continental crust (*Nikolayeva, 1990*), or second, a more mafic, primitive group of rocks such as lamprophyres.

Panoramic images returned by Veneras 9, 10, 13 and 14 allowed investigation of the immediate surface surrounding the landers. The black and white image from Venera 9 shows plate-like fragments 10s of centimetres in size separated by smaller fragmented fine materials. The size distribution of the blocks is bimodal, with modes falling between 1-10 cm and 30-70 cm (*Garvin et al., 1981, 1984; Florensky et al., 1977b*). Venera 10, which landed near the SE edge of Beta Regio, also transmitted one black and white panoramic image. The image shows 60 % of the visible area composed of rock slabs. Fines occur in bedrock surface depressions, forming regular and irregular dark spots and patches (*Garvin et al., 1984*). Materials were found to be friable and porous.

Colour panoramic images were returned in 1982 by Veneras 13 and 14 with resolution improved by a factor of 2 (4-5 mm per

Spacecraft	U ($\times 10^{-4}$ wt %)	Th ($\times 10^{-4}$ wt %)	K (wt%)
Venera 8	2.2 ± 0.7	6.5 ± 0.2	4.0 ± 1.2
Venera 9	0.06 ± 0.16	3.65 ± 0.42	0.47 ± 0.08
Venera 10	0.46 ± 0.26	0.70 ± 0.34	0.30 ± 0.16

Table 1.3a Venera measurements of radioactive elements. After Barsukov (1982).

Oxide	Venera 13	Venera 14	Oceanic Basalt
SiO ₂	45.0 ± 3.0	49.0 ± 4.0	51.4
Al ₂ O ₃	16.0 ± 4.0	18.0 ± 4.0	16.5
MgO	10.0 ± 6.0	8.0 ± 4.0	7.56
CaO	7.0 ± 1.5	10.0 ± 5.0	9.4
TiO ₂	1.5 ± 0.6	1.2 ± 0.4	1.5
MnO	0.2 ± 0.1	0.16 ± 0.08	0.26
FeO	9.0 ± 3.0	9.0 ± 2.0	12.24
K ₂ O	4.0 ± 0.8	0.2 ± 0.1	1.0

Table 1.3b Chemical measurements for Venera 13 and 14 . After Barsukov (1982).

pixel versus 10 mm for Venera 9). The panoramic images show plains dominated by layered bedrock with a minor amount of fragmented materials in local depressions. From the images, *Florensky et al.* (1983) suggest that the surface at the Venera 13 and 14 landing sites is undergoing *in situ* geomorphic degradation.

Florensky et al. (1983) and *Basilevsky et al.* (1985) discuss six possible origins for the observed rock units at the Venera 13 and 14 sites: lava, an igneous intrusion later exposed by erosion, pyroclastic fall, impact ejection and lithification, lithification of materials forming sedimentary rocks, or surface metamorphism owing to the unique venusian surface conditions. From surface data, *Florensky et al.* (1983) and *Basilevsky et al.* (1985) consider the last hypothesis most likely, although none of the above can be tested with Venera results alone. It is suggested (*Basilevsky*, 1985) that the rock units are sedimentary or sedimentary-volcanic with lithification occurring from chemical effects, forming a duricrust (*Florensky et al.*, 1983).

Two interesting features emerge from the Venera panoramic images. First, as *Garvin et al.* (1984) point out, although separated by thousands of kilometres, all four Venera landing sites appear morphologically very similar. Second, aeolian features such as microdunes, windtails and moats are not observed at any of the landing sites, in contrast to the landing sites of Viking 1 and 2 on Mars (and more recently, Mars Pathfinder). The Venera landers carried anemometers: Venera 9 and 10 measured winds one meter above the surface between 0.3 and 1 ms⁻¹ (*Avduevsky et al.*, 1976a, 1976b). The lack of small aeolian features at the landing sites is surprising as *Greeley et al.* (1984, 1992) calculated that saltation and traction can transport particles up to a maximum size of approximately one millimetre on Venus. This is partly owing to the density of the venusian atmosphere, recorded as 90 bars in lowland plains.

Vega 1 and 2, two further Russian landers, were deployed on the surface of Venus in 1985 (Figure 1.1). Vega 1 landed in Rusalka Planitia, north of Aphrodite Terra about 1000 km west of the volcano Sapas Mons. Vega 2 landed approximately 1500 km

south of the Vega 1 landing site. Each lander conducted surficial chemical analyses. Spectroscopy measurements detected low K, U and Th concentrations, analogous to terrestrial tholeiitic basalts similar to earlier Venera results. No panoramic images were taken at either landing site.

In summary, surface geochemical data obtained by the Venera and Vega missions imply that the surface composition of Venus is analogous to that of oceanic basalts. At only one landing site (Venera 8) was there chemical evidence to suggest more evolved volcanic materials. From the lander observations it is assumed the bulk of the plains of Venus are volcanic in origin.

1.2.4 Orbital Atmospheric Observations

1978 saw the successful deployment of the United States Pioneer-Venus Orbiters (PVO, also known as Pioneer-Venus 1 and 2). The PVO missions carried instruments to study the planet's magnetic field and its interaction with the solar wind. The gravitational field of Venus was also investigated. One PVO craft released four probes into the venusian atmosphere at different locations to determine diurnal differences in composition and structure (*Colin*, 1980). Figure 1.2 shows the structure of the venusian atmosphere based on Pioneer data. *Pettengill et al.* (1980a, 1980b) and *Masursky et al.* (1980) provide a detailed discussion of the findings from the Pioneer missions. The main results of the atmospheric studies concluded:

(1) The bulk component of the venusian atmosphere is CO₂ (95.32%). The atmosphere is essentially dry, approximately 10⁻⁵ of the amount of water contained in the Earth's oceans is observed in the venusian atmosphere.

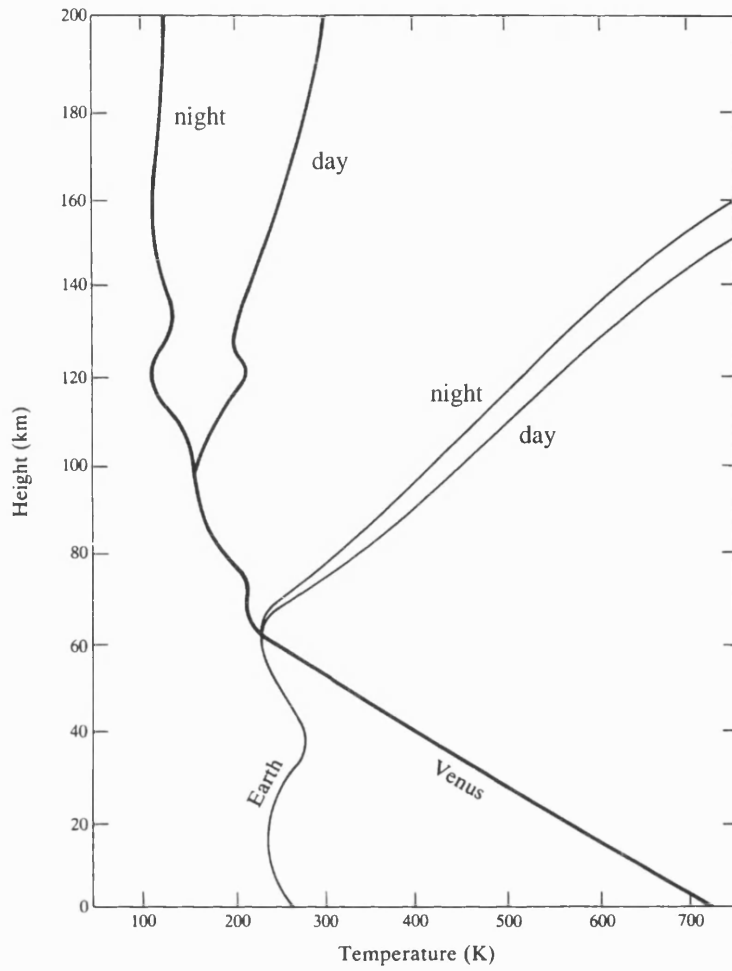


Figure 1.2 Comparison of the vertical thermal structure of the atmospheres of Venus and Earth. After *Hunt and Moore (1982)*.

(2) The deuterium/hydrogen (D/H) ratio (an indicator of atmospheric evolution and a tracer for water molecules) is approximately 150 times greater on Venus than Earth (*Donahue et al.*, 1982).

(3) The venusian ^{40}Ar value is one fourth to one third less than that for the Earth (*Hoffman et al.*, 1980a, 1980b; *Donahue and Pollack*, 1983).

The atmospheric observations have a number of implications regarding the geological evolution of Venus. The lack of water on the surface of Venus is thought to contribute towards the lack of plate tectonics (*Mian and Tozer*, 1990). The liberation of water from hydroxides within terrestrial crust is considered to act as a lubricant for plate motion (*Mian and Tozer*, 1990). Furthermore, a dearth of water results in a significant lack of physical and chemical weathering. Consequently, the bulk of the planet's CO_2 inventory resides in the atmosphere, whereas on Earth it resides within carbonaceous rocks. This is a primary cause of the runaway greenhouse situation observed at Venus.

An implication of an enriched deuterium atmosphere is that Venus may once have had considerably more water than at present. The past water inventory is considered to have been reduced by photo dissociation and thermal (Jeans) escape (*Pollack and Black*, 1979; *Kasting*, 1988).

The ratio of ^{36}Ar to ^{40}Ar also gives an insight into planetary and atmospheric evolution. ^{36}Ar is considered to have been most abundant during the formation of the solar system, while ^{40}Ar , derived from radiogenic potassium (^{40}K), has the greater atmospheric abundance today. A greater $^{36}\text{Ar}/^{40}\text{Ar}$ ratio may be explained by a lower initial potassium concentration on Venus, or differences in the timing and/or extent of outgassing responsible for introducing ^{40}Ar into the venusian atmosphere. Similar K/U values for Earth and Venus suggest the latter process is responsible for the dearth of ^{40}Ar on Venus (*Surkov et al.*, 1987).

1.2.5 Orbital altimetric and Radar observations

A modest-resolution altimeter instrument carried by PVO obtained the first accurate topographic data of Venus. The data yielded a topographic map covering 93% of the venusian globe between 74° N and 63° S, with the vertical resolution exceeding 200 metres, and a horizontal resolution of 100 km. Pioneer Venus data showed the planet to consist of 65% rolling plains, 27% lowlands and 8% highlands (*Masursky et al.*, 1980, Figure 1.3). In contrast to the bimodal distribution of surface elevation on Earth, elevations on Venus exhibit a unimodal distribution (*Pettengill et al.*, 1980a, 1980b, Figure 1.4). Approximately 80% of the venusian surface lies within 1 km of the mean planetary radius, mpr, 6051.84 km (*Ford and Pettengill*, 1992). PVO also provided radar images of approximately 50% of the surface of Venus in a swath between 45° N to 15° S with spatial resolution ranging from 20 to 40 km. The data were used to identify and map geological units (*Senske et al.*, 1990).

The Venera 15 and 16 spacecraft arrived at Venus in 1983. Both were placed in highly elliptical orbits (periapsis approximately 1000 km above 62° N, apoapsis 62,000 km). Acquisition of synthetic aperture radar (SAR) images of the surface of Venus were obtained north of approximately 30° N. A number of volcanic and tectonic landforms were first identified by the Venera 15/16 radar data.

Ten to fifteen percent of the area imaged by the two craft contained elevated, intensely deformed materials with intersecting ridges and arcuate troughs, named tessera. Mountain belts, for example Akna, Danu, Freyja and Maxwell Montes (the highest mountain on Venus, standing 11 km above mpr) which surround the large landmass of Ishtar Terra, were interpreted as compressional folds and thrust faults considered to have formed from crustal shortening and underthrusting (*Head et al.*, 1990). Plains areas were also seen to have undergone deformational processes shown by ridge belts occurring in the northern

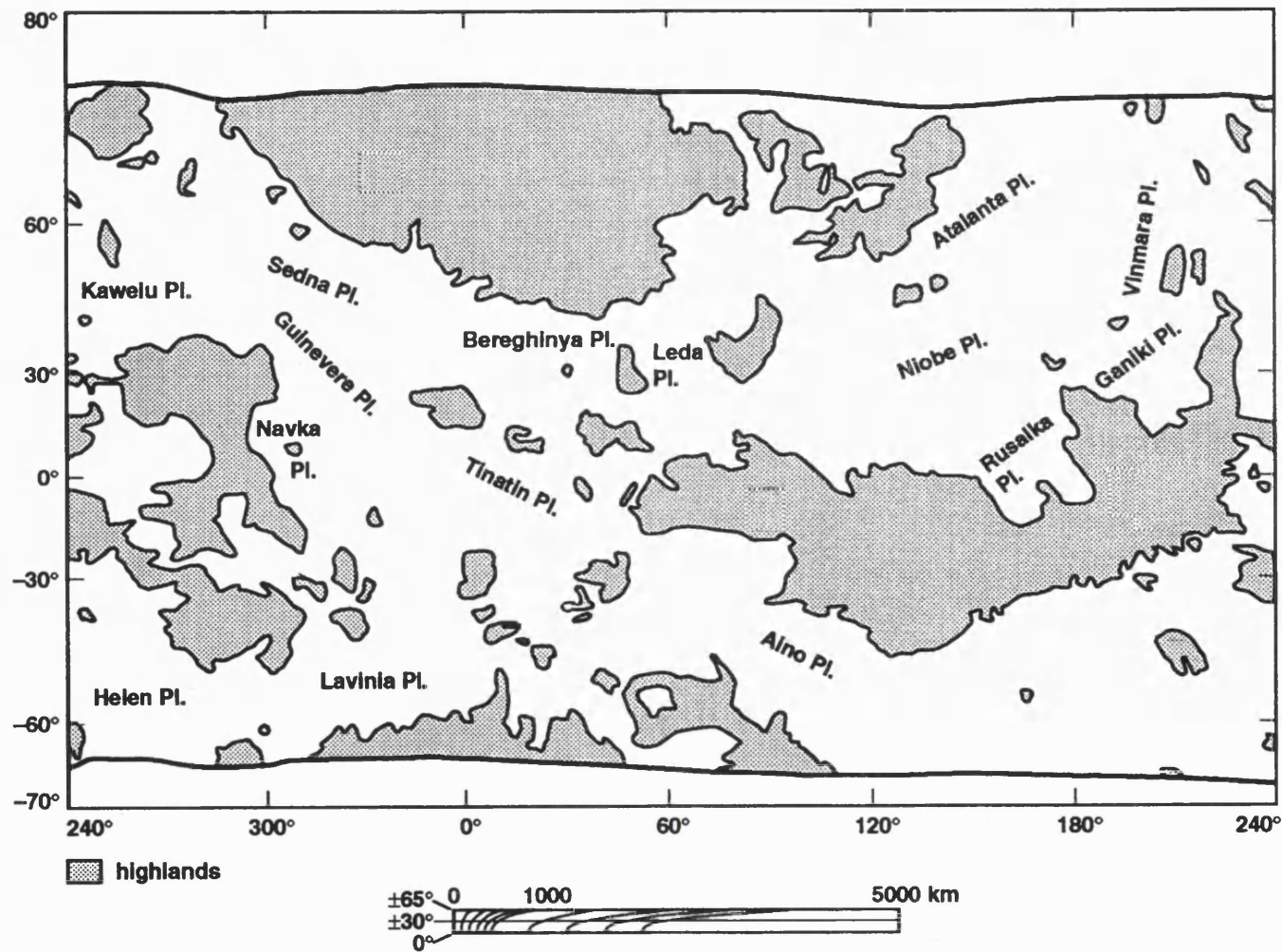


Figure 1. 3 Distribution of the low lying plains of Venus. After *Guest et al. (1992)*.

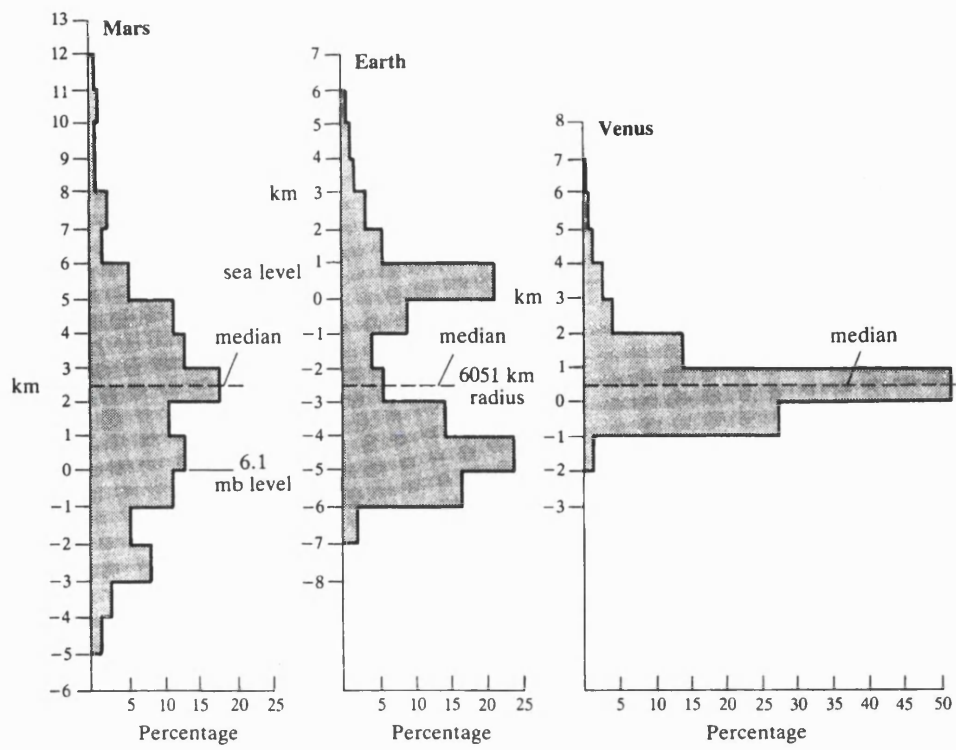


Figure 1.4 Comparison of elevation for Earth, Venus and Mars. After *Cattermole*, (1994).

hemisphere in Atalanta Planitia and the northern polar plains (*Basilevsky et al.*, 1986; *Kryuchkov*, 1990).

Coronae, volcano-tectonic landforms which have a circular to oval shape in plan view, were first identified in Venera data (*Barsukov et al.*, 1984; *Barsukov et al.*, 1986). A total of 36 coronae were identified from the data returned. A three stage model for coronae evolution (see Chapter 2, 2.6.1) was proposed involving uplift, radial and concentric deformation followed by volcanism and topographic degradation (*Stofan and Head*, 1990).

Further volcanic landforms observed included small shield volcanoes and domes (*Aubele and Slyuta*, 1990), and larger shield volcanoes of which 800 were identified which range from 20 to 100 km in diameter (*Slyuta and Kreslavsky*, 1990). Venera 15 and 16 also showed the radar-bright and dark extensive flow materials associated with Neago Fluctus, located in northern Sedna Planitia, described in Chapter 3 (*Barsukov et al.*, 1986). *Barsukov et al.* (1986) inferred from Venera data the plains on Venus are the product of extensive basaltic volcanic activity.

A crater population of 139 identified from Venera craft (*Ivanov et al.*, 1986; *Basilevsky et al.*, 1987) resulted in a crater density of 1 per 10^6 km². The results imply a surface retention age of between 0.5 and 1 billion years, considerably younger than the Moon Mars and Mercury, but older than the majority of the Earth's surface (*Schaber et al.*, 1987; *Neukum*, 1988). The findings of the Venera 15 and 16 missions are summarised by *Barsukov et al.* (1986) *Basilevsky et al.* (1986), *Ivanov et al.* (1986), *Basilevsky and Head* (1988), and *Schaber* (1990).

1.3 The Magellan Mission

1.3.1 The aims of the Magellan Mission

The pre-Magellan investigations described above began to address important questions about the geological and atmospheric evolution of Venus. However, a number of fundamental scientific

questions remained unanswered. The Magellan mission was designed to answer these questions. Concisely, the aims of the mission were 'to improve the knowledge of the geological history of Venus by analysis of the surface morphology and electrical properties and processes which control them, and to improve the knowledge of the geophysics of Venus, principally its density distribution and interior dynamics' (*Saunders et al.*, 1991). The above statement encompassed a global characterisation of landforms, to define and explain erosion, deposition and chemical processes, and to distinguish and understand impact processes.

In order to achieve the above, Magellan was designed to map at least 70% of the surface at a resolution better than 300 metres. Global topography would be acquired at a horizontal resolution of approximately 10 km, with a vertical precision of 80 metres or better. After an aerobreaking manoeuvre into a circular orbit, tracking of the spacecraft would allow the acquisition of high resolution global gravity data (*Saunders et al.*, 1992). A chronology of the mission is shown in Table 1.4.

1.3.2 Magellan Instrumentation and Operation

Magellan carried one prime instrument, the radar sensor, which acquired data in three different modes: (1) a synthetic aperture radar (SAR) mode made with a fixed High Gain Antenna (HGA); (2) a nadir-directed altimetry mode, made with a fixed smaller nadir-directed horn antenna; and (3) a passive thermal radiometer mode which also used the HGA (*Saunders and Pettengill*, 1991). Comparisons between the Magellan SAR instrument and other terrestrial and venusian radar instruments are summarised in Tables 1.5 and 1.6. The Magellan spacecraft and its observing geometry are shown in Figure 1.5. Since both antennas were fixed, aiming them required orienting the entire spacecraft. There was no provision for real-time transmission of radar data, it was stored on two multi-track digital tape recorders (DTRs).

Mission Sequence	Date
Launch Date	04 May 1989
Date of Orbit Insertion	10 August 1990
Beginning of Systematic Radar Imaging	15 September 1990
Completion of Cycle One	15 May 1991
Completion of Cycle Two	14 January 1992
Completion of Cycle Three	15 September 1992
Completion of Cycle Four	24 May 1993
Aerobraking Maneuver	1994
Destruction of spacecraft	12 Oct 1994

Table 1.4 Chronology of the Magellan Mission.

Parameter	Value
<i>Radar Imaging</i>	
Radar frequency	12.6 cm/2.385GHz
Polarisation	HH
Slant range resolution ¹	120 - 360 m
Azimuth resolution ¹	120 - 150 m
Radar image pixel size	75 m (Full resolution)
Antenna look angle ¹	13 to 45 degrees from nadir
Swath width ¹	20 - 25 km
Image strip length	17,000 km
Number of looks per pixel ¹	5 to 17
<i>Altimetry</i>	
Footprint variation ¹	10x12 km ² to 20x29 km ²
Spacing of footprints along orbit	8 km, greater at pole
Error of altimetric resolution	> 5 m
<i>Passive Radiometry</i>	
Footprint variation ¹	16x24 km ² to 83x87 km ²
Sample interval	5 km x swath width

¹ Dependent on spacecraft altitude which changes with latitude

Table 1.5 Parameters of Magellan SAR instrument.

Imaging Device	Parameter
<i>Pioneer Venus</i>	
Wavelength	17 cm
Resolution of radiometry	200 - 800 km
Altimetry resolution	120 km x150 km
Vertical resolution	> 200 m
Radar reflectivity resolution	30 km per pixel
Radar look angle (off nadir)	15 ⁰ to 65 ⁰
<i>Venera 15 and 16</i>	
Wavelength	8 cm
Radar reflectivity resolution	0.8 km
Range resolution	1.5 km
Radar look angle (off nadir)	10 ⁰
<i>Earth Based Imaging</i>	
Wavelength	12.6 cm
Polarisation	HH
Arecibo resolution (Puerto Rico)	1 - 2 km
Goldstone resolution (California)	2 - 3 km
<i>Earth Observational Radar</i>	
<i>Seasat</i>	
Wavelength	23.5 cm
Polarisation	HH
Resolution	25 m
Radar look angle	23 ⁰
<i>ERS 1/2</i>	
Wavelength	6 cm (C band)
Polarisation	VV, LV
Radar look angle	23 ⁰
Resolution	30 m
<i>SIR/C</i>	
Wavelengths	X (3 cm) C (6 cm) L (24 cm)
Polarisation	HH HV VH VV
Radar look angle	15 ⁰ to 60 ⁰
Resolution	5 to 40 m

Table 1.6 Other radar instruments in comparison with Magellan SAR.

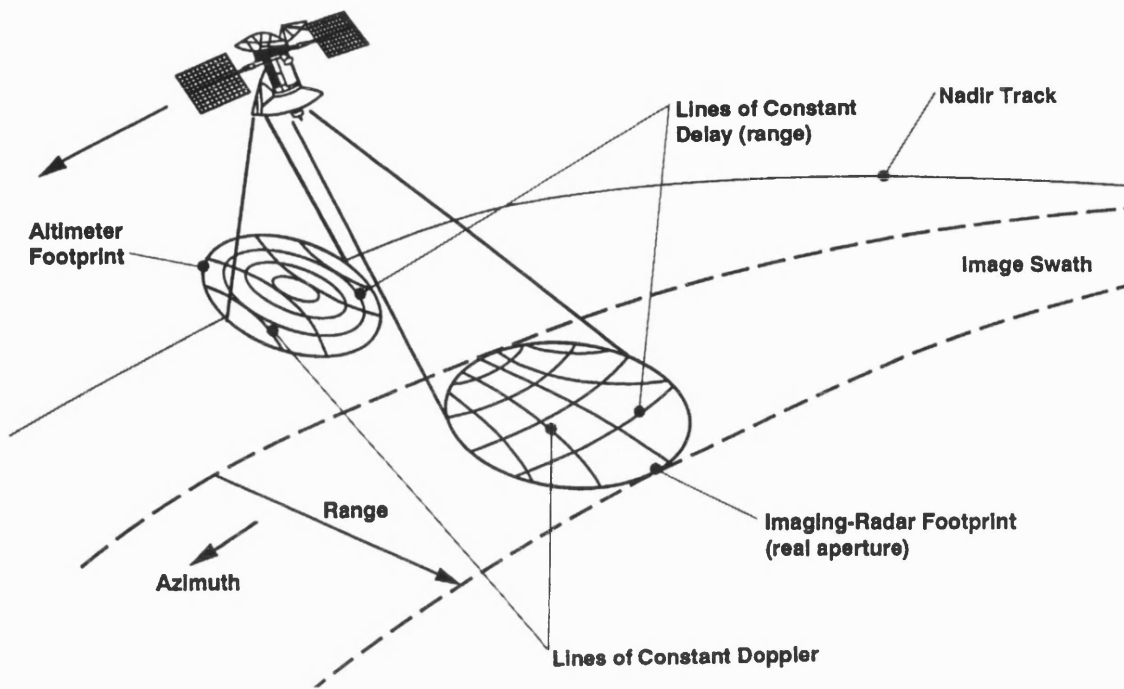


Figure 1.5 Magellan observing geometry in the SAR imaging, altimeter, and radiometer modes of operation. Cross-track resolution (120-350 m) is obtained from the time-delay (range) co-ordinate. Along track resolution (120 m) is calculated from Doppler-frequency analysis. The resolution of radiometric data is determined from the high-gain antenna pattern. After *Ford (1993)*.

1.3.3 Mapping Cycles

Magellan undertook four mapping cycles before entering the venusian atmosphere on the 12th October 1994. Each cycle lasted for 243 days, the time Venus took to complete one axial rotation with respect to the orbital plane of the spacecraft. Since Magellan data are classified by mapping cycles, it is helpful to provide a brief summary of each cycle:

- Cycle 1 ran from 15th September 1990 to 15th May 1991. This cycle constituted the primary mission. In total 83.7% of the planet was imaged between 90° N and 70° S. All radar images are left-looking; radar illumination of the surface is from the left. Incidence angles varied from approximately 45° at periapsis (9.5° N) to 16° at the highest latitudes. Data gaps (black strips in SAR images) occurred owing to superior conjunction (when the Sun lies between the Earth and Venus, hence no data can be transmitted back to Earth), geometrical limitations and mechanical quirks (*Saunders and Pettengill, 1991; Ford and Plaut, 1993*).
- Cycle 2 (the beginning of the extended mission) ran from 15th May 1991 to 15th January 1992, filling gaps from Cycle 1 and obtaining coverage of the south polar area. Cycle 2 imagery differs from Cycle 1 in that all Cycle 2 data are right looking. Furthermore, the incident angle was fixed at 25° . Images were obtained between 75° N and 60° S. 54.5% of the planet was mapped during cycle 2 which resulted in the cumulative surface coverage reaching 96%.
- Cycle 3 lasted from 15th January 1992 to 15th May 1992 and emphasised the acquisition of true stereo image coverage. Approximately 21.3% of the surface was covered by left looking images at incidence angles smaller than those of Cycle 1. An additional 2% of Venus was imaged, resulting in a total of 98% coverage (*Ford and Plaut, 1993*). Radar mapping was terminated after Cycle 3.

- Cycle 4 was dedicated to gravity observations obtained by directing Magellan's HGA towards Earth and recording changes in the radio signal's Doppler shift. Gravity data resolution varies as a function of altitude. Thus, in order to obtain more constant high resolution data, the spacecraft's orbit was circularised by using the venusian atmosphere to aerobreak the probe.

1.4 The Magellan Data Set

The Magellan mission returned more data than all previous planetary missions combined, producing the first global high resolution data set of Venus of 4225 usable SAR imaging orbits (*Ford and Plaut, 1993*). In total, approximately 98% of the planet was imaged between 120-300 meter resolution; some areas were imaged on more than one occasion with different geometries and/or directions of illumination. A more detailed description of data collection and reduction methods is found in Appendix I.

1.4.1 SAR Data

In order to maximise the scientific value of Magellan data, individual images were assembled to produce Mosaiced Image Data Records (MIDRs). Raw SAR data received from Magellan were processed into full resolution basic image data records (F-BIDRs). F-BIDRs represent one orbital strip and are extremely narrow swaths of image data, typically 300 pixels (22 km) E-W, by 200,000 pixels (16,000 km) N-S. Each pixel is a measure of the reflectance of the represented surface element, of diameter 75 metres, expressed in decibels (dB), relative to the model of the average venusian reflectance (*Saunders et al., 1992; Wall et al., 1995*). The surface area represented by each 75 meter pixel has been rescaled from the true resolution of the radar instrument, which is latitude dependent and never better than 120 meters.

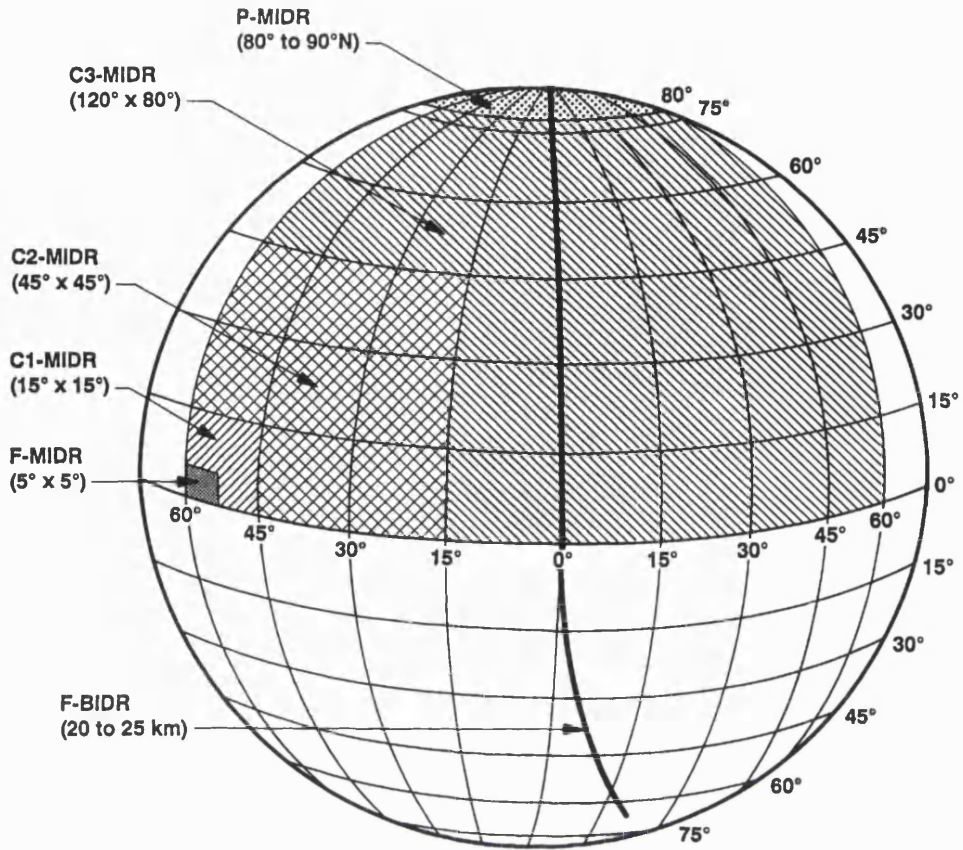
Image mosaics consist of 7168 pixels vertically (lines) by 8192 pixels horizontally (samples) and provide the base for standard Magellan photographic image products (*Ford, 1993; Wall et al., 1995*). Each MIDR has a photomosaic identifier given in general form by X-MIDR. yyHzzz; C, where:

- X is the resolution (F = full resolution data where 1 pixel corresponds to 75 meters; C1, C2 and C3 data, compressed once, twice and thrice data, with 1 pixel corresponding to 225, 675 and 2025 meters respectively).
- yy and zzz are the approximate latitude and longitude at the centre of the mosaic in degrees (e.g. 15 N, 335 E).
- H represents the hemisphere (N for north and S for south)
- C denotes the Cycle in which the data were required e.g. 1 = Cycle 1 etc.

In Cycle 2 and 3 data, three digit numbers are used; the first digit indicates the Cycle and the last is the version number (*Ford, 1993*). Figure 1.6 and Table 1.7 summarises the Magellan products.

The Magellan data set includes photoproducts and digital CD-ROM images. Photoproducts are available for the MIDR products, although owing to financial restrictions only a limited area of the planet is represented by processed F-MIDR images. However, full resolution left-looking FMAPs (75 metres, resampled pixels) are available as photoproducts typically measuring 1 by 1 meter in size. Right-looking FMAPs are currently being produced for the whole of the planet.

F-MIDRs and C-MIDRs are also stored on CD-ROM. Each have MIDRs segmented into 56 individual framelets measuring 1024 lines by 1024 samples, the complete image measuring 7168 lines by 8192 samples. A sampled 1/8th scale browse image accompanies each MIDR measuring 896 lines by 1024 samples.



- F-BIDR** Full-Resolution Basic Image Data Record
- F-MIDR** Full-Resolution Mosaicked Image Data Record
- C1-MIDR** Compressed-Once Mosaicked Image Data Record
- C2-MIDR** Compressed-Twice Mosaicked Image Data Record
- C3-MIDR** Compressed-Thrice Mosaicked Image Data Record
- P-MIDR** Polar Mosaicked Image Data Record

Figure 1.6 Magellan SAR data products. After *Ford and Plaut (1993)*.

Acronym	Product	Area	Resolution
F-BIDR	Full Resolution Basic Image Data Record	20 x 17,000 km	75 m pixel
F-MIDR	Full resolution Mosaicked Image Data Record	5 x 5 ⁰	75 m/pixel
C1-MIDR	Compressed-Once Mosaicked Image Data Record	15 x 15 ⁰	225 m/pixel
C2-MIDR	Compressed-Twice Mosaicked Image Data Record	45 x 45 ⁰	675 m/pixel
C3-MIDR	Compressed-Thrice Mosaicked Image Data Record	120 x 120 ⁰	2025 m/pixel
GEDR	Global Emissivity Data Record	Global	4.6 km/pixel
GREDR	Global Reflectivity Data Record	Global	4.6 km/pixel
GSDR	Global rms slope Data Record	Global	4.6 km/pixel
GTDR	Global Topographic Data Record	Global	4.6 km/pixel

Table 1.7 Magellan data products.

1.4.2 Altimetric and Radiometric Data

As well as SAR data, Magellan collected information on topography and thermal properties of the venusian surface. A detailed account of the collection and reduction of these data is given in Appendix I. Altimetry and radiometric data are available in two primary forms: the Altimetry-Radiometry Composite Data Record (ARCDA) and the Global Data Record (GxDR), both are stored on CD-ROM. The ARCDA is an orbit-by-orbit data set which contains all of the derived parameters such as radius, rms slope, reflectivity and emissivity for each altimeter and radiometer footprint. The GxDR is a more condensed map product represented in several map projections: the projection used is dependent on latitude. Topography, emissivity, rms slope and reflectivity data are shown on the GTDR, GEDR, GSRD and GREDR respectively and have a similar browse and framelet configuration as the SAR CD-ROM data.

1.4.3 Synthetic Stereo Data

Geometrically re-registering pixels within MIDR data was used to artificially introduce parallax in order to create synthetic stereo image data. The degree the pixels are shifted within the MIDR data (either to the left or right) is proportional to their corresponding altimetric data. The greater the topographic height, the greater the geometric movement of the pixel within the image data, and hence the greater artificial parallax produced. Magellan altimetry data gaps were filled using PVO and Venera data. By an empirical process, two exaggerations were found to be most appropriate, 10x and 50x exaggeration. No one exaggeration is appropriate for all areas of Venus. However, 50x works well for smoother areas such as the plains, and 10x for more rugged areas.

1.5 Implications of the New Magellan Data

What are the implications of such an extensive data set? As previously mentioned, Magellan has provided near global coverage (nearly 98%) of an Earth sized planet. The resolution of the data exceeds that of previous missions and, in comparison to remote sensing images of the Earth, a larger proportion of the surface of Venus is imaged at a greater resolution. This allows near global geological investigation of the planet. The data from this mission are currently being used to address a multitude of important geological questions.

Of fundamental importance for Venus (indeed any planet) is the question regarding the mechanisms of heat loss. Since Venus has approximately the same size, mean density and bulk composition as the Earth, it is considered that it should have similar geological activity as the Earth (*Solomon and Head, 1982, 1991*). Three distinct mechanisms are responsible for heat loss on solid surface planets: (1) plate tectonics, the recycling of the lithosphere; (2) hotspot volcanism, the transportation of heat via large upwelling mantle plumes; and (3) lithospheric conduction through a globally continuous shell (*Morgan and Phillips, 1983; Solomon and Head, 1982, 1991*). On Earth, the dominant mechanism of heat loss is plate tectonics. However, heat loss on Venus is still poorly understood.

The mechanism of heat transport on a planet is intimately linked to its tectonic and volcanic evolution (*Solomon and Head, 1991*). In order to help define and constrain heat loss processes throughout the evolution of Venus, it is fundamental to resolve a number of geological and geophysical issues. These issues include: (1) the venusian stratigraphy, in particular a qualitative understanding of volcanic activity with time. In constraining geological activity, the theory that Venus may have undergone periods of catastrophic resurfacing and global tectonic events may be assessed; and (2) the styles of volcanism prevalent on Venus in comparison to Earth. With the advantage of Magellan data, this thesis will attempt to contribute to the two points above.

1.5.1 The VMAP Project

A specific programme currently addressing the question of the global stratigraphy of Venus is the Venus Geological Mapping Project (VMAP). This collaborative project between NASA and United States Geological Survey (USGS) aims to provide systematic scientific investigations of defined quadrangles of Venus in order to produce a global set of geological maps published by the USGS. Each map will provide a description and interpretation of the geology of the quadrangle. Assimilating the findings from detailed mapping will improve the geological understanding of Venus on a global scale, in particular its stratigraphy. The VMAP project represents a major objective of the post-Magellan mission activities and involves the integration of the various Magellan data sets.

A primary task of the thesis was to investigate the geology and stratigraphy of two quadrangles, V19, Sedna Planitia and V31, Sif Mons. Chapter 3 presents the findings from the mapping of the designated quadrangles. An extended survey of the rest of Guinevere and Sedna Planitiae using full resolution FMAP data products is drawn upon to verify unit descriptions and stratigraphic observations from the two quadrangles.

A global set of synthetic stereo images was acquired by the Planetary Image Centre (UCL) which, to date, is one of the few institutes to have access to this data set. Synthetic stereo greatly aids in the construction of unit boundaries and cross-cutting relations. Synthetic stereo images have significantly aided the interpretation of stratigraphic relations within the quadrangles mapped in this thesis and at other localities on the planet. The new observations and interpretations from the study area are used to assess current global stratigraphic and resurfacing models.

Synthetic stereo has been useful in understanding the formation and stratigraphy of coronae (tecto-volcanic landforms abundant on Venus). The ability to view coronae in three dimensions is particularly useful in constructing a time frame for various styles and scales of structures at these landforms. Chapter

4 presents the findings of a detailed study of coronae within the Sif Mons mapping quadrangle. The results from detailed mapping not only test current models of corona formation but have given considerable insight into venusian stratigraphy.

Full resolution FMAP and stereo data have also enabled a detailed study of Sif and Gula Montes, two large venusian volcanoes contained within V31. The eruptive history and interpretation of internal and external processes are discussed based on the new observations, and compared with a number of extensively studied terrestrial volcanoes in Chapter 5. The Chapter also serves to test some of the models associated with large shield formation on Venus. Chapter 6 summarises the conclusions of the research and outlines potential future work.

Before presenting the findings of the research, Chapter 2 reviews and compares current models which describe the global stratigraphy of Venus. Models of formation of coronae and large shield volcanoes are also discussed. The models described in Chapter 2 are those to be tested using observations from the research undertaken here.

1.6 Summary

Venus has a diameter, mean density and bulk chemical composition similar to that of the Earth. However, the atmosphere is dominated by CO₂, and surface temperatures and pressures are 470 and 90 bars respectively. Venus rotates in retrograde motion and has a day which is longer than its year.

The first global scale observations using terrestrial radar showed continent sized land masses and identified distinct volcanic landforms similar to those on Earth, and areas which had undergone tectonic modification (*Campbell et al.*, 1989, 1990; *Senske et al.*, 1991b).

Pre-Magellan spacecraft investigations have included fly-by, orbiter and surface lander missions. The first fly-by missions added to the understanding of the venusian environment, in particular atmospheric characteristics. The Venera and Pioneer orbiters carried modest-resolution synthetic aperture radar instruments which resolved the main components of the venusian surface: volcanoes, mountain belts, volcanic plains, deformed uplands named tesserae, and circular volcanic structures named coronae (*Pettengill et al.*, 1980a, 1980b; *Masursky et al.*, 1980; *Barsukov et al.*, 1986; *Basilevsky et al.*, 1986; *Ivanov et al.*, 1986; *Basilevsky and Head*, 1988; and *Schaber*, 1990).

Seven Russian landers collected chemical data of the surface and found compositions consistent with tholeiitic basalt (*Florensky*, 1977b) except at the Venera 8 site. Here, compositions are more akin to more evolved rocks (*Nikolayeva*, 1990). Panoramic images show the venusian surface composed of slabs of rock separated by an assortment of fines.

The Magellan radar mapping mission was designed to answer a number of outstanding scientific questions from the previous missions including how Venus loses heat and the main research areas of this thesis: venusian stratigraphy and the evolution of volcanic landforms. Approximately 98% of the planet was imaged by SAR radar at a resolution of between 120 and 300 metres. The SAR data are complemented by ancillary data (emissivity, reflectivity and rms slope measurements) as well as synthetic C1 and C2-MIDR stereo images. The Magellan data are available in a number of formats both on CD-ROM and as photoproducts. The availability of these new data sets has been used in this research to further constrain the stratigraphy of Venus and investigate selected volcanic and volcano-tectonic processes.

Chapter 2

Current Models of Stratigraphy and Volcanic processes on Venus

2.1 Introduction

Detailed mapping undertaken during the course of this thesis, using new data (described in Chapter 1), is used to investigate three areas of venusian geology: (1) Stratigraphy; (2) coronae evolution and their stratigraphic significance; and (3) the evolution of Sif and Gula Montes, two large shield volcanoes. Various models are proposed to explain the stratigraphy and volcanic landforms seen on the surface of Venus. With new observations presented here, these models are tested and refined in the subsequent chapters. The purpose of this chapter is to summarise previous models which attempt to explain the global venusian stratigraphy, coronae evolution, and the morphology of large shield volcanoes.

2.2 A Model of the Global Stratigraphy of Venus

Basilevsky and Head (1994, 1995a, 1995b, 1996), *Head and Basilevsky* (1996) and *Basilevsky et al.* (1996, 1997) have created a first attempt at a 'global stratigraphy model' for Venus, based on mapping using standard techniques describe by *Tanaka et al.* (1994). The model was constructed by analysing the stratigraphic relations at 36 sites which contained craters surrounded by radar-dark paraboloid materials (paraboloid craters). The use of 36 paraboloid craters is considered by the authors of the model to avoid a bias in preference of site selection, made because the crater distribution is assumed to be random on Venus (*Schaber et al.*, 1992; *Strom et al.*, 1994). Furthermore, paraboloid craters are interpreted to be among the youngest 10% of the venusian crater population (*Campbell et al.*, 1992) and are considered by the

authors of the model to represent a convenient stratigraphic marker.

For each site selected, the stratigraphic relations between all major features, structures and terrains within an area of approximately 1000 x 1000 km (centred at the crater) were established. The results from each site were compared and a stratigraphic model created. The 36 sites have a combined area of about 36×10^6 km², approximately 8% of the total surface of Venus. Photoproduct and CD-ROM C1-MIDRs and F-MIDRs (where available) were consulted at each locality as well as altimetry data. However, the use of FMAPs and C1-MIDR synthetic stereo photoproducts, which are of vital importance in constructing stratigraphic relations (Chapter 1, 1.5), is not mentioned.

From the study, *Basilevsky and Head* (1994, 1995a, 1995b, 1996) and *Basilevsky et al.* (1997) recognise four geological time subdivisions (Periods), four related time-stratigraphic units (Systems), and seven rock-stratigraphic units (Groups) (Figure 2.1). In all 36 sites, the stratigraphy could be constructed with just 10 different terrain units and six types of structures. The four proposed Periods, associated Systems and Groups defined are considered to represent geological processes which acted globally: different styles of volcanism and deformation characterise specific time periods of venusian history. The above model is referred to as a 'directional' stratigraphic model within the thesis. The directional nature of this model will be tested against observations presented in Chapter 3. The divisions of the stratigraphic model are as follows:

2.2.1 The Pre-Fortunian Period

The period represents the first 80-90% of venusian history. The Pre-Fortunian System is the only rock-stratigraphic system and is considered no longer preserved in the surface geomorphologic record (*Basilevsky and Head*, 1995a, 1995b, 1996; *Basilevsky et al.*, 1997). The conclusion is based on present surface crater retention ages.

	Geologic Time Units	Time-Stratigraphic Units	Rock-Stratigraphic Units	
	Aurelian Period	Aurelian System	Aurelia Group	Cdp Ss, Sp
0.1T *	Guineverian Period	Guineverian System	Guinevere Supergroup	Atla Group Ps, Pl
T +				Rusalka Group Pwr
				Lavinia Group Pfr, RB
				Sigrun Group Pdf, COdf
1.47 0.46T ‡	Fortunian Period	Fortunian System	Fortuna Group	Tessera Maxwell Fm
	Pre-Fortunian Period	Pre-Fortunian System	?	?

Figure 2.1 Proposed global rock-stratigraphic, time stratigraphic, and geological time units for the global stratigraphic model, *Basilevsky and Head (1995b)*. * refer to references from *Basilevsky (1993)* and *Strom (1993)*. T⁺ is the crater retention age of the surface of Venus (see text for estimates of this age). ‡ calculation by *Ivanov and Basilevsky (1993)* of crater retention age for tessera. After *Basilevsky and Head (1995b)*.

As with other bodies in the solar system (*Wilhelms*, 1990), the crater density on Venus may be used to estimate the retention age of the surface. Analysis of Magellan images has identified approximately 932 craters (*Schaber et al.*, 1992, Figure 2.2). A further 401 failed impact sites (craterless splotches) are identified (*Strom et al.*, 1994). *Strom et al.* (1994) state impact craters on Venus cannot be distinguished from a random distribution model, both spatially and hypsometrically (Figures 2.3 and 2.4). From these observations, the crater retention age of Venus places the average absolute age of the entire surface of Venus between 500 and 300 Ma (*Phillips et al.*, 1992; *Strom et al.*, 1994; *Price and Suppe*, 1994; and *Price et al.*, 1996). Variations of this average range from 800 Ma to 190 Ma (*Schaber et al.*, 1992; *Strom et al.*, 1994). The conclusion drawn is that the bulk of the surface of Venus is considerably younger than that of Mercury, Mars and the Moon.

2.2.2 The Fortunian Period

This Period contains the Fortunian System. The materials contained in the Fortunian System are considered to be the most ancient on Venus. The bulk are defined as tessera units (Tt), with compressional mountain belts (e.g. those which surround Lakshmi Planum) included as structural facies. Tesserae are described as heavily modified materials which have undergone multiple episodes of deformation, resulting in at least two sets of intersecting ridges and grooves.

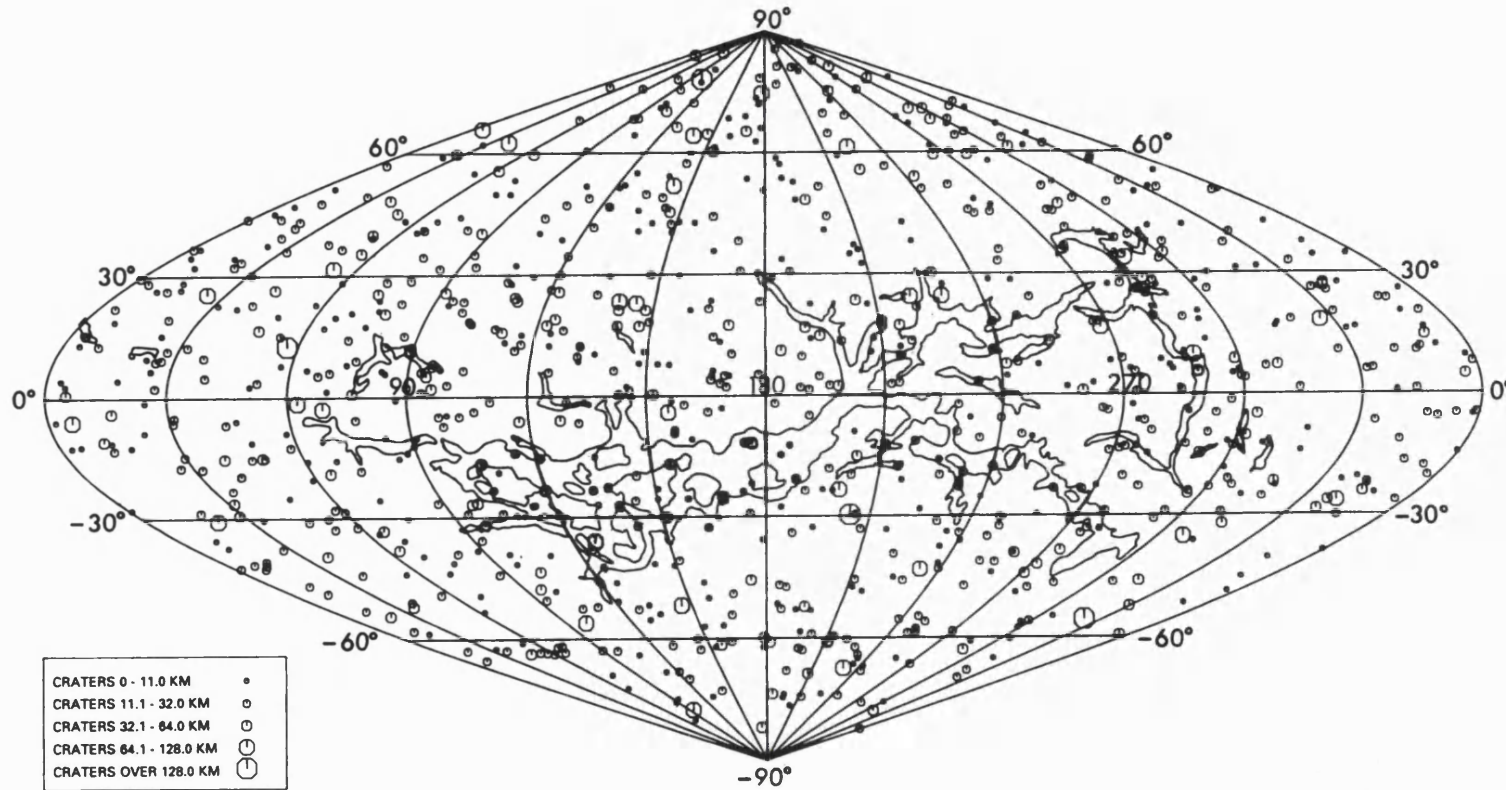


Figure 2.2 Sinusoidal equal-area projection showing the sizes and distribution of 932 craters identified on 98% of the surface of Venus. After *Strom et al. (1994)*, modified from *Schaber, (1992)*.

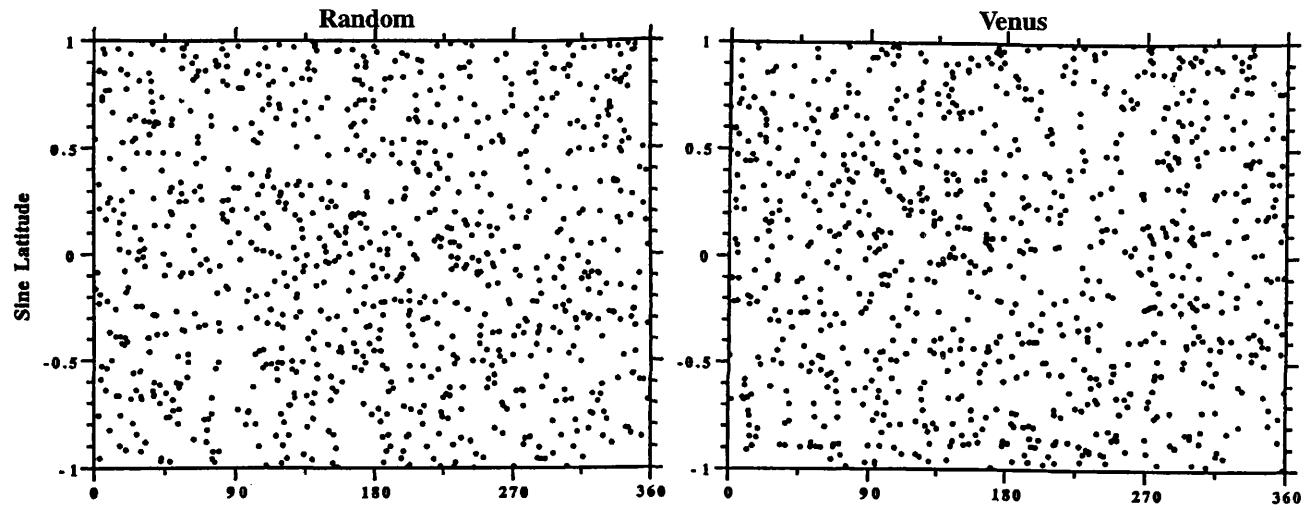


Figure 2.3 Comparison of a Monte Carlo simulation (Random) and the actual distribution of 932 impact craters (98% surface area) on Venus (*Strom et al., 1994*). The clusters and holes within the Monte Carlo simulation are stochastic variations, while some of those seen in the Venus plot are due to gaps in the coverage (2%). After *Strom et al. (1994)*.

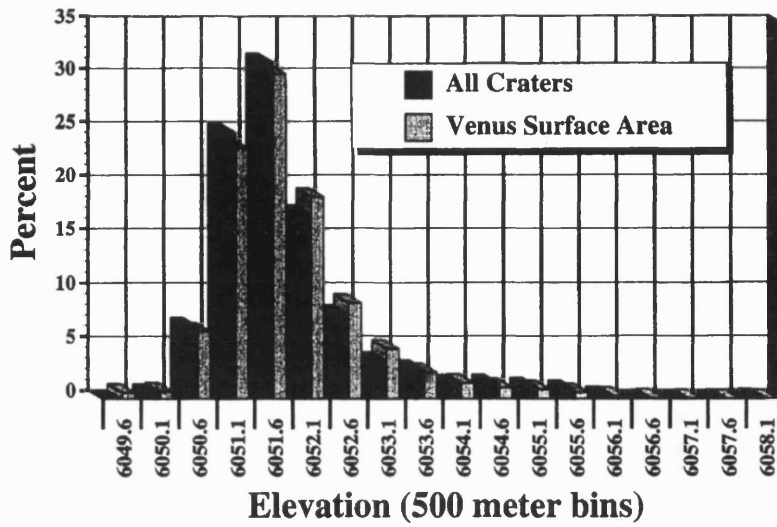


Figure 2.4 Histogram showing the percentage of impact craters compared with surface area in 500 m elevation bins (*Strom et al., 1994*). *Strom et al. (1994)*, state that craters are randomly distributed with respect to elevation. After *Strom et al. (1994)*.

Tesserae are considered to represent a tectonically deformed precursor terrain belonging to the Pre-Fortunian Period (*Barsukov et al.*, 1986; *Basilevsky et al.*, 1986; *Bindschadler and Head*, 1991). Tesserae have upstanding topography, a strong radar return and high rms slopes. Some authors have referred to tessera as Complex Ridged Terrain (CRT) for instance *Solomon et al.* (1992). The unit constitutes approximately 8% of the venusian surface (*Ivanov and Head*, 1993) and is considered embayed and overlain by all younger plains materials. The authors of the model state that this observation establishes the stratigraphic position of tessera to be pre-plains emplacement (*Basilevsky and Head*, 1995a, 1995b; *Basilevsky et al.*, 1997).

The density, distribution, and deformation characteristics of craters on tessera terrain have been used by *Gilmore et al.* (1997) to constrain late-stage tessera extension to approximately 30-60 Ma, less than 20% of the average crater retention age for tessera.

2.2.3 The Guineverian Period

Basilevsky and Head (1995a, 1995b, 1996) and *Basilevsky et al.* (1997) claim in their global stratigraphy model that all plains materials are contained in one system: the Guineverian System. The System contains the 'Guineverian Supergroup', comprising a sequence of four rock-stratigraphic Groups: Sigrun, Lavinia, Rusalka and Atla Groups. The authors observe 'unconformities caused by episodes of tectonic deformation' which allow the separation of the groups (*Basilevsky et al.*, 1997). Unconformities also separate the Guineverian Period from the older Fortunian and younger Aurelian Periods. The rock-stratigraphic units that make up the four groups are summarised below.

The Sigrun Group: Densely fractured plains terrain (Pdf) and deformed materials within the interiors of coronae (COdf). The deformation is characterised by swarms of graben considered to represent a global period of crustal extension which cut plains materials and tesserae. Pdf units are observed as inliers embayed by younger plains materials. The materials are claimed by Basilevsky and Head to embay the Fortunian Tessera terrain. The Group represents 3-5% of the total surface area of the 36 selected sites (*Basilevsky and Head, 1995b; 1996; Basilevsky et al., 1997*).

The Lavinia Group: Represents two rock units: ridged plains materials (Pfr) and ridge belts (RB) which deform widespread plains materials with a similar appearance to the Rusulka plains materials described below. Pfr and RB are considered structural facies of the Lavinia Group and are observed as: (1) broad ridging over a wide area, classified as Pfr; (2) clustered ridging also classified as Pfr; and (3) ridge belts (RB) observed as a 'chain of islands' or a 'long island' of ridging embayed by younger plains materials (*Head and Basilevsky, 1996; Basilevsky et al., 1997*). The two rock units comprise 1-3% of the total area represented by the 36 sites.

The Rusulka Group: Represents widespread global (70% of the venusian surface) volcanism forming extensive plains materials of intermediate radar brightness with small and large radar-bright and radar-dark flows (*Basilevsky and Head, 1995b*). The units were subsequently deformed by a 'global network' of compressional wrinkle ridges (Pwr), considered symptomatic of Rusulka plains materials. The materials are interpreted as flood lavas, analogous to terrestrial tholeiitic basalts based on chemical analysis of the surface (*Basilevsky and Head, 1995a, 1995b, 1996; Basilevsky et al., 1997*).

The Atla Group: Two rock-stratigraphic units are defined within the Atla Group: smooth (Ps) and lobate (Pl) plains materials. The units are associated with rift zones, large shield volcanoes such as

Sif and Gula Montes (Chapter 5), and coronae. The landforms are inferred to indicate a more localised style of volcanism (*Basilevsky and Head, 1995b, 1996; Basilevsky et al., 1997*). The group 'represents about 10% of the surface' (*Basilevsky and Head, 1995b; Basilevsky et al., 1997*).

2.2.4 The Aurelian Period

The youngest geological Period has one system containing one rock-stratigraphic unit, the Aurelia Group. The Aurelia group is composed of parabolic radar-dark mantles (Cdp), crater ejecta materials and central peaks (named after the crater Aurelia in the V31 mapping quadrangle). Aeolian features described by *Greeley et al. (1992)* are also included in this Group (Ss). The total area occupied globally by Cdp is estimated by *Campbell et al. (1992)* to be 8%. The authors state Aurelia group materials overlay all stratigraphic units described above, except for the rare cases where volcanism postdates paraboloid craters, for instance at Maat Mons, 0.5° N, 194.6° E (*Basilevsky, 1993*).

2.3 A Sequence of Deformation within the Global Stratigraphy Model

Structural relations observed by *Head and Basilevsky, (1996)* are placed in context within the global stratigraphy model (Figure 2.5). The authors distinguish between well-defined stratigraphic units, and structures associated with periods of deformation.

Broadly, structures within the model are divided into two groups: structures associated with tessera, and structures which deform plains materials. Plains structures are subdivided into ridge belts (RB), wrinkle ridges (Wr), three coronae structures: COdf (deformed coronae interiors), COar (concentric and/or radial fractures), and COaf (ridges forming corona annuli), and rift zones.

VENUS REGIONAL AND GLOBAL STRATIGRAPHY

Units	Stratigraphic Column	Events	Processes	GEOLOGICAL ACTIVITY
Ss, Sp Cdp Fra, F, Pa, Pl,		<ul style="list-style-type: none"> • Wind Streaks • Debris Sheets • Paraboloid Craters • Local Intense Fracturing • Smooth Plains 	<ul style="list-style-type: none"> • Rifting • Associated Volcanism 	
COaf F Pa, Pl,		<ul style="list-style-type: none"> • Minor Fractures • Smooth Plains Emplacement 	<ul style="list-style-type: none"> • Minor Extensional Tectonics • Basaltic Volcanism 	
Pwr Aar, COar		<ul style="list-style-type: none"> • Wrinkle Ridge Formation • Coronae/Arachn. Ridges • Plains Emplace. 	<ul style="list-style-type: none"> • Compressional Tectonics • Volcanism 	
RB Pfr		<ul style="list-style-type: none"> • Ridge Belt Formation • Plains Emplacement 	<ul style="list-style-type: none"> • Compressional Tectonics • Volcanism 	
COdf Pdf		<ul style="list-style-type: none"> • Plains Fracturing • Plains Emplacement 	<ul style="list-style-type: none"> • Vast Extensional Tectonism • Corona Formation • Volcanism 	
Tt		<ul style="list-style-type: none"> • Tessera-Forming Deformation • Tessera Precursor Formation 	<ul style="list-style-type: none"> • Vast Extensional and Compressional Deformation 	

Figure 2.5 Summary of Venus global stratigraphy model proposed by *Basilevsky and Head* (1994). The left column shows map units in order of stratigraphic position (oldest at the bottom) and associated structures. Interpreted geological history is sketched in the next column. The right hand columns describe the geological processes responsible for the units. Note how stages of corona formation (COdf, COar, and COaf) are restricted to specific periods of geologic time, an observation inconsistent with coronae observed in the V31 mapping quadrangle (Chapter 4). After *Basilevsky and Head* (1994).

As with volcanism, the deformational processes are considered strongly directional (i.e. distinct styles of deformation have occurred one after another at discrete times throughout the history of Venus). The deformation and resulting structures are described in stratigraphic order by *Head and Basilevsky* (1996) as follows:

Tessera deformation event - tesseration (Tt): This initial event represents the earliest deformation processes and gave rise to the structures observed within tessera units. The event implies initial crustal shortening which changed to extensional deformation, producing first ridges then cross-cutting graben (*Bindschadler and Head* 1991; *Bindschadler et al.*, 1989, 1992a, 1992b; *Ivanov and Head* 1995; *Basilevsky et al.*, 1997). The graben, as well as 'possible' shear faulting (*Basilevsky et al.*, 1997), form densely fractured terrain within the Fortunian and Sigrun Groups. The shear faulting is claimed to cut into tessera materials.

Ridge belt deformation event (RB): The global period of deformation which gave rise to ridge belts only deforms Lavinia Group plains materials. The authors interpret ridge belts as representing a transition from a dominance of global extensional deformation to global compression (*Head and Basilevsky*, 1996; *Basilevsky et al.*, 1997).

Wrinkle ridge deformation event (Wr). The model implies a global period of compressional deformation occurred after the emplacement of the Rusulka plains materials which produced pervasive wrinkle ridge structures. Wrinkle ridges are claimed not to deform the younger Atla Group and are rare within the older Sigrun Group. (*Basilevsky and Head*, 1995a, 1995b, 1996; *Basilevsky et al.*, 1997).

Based on the paucity of craters deformed by wrinkle ridges (*Schaber et al.* 1992, and *Strom et al.* 1994, show that between 62% and 84% of craters on Venus are unmodified by deformation). *Basilevsky et al.* (1997) claim that wrinkle ridges were emplaced

in a relatively short period of time, probably less than 30-45 Ma after the emplacement of the Rusulka plains materials.

A sequence of deformation associated with coronae (COdf, COar and COaf). Basilevsky and Head (1995b, 1996) and Basilevsky et al. (1997) assume an 'ideal sequence' for corona formation. The sequence implies sequential periods of deformation associated and restricted within the geological Groups described above. The sequence postulated is as follows: (1) early interior deformation (COdf), restricted to the Sigrun Group; and (2) intermediate stages of corona evolution contemporaneous with the Rusulka Group and wrinkle ridge formation (COar, COaf). It is claimed that corona evolution is controlled by the tectonic environment dominant during each system or group (Basilevsky et al., 1997).

2.4 Summarising the Global Stratigraphy Model

Basilevsky and Head (1995a, p. 285) infer a 'distinctive regional and global stratigraphic, and geologic sequence' from their observations, the key stages being:

1. A global catastrophic tectonic event (or *tesseration*) destroyed pre-existing units and produced tesserae, the oldest widespread geological unit.
2. Widespread plains emplacement subsequently deformed by extensive and closely-spaced graben which define the Sigrun group.
3. Further plains emplacement, deformed by a period of compressional stresses resulting in the production of ridge belts (RB) confined to the Lavinia group.

4. Emplacement of Rusulka Group flood basalts, considered the most widespread of all plains materials. The materials subsequently underwent compressional wrinkle ridge deformation. The wrinkle ridges formed globally in a relatively short period of time, since they are not seen (by the authors of the model) to deform the younger volcanic materials which belong to the Atla Group, nor do they deform many venusian craters.

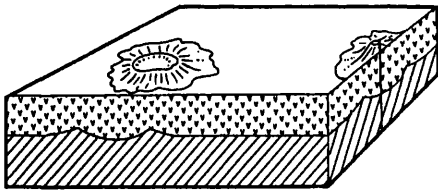
5. A switch to more recent localised volcanism associated with coronae, large shield volcanoes and rifts. The Aurelia Period began 30-50 Ma ago, and represents low levels of volcanism and rifting.

The model is strongly directional, represented by periods of extensional and compressional tectonism which occurred on a global scale, together with distinct styles of volcanic activity, resurfacing the planet at different times. Volcanic activity is considered to have declined from widespread regional (Lavinia and Rusulka Group plains formation) to more local events (Atla Group large shield formation) with increasing age, interpreted as the result of a thickening lithosphere. The model implies that tectonic activity has declined over time in a similar fashion to volcanism (*Phillips and Hansen, 1997*).

2.5 A Global Resurfacing Model (GRM) and Equilibrium Resurfacing Model (ERM): Two 'end member' scenarios

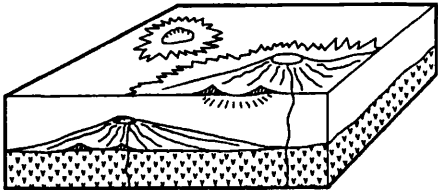
The interpretation of volcanic units, structures and the crater population has led to two opposing resurfacing models which attempt to explain the geological history of Venus (Figures 2.6 and 2.7): (1) A synchronous global resurfacing event, (the Global Resurfacing Model, GRM, or Catastrophic Resurfacing Model); and (2) a more localised resurfacing process active throughout the bulk of observed venusian history (the Equilibrium Resurfacing Model, ERM).

(a) Catastrophic resurfacing



- resurfacing takes place infrequently at extremely high rates
- resurfacing rate very low between events
- production crater population
- almost all craters pristine

(b) Regional resurfacing: "collage"



- resurfacing events local and sufficiently large to obliterate craters completely
- resurfacing patch size, frequency and integrated resurfacing rate specified by crater population
- vast majority of impact craters are unmodified

Figure 2.6 Block diagrams of Venus resurfacing models, illustrating the catastrophic and equilibrium resurfacing models of (a) *Strom et al. (1992)* and (b) *Phillips et al. (1992)*. After *Head et al. (1992)*.

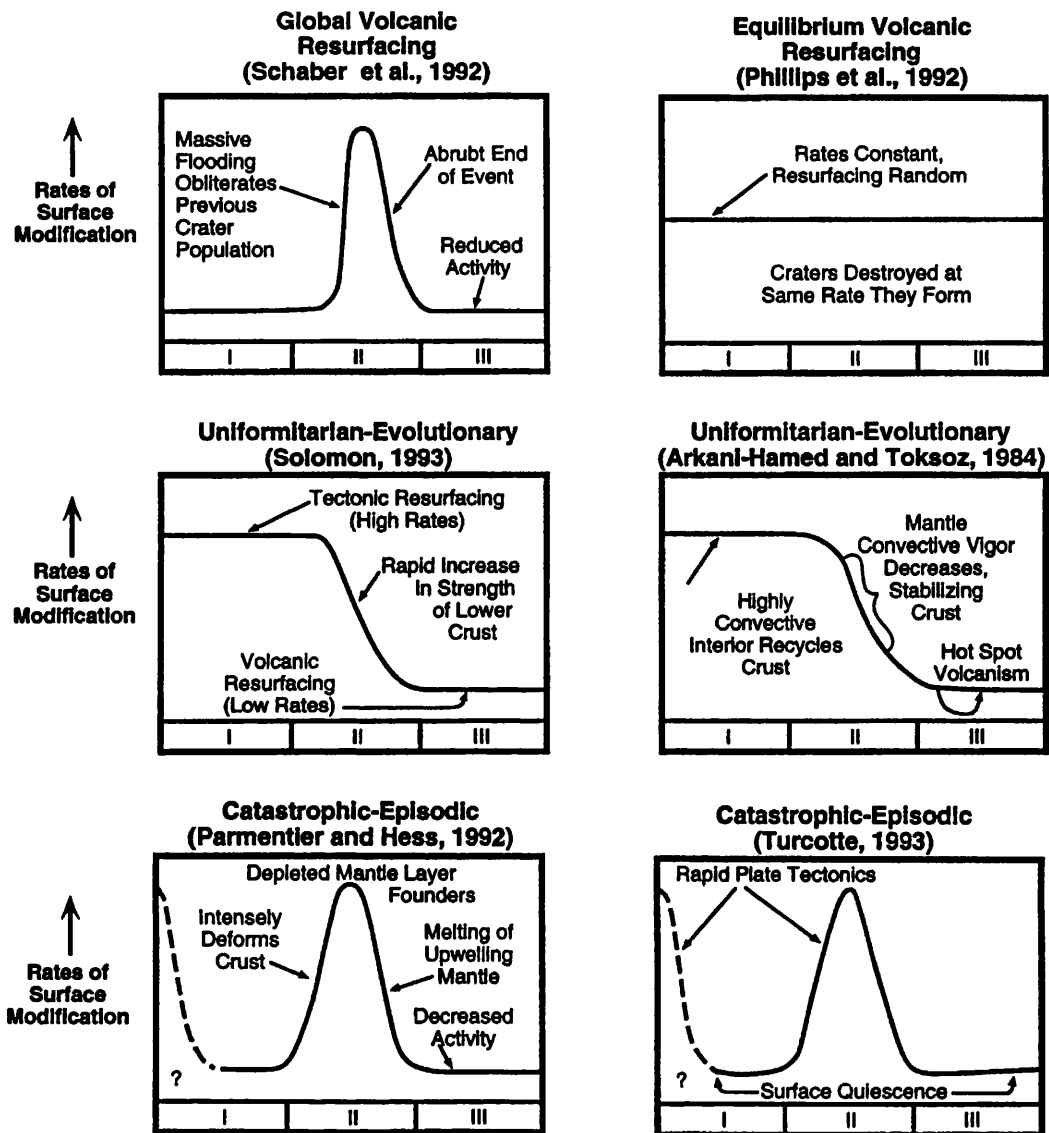


Figure 2.7 Paradigms for models of geological formation evolution of Venus. Each model is plotted against 3 periods described by *Ivanov and Head (1996)*. Period I represents material which predates the first preserved surface terrain on Venus (tessera). Period II represents the formation of presently observed tessera and widespread deformed volcanic plains (Sigrun Period). Period III represents the emplacement of smooth volcanic plains, regional rifting and volcanic edifice formation. The bulk of cratering took place during period III. After *Ivanov and Head (1996)*.

The two opposing models were first discussed by *Schaber et al.* (1992) and *Phillips et al.* (1991a, 1992) respectively, and were subsequently developed by other authors (e.g. *Bullock et al.*, 1993; *Herrick*, 1993, 1994; *Izenberg et al.*, 1993; and *Strom et al.*, 1994).

The Global Resurfacing Model - GRM

This model suggests Venus experienced 'a global resurfacing event about 300 m.y. ago, followed by a dramatic reduction of volcanism and tectonism' (*Strom et al.*, 1994, p. 10,899). The emphasis is on reduction rather than total shutdown of volcanic and tectonic activity (*Schaber et al.*, 1992; *Strom et al.*, 1995). The global resurfacing event is considered to have ended abruptly (< 10 m.y). The model assumes a production crater population (i.e. one where the number of craters on the surface are increasing with time). The present crater population reflects the later, less intensive bombardment of Venus, while the early heavy bombardment, as seen on the Moon, is considered to have been erased by the synchronous global resurfacing event.

The Equilibrium Resurfacing Model - ERM

In contrast to the GRM, *Phillips et al.* (1992) assume the crater population is an equilibrium population. *Phillips et al.* (1992) *Herrick and Phillips* (1994) *Herrick et al.* (1995) question whether the random areas where craters are lacking, or where craters cluster, occur purely by chance. *Phillips et al.* (1992) suggest that the distribution of embayed and deformed craters is non-random and may potentially aid in defining the amount and style of geological activity on Venus subsequent to plains formation.

The model implies craters are being destroyed at approximately the same rate at which they are produced on a global scale. Local resurfacing occurs in 'small patches' (no greater than 400 km across) at a limited number of regions on the planet at any one time. The authors claim that resurfacing has occurred at specific times throughout the observable history of Venus, that a major resurfacing episode is unlikely to have occurred, and that

there are clearly distinct surface ages on the planet (*Phillips et al.*, 1992).

Supporters of the equilibrium resurfacing model substantiate the theory with evidence that craters which are embayed (approximately 3.4% of the crater population, *Strom et al.*, 1994) and deformed tend to occur in areas of low crater density, implying resurfacing has occurred on a local scale more akin to volcanic surfacing currently observed on Earth.

Several geophysical models describe how global resurfacing may be responsible for the emplacement of ubiquitous plains materials on Venus employing various forms of mantle overturn summarised in Figure 2.7 (e.g. see *Arkani-Hamed and Toksoz*, 1984; *Arkani-Hamed et al.*, 1993; *Arkani-Hamed*, 1994; *Parmentier and Hess*, 1992; *Turcotte*, 1993, 1995; *Herrick*, 1994). In considering resurfacing on Venus, evidence exists for enhanced, episodic regional resurfacing events on Earth. *Larson* (1991a, 1991b), *Garzanti* (1993), and *Coffin and Eldholm* (1992, 1993, 1994) suggest periods of accelerated mantle convection result in superplumes, recognised in the geological record by anomalies including enhanced alkalic basalt production, enhanced spreading rates, and environmental changes owing to increased volcanic activity. *Coffin and Eldholm* (1992, 1993, 1994) discuss the formation of 'Large Igneous Provinces' (LIPs) which represent a continuum of voluminous mafic rocks attributed to mantle plumes and hotspots. LIPs are considered to represent episodic punctuations in the relatively steady state production of crust on Earth. Similar processes may have acted during the evolution of Venus, on larger scale to produce the volcanic plains materials.

Basilevsky and Head (1995a, 1995b) and *Basilevsky et al.* (1997) conclude that Strom's global resurfacing model agrees well with the stratigraphic relations they observed. They reject the equilibrium resurfacing model because they do not identify unit repetition within their 36 sites: the area of each 36 study sites being considerably larger than the 'patch size' resurfacing area described by *Phillips et al.* (1992).

2.6 Models of Evolution for Volcanic Landforms on Venus

The second half of this chapter focuses on models of volcanic evolution for coronae and large shield volcanoes. The models described below are tested qualitatively using observations from detailed studies of coronae and Sif and Gula Montes, located within the V31 mapping quadrangle (Chapters 4 and 5 respectively).

2.6.1 A Model for Corona Evolution and Stratigraphic Significance.

Coronae consist of concentric annuli of ridges and/or graben (*Barsukov et al.*, 1986; *Stofan et al.*, 1992; *Squyres et al.*, 1992). Most have a circular or ovoidal planform shape, with maximum diameters of 65 to 2100 km. The topography of coronae varies, however most display a raised rim (*Stofan et al.*, 1992, 1997). Volcanism is nearly always associated with coronae, the amount and style of which varies both spatially and temporally (*Stofan et al.*, 1992; *Head et al.*, 1992; *Roberts and Head*, 1993).

A number of models have been presented to account for the morphology and formation of coronae. However, current models do not explain the many variations in morphology which are observed (*Stofan et al.*, 1992; *Stofan and Smrekar*, 1996). Coronae occur in several tectonic environments including volcanic rises, the plains and, most commonly, along chasmata systems (*Stofan et al.*, 1997). Three stages of corona evolution are inferred from previous observations and theoretical models have been developed to explain these observations (*Stofan and Head*, 1990; *Stofan et al.*, 1992; *Squyres et al.*, 1992). The three stages are as follows:

Stage 1: Uplift and volcanism

In the first stage of evolution, uplift and volcanism occur accompanied by interior, radial extensional deformation (*Stofan et al.*, 1992; *Squyres et al.*, 1992). *Stofan and Smrekar* (1996) suggest that an initial voluminous extrusive episode, which predates annulus formation, occurs during this first stage. The first stage has been modelled as a rising spherical diapir resulting in uplift and associated deformation consistent with that observed at many coronae (*Stofan et al.*, 1991; *Tackley and Stevenson*, 1991; *Janes et al.*, 1992; *Koch*, 1994; *Koch and Manga*, 1996).

Stage 2: Formation of annulus

The second stage of evolution involves the formation of an annulus of either ridges and/or graben. During the second stage, it is predicted that the diapir impinges on the lithosphere, flattening and spreading laterally, to form concentric fractures at the rim of a plateau (*Janes et al.*, 1992; *Koch*, 1994).

Stage 3: Topographic reduction and volcanism

The third and last stage of coronae formation is considered to involve reduction of topographic relief and continued volcanism. The reduction in relief and production of the outer trough has been modelled as gravitational relaxation (*Stofan et al.*, 1991; *Janes et al.*, 1992). A second model, proposed by *Sandwell and Schubert* (1992), suggests that during the last part of mantle upwelling, material breaches the lithosphere and emplaces a substantial load on the surface. In time, the lithosphere is 'rolled back' and retrograde subduction occurs forming an annular ridge and trough.

The stratigraphy of Coronae

Various stratigraphic and/or absolute age dates have been proposed for corona formation (*McGill*, 1994; *Namiki and Solomon*, 1994; *Price and Suppe*, 1994; *Basilevsky and Head*, 1994, 1995a, 1995b; *Head and Basilevsky*, 1996; *Price et al.*, 1996; *Basilevsky et al.*, 1997). These studies place the majority of corona formation

after that of regional plains and before the large volcanic shields (*McGill*, 1994), with absolute ages calculated at 120 ± 115 Ma (*Namiki and Solomon*, 1994; *Price and Suppe*, 1994; *Price et al.*, 1996).

However, of considerable importance is whether crater densities can be used to infer the date of specific mapped units on Venus. *Strom et al.* (1994) state that because impact craters on Venus cannot be distinguished from a random distribution model, (both spatially and hypsometrically) trying to obtain relative and absolute dates of local and regional terrains from crater densities alone is prone to errors.

As coronae have important implications for the internal dynamics of Venus, it is important to better constrain how they form, the contribution they make to venusian volcanism, and their significance through time. Work presented in Chapter 4 is used to validate the three stage evolutionary model, and tests whether the stratigraphic model proposed by *Basilevsky and Head*, and the interpretation of statistical dating methods of *Namiki and Solomon* (1994), *Price and Suppe* (1994) and *Price et al.* (1996) apply to coronae observed in V31.

2.6.2 Large Shield Volcanoes

Another way in which volcanism is manifested on the surface of Venus is in the form of large volcanic edifices, first identified with Arecibo and Venera 15/16 radar data (*Masursky et al.*, 1980; *Campbell et al.*, 1989; *Schaber and Kozak*, 1989; *Campbell and Campbell*, 1990; *Schaber*, 1991). A global survey by *Crumpler et al.* (1997), which uses Magellan data identifies 167 large shield volcanoes with diameters greater than 100 km.

Large shield volcanoes on Venus are considerably lower and broader than their terrestrial counterparts (*Schaber and Kozak*, 1989). *Schaber* (1991) measured the heights of 12 large venusian shield volcanoes and showed the majority were < 2.5 km in relief, while *Ivanov and Basilevsky* (1990) measured basal diameters

and recorded a median area of ~60,000 km². In comparison, Mauna Loa (Hawaii) is more than 8 km high, with a diameter of ~15,000 km².

What may account for the difference in dimension of venusian volcanoes? From modelling, *Head and Wilson* (1992) suggest the greater width to height ratio of venusian volcanoes is linked to the development of neutral buoyancy zones (NBZs). The vertical position of NBZs are considered different on Venus in comparison to Earth, owing to the ambient environmental conditions, in particular atmospheric pressure. *Ryan* (1987a, 1987b) defines NBZs as regions of neutral buoyancy produced when the *in situ* densities of magmatic fluids and surrounding country rocks are equal, and considers their development important within terrestrial volcanoes.

How do NBZs change with the evolution of shield volcanoes? Geodetic data from the Hawaiian shields indicate that as they grow, their summit magma reservoirs rise progressively with edifice construction (*Decker et al.*, 1983). Progressive eruptions at the summit of the volcano raise the floor of the caldera or rift (the zero confining pressure datum) and changes the pressure distribution within the edifice. In order to remain in equilibrium with its surroundings (i.e. neutrally buoyant), the summit storage reservoir must move upwards to adjust for the growth of the edifice and change in pressure: as *Ryan* (1987a) states, 'Hawaiian magma reservoirs lift themselves up by their own boot straps.'

Furthermore, Hawaiian volcanoes show an evolutionary track along which continuously readjusting NBZs of summit magma storage regions move upwards: the higher the volcano, the greater distance the magma reservoir has moved vertically. Loihi and Mauna Loa are current end members of the evolutionary track (*Ryan*, 1987a, 1987b, Figure 2.8).

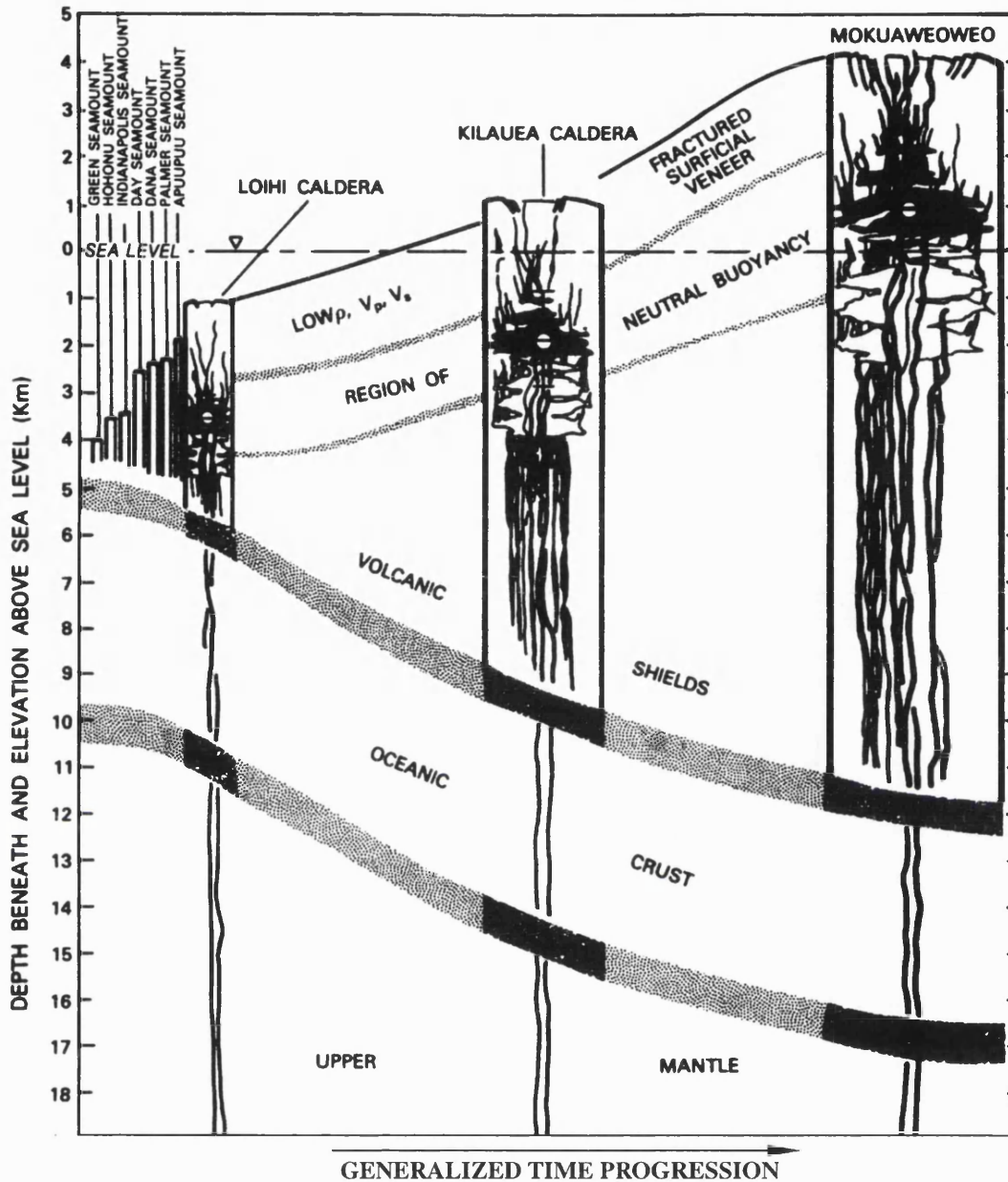


Figure 2.8 The growth and development of oceanic terrestrial volcanoes. The diagram shows how, on Earth, the neutral buoyancy zone of the magma reservoir (circle with horizontal dash) moves vertically upwards with the growth of the edifice. In comparison, it is considered that magma reservoirs on Venus are more likely to remain below the volcano owing to the great variation in atmospheric pressure, with lateral growth being more dominant than vertical growth (*Head and Wilson, 1992*). The difference in the magma reservoir and neutral buoyancy position may explain the greater width to height ratio of venusian volcanoes compared with terrestrial volcanoes. After *Ryan (1987a)*.

For both Kilauea and Mauna Loa, the calculated position of the NBZ coincides with a geodetically and seismically determined summit storage magma reservoir, at approximately 3 km local depth (Ryan, 1987a, 1987b). Similar observations were found at Icelandic volcanoes (Ryan, 1987a, 1987b). Hence it is concluded that the magma reservoir lies within the edifice.

But what of Venus? *Head and Wilson* (1992) modelled NBZ development on Venus and Earth. Their results highlight several important considerations regarding volcanism. For large shield volcanoes, it is shown that for magma with a fixed volatile content, NBZs become deeper with increasing edifice elevation (Figures 2.9 and 2.10, Table 2.1). Hence, the magma reservoir may not reside within the volcanic pile.

The deepening of the magma reservoir relative to edifice growth on Venus is considered a consequence of the significant vertical change in atmospheric pressure. *Head and Wilson* (1992) suggest that as a venusian volcano increases in elevation, successive flow units have lower densities. A decrease in atmospheric pressure allows an increase in volatile exsolution, resulting in more vesicular extrusives and a greater negative density contrast between the magma and country rocks. Hence the rise of magma becomes progressively more difficult as it encounters layers of lower density. The results from the comparative model of large shield growth on Venus and Earth by *Head and Wilson* (1992) may be summarised as follows:

1. Over a range of reasonable magma volatile contents for Venus and Earth, neutral buoyancy zones and magma reservoirs on Venus will generally remain in the prevolcano substrate longer than on Earth. It is predicted that for venusian edifices less than about 2.5 km in elevation, the magma reservoir remains below the base of the volcano.
2. The greater the elevation of the volcano and/or volatile content of the magma on Venus, the greater the depth to the NBZ.

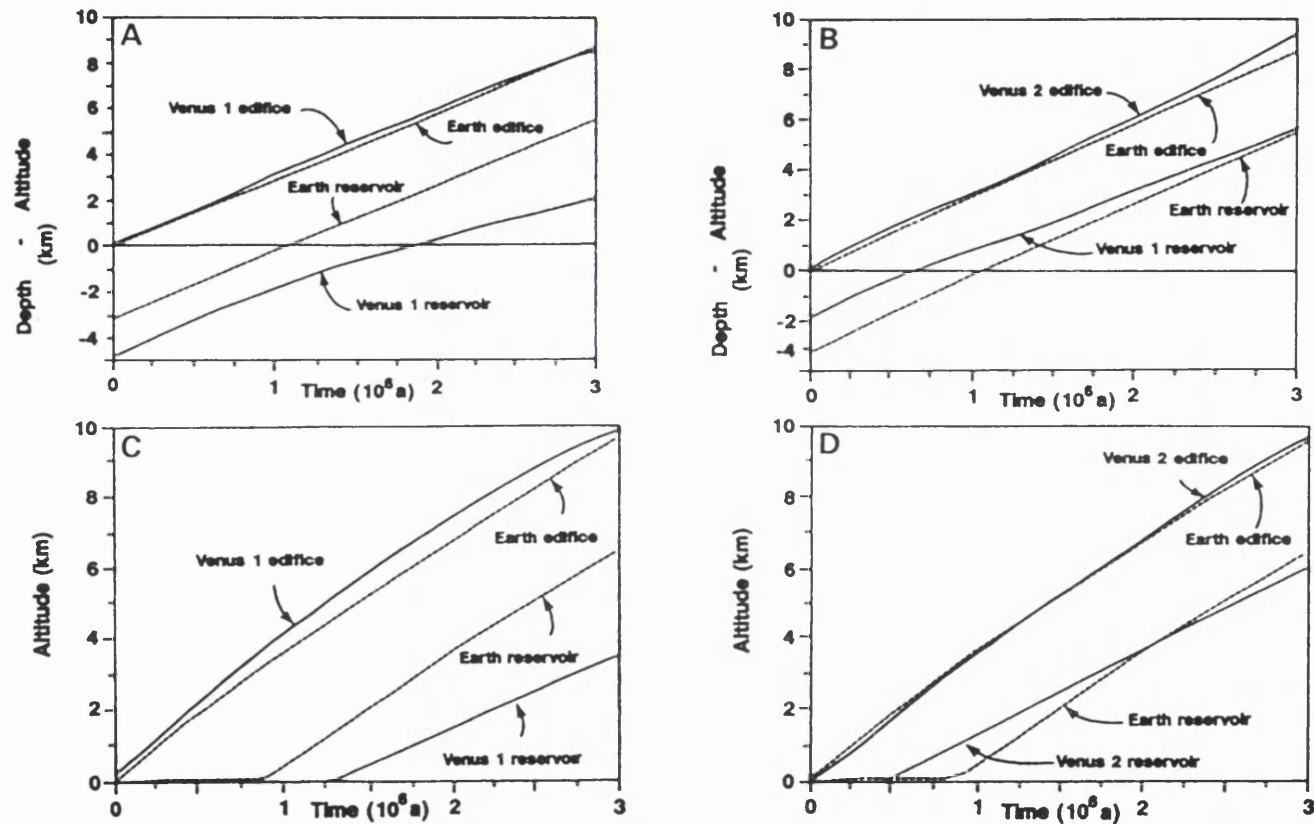


Figure 2.9 Volcano growth and migration of magma reservoir centre (NBZ) for various magma volatile contents and country rock density on Earth and Venus. Starting conditions are as follows: Earth case (E) $P_{surf}=0.1$ Mpa, $CO_2=0.40$ wt %, $H_2O=0.7$ wt %. Venus case 1 (V1), $P_{surf}=9.81$ Mpa, $CO_2=0.40$ wt %, $H_2O=0.7$ wt %. Venus case 2 (V2), $P_{surf}=9.81$ Mpa, $CO_2=0.40$ wt %, $H_2O=0.0$ wt %. (a) Comparison of E and V1 and (b) comparison of E and V2: both case use initial country rock density profiles produced by the eruption and subsequent subsidence (maintaining the same surface elevation) of magmas with the same volatile contents as those of the magmas building the edifices. (c) Comparison of E and V1 and (d) comparison of E and V2; these two cases use initial country rock densities produced by the eruption and subsequent subsidence of volatile-free magmas. After *Head and Wilson (1992)*.

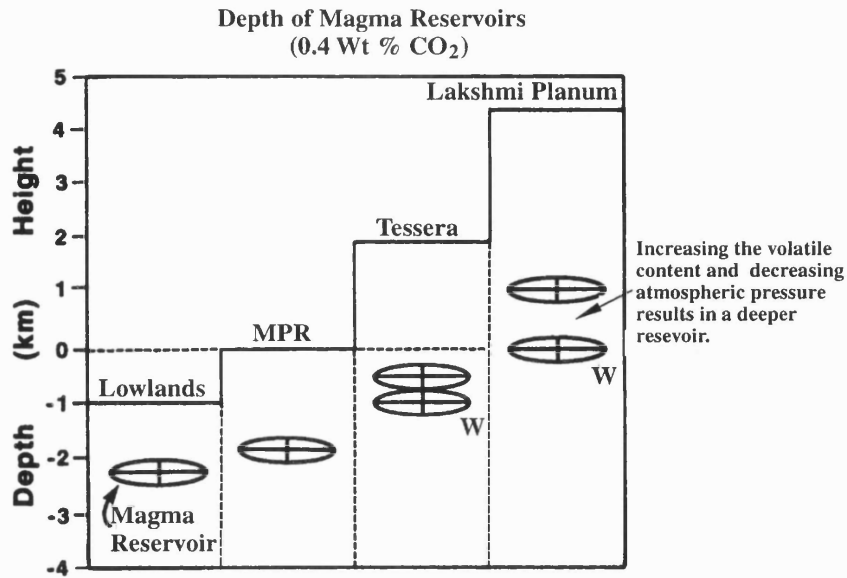


Figure 2.10 Modelled effect of different surface elevations on the depth of magma reservoirs (the centre of which is indicated by cross within oval) for a magma with a volatile content of 0.40 wt % CO₂ (see Table 2.1). In the model, addition of 0.5 wt % H₂O (Table 2.1) does not effect the position of the reservoir at high atmospheric pressures (lowland plains), but deepens it at lower atmospheric pressures (indicated by W). After *Head and Wilson* (1992).

(a)

N_{IC} , wt %	P_{surf} , MPa			
	10.453	9.811	8.645	7.405
H_2O CONTENT = 0 wt %				
0.20	--	--	--	--
0.25	--	--	--	1385
0.30	--	--	1105	2205
0.35	--	--	2005	2765
0.40	1224	1815	2516	3213
0.45	1934	2305	2924	3592
0.50	2360	2685	3270	3920
0.55	2702	3010	3320	4205
H_2O CONTENT = 0.5 wt %				
0.05	--	--	--	1340
0.10	--	--	--	2105
0.15	--	--	--	2725
0.20	--	--	--	3200
0.25	--	--	1020	3590
0.30	--	--	1910	3930
0.35	--	--	2440	4225
0.40	1225	1815	2860	4490
H_2O CONTENT = 1.0 wt %				
0.05	5960	6340	7040	7840
0.10	6105	6470	7165	7955
0.15	6240	6600	7285	8060
0.20	6370	6725	7400	8170
0.25	6495	6845	7510	8270
0.30	6615	6960	7615	8370
0.35	6705	7060	7715	8465
0.40	6767	7116	7773	8529

Depths are in meters. A null entry indicates that no neutral buoyancy zone exists for a particular combination of conditions. P_{surf} of 10.453 corresponds to the mean planetary radius (MPR) - 1 km; 9.811 to MPR; 8.645 to MPR + 2 km; and 7.405 to MPR + 4.4.

(b)

N_{fw} , wt %	P_{surf} , MPa			
	10.453	9.811	8.645	7.405
0.00	1224	1815	2516	3213
0.20	1224	1815	2516	3213
0.40	1224	1815	2516	3213
0.50	1224	1815	2859	4492
0.60	2744	3487	4660	5813
0.70	4350	4863	5770	6737
0.80	5378	5804	6588	7453
0.90	6149	6526	7235	8036
1.00	6767	7116	7773	8529

Table 2.1 (a) Depths to centres of magma reservoirs on Venus as a function of the surface atmospheric pressure and magma CO₂ and H₂O contents (*Head and Wilson 1992*). Lower atmospheric pressures are found at greater elevations on Venus which result in magma with a lower volatile content reaching a NBZ. (b) Depths to the centres of magma reservoirs on Venus as a function of the surface atmospheric pressure and magma CO₂ and H₂O contents for a constant CO₂ content of 0.4 wt %. After *Head and Wilson (1992)*.

3. The vertical migration of a magma reservoir on Venus will be slower than on Earth owing to the ambient atmospheric pressure.

4. Since, in general, the vertical migration of magma is slower, magma reservoirs are predicted to stabilise and grow to a larger size on Venus than Earth.

The model is dependent on several factors: (1) the mass flux per unit area for each eruption is equal (i.e. the added layers constructing the volcanoes in the model are the same); (2) little subsidence takes place during the history of the volcano; and (3) the volatiles remain within each extruded layer. Liberation of the volatiles from the extruded lava would result in materials with a greater density.

Should the model above apply, it is suggested (*Head and Wilson, 1992*) that environmental factors on Venus will: (1) result in greater lateral growth of venusian volcanoes than vertical growth; and (2) the bulk of growth will occur in the prevolcano substrate rather than the edifice itself. This would result in the observed high width to height ratio of venusian volcanoes in comparison to Earth (*Head and Wilson, 1992*). A summary of large edifice growth on Venus in comparison with Earth is shown in Figure 2.11. A number of consequences regarding larger magma reservoirs with predominant lateral growth are predicted by *Head and Wilson (1992)*:

1. Larger stable reservoirs should promote a greater opportunity for magma differentiation.

2. Calderas are predicted to be significantly larger on Venus, owing to a larger magma reservoir located at a predicted greater depth.

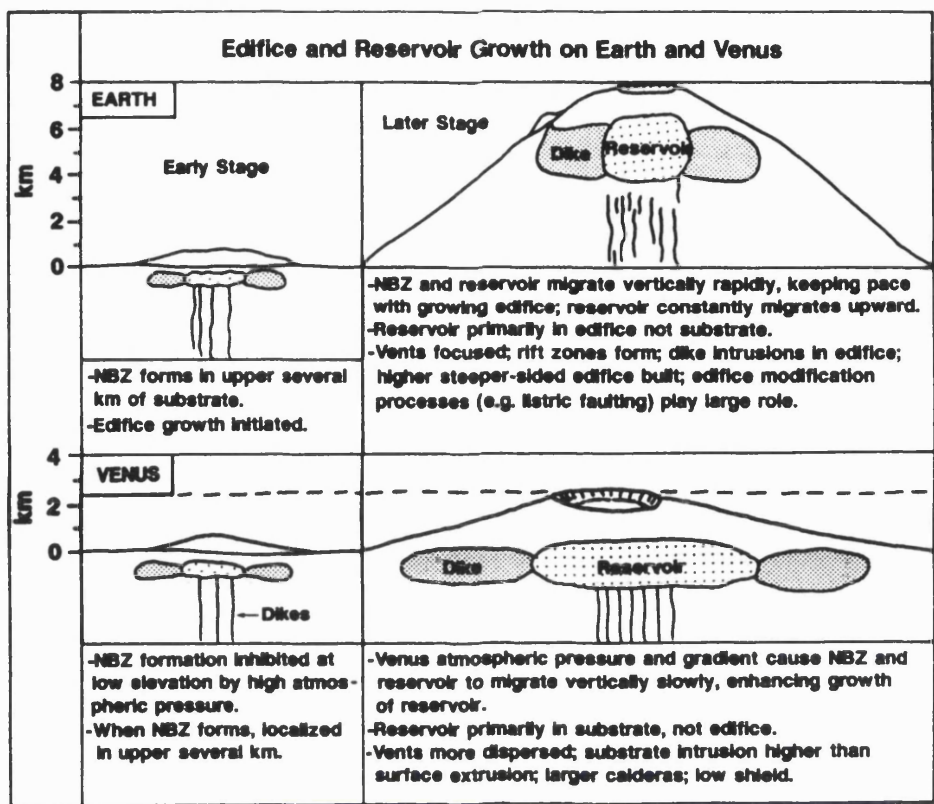


Figure 2.11 Schematic illustration showing models of edifice and subsurface reservoir growth for Venus and Earth. After *Head and Wilson (1992)*.

3. The stress state in the rocks surrounding the reservoir is such that lateral propagation of dykes is more probable than fracturing of the overlying roof (*Wilson and Head, 1990*).

When a reservoir becomes over pressurised owing to further injections of magma, the stress regime favours lateral growth by radial injections of dykes. Since magma reservoirs on Venus are considered prone to grow more laterally than vertically, it is probable that volcanoes will show the surface manifestations of radial dykes (*Parfitt and Head, 1993*).

2.6.3 Pyroclastic Eruptions

Owing to a greater atmospheric pressure on Venus, nucleation and disruption of magma is considered to occur at greater depths on Venus than Earth (*Garvin et al., 1982; Wilson and Head, 1983; Head and Wilson, 1986; Thornhill, 1993*). On Earth, magma fragmentation must occur at or below the surface if the total volatile content in a basalt exceeds approximately 0.1 wt%. On Venus however, the volatile weight fraction must exceed approximately 2.5 wt% for H₂O in basaltic magmas and approximately 4 wt% for CO₂ in any magma before explosive eruptions occur: the results are specific for a surface atmospheric pressure of 10 MPa, corresponding to the venusian lowlands. This falls to 1.1 wt% for water in Basalt, 1.6 wt% for water in rhyolite and 2.0 wt% for CO₂ in any melt at an atmospheric pressure of 4 MPa (*Wilson and Head, 1983; Head and Wilson, 1986*). Given the environmental and volatile conditions, the question arises can explosive eruptions occur on Venus?

The minimum amount of water needed for an eruption at high altitudes on Venus (4 MPa) is considered to be near the upper end of the range common in terrestrial magmas. CO₂ is considered more important in exsolution on Venus, than on Earth (*Head and Wilson, 1982, 1986*) as water is extremely rare on Venus (see Chapter 1, 1.2.4).

However, it is generally accepted that to trigger substantial magma disruption under the present venusian conditions, volatile concentrations much greater than those observed in typical terrestrial magmas are needed (*Garvin et al.*, 1982). This implies that explosive volcanism is rare, unless a more soluble volatile can be substituted.

While magma volatile content may be less on Venus than on Earth, particular styles of eruption may result in pyroclastic activity, for instance Strombolian eruptions. On Earth, bubble coalescence can concentrate gas sufficiently to cause intermittent explosions in low-viscosity magmas which ascend slowly to the surface (*Blackburn et al.*, 1976; *Head and Wilson*, 1986). Such eruptions can produce convection columns 5-10 km in height. *Garvin et al.* (1982) showed that on Venus coalescence may produce bubbles 1 metre in size for magma ascending at 0.03 m/s with a total wt% CO₂ greater than 0.5. However, more typical bubble sizes are predicted to lie between 0.1 and 100 mm.

Vulcanian and Pelean eruption styles may also be responsible for localised pyroclastic deposits on Venus (*Head and Wilson*, 1986; *Fagents*, 1994). The formation of debris in the vent and/or a chilled carapace results in a build-up of gas pressure in the upper part of the magmatic system. Terrestrial modelling of Vulcanian eruptions by *Self et al.* (1979) suggest pressures of 200-300 bars are needed before gas can escape. On Venus, owing to the high ambient atmospheric pressure, the energy from such an eruption is calculated to be only one fifth of that expected from a similar explosion on Earth.

A further consequence of the greater ambient temperature is the production of denser eruption clouds. The predicted result is less clast cooling, resulting in the probable formation of spatter material and lava flows, rather than a pyroclastic cone (*Head and Wilson*, 1986). Hence ignimbrites are predicted to weld together more easily and extend for greater distances under greater venusian temperatures (*Kieffer*, 1995).

The predictions above may be tested by looking for characteristic landforms (size of calderas, fissures, dykes, material

with radar characteristics and morphologies similar to terrestrial pyroclastic deposits) indicative of specific volcanic activity, at Sif and Gula Montes and other large shield volcanoes. Furthermore, observations from well known terrestrial volcanoes may be used to give possible insights into the evolution of Sif and Gula Montes, as discussed in Chapter 5.

2.7 Summary

Various models are proposed to explain the stratigraphy and volcanic landforms seen on the surface of Venus. *Basilevsky and Head* (1994, 1995a, 1995b, 1996), *Head and Basilevsky* (1996) and *Basilevsky et al.* (1996, 1997) have developed a preliminary stratigraphic model for Venus. The model implies a sequence of events in which different styles of volcanic and tectonic activity acted during separate periods of geological time, each represents a discrete stage in the planet's formation. The volcanic and tectonic events occurred at the same time on a global scale but have declined from regional to local processes considered a consequence of crustal thickening (*Phillips and Hansen, 1997*).

From the low crater population on Venus (< 1000) and the observation that most are unmodified by tectonism or volcanism, an average absolute age of the venusian surface has been calculated between 800 and 190 Ma, typically considered between 500 and 300 Ma (*Strom et al., 1992; Schaber et al., 1992; Phillips et al., 1992; Strom et al., 1994; Price and Suppe, 1994; Price et al., 1996*). While some workers consider the spatial and hypsometric distribution of craters to be random (*Schaber et al., 1992; Strom et al., 1992*), others suggest that the paucity corresponds to areas of most recent geological activity (*Phillips et al., 1992*). Hence, two opposing models for the resurfacing of Venus are considered: the global resurfacing model (*Schaber et al., 1992; Strom et al., 1994, 1995*), implying a relatively rapid resurfacing of Venus and subsequent decline in geological activity, and the equilibrium resurfacing model (ERM) in which localised patches of the surface are renewed destroying craters at the same rate of production

(Phillips *et al.*, 1992; Herrick and Phillips, 1994; Herrick *et al.*, 1995).

Detailed mapping presented in Chapter 3 (together with other stratigraphic observations) will be used to test the directional nature of the global stratigraphic model. The new results also test which of the resurfacing models (if any) are applicable to the V31 and V19 mapping quadrangles, and for the contiguous regions of Guinevere and Sedna Planitiae.

Two volcanic landforms previously identified on Venus are coronae and large shield volcanoes (Barsukov *et al.*, 1984, 1986). Three stages of corona evolution are inferred from previous observations, initial uplift and volcanism, the formation of an annulus of either ridges or graben, and lastly by topographic reduction and late stage volcanism (Stofan and Head, 1990; Stofan *et al.*, 1992; Squyres *et al.*, 1992). Work presented in Chapter 4 is used to validate the three stage evolutionary model, and test whether the stratigraphic model proposed by Basilevsky and Head apply to coronae observed in V31.

Large shield volcanoes on Venus are considerably lower and broader than their terrestrial counterparts (Schaber and Kozak, 1989). Head and Wilson (1992) suggest the greater width to height ratio is a consequence of environmental conditions on Venus which favour lateral over vertical movement of the magma reservoir, with neutral buoyancy zones generally being lower or absent within the volcanic piles in comparison with terrestrial volcanoes. Furthermore, it is suggested that magma reservoirs are larger on Venus (Head and Wilson, 1992). As a consequence, calderas are predicted to be larger. Owing to the lack of water, and great atmospheric pressure, pyroclastic eruptions are considered to be rare, unless a build-up of exsolved volatiles occurs.

Chapter 5 presents a detailed description of Sif and Gula Montes and compares their edifice and flow morphology with well documented terrestrial volcanoes. As part of this study, the models of large shield volcanism outlined above will be tested by looking for characteristic landforms indicative of the processes described above acting at the two volcanoes.

Chapter 3

Guinevere and Sedna Planitiae: Mapping, Description and Interpretation

3.1 Introduction

This chapter presents the findings from (1) observations of the Sif Mons (V31) and Sedna Planitia (V19) mapping quadrangles of Venus, and (2) observations from a more areally extensive study area combining the whole of Guinevere and Sedna planitiae. These planitiae were selected as they form a contiguous area and contain both the mapping quadrangles V19 and V31.

Detailed mapping shows materials within the quadrangles may be subdivided into distinct geological units (*Copp and Guest, 1995, 1997*). They include regional plains materials and materials associated with large shield volcanoes, edifice fields and coronae. Geological maps of V31 (map 1) and V19 (map 2), together with copies of each base map (basemap 1 and basemap 2) are contained in the sleeve at the back of the thesis. Similar units are identified throughout Guinevere and Sedna Planitiae. The selected study area allows the stratigraphy of volcanically diverse landforms and structural fabrics over a large contiguous area of plains to be established. From this study, a quantitative appraisal of flow materials which can be seen to originate from a source is presented. The observations and inferred interpretations are used to test the models of stratigraphy and resurfacing discussed in Chapter 2.

The chapter first presents a cartographic description of each quadrangle and summarises geological mapping on Venus using radar. Next, the descriptions and interpretations of units from within the mapping quadrangles are presented and interpretations of their formation discussed. Appendix II and III contain USGS map unit descriptions for V31 and V19. The stratigraphy of the study area (including the quadrangles) is then

summarised. Finally, the global stratigraphic and resurfacing models are evaluated based on the new observations.

3.2 Geological Mapping of Venus

The VMAP project (Chapter 1, 1.5.1) divided Venus into 62 mapping quadrangles (Figure 3.1) each at the scale of 1:5,000,000. The map series includes Mercator, Lambert Conformal Conic and Polar Stereographic projections for latitudes $<25^{\circ}$, 25° to 75° , and $>75^{\circ}$ respectively. All projections are conformal and retain the approximate shape of small landforms (*Tanaka et al.*, 1994; *Batson et al.*, 1994).

The Sif Mons quadrangle (V31) uses a Mercator projection, measures 2632.2 km N-S by 3158.6 km E-W, and has an area of $8,103 \times 10^6 \text{ km}^2$, comparable to the surface area of Brazil. V31 extends from 0° to 25° N and from 330° to 0° E (Figure 3.1). Sedna Planitia quadrangle (V19) extends from 25° to 50° N and 330° to 0° E (Figure 3.1), and is presented on a Lambert Conformal Conic projection. The quadrangle measures 2600 km N-S and covers an area of $6,580 \times 10^6 \text{ km}^2$. Base products for each map included a SAR mosaic photo-base, composed of 90% left looking imagery for Sedna Planitia (10% data loss), and 95% left looking images for the Sif Mons quadrangle (5% data loss). A graticule and nomenclature overlay, 16 level grey slice altimetry photoproduct, and a colour transparency set of radiometric and altimetric data were produced for V31 only.

The data from which the geological maps were produced include the base materials above, full resolution (120 m data rescaled to 75 meter pixels) mosaiced FMAP photoproducts, and a set of synthetic stereo images of each quadrangle. Other data products used to interpret geology include C1-MIDR, F-MIDR and FMAP photoproducts, full resolution CD-ROM data, and the GxDR CD-ROM for altimetric (topography), emissivity and reflectivity measurements, collectively known as ancillary data (described in Appendix I). Figures 3.2 and 3.3 show FMAP coverage for the two planitiae, Figure 3.4 shows C1-MIDR coverage.

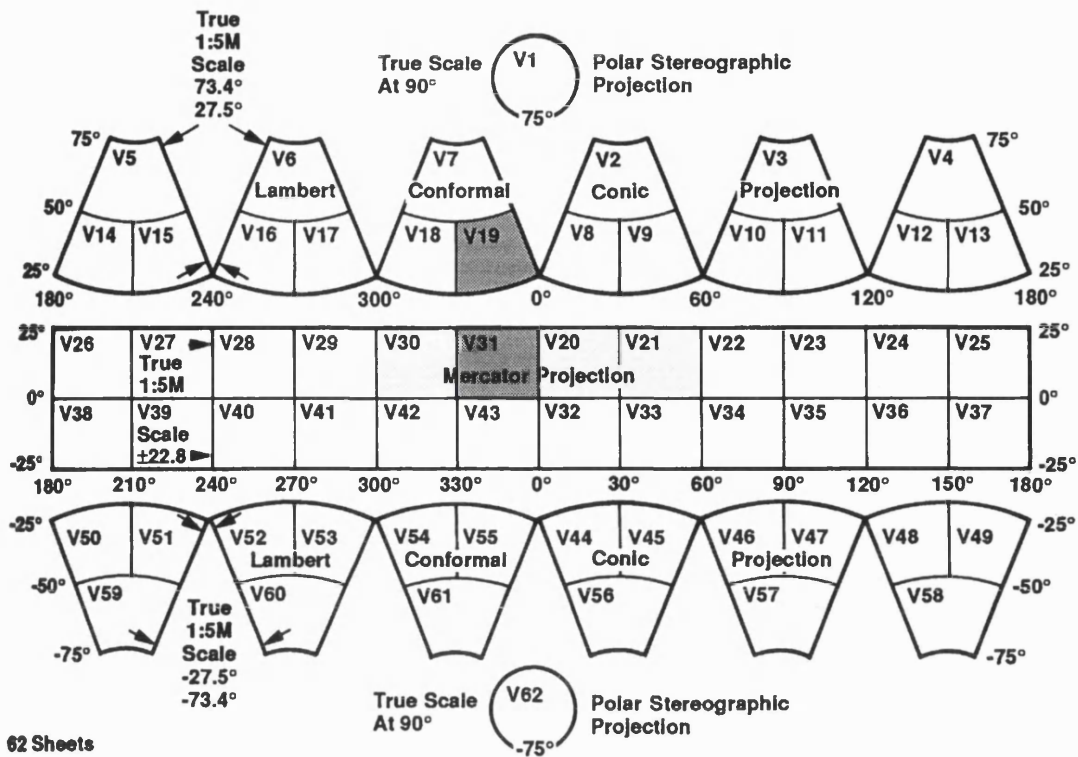


Figure 3.1 Location of 62 quadrangles devised for the Venus Mapping Project (VMAP). Each quadrangle is mapped at a scale of 1:5,000,000. Mercator, Lambert, Conformal Conic and Polar stereographic projections are used for this series. The mapping of shaded quadrangles are presented in the thesis. After Ford et al. (1989).

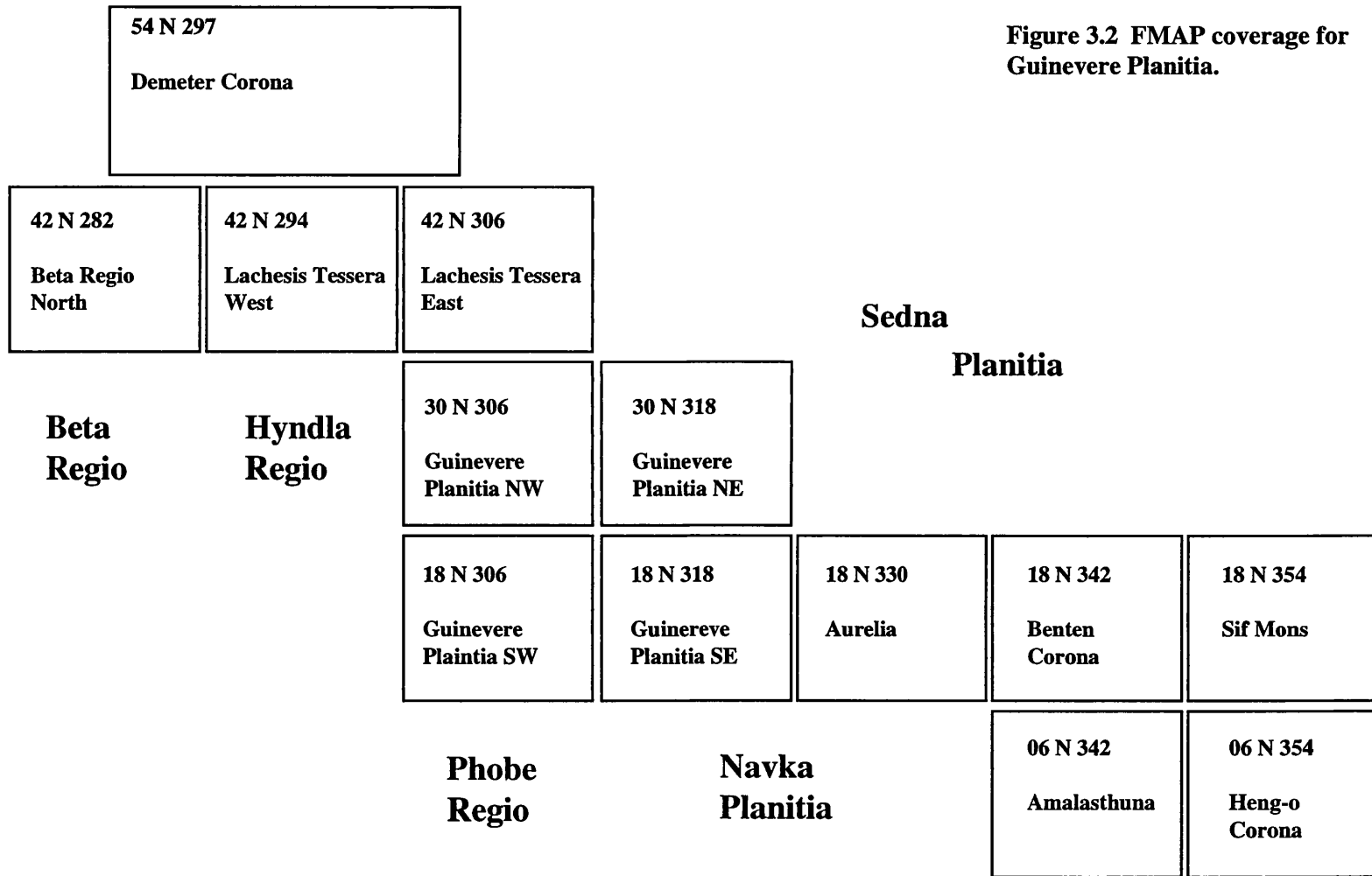


Figure 3.2 FMAP coverage for Guinevere Planitia.

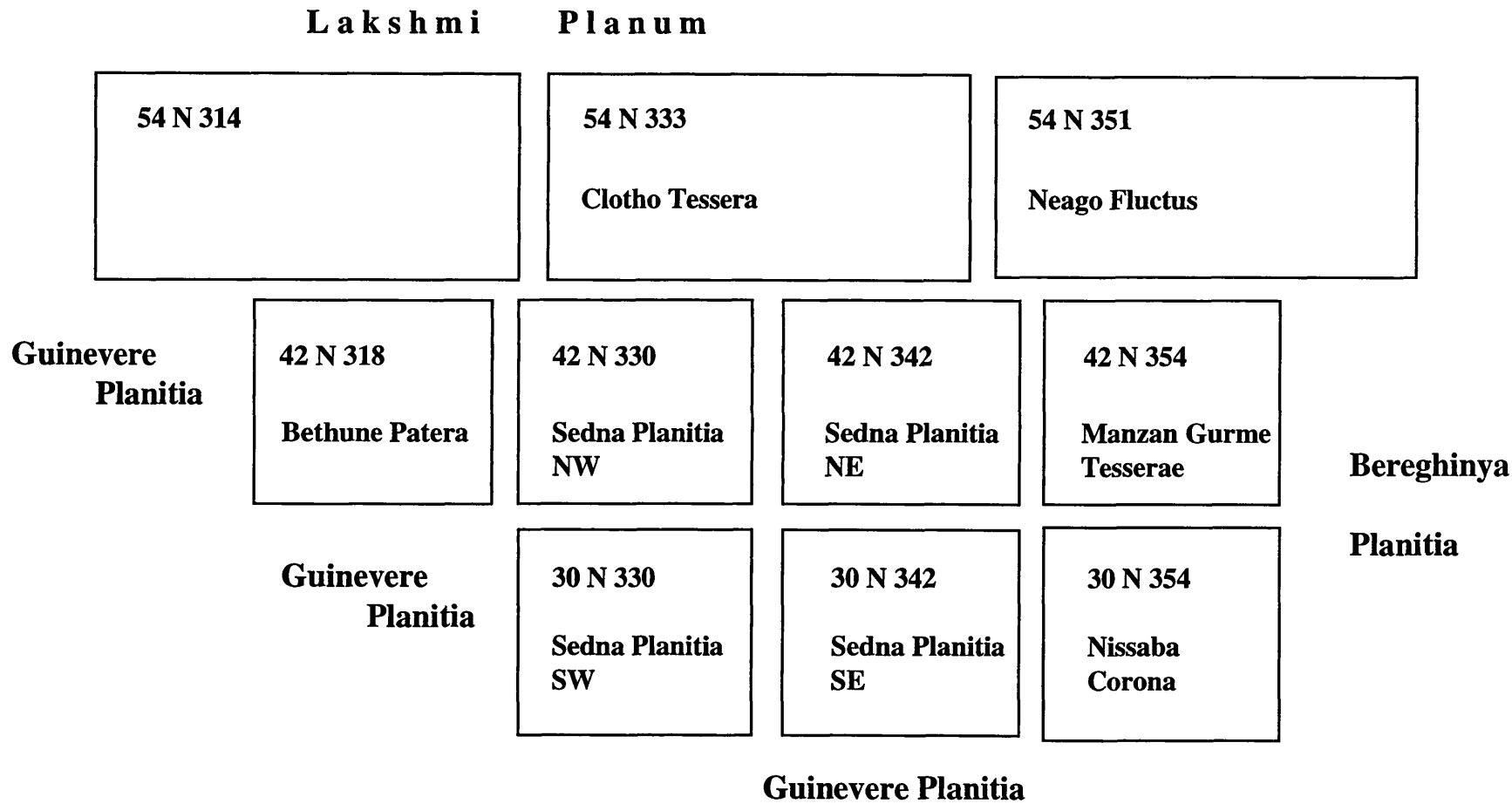


Figure 3.3 FMAP coverage for Sedna Planitia

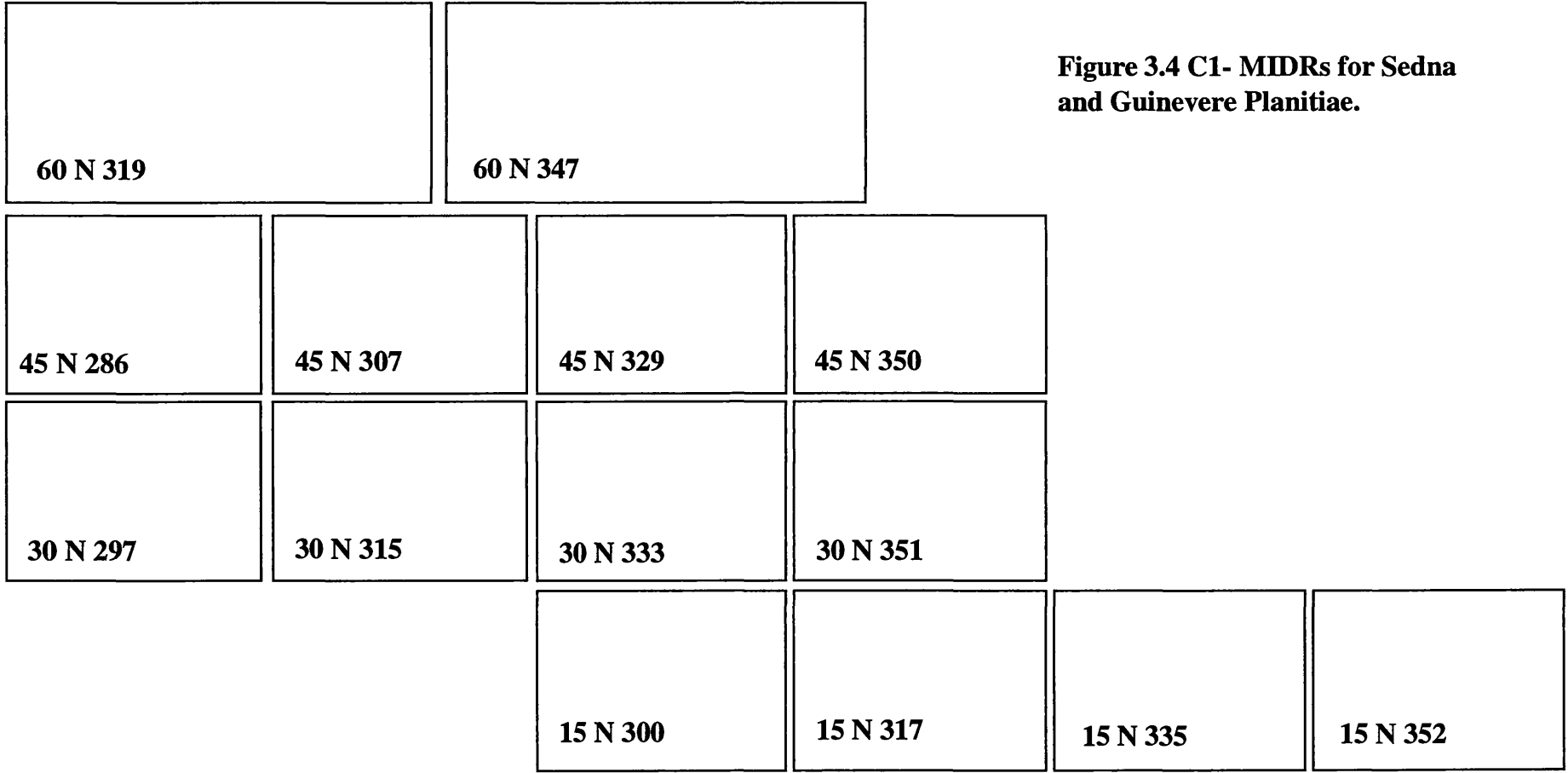


Figure 3.4 C1- MIDRs for Sedna and Guinevere Planitia.

3.3 Geological Mapping using SAR Radar

A geological map allows materials to be characterised and classified in order to obtain a two-dimensional representation of the three dimensional spatial relations and chronological sequences of materials and structures of a given area (*Wilhelms, 1990*). It provides a convenient way of spatially representing a considerable amount of information in a standard visual format, which can readily be interpreted.

With terrestrial geological mapping, rock units are delineated by their lithology, chemical composition and mineralogy. However, the composition of venusian rocks has only been analysed in a few very localised areas by Soviet landing craft (*Barsukov et al., 1982, 1986; Surkov et al., 1986a, 1986b, Chapter 1, 1.2.3*).

Magellan SAR images approximately reproduce the geomorphology of the venusian surface. By integrating and interpreting backscatter coefficients (referred to here as radar backscatter), emissivity, rms slope and topographic data sets, geological units defined by morphology, textural, structural and electrical characteristics can be identified and a geological map produced (*Campbell, 1994*). However, radar images have important differences from images recorded at visible wavelengths and a number of complications may arise with interpretation.

3.3.1 Radar Interpretation

The correct geological interpretation of radar images depends critically on a knowledge of how the radar energy interacts with the surface. The brightness variations seen in Magellan images are controlled primarily by three different surface variables: (1) topography, (2) surface roughness, and (3) electrical properties of the surface materials. These variables are influenced to some extent by variations in the radar incidence angle and the look direction (*Farr, 1993*). Figure 3.5 and Table 3.1 show how the

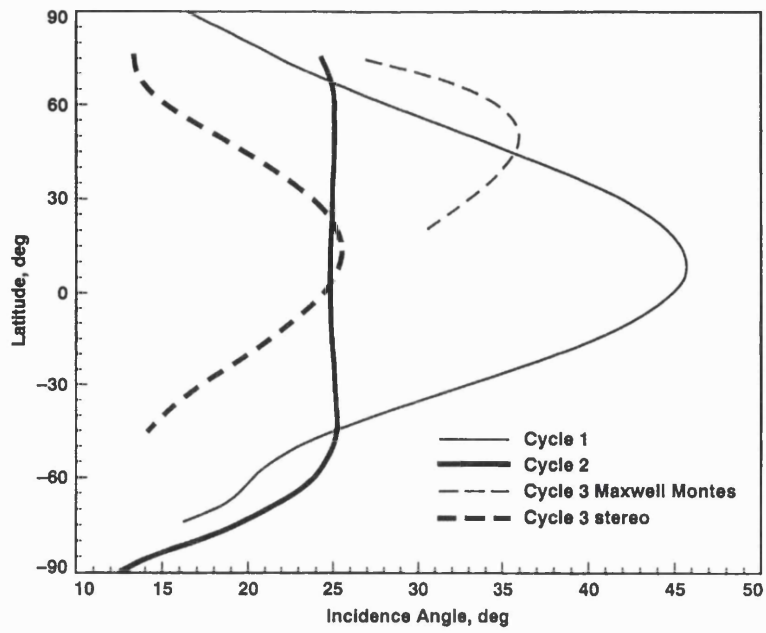


Figure 3.5 Magellan SAR incidence angle as a function of latitude for cycles 1, 2 and 3. Maxwell Mons data were collected during orbits 4031 to 4131. After *Plaut (1993)*.

Latitude, deg	Incidence angle, deg			
	Cycle 1	Cycle 2	Cycle 3, Maxwell Montes	Cycle 3, stereo
90	16.5			
85	18.5			
80	20.2			
75	22.0	24.4	27.1	13.4
70	23.9	24.9	30.8	13.5
65	26.0	25.1	33.4	14.1
60	28.3	25.1	35.1	15.2
55	30.8	25.1	35.9	16.6
50	33.3	25.1	36.1	18.2
45	35.8	25.1	35.8	19.8
40	38.1	25.1	35.1	21.4
35	40.3	25.0	34.2	22.7
30	42.1	25.0	33.1	23.9
25	43.6	25.0	31.9	24.8
20	44.8	24.9	30.6	25.3
15	45.5	24.9		25.6
10	45.7	24.9		25.5
5	45.6	24.9		25.2
0	44.9	24.9		24.5
-5	43.8	24.9		23.6
-10	42.3	24.9		22.6
-15	40.4	25.0		21.4
-20	38.1	25.1		20.1
-25	35.5	25.1		18.7
-30	32.8	25.2		17.4
-35	30.1	25.3		16.2
-40	27.5	25.3		15.2
-45	25.1	25.3		14.3
-50	23.1	25.1		
-55	21.6	24.7		
-60	20.5	24.1		
-65	19.7	23.1		
-70	18.5	21.6		
-75	16.3	19.7		
-80		17.4		
-85		14.8		
-90		12.7		

Table 3.1 Variation of incidence angle with latitude. Angles are representative for each cycle and are accurate to within 0.5°. After *Ford* (1993).

radar incidence angle varied with latitude. As the radar instrument has a side-looking illumination geometry, all radar images are distorted to some degree (*Farr, 1993, Figure 3.6*).

Topography

Topography may have a pronounced effect on radar backscatter. A slope oriented towards the incoming radiation will reflect significantly more energy than a flat surface or surface which slopes away from the incoming radiation. Strong radar returns received at the spacecraft from the surface of Venus are translated into pixels with high DN values, recorded as bright areas in radar images. Conversely, areas which return little radar energy have low DN pixel values and hence are darker in the radar images.

Within radar images, bright areas may be spatially compressed (foreshortened) while dark areas are expanded. Foreshortening (*Figure 3.7a*) results in a given terrain or feature appearing to have a steeper slope on its near range side, and an exaggerated shallow far range slope (*Pettengill et al., 1991*). With extreme slopes, radar layover may occur where the top of a slope is imaged before the bottom (*Figure 3.7b*). Another more common effect resulting from pronounced topography is radar shadowing, where the backslope of a mountain or graben is not illuminated by the radar and no data are acquired for this region (*Figure 3.7c*).

Surface roughness

Surface roughness at the scale of the radar wavelength dominates radar backscatter in Magellan images where the incidence angle is greater than 20° and less than 60° (*Farr, 1993, Figure 3.8*). Incidence angles for the V19 and V31 quadrangles lie between 32° and 46° , hence surface roughness is an important consideration when mapping surface materials. The detection of surface roughness is wavelength dependent, the longer the wavelength the coarser the surface material must be for dominant backscatter to occur. The wavelength of the Magellan SAR instrument was fixed at 12.6 cm, so surface roughness will control

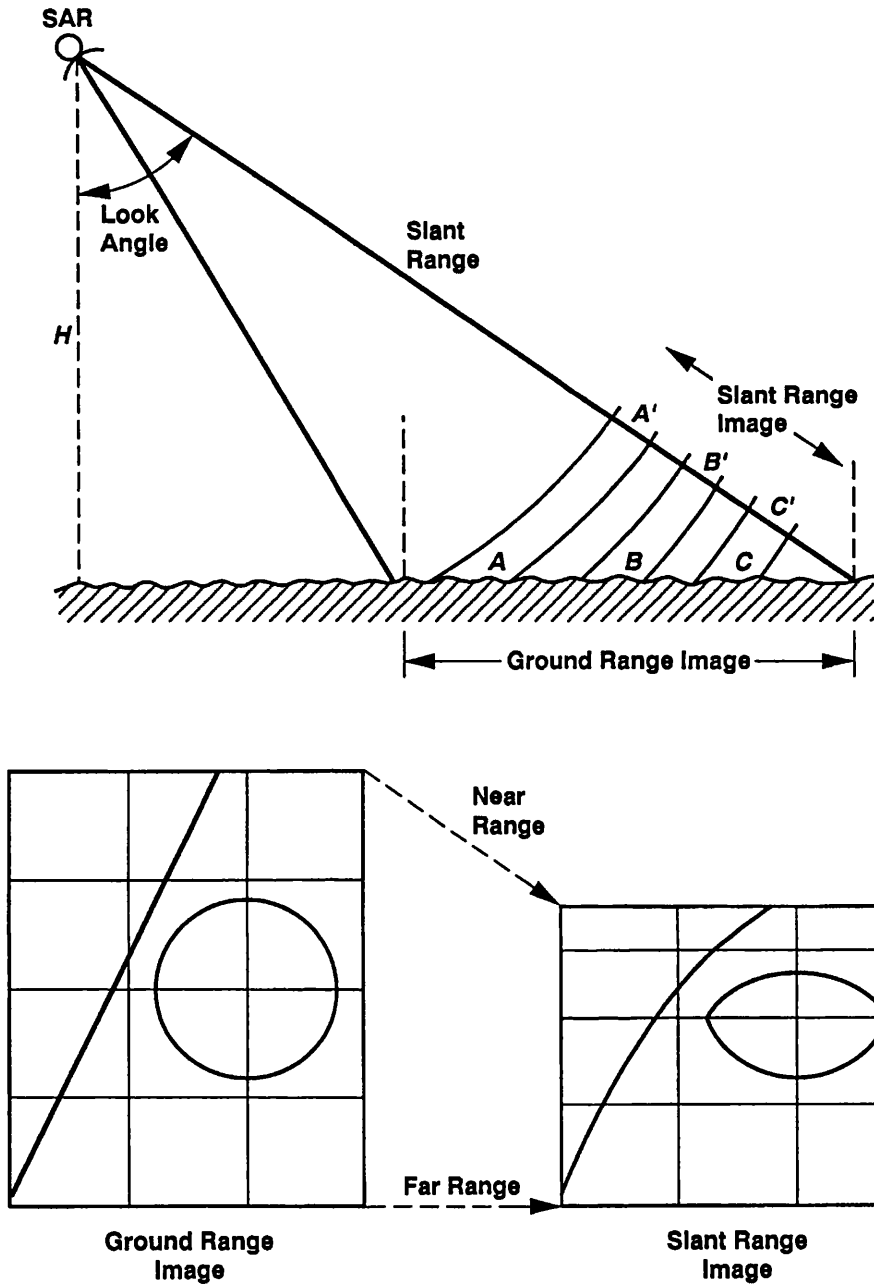


Figure 3.6 Slant-range and ground-angle geometries. By knowing the height of the spacecraft, H , and incidence angle a correction can be applied to slant-range geometry which causes compression of targets in the near range compared with those in the far range. After *Farr (1993)*.

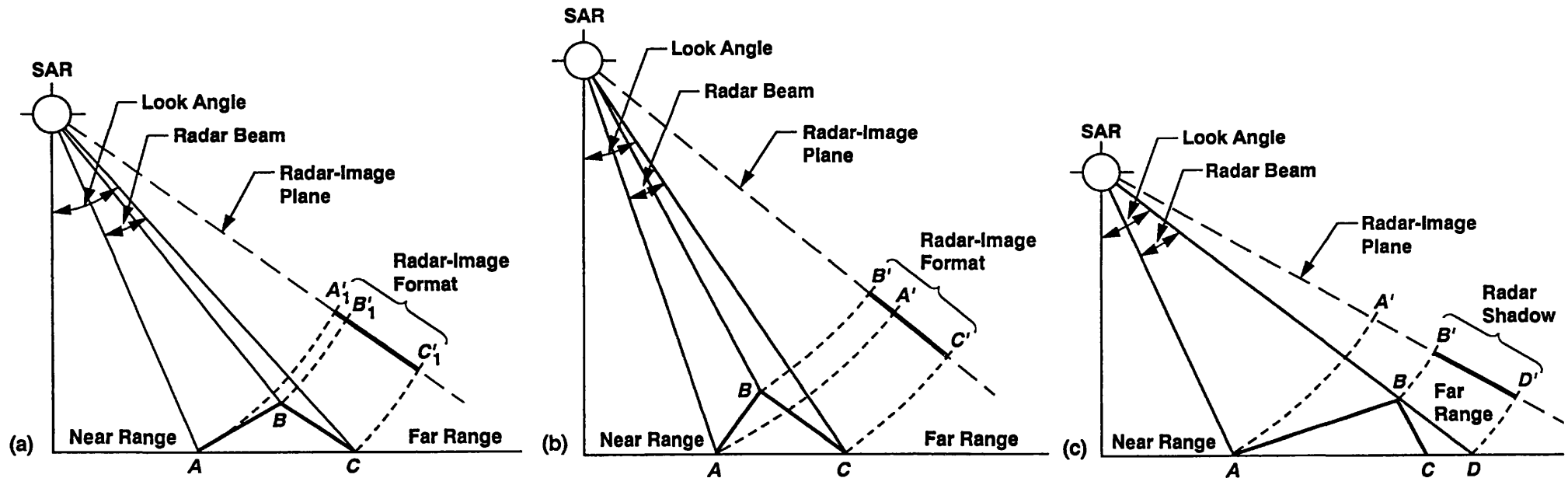


Figure 3.7 Illustration of geometry distortions in radar images: (a) radar image foreshortening, where the slope facing the radar is compressed to segment $A'-B'$ while the backslope is extended to segment $B'-C'$; (b) radar layover, an extreme case of foreshortening, where the top of the mountain, B' , is imaged *before* the bottom, A' ; (c) radar shadowing, where the backslope of the mountain, $B'-D'$, is not illuminated by the radar, and no data is acquired. After *Farr*, (1993).

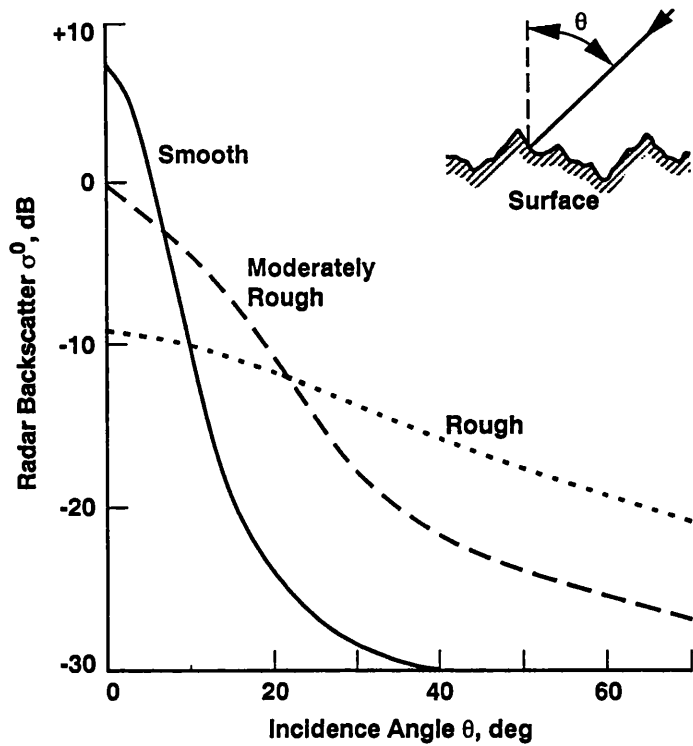


Figure 3.8 Radar backscatter as a function of incidence angle for representative surfaces. For angles less than approximately 25° , smoother surfaces have greater backscatter than rougher surfaces (Farr, 1993). Incidence angles for Venus quadrangle V31 and V19 range between 33.3° and 44.9° with cycle one data (see Table 3.1). After Farr (1993).

the degree of radar backscatter (Figure 3.9). In the unit descriptions below wavelength roughness refers to multiples of 12.6 cm (see Chapter 5 (5.2) for specific examples).

Dielectric properties

In addition to topography and surface roughness, variations in the dielectric constant of surface materials can affect the intrinsic reflectivity properties of surface materials, influencing image brightness. Materials of high dielectric coefficients are generally good reflectors and hence poor emitters. Two prominent examples of low emissivity readings and related high dielectric constants are (1) near the summits of the planet's highest mountains which are radar bright, corresponding to areas approximately above the 6053.5 km radius contour, and (2) parabolic debris associated with some of the venusian craters e.g. Neva crater (0.90° N, 338.70° E, V31) (*Campbell et al.*, 1992; *Plaut*, 1993). An explanation for the enhanced dielectric constants near mountain summits is the concentration of iron sulphide such as pyrite and pyrrhotite (*Pettengill et al.*, 1988; *Klose et al.*, 1992).

Spatial comparison of SAR data

Quantitative comparisons between map units can only be achieved once the backscatter coefficient, σ_0 (sigma-0) is in its original linear format. The backscatter coefficients on Magellan CD data are scaled in a logarithmic form (value in dB) in order to compress the very wide dynamic range of the SAR data. Any averaging of pixels within Magellan images must be calculated with backscatter coefficient values in the original linear format (see Appendix I). Significant errors may occur if DN values are averaged prior to linear rescaling (*Campbell*, 1995). A Macintosh program which calculates σ_0 from the DN value and averages the measurements within the sample area has been created by *Campbell* (1995). All numeric radar data in this thesis have been reduced to obtain the true radar backscatter coefficients. Further constraints of radar data when used for geological mapping are discussed in Chapter 5 (5.2).

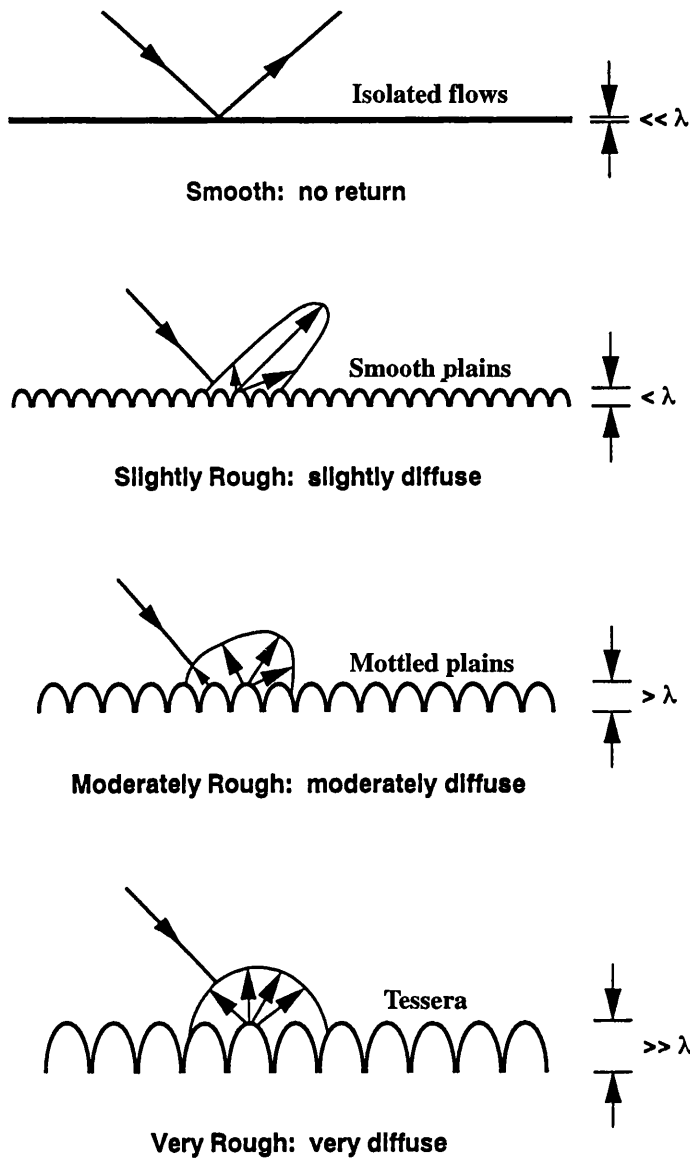


Figure 3.9 Surface roughness effects on radar backscatter. Surfaces whose roughness is much less than the radar wavelength scatter in the specular direction. Rougher surfaces scatter more energy in all directions, including back to Magellan's high gain antenna, and hence appear brighter in radar images. Typical units identified in this study which have different backscatter properties are noted. After *Farr* (1993).

3.4 Unit Description and Interpretation

The units observed within the mapping quadrangles are described below. Figures 3.10 and 3.11 show locations of named features referred to in the text. Some observations are drawn from outside the quadrangles to illustrate description and stratigraphic relations. USGS format unit descriptions are found in Appendix II and III. SAR backscatter and ancillary radar data of type localities for units within each quadrangle are found in Appendix IV and V. Figures 3.12 and 3.13 show the radar backscatter plotted against incidence angle for type localities of each unit described in V31 and V19 respectively.

3.4.1 Tesserae - *t*, and Deformed Plains - *pd*

A strong radar backscatter, multiple intersecting ridge and groove structures which intersect at high angles, and upstanding topography are symptomatic of tessera materials. V31 contains relatively little tessera material. However, V19 contains Manzan-Gurme Tessera which represents three discrete blocks of tessera materials. These blocks display materials which are deformed by ridges and graben of variable spacing, typically less than 20 km. Weaker radar materials may be seen between some structures. The tesserae here are embayed by younger mottled and lineated, and regional plains materials which are described below (e.g. at 41°N, 357°E, Figure 3.14).

Deformed plains materials also have a strong radar return and, as the name implies, are typically deformed by both extensional and compressional structures. Materials which cannot confidently be identified as tesserae have been given the name deformed plains. Within the mapping areas, deformed plains are embayed by plains materials.

- ★ - Named craters
- - Coronae
- ◻ - Volcanoes

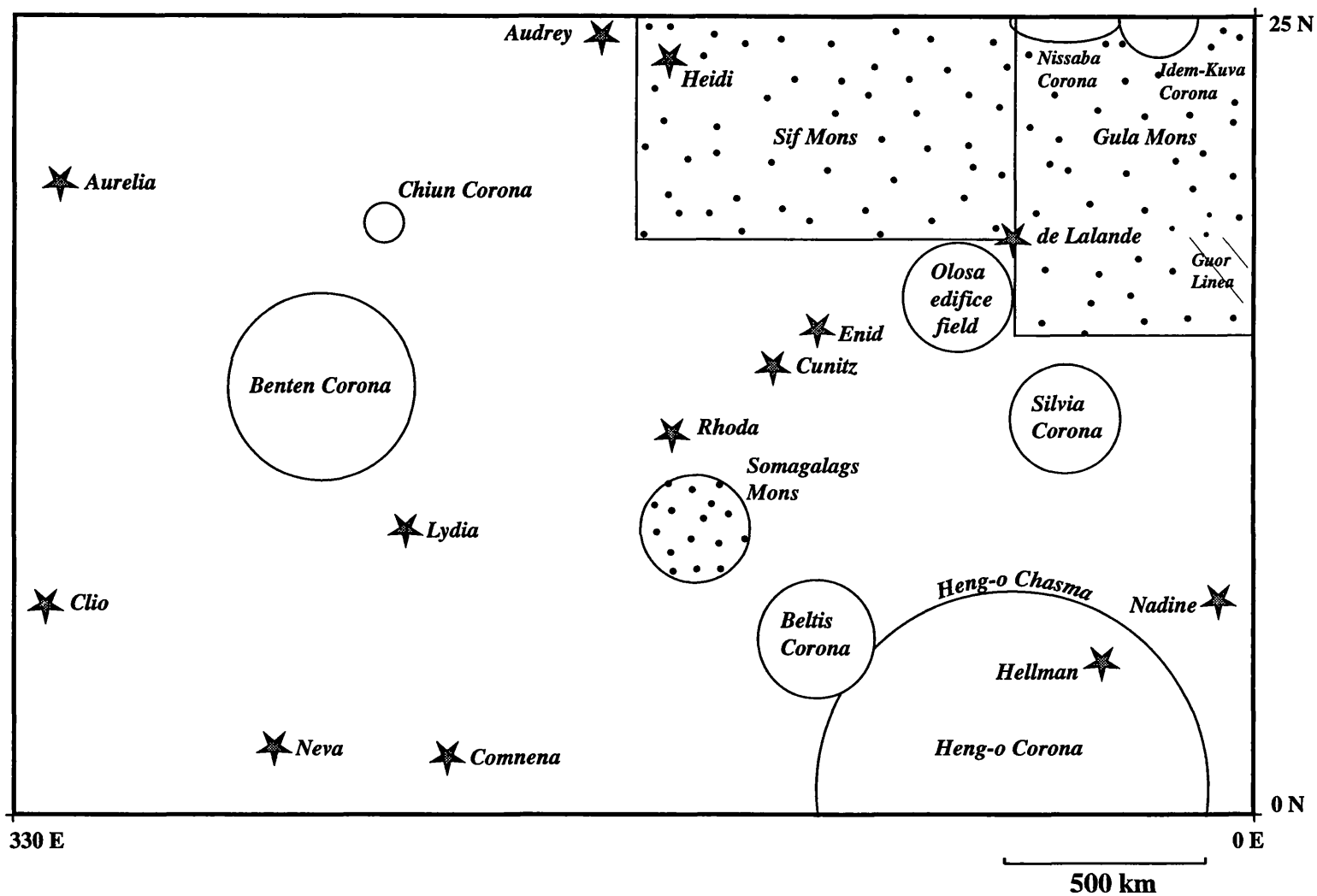


Figure 3.10 Location map for features in V31: Sif Mons Quadrangle.

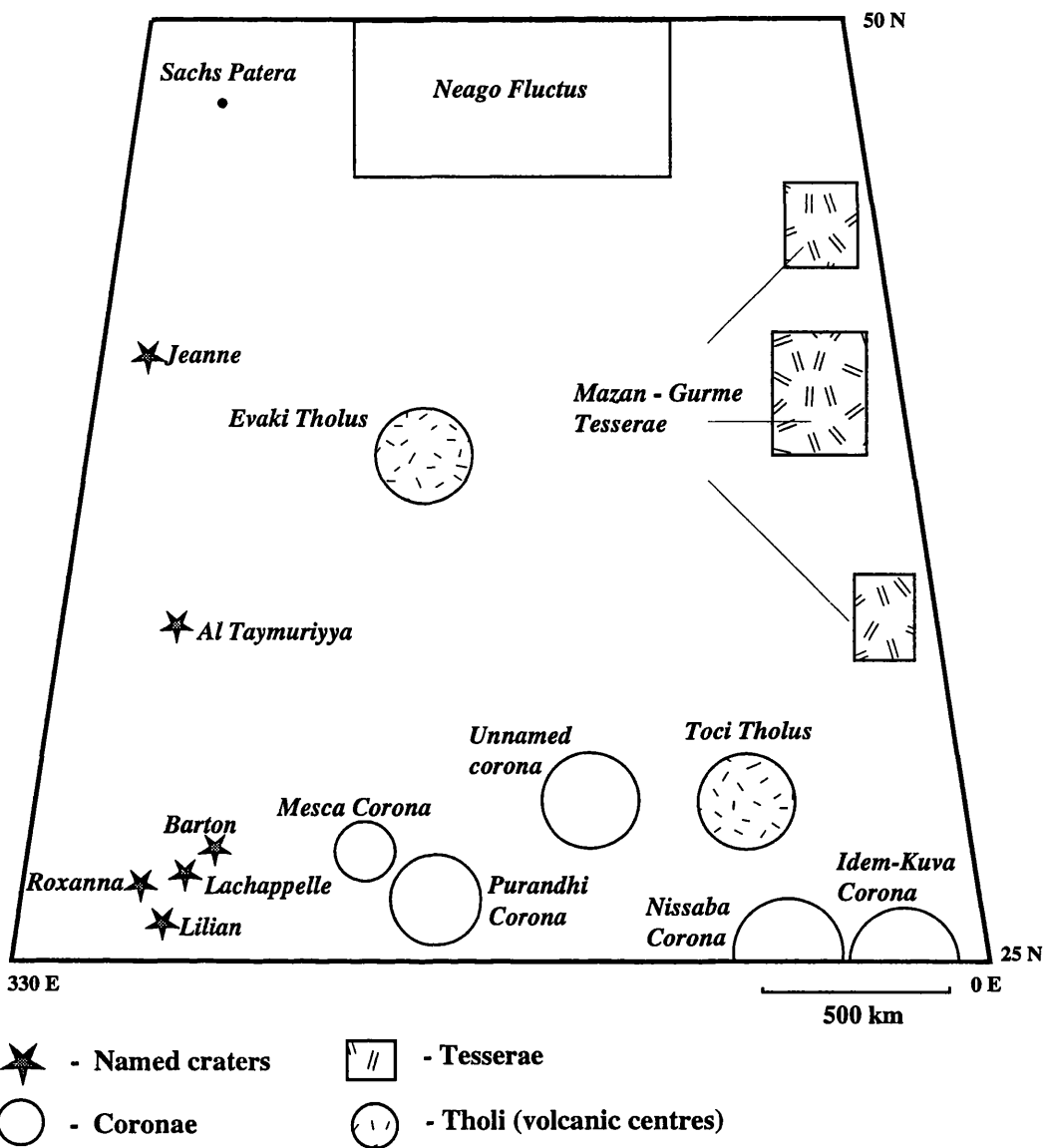


Figure 3.11 Location map for features in V19: Sedna Planitia.

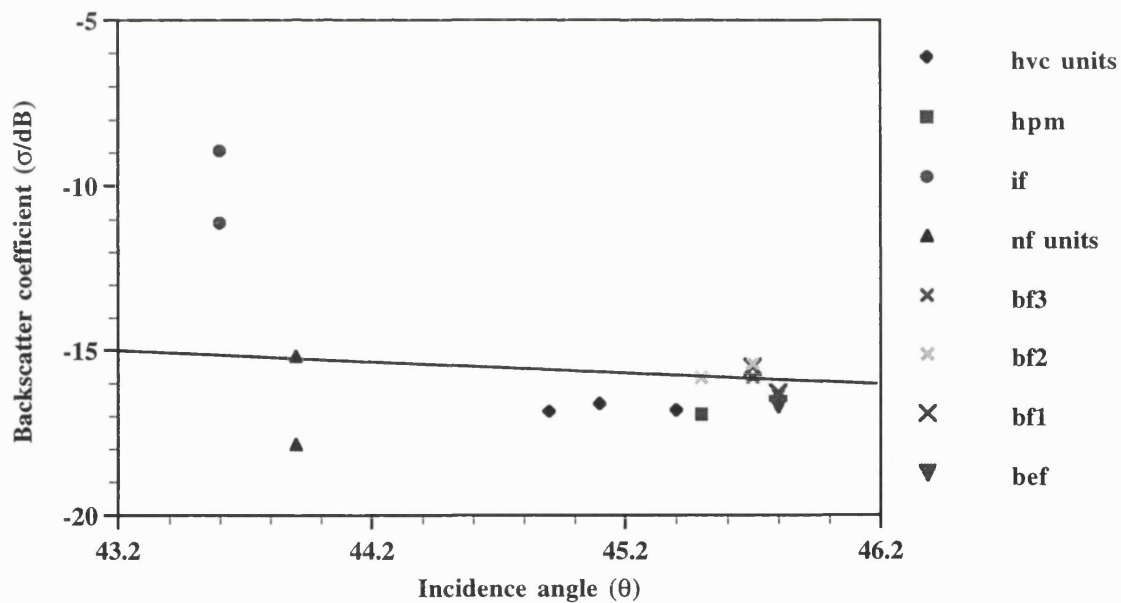
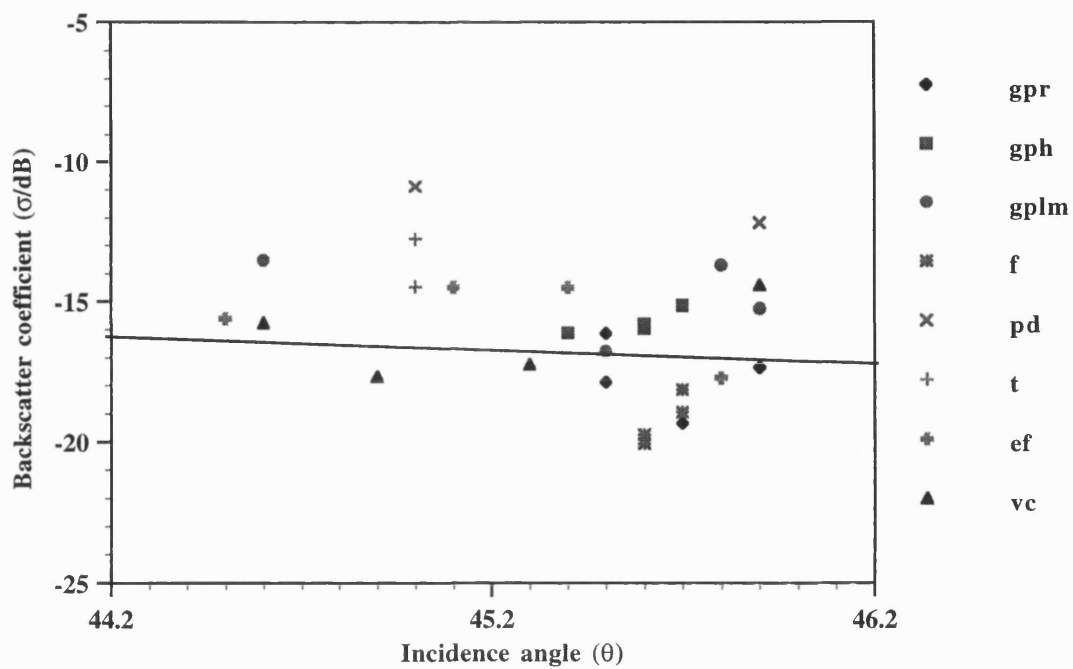


Figure 3.12 Radar backscatter of V31 units plotted against incidence angle. Solid line represents Venusian mean backscatter.

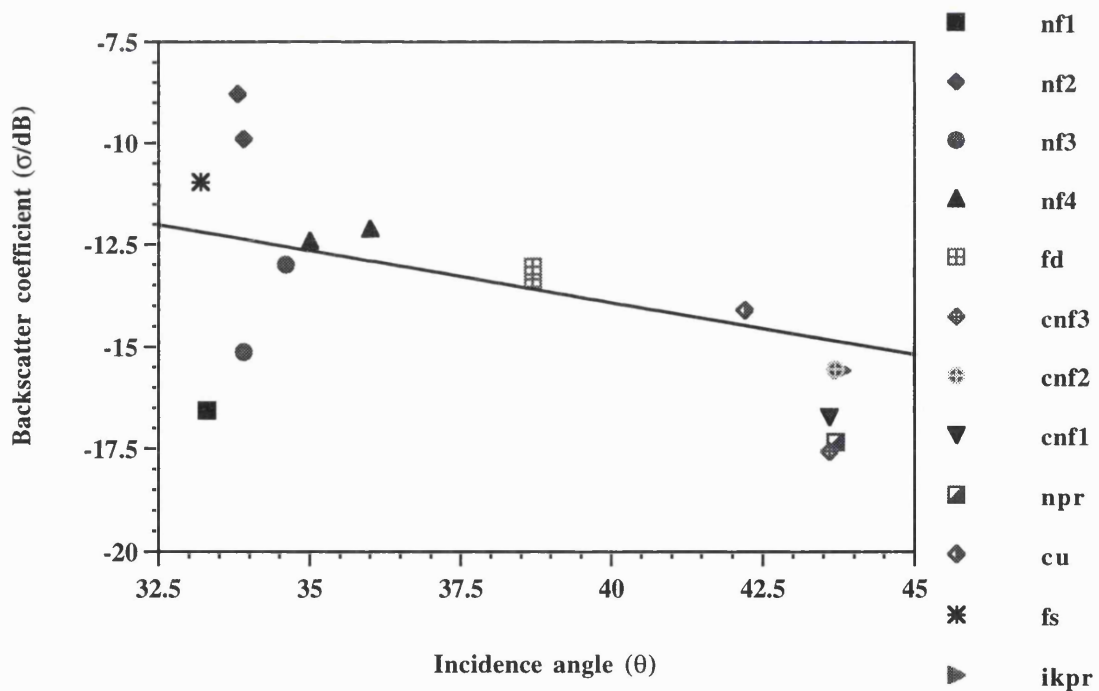
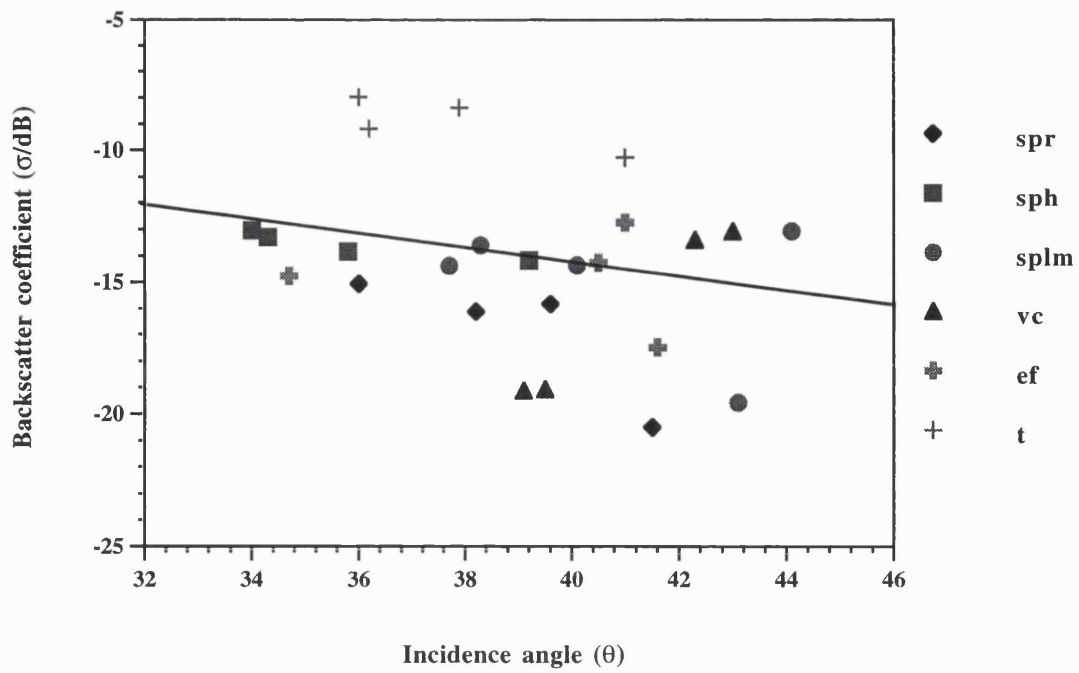


Figure 3.13 Radar backscatter for units in V19 plotted against incidence angle. Solid line represents Venusian mean backscatter.

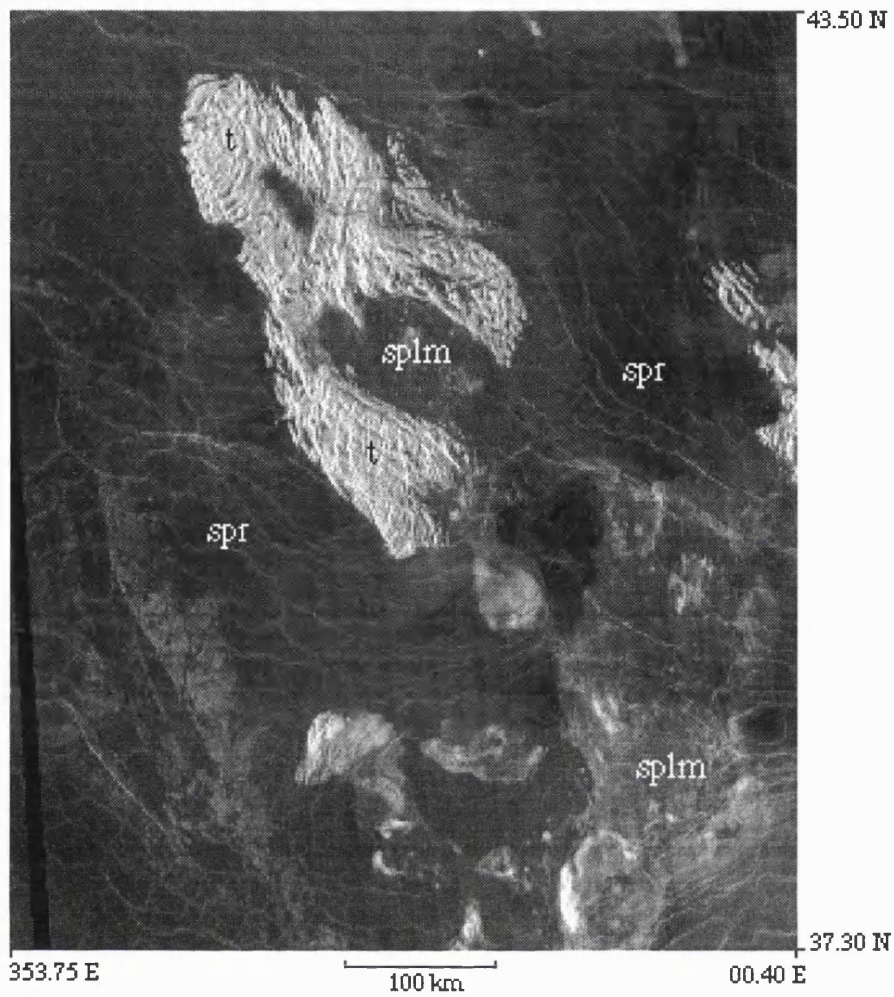


Figure 3.14 Southern portion of Manzan-Gurme Tessera (*t*). Tessera is characterised by a strong radar backscatter and upstanding topography in relation to the surrounding plains. Here, both the Sedna regional plains and lined and mottled plains materials embay Manzan-Gurme. The *splm* materials are embayed by *spr* (C1-MIDR.45N350;1 browse).

Interpretation

Tesserae materials are considered to represent the remnants of a highly deformed crust (*Bindschadler and Head, 1991; Bindschadler et al., 1992a, 1992b; Ivanov and Head 1995*). The deformation is considered both compressional and extensional. *Phillips et al. (1991b)* and *Herrick and Phillips (1990)* propose that tessera initially formed above hotspots or plumes. These large areas of mantle upwelling enhanced volcanism and crustal thickening. Gravitational collapse and subsequent spreading owing to thermal decay resulted in the volcanism and thickened crust becoming highly deformed. A second model proposed by *Bindschadler et al. (1992b)* suggests tesserae are the result of crustal deformation over areas of long-term downwelling, with the characteristic fabric resulting from the coupling of the downwelling mantle with the crust. From recent global surveys of tesserae, *Ivanov and Head (1996)* suggest the downwelling model may be more applicable since the high topography and tectonic structures characteristic of tesserae are consistent with marginal underthrusting and accretion. Deformed plains materials may well have undergone similar deformational processes as tessera materials, but owing to the small outcrop size, the relation between styles of deformation within the unit are difficult to establish.

3.4.2 The Lineated and Mottled Plains - *gplm* and *splm*

The Guinevere and Sedna lineated and mottled plains materials (marked *gplm* and *splm* on the V31 and V19 maps respectively) are characterised by a moderate radar backscatter which varies considerably on a local-scale, typically 10s to 100s of km. The variation in backscatter results in a characteristic mottled appearance in Magellan SAR images (Figure 3.15).

Both *gplm* and *splm* have a large scale undulating topography and are typically higher than mpr. The materials have experienced a greater amount of deformation in comparison to

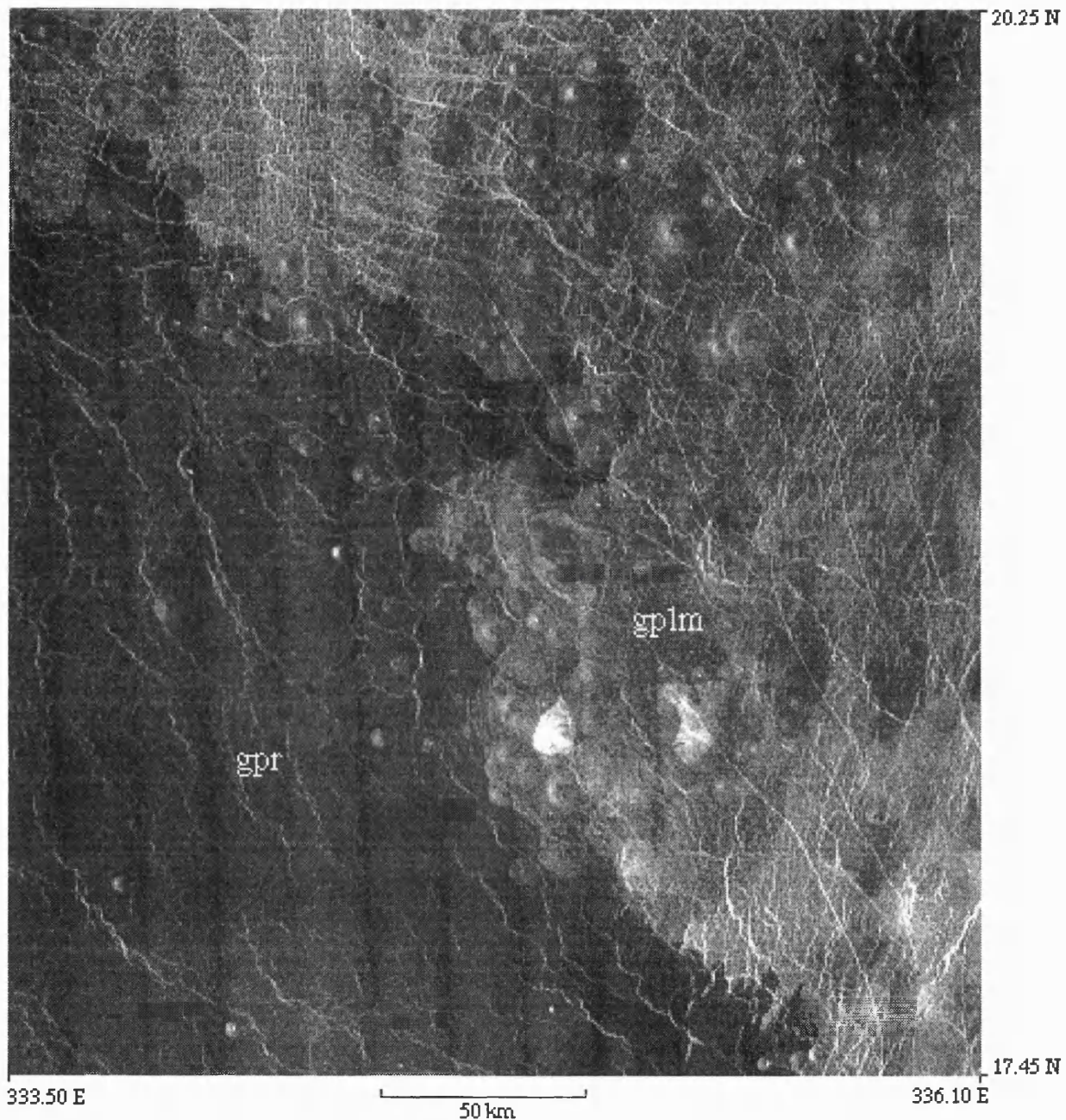


Figure 3.15 Full resolution image showing the contact between the Guinevere regional plains (*gpr*) and the Guinevere lineated and mottled plains materials (*gplm*). Note how *gpr* embays *gplm* materials, which are seen to be upstanding in topographic data. Isolated edifices associated with *gplm* have become inliers. The *gplm* materials have undergone greater deformation than *gpr*, and they are considered older (F-MIDR.20N334;1 browse).

other plains units. Structures include widespread wrinkle ridges coherent for hundreds of kilometres, for instance those which deform *gplm* materials in the NW sector of V31. At least two sets of wrinkle ridges are observed here, one of which is confined to *gplm* materials and does not extend into younger regional plains (Figure 3.15). Another example of wrinkle ridges confined to the lineated and mottled plains is around 27.0°N, 351.5° E, in V19. Here a set of wrinkle ridges are embayed by younger plains materials (Figure 3.16). Other structures include fractures trending NW-SE in the NW sector of V31. The fractures are roughly parallel to each other and are approximately equidistant, typically at a spacing of 250 km and 800 km in length. Denser swarms of parallel fractures are observed within the *splm* materials (30° N, 340.5° E) and extend for more than 500 km.

Zorile Dorsa (40.0° N, 357.0° E) a prominent ridge belt is contained within and deforms a NW extension of the Sedna lineated and mottled plains materials (Figure 3.17). The compressional structures associated with Zorile Dorsa do not deform the more extensive Sedna regional plains materials (*spr*, described below). Along the eastern and northern margin of Zorile Dorsa, regional plains materials embay lineated and mottled plains materials.

Ridges (typically 45 km in length and a few hundreds of meters high), with a moderate to strong backscatter occur within *gplm* materials in V31 (e.g. at 19.74° N, 340.15° E, Figure 3.18). The ridges are narrow (typically <10 km), trend SW-NE, and are frequently surrounded by diffuse radar-bright aprons. The minor ridges represent a relatively local style of deformation in comparison to that which formed the regionally extensive wrinkle ridges and NW-SE trending lineations.

Small-scale local fabrics include reticulate and polygonal fracture patterns (e.g. 21° N, 334° E, V31, Figure 3.19). Here, the fabric can be resolved into three individual fracture sets: a prominent NW-SE trending set typically spaced 1.2 km apart, a prominent set trending almost NS typically with a 1.6 km spacing, and a third irregular fracture set. Each fracture set varies in

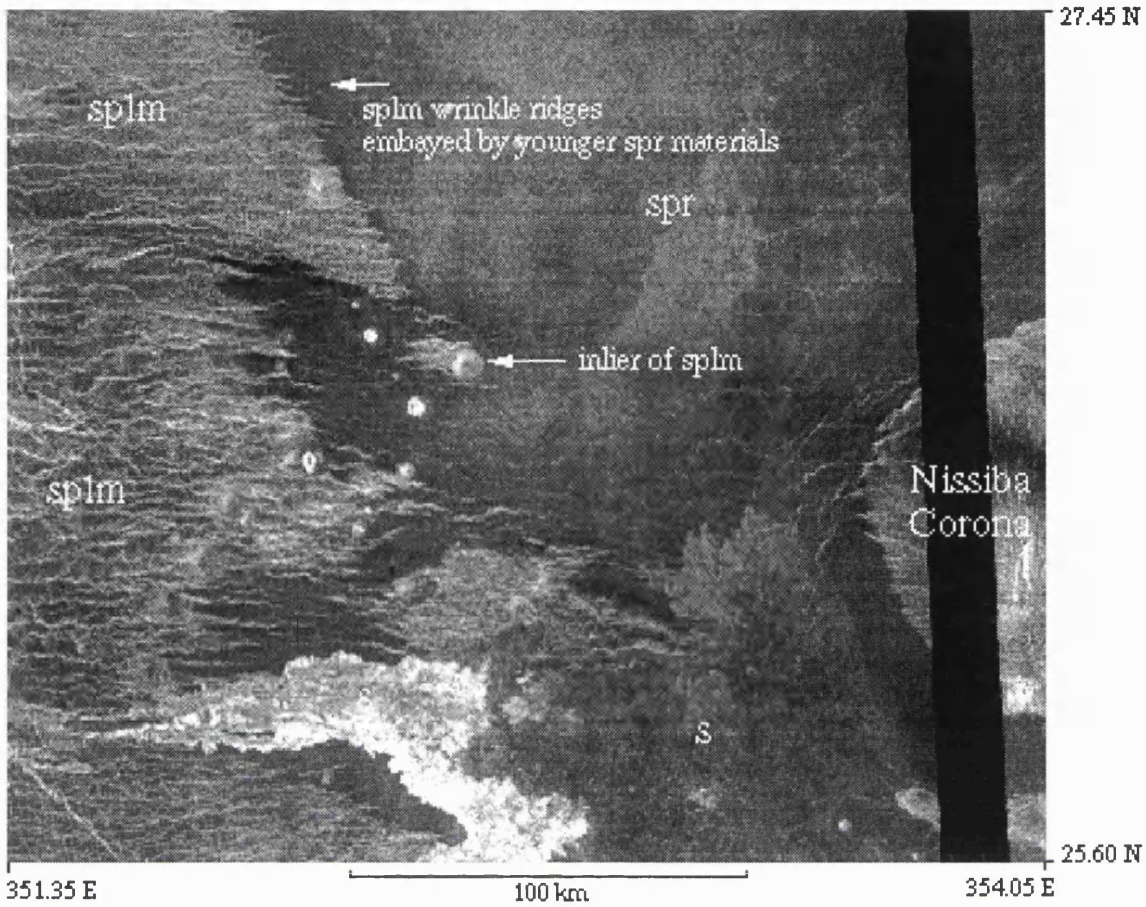


Figure 3.16 Stratigraphic relation between Sedna plains materials (*spr* and *sprm*) and Sif Mons flows (*s*). Sedna regional plains materials (*spr*) embays the wrinkle ridge fabric within the Sedna lineated and mottled plains (*sprm*). A small inlier of *sprm* is also seen. Flow materials from Sif Mons are superposed over both *spr* and *sprm* (F1-MIDR.25N357;1 browse).

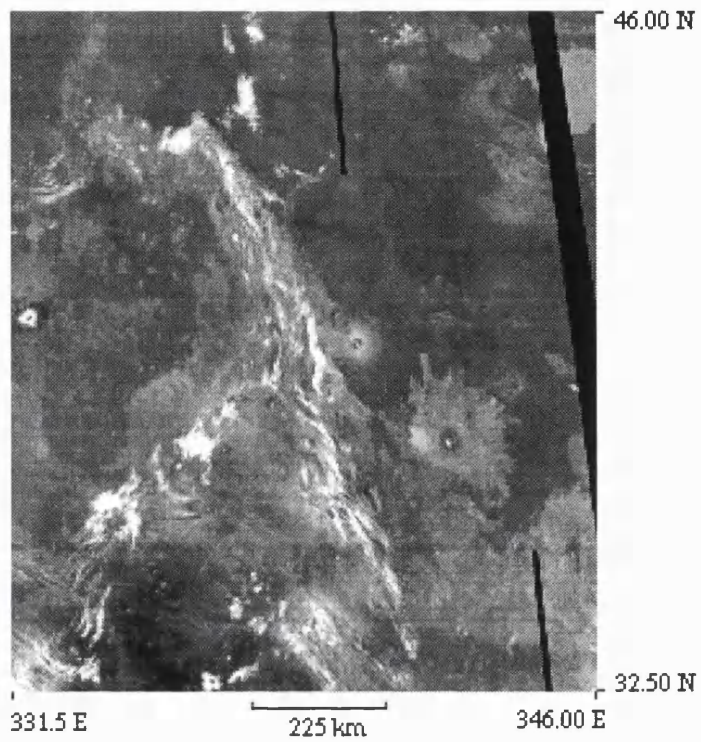


Figure 3.17 Zorile Dorsa, contained within Sedna lineated and mottled plains. This ridge belt is considered older than the surrounding Sedna regional plains. The compressional structures cut the lineated and mottled plains materials but not regional plains materials. Compare this ridge belt with the one in Figure 3. 23 (C2MIDR.30N335;2 browse).

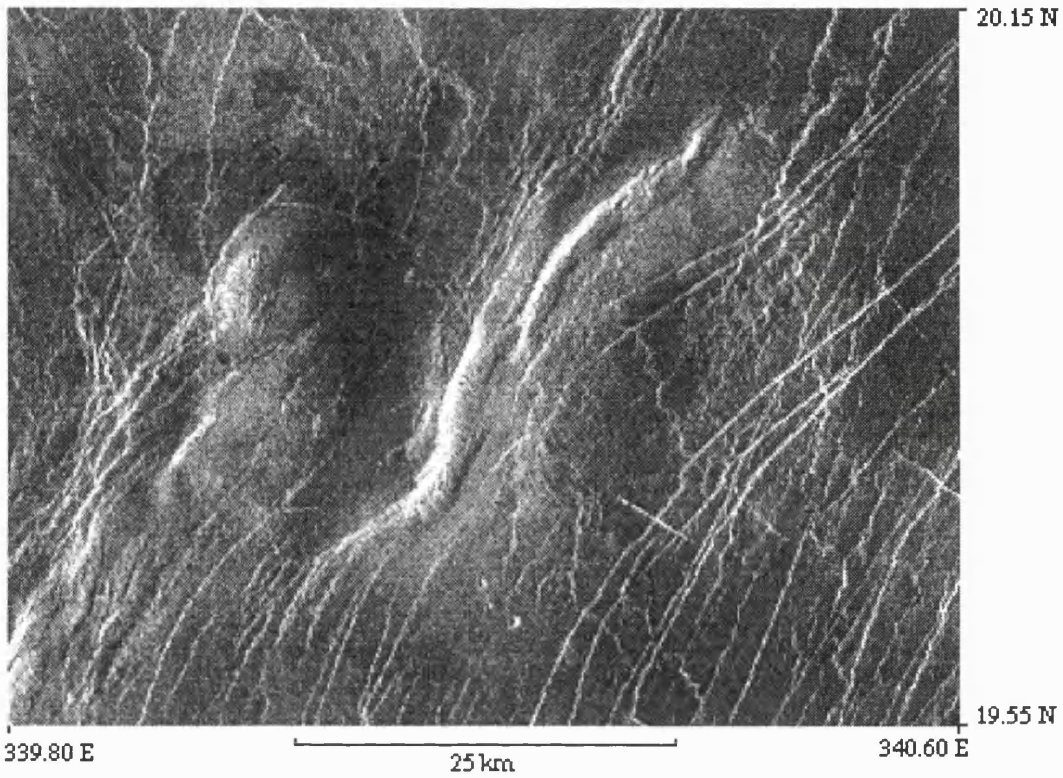


Figure 3.18 Minor ridge belt within the Guinevere and lineated mottled plains. The western face of the compressional ridge has a strong radar return. The ridge belt is surrounded by radar-bright diffuse materials which may be the result of ridge modification or preferential aeolian deposition (C1-MIDR.15N335;1 framelet 15).

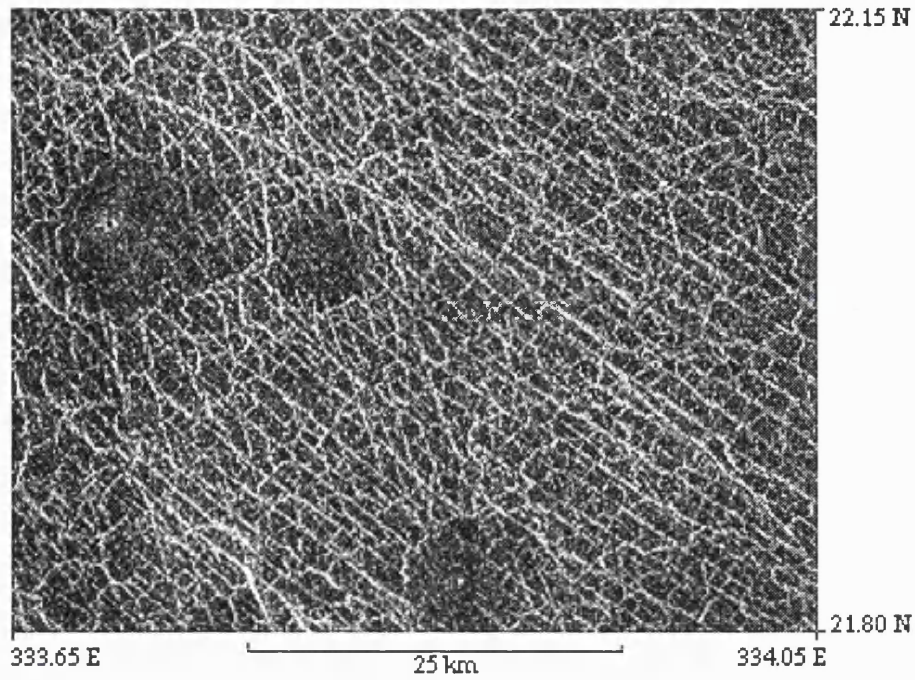


Figure 3.19 Full resolution image showing structures associated with areas of the mottled and lineated plains. At least three structural components are visible, intersecting to form a polygonal deformation pattern. A number of small shields occur which appear partly altered by the deformation. The structures are often enhanced by superficial crater materials (F-MIDR.20N334;1 framelet 05).

spatial density.

Common within the lineated and mottled plains are small volcanic edifices. Edifice diameter ranges between 1.5 and 15 km, and more typically between 2 and 5 km. The most common edifice morphology are shields, however cones and small domes are observed, identified by a steeper slope angle and stronger radar backscatter (*Guest et al.*, 1992). A variable radar backscatter is associated with the small edifices. Pits are observed within the bulk of small edifices. Typically, a pit is a single circular or elongate depression with the largest dimension no greater than 2 km.

The margins of the small edifices within lineated and mottled plains materials vary considerably. Many are surrounded by deposits which have a variable radar backscatter and partially obscure pre-existing structural fabrics, for example at 20° N 335° E (V31). Here, roughly circular aprons of thin mantling materials surround a number of isolated edifices and subdue a fine scale polygonal fracture fabric. Six edifices (each < 5 km in diameter) located at 34.76° N, 335.00° E show mantle deposits with a preferential SW direction, extending a maximum of 7 km (Figure 3.20). The mantle deposits have gradational boundaries whose radar backscatter becomes weaker to the SW, indicative of thinning. Other edifices have small flows associated with them. The flows have sharper boundaries than the mantle deposits.

Lineated and mottled plains materials are not unique to the V31 and V19 quadrangles. Other investigators describe analogous units which are areally extensive and display similar radar backscatter properties and styles of structure (e.g. *Head et al.*, 1994; *Crown et al.*, 1994; *Tapper and Guest*, 1997). *Aubele* (1994, 1995) describes a similar plains unit identified in Vellamo Planitia, the 'Small Volcanic Plains' unit (*Aubele*, 1994) later named the 'Hilly Mottled Plains Materials' (*Aubele*, 1995). This unit has a mottled appearance in radar imagery, contains a relatively high percentage of small edifices, and has undergone substantially greater deformation over a more extensive area than younger plains materials. Observations from FMAPs showed a

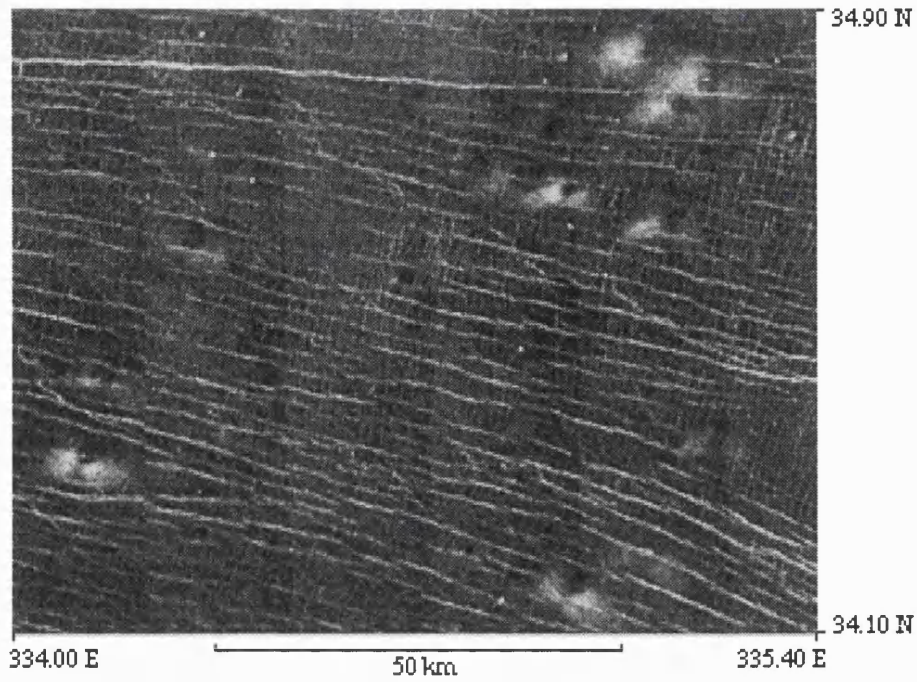


Figure 3.20 Small volcanic edifices and associated mantle deposits contained within the Guinevere lineated and mottled plains. A number of the edifices show bi-directional mantle materials, for instance the edifice located in the SW corner of the image. The mantle deposits may represent edifice modification, such as debris flows, or alternatively coarse pyroclastic materials (C1-MIDR.30333;1 framelet 13).

consistent stratigraphic relation between mottled and lineated, and regional plains: the former are embayed by the latter.

Interpretation

The lineated and mottled plains are considered here to represent an amalgamation of volcanic materials. Although the unit is characterised by a relatively large population of small shields, compared with other plains units, it is unlikely that this style of volcanism is responsible for the total areal extent of the unit. The unit is considered to have other sources which cannot be identified. The unit is considered relatively old as it is deformed by a sequence of structures, the density of which is not observed in younger units. Supporting this interpretation is the consistent relation with the regional plains units (described below) which superimpose on lineated and mottled plains materials.

A suggested scenario for the evolution of the unit is one where plains materials were emplaced either on a regional or local scale, and amalgamated to cover a greater area. Subsequent periods of deformation and continued local volcanic activity modified the surface of the original plains. The modification is considered to be a gradual accumulative process resulting in the mottled radar appearance and structural sequences seen in the radar images. There is no evidence to suggest this unit was emplaced rapidly. The edifices located at 40.0° N, 334.0° E support this theory. Here, numerous patches of radar bright materials associated with small edifices (identified in full resolution data) superimpose the regional plains materials (Figure 3.21). The result is a mottled appearance in the radar images. It is conceivable that further extrusion of volcanic materials and episodes of deformation at this location could produce an area with a similar appearance to areas of mottled and lineated plains materials. However, the period of time over which modification occurs cannot be constrained: different areas of lineated and mottled plains probably formed over different time periods depending on geological activity.

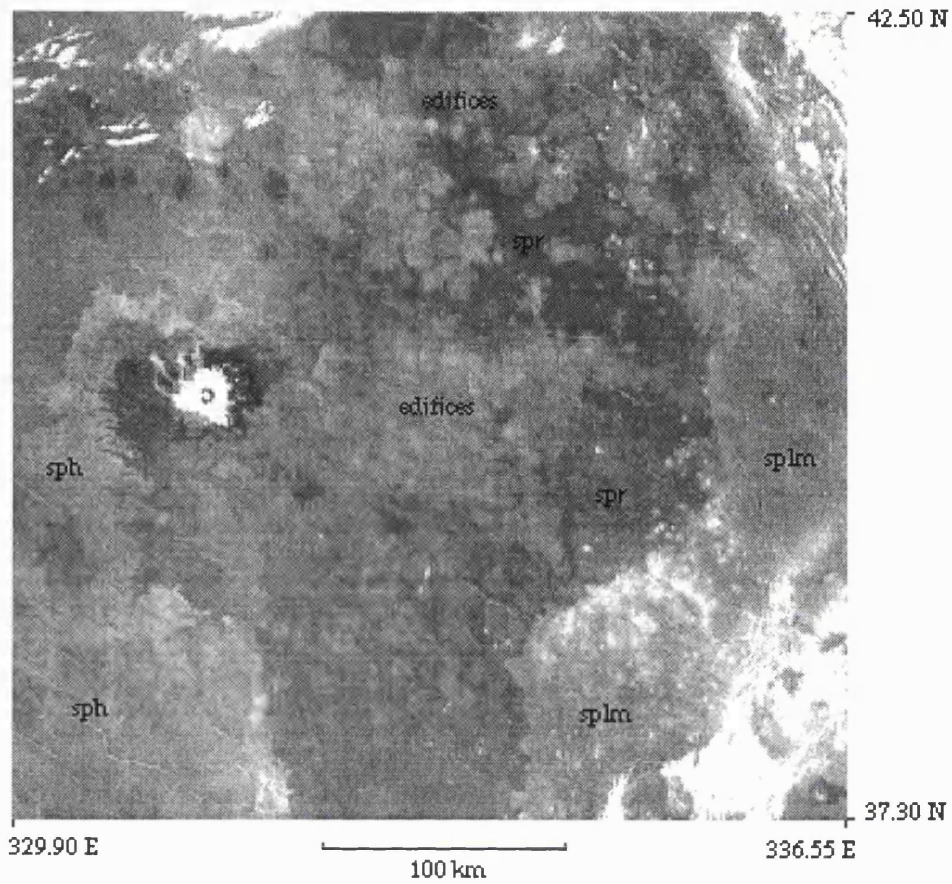


Figure 3.21 Area within V19 where patch shield volcanism is seen to modify Sedna regional plains materials. The patch edifice fields postdate plains emplacement. It is considered the formation of lineated and mottled plains materials may result from the gradual accumulation of volcanic deposits which undergo phases of deformation; both are indicative of repetitive styles of geological activity (C1MIDR.45N329;2 browse).

The impact crater population within the lineated and mottled plains in the mapping area is considered to small to be of any use statistically in constraining an age for the proposed gradual formation. It is noted, however, that the craters which do occur appear unmodified by deformation and flow materials.

3.4.3 The Regional Plains - *gpr* and *spr*

The regional plains units, Guinevere regional plains materials (*gpr*) and Sedna regional plains materials (*spr*), are the most extensive materials found in Guinevere and Sedna Planitiae. The materials constitute approximately 30% and 40% of the V19 and V31 quadrangles respectively. In contrast to the lineated and mottled plains materials, the regional plains materials have a characteristic weak radar backscatter (Appendix IV and V). Local superficial deposits (interpreted as fallout materials) associated with large craters (> 30 km) can change the radar backscatter of the regional plains. For instance, fallout materials associated with Cunitz crater result locally in a stronger radar backscatter (a radar-bright halo in SAR images), while fallout materials associated with Aurelia (in V31) have a weak radar backscatter.

Various scales of deformation are associated with the regional plains. Rms slope readings show the surface materials to be relatively smooth on the scale of tens to hundreds of meters (Appendix IV and V). However, altimetric data show the topography undulates over tens to hundreds of kilometres. Most regional plains within the quadrangles occur below mpr, except where elevated by continued uplift associated with the equatorial rise of Western Eistla Regio, for instance directly north of Idem-Kuva Corona. Here, synthetic stereo images show materials associated with an intermediate volcano (Toci tholus, 29.50° N, 355.29° E) which appear to have flowed up-slope. The volcano postdates the plains (Figure 3.22). The majority of uplift associated with Western Eistla Regio occurred before regional plains emplacement as the regional plains embay the rise.

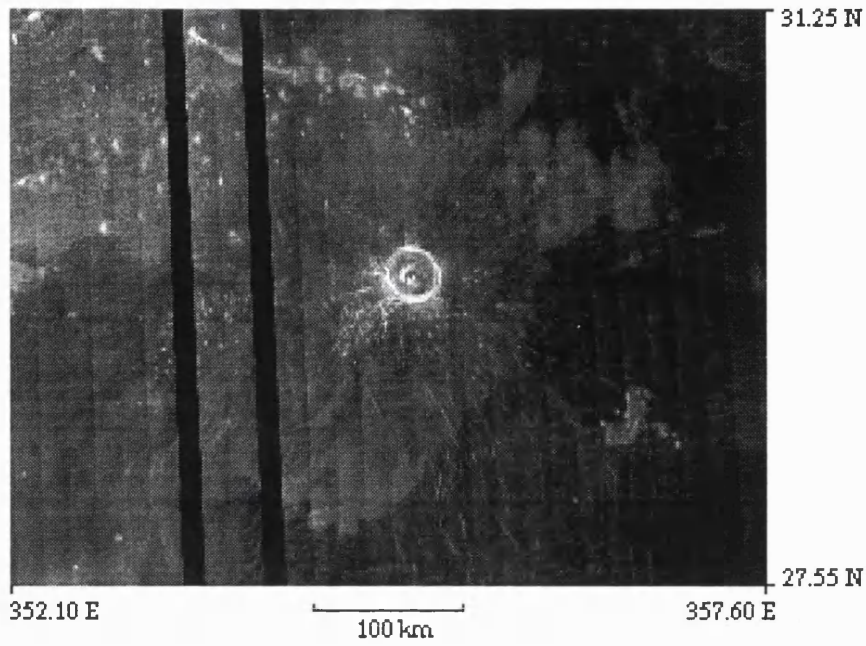


Figure 3.22 Toci Tholus (centre of image), an example of intermediate volcano centre (*vc*) situated on the northern flank of Western Eistla Regio, overlying on Sedna regional plains. The southern flows from this intermediate volcano are seen to flow ‘uphill’ in topographic data. This is evidence for relatively recent continued uplift of Western Eistla Regio after the emplacement of Toci Tholus (C1-MIDR.30N351;1 browse).

As with the lineated and mottled plains materials, the regional plains are deformed by ridge belts. The ridge belt seen in FMAP 42° N, 306° E (Lachesis Tessera East) centred at 38° N, 329.5° E cuts regional plains materials (Figure 3.23). Another ridge belt seen in FMAP 42° N 318° E (Bethune Patera) shows fractures which deform lineated and mottled plains materials, but which clearly extend into and deform regional plains as well (Figure 3.24). In contrast to Zorile Dorsa, fractures associated with these two ridge belts postdate regional plains emplacement.

Wrinkle ridges are common to both Guinevere and Sedna regional plains units. The wrinkle ridges have a sinuous, often braided appearance, are typically less than a kilometre wide, and are tens to hundreds of km long. The spacing of the ridges within the regional plains materials is variable, typically between 20-50 km. The ridges show a reticulate pattern in places (e.g. V31, 14° N, 348° E, Figure 3.25) however, a stratigraphic relation between the two orientations could not be confidently established. Wrinkle ridges which deform the regional plains also deform the lineated and mottled plains materials.

Full resolution FMAP images show local areas of regional plains which contain numerous small (<1 km) pits. Associated with some of these pits are poorly defined aprons of material. The aprons are difficult to see in radar images because their radar backscatter is similar to that of the adjacent plains. The pits and aprons are referred to as *Stealth* volcanoes (Copp and Guest, 1995, 1997). Examples of stealth volcanoes occur in the vicinity of 09.0° N, 352.5° E (Figure 3.26).

Within the NW sector of V19, a number of weakly defined flow fronts are observed. The flow fronts are delineated on the geological map by dashed lines with small arrows indicating possible flow direction. Observations from the study area, (incorporating the rest of Guinevere Planitia) show a similar patchwork appearance of flow materials (best seen using C2 data). This observation is significant when considering the formation and stratigraphy of regional plains materials. In order to quantify the

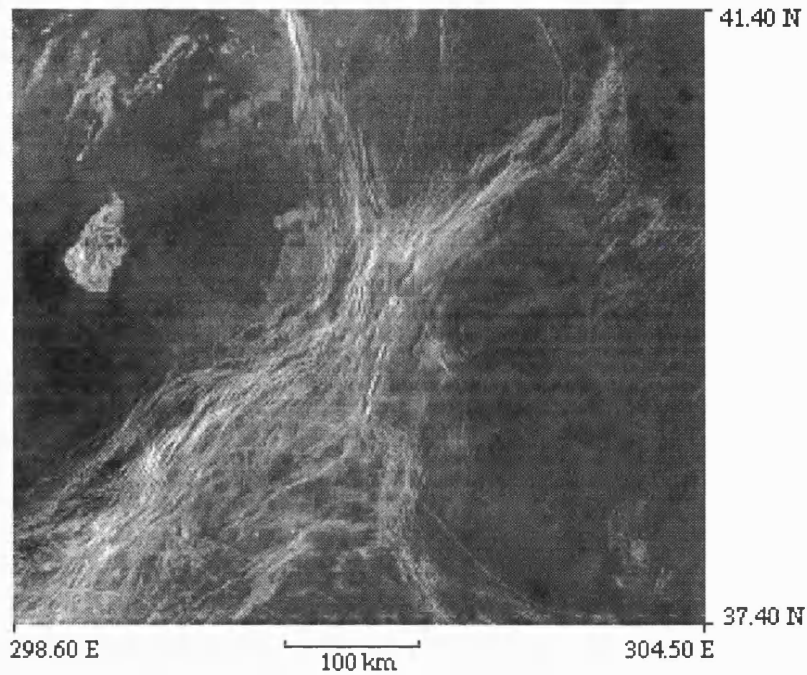


Figure 3.23 A compressional ridge-belt analogous to those described by *Basilevsky and Head* (1995a, 1995b, 1996). The structure clearly cuts Guinevere regional plains materials, hence postdates their formation. This observation contradicts the conclusions drawn by Basilevsky and Head regarding the age of ridge-belts in their global stratigraphy model (C1-MIDR.45N307;1 browse).

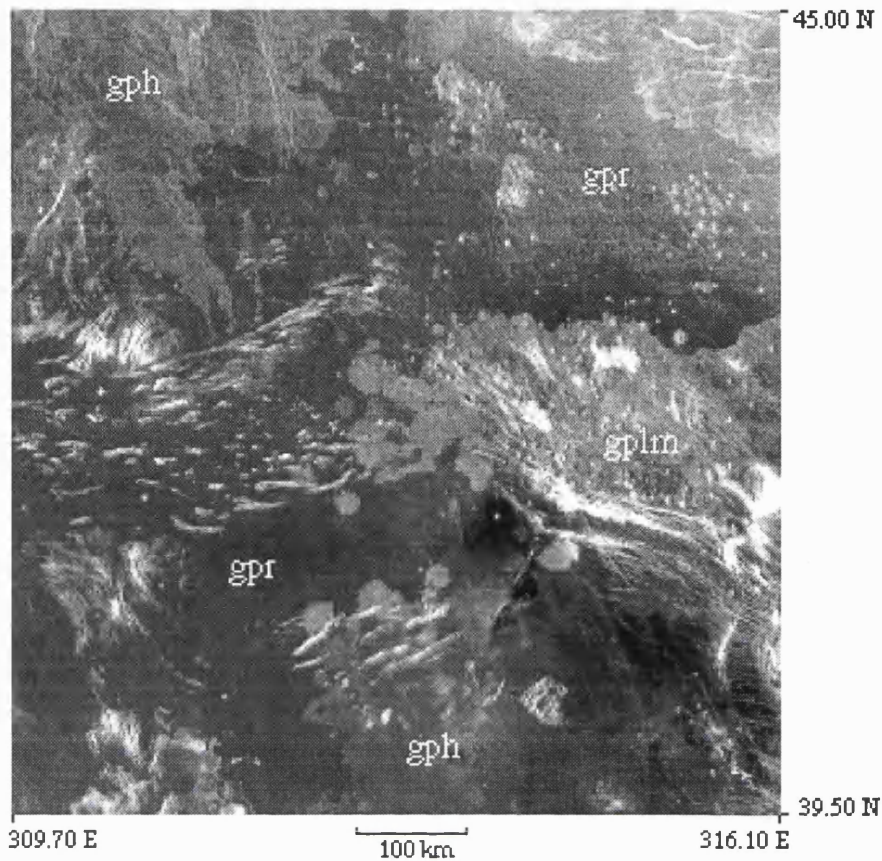


Figure 3.24 Stratigraphic relations between various plains units and structures seen in north central Guinevere Planitia. The oldest unit is the Guinevere mottled and lineated plains (*gplm*) to the east of the image which contains a fracture belt. Some of the fracturing is seen to extend into the Guinevere regional plains (*gpr*) materials, which may be a result of reactivation of the structure. Conversely, the belt may be younger than both *gplm* and *gpr*. Inliers of structures are embayed by *gpr*, as are numerous volcanic edifices (seen in the NE corner of the image). The homogeneous plains embay *gplm*, and are embayed by *gpr* (C1-MIDR.45N307;1 browse).

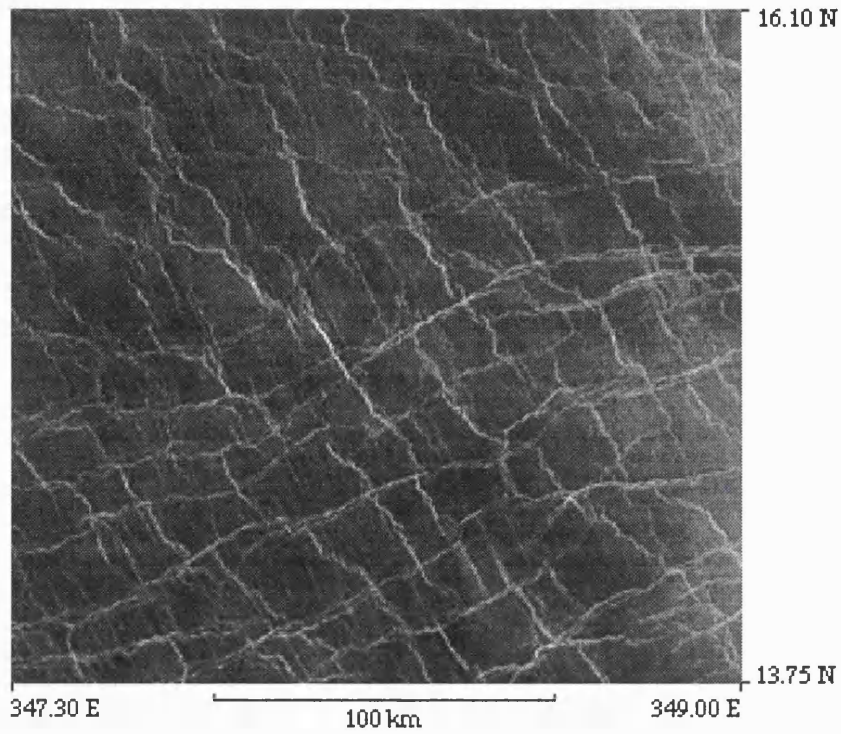


Figure 3.25 Bi-directional wrinkle ridge structures seen within the Guinevere regional plains. The two directions of wrinkle ridges are indicative of two phases of deformation, however it is difficult to establish a time frame between the two phases. This form of compressional deformation is characteristic of regional plains materials. The brighter streaks which traverse the image are superficial deposits from Cunitz crater approximately 200 km to the SE (C1-MIDR.15N352;1 framelet 27).

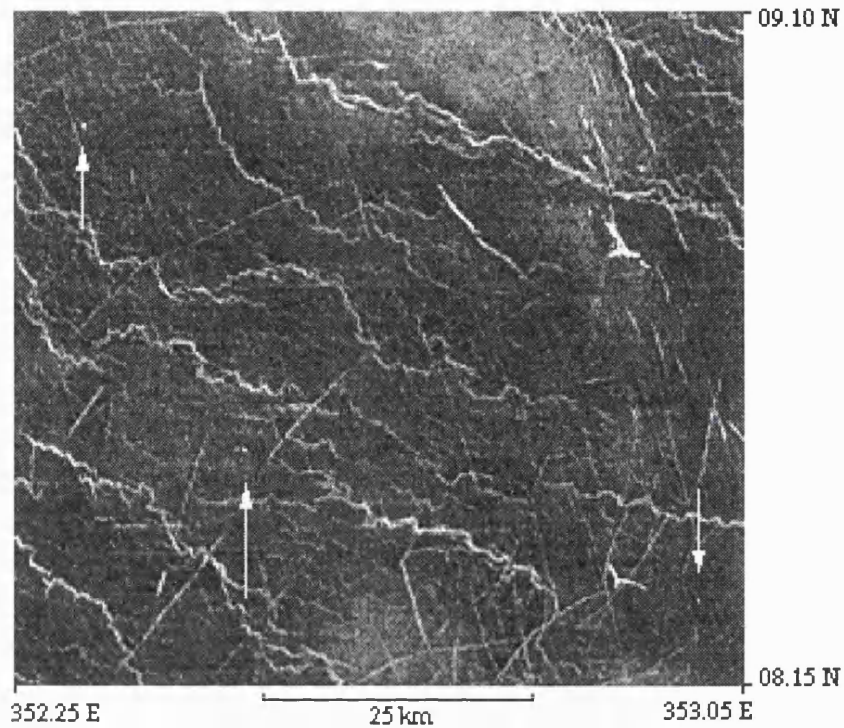


Figure 3.26 Stealth volcanoes. The arrows indicate small volcanic shields which have very little relief and have flow apron with a radar backscatter almost identical to that of the regional plains. Each stealth volcano has a small radar-bright pit at the centre of its flow apron. Stealth volcanoes may have contributed to plains formation, although owing to their radar characteristics, it is difficult to quantify the contribution (C1-MIDR.15N352;1 framelet 53).

observation, the study area (Guinevere and Sedna Planitiae) was divided into 33 squares each measuring 10^0 by 10^0 . The percentage of plains materials which could be linked to a volcanic landform was estimated in each square. The results of this study are presented and discussed later in the chapter (3.5).

Interpretation

The regional plains units are interpreted as relatively young, extensive materials with smooth surfaces at radar wavelength scales. The materials are considered volcanic in origin as these plains are morphologically similar to those chemically sampled by the Venera landers (*Basilevsky et al.*, 1997). Regional compressional deformation has resulted in least two sets of wrinkle ridges indicative of two periods of formation. The relation between the two sets is difficult to establish. The observation of more than one phase of wrinkle ridge formation is consistent with observations of *Squyres et al.* (1992) who recognise three distinct wrinkle ridge fabrics of different ages occurring within plains materials of Lavinia Planitia. Locally, deformation has also formed ridge-belts which postdate the regional plains materials.

What styles of volcanism may be responsible for regional plains emplacement? In answering this question, analogues may be drawn from the large igneous provinces (LIPs) on Earth (*Coffin and Eldholm*, 1994). LIPs have characteristics similar to the venusian plains materials described above in that LIPs represent voluminous flows and have relatively smooth, homogeneous crustal surfaces. The interpreted emplacement times for terrestrial flood basalts, such as the Columbia River Basalts, range from as little as a few days (*Tolan et al.*, 1989) to a number of years (*Self et al.*, 1996). Such voluminous flood basalts are typically associated with plume heads, where $1-2 \times 10^6$ km³ of magma can be extruded in a few million years (*Richards et al.*, 1989). The mode of emplacement of venusian plains materials is considered similar to those of LIPs (*Guest et al.*, 1992), however the emplacement times for individual venusian flows remain unknown.

3.4.4 The Homogeneous Plains - *gph* and *sph*

Materials which compose the homogeneous plains units have a similar morphology to the regional plains materials but have a greater radar backscatter (compare radar backscatter values in Appendix IV and V). The unit is less extensive than the regional plains materials within the mapping quadrangles. Wrinkle ridges which deform regional plains materials also affect the homogeneous plains but are more difficult to identify owing to the ridges and materials which they deform having similar radar backscatters (Figure 3.27).

As with the regional plains, definitive sources for the homogeneous plains materials are not identified within the mapping quadrangles. The materials do have flow fronts, that are often weakly defined. Typically, the unit is embayed by regional plains materials (e.g. 3.5⁰ N, 337.0⁰ E) and superimpose lineated and mottled plains materials (Figure 3.27).

Interpretation

Owing to a similar morphology and areal extent as the regional plains materials, the homogeneous plains materials are interpreted to have formed in a similar way to volcanic flows but have a greater surface roughness implying the final crust suffered greater breakup during emplacement.

3.4.5 Edifice Fields - *ef*

Edifice fields represent local concentrations of small volcanic edifices with a predominant shield morphology. Typical concentrations of volcanoes within edifice fields number around 100 with a density of 4 to 10 edifices per 10³ km², over an area of 10⁴ km² (Aubele *et al.*, 1992; Crumpler *et al.*, 1997). The edifice fields typically measure between 50 and 350 km in diameter. Edifice fields are associated with a number of other units and structures such as coronae, large volcanoes, and extensional

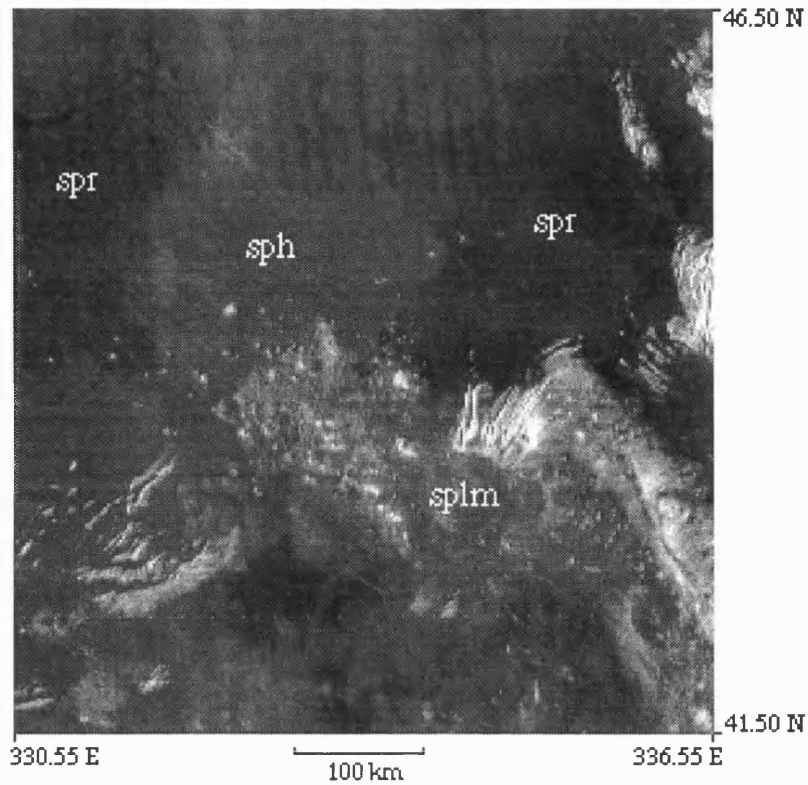


Figure 3.27 Radar characteristics and relations of the Sedna regional (*spr*), homogeneous (*sph*) and mottled and lineated plains (*splm*). The Sedna homogeneous plains have a relatively stronger radar backscatter than the regional plains. The lineated and mottled plains have a greater number of small edifices, have undergone more deformation, and are embayed by the homogeneous plains. The homogeneous plains materials are embayed by the Sedna regional plains materials. Notice the weakly defined flow fronts between *sph* and *spr* (C1-MIDR.45N329;2 browse).

deformation. Observations within the study area identify three principal categories:

(1) *Edifice fields with associated flow materials*

This category is typified by prominent flow materials which radiate for hundreds of kilometres, measured from the centre of the edifice field, typically demarcated by the greatest density of edifices. The flow materials have variable morphologies and radar characteristics.

Examples include two edifice fields in SW Guinevere Planitia which have extensive flow materials 200 to 400 km long (13.5° N, 314.5° E and 17.5° N, 314° E, Figure 3.28). The flow materials which originate from the edifices overlie the local regional plains and have distinct flow boundaries. Similarly, Olosa Colles in V31 (18.5° N, 354° E, SE of Sif Mons, Figure 3.29) has a series of digitate flows which are topographically controlled by wrinkle ridges which deform the local Guinevere regional plains materials.

Common to all three edifice fields are a number of graben. The graben both cut and are overlain by flow materials from the edifices (Figure 3.30). Some graben dissect the edifice fields and have edifices, pits and pit chains along their lengths. The graben also cut the regional plains materials. The edifices of these fields show considerable morphological diversity and display a range of radar backscatter (Figure 3.31).

(2) *Edifice fields without extensive flows*

In contrast to the category above, these edifice fields typically lack extensive flow materials with well defined flow morphologies. Materials associated with these fields normally display a moderately uniform radar backscatter. Volcanic edifices within this second category differ from the category described previously in that: (1) they do not show a wide range in radar backscatter, all typically have a moderate radar backscatter; (2) the edifices have uniform morphologies within the field; and (3) the edges of the edifices are demarcated by diffuse materials with a radar backscatter similar to that of the edifice.

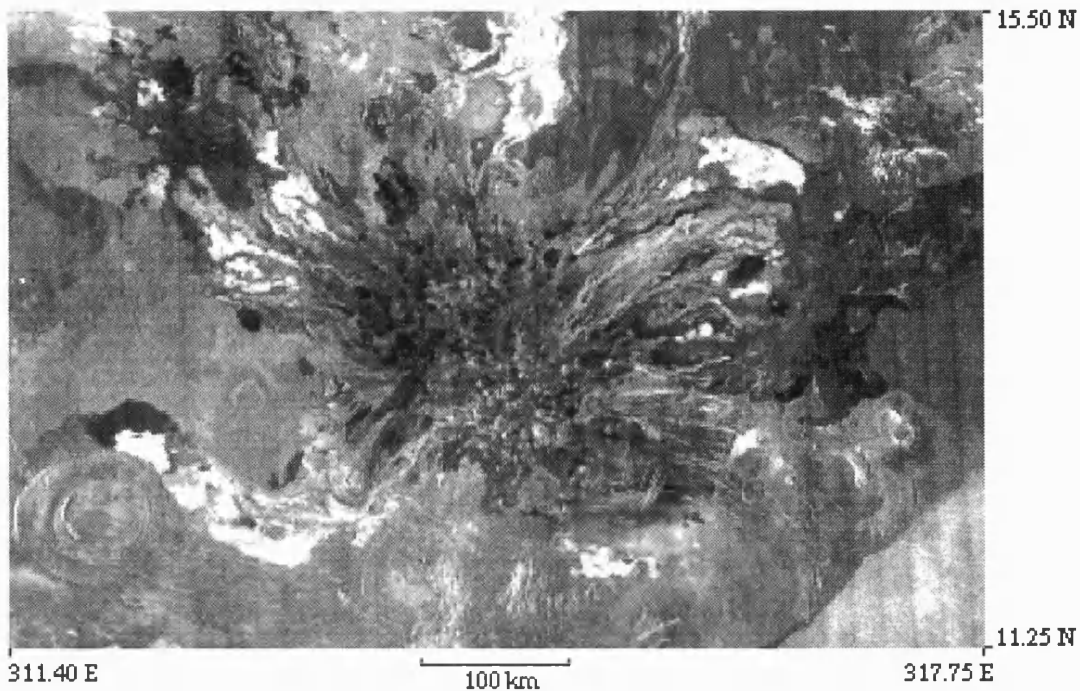


Figure 3.28 An example of a relatively young edifice field situated in western Guinevere Planitia. The edifice field overlies regional plains materials. SW flows from the edifice field are controlled by a small corona and hence post-date it. Volcanic edifices within the centre of the field have a well defined shield morphology and show variable radar backscatters, their margins are well delineated. The extensive flow apron surrounding the edifices displays numerous individual flow units of varying morphology, radar backscatter and emplacement mechanisms. Compare this type of edifice field with that of a relatively older edifice field (Figures 3.32 and 3.33) (C1-MIDR.15N 317;1 browse).



Figure 3.29 Olosa Colles. The edifice field consists of two sections, a NW section composed of relatively radar-bright edifices and associated flow materials, and a SE section, composed of darker edifices with radar-dark flow materials. The edifice postdates the Guinevere regional plains materials. The edifice field is associated with a belt of graben along which some edifices are preferentially oriented (C1-MIBR.15N352 browse).

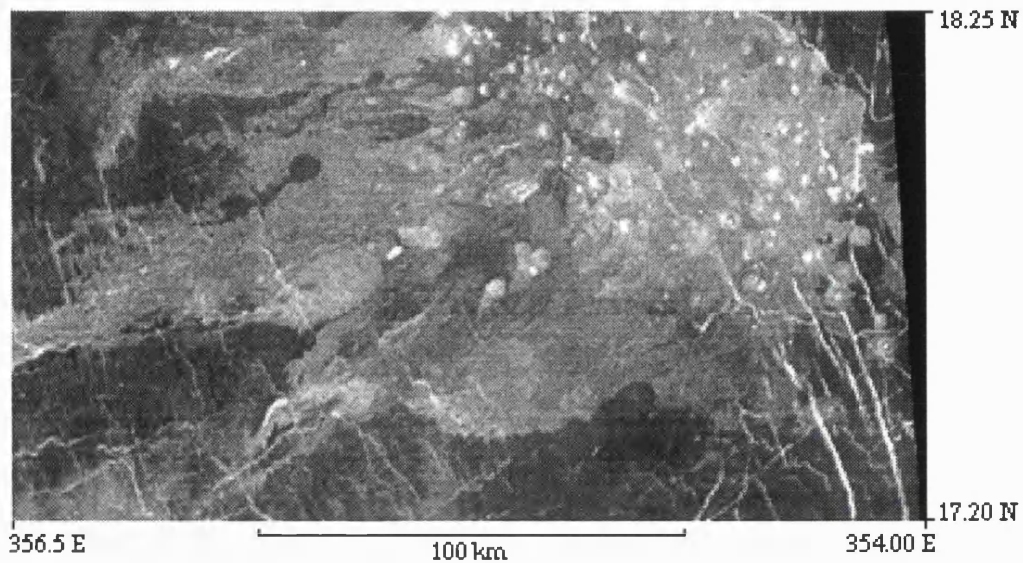


Figure 3.30 Enlarged image of Olosa Colles. The graben to the SE can be traced through the edifice field. Relatively rough flows extend to the SW, some are topographically controlled by wrinkle ridges which cut the regional plains. Olosa Colles is a relatively young edifice field which postdates regional plains materials (C1-MIDR.15N352;1 framelet 21).

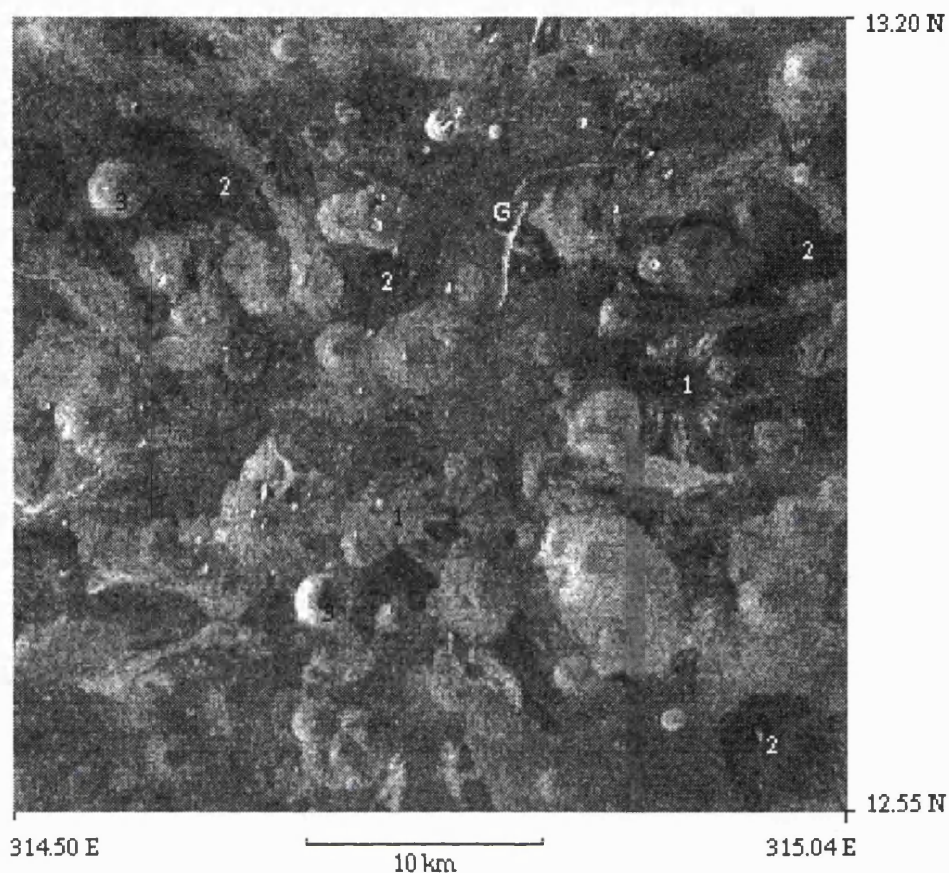


Figure 3.31 Enlarged view of the centre of the edifice field located at 13.5° N, 314.5° E (Figure 3.28). The edifice field postdates the local regional plains and is surrounded by a series of flow materials, it is considered relatively young. From the image, it is seen that the edifices show a variety of morphologies: 1 - edifices with digitate flows of variable radar return, 2 - edifices with a weak homogeneous radar backscatter, 3 - edifices which show relatively greater relief (possible cones). The margins of the edifices are generally well delineated. Compare this image with Figures 3.32 and 3.33 which show relatively older edifice fields. G marks a small graben (C1MIDR.15N317; framelet 35).

This category of edifice field is often associated with stratigraphically older materials such as mottled and lineated plains. Examples include an edifice field located within lineated and mottled plains materials centred at 34.0⁰ N, 331.0⁰ E (V19, Figure 3.32) and at 42.0⁰ N, 314.0⁰ E (Guinevere Planitia). At the latter example, younger regional plains materials clearly embay the edifices, leaving some isolated as inliers. A similar situation is observed with small volcanoes contained in edifice fields and *splm* materials in V19; edifices are embayed and isolated by *spr* materials (e.g. around 39.0⁰ N, 350.5⁰ E, Figure 3.33).

(3) Patch edifice fields

These fields of volcanoes are composed of the amalgamation of distinct circular radar-bright patches, typically 20 km in diameter. Individual patch edifice fields are often amalgamated and form coherent areas typically hundreds of kilometres in diameter. The individual patches show no relief in Magellan data, and are interpreted to be relatively flat; no central construct is observed and the patches rarely show pits. Where pits are observed, they occur near the centre of the patch and are usually less than 300 m in diameter. Smaller pits may exist below the resolution of Magellan SAR.

Large scale linear structures (such as graben) are not typically associated with this category of edifice field. However, a detailed polygonal fracturing, similar to that seen within the lineated and mottled plains, may be observed. The style of deformation is unclear owing to its fine nature and the limiting resolution of the radar instrument. The structure is typically restricted to the patch. Examples occur in V19 at 41.5⁰ N, 333⁰ E (Figure 3.21), and are observed elsewhere on Venus (e.g. 1.0⁰ N, 164⁰ E Figure 3.34). The edifice fields may predate or postdate regional plains materials.

Interpretation

How do edifice fields form, and what styles of volcanism do they represent? *Aubele et al.* (1992), *Aubele* (1995), and

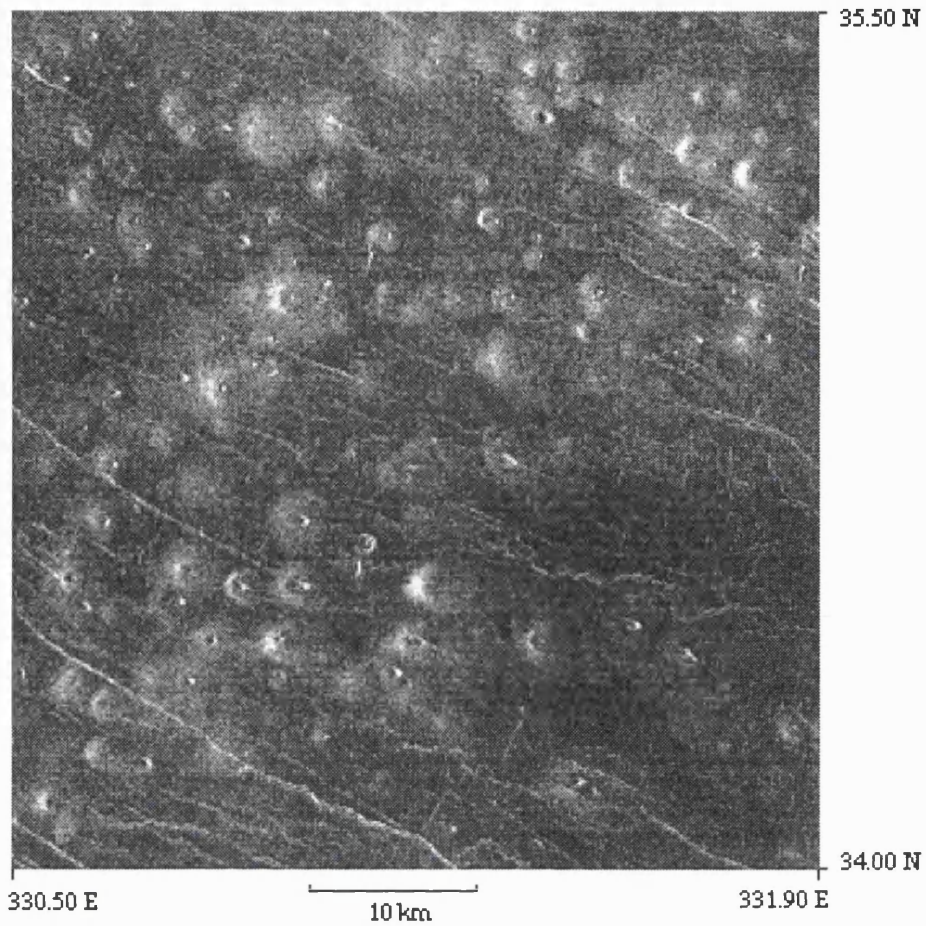


Figure 3.32 An example of a relatively old edifice field situated in lineated and mottled plains materials (V19). The edifice field lacks prominent flow materials. Edifices have relatively uniform morphologies with diffuse boundaries. Some edifices are deformed by the local fabric. (C1-MIDR.30N333;1 framelet 12).

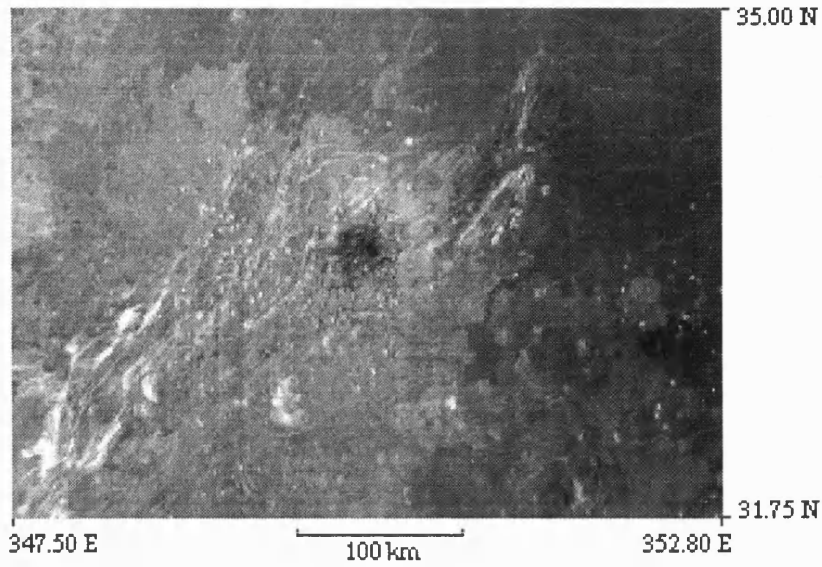


Figure 3.33 An example of a relatively old edifice field situated in the Sedna lineated and mottled plains, southern Sedna Planitia. The edifice field has been embayed by Sedna regional plains to the NE. When compared with a relatively young edifice field, such as those seen in western Guinevere Planitia (Figure 3.28), which overlie regional plains materials, the edifices of the older field are less defined and show less diversity in morphology. Older edifice fields generally have less flow material associated with them. It is suggested that the older edifice field has undergone a degree of degradation (C1-MIDR.30N351;1 browse).

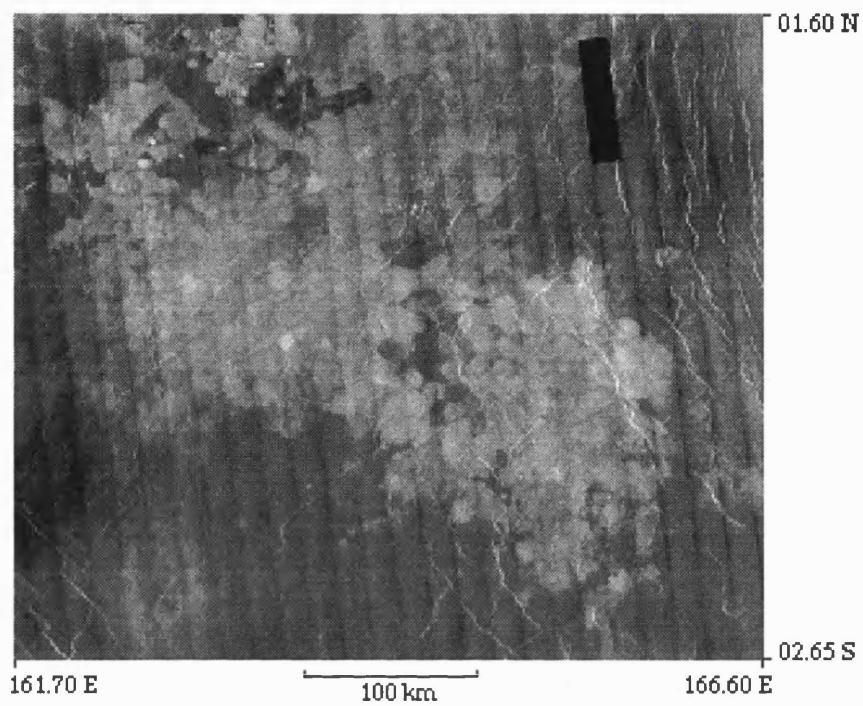


Figure 3.34 Example of a Patch edifice field. The field is composed of an amalgamation of circular radar-bright volcanic edifices with little relief, and associated flow materials. The edifice field postdates the regional plains. Few pits are seen within individual volcanic edifices (C-MIDR.00N163 browse).

Crumpler et al. (1997) have suggested that edifice fields represent islands of topographically high, old plains materials which have been flooded and isolated by younger volcanic plains. This model implies an areally extensive unit existed prior to flooding such as the 'Hilly Mottled Plains Material' described earlier (*Aubele*, 1995; *Crumpler et al.*, 1997).

While the observations presented here show that edifice fields may be embayed by younger plains materials, this is not the case with all edifice fields; Olosa Colles postdates local regional plains materials in V31, as do others in the study area. The actual emplacement of edifices fields is considered a consequence of local melting, with the area of the field controlled by the extent of a shallow regional reservoir or trap (*Aubele et al.*, 1992; *Guest et al.*, 1992).

Associated with relatively young edifice fields are graben (e.g. Olosa Colles, Figure 3.30). This observation implies local crustal extension is important in the formation of some edifice fields. The variation in morphology and radar characteristics of edifice fields seems to correlate with their relative ages. The processes which give rise to edifice fields are considered to have been active over a relatively long period of time.

3.4.6 Isolated Flows - *f*

These materials are recognised as isolated small patches with a weak radar backscatter (see Appendix IV). Typically, the materials can be traced to small pits (< 650 m in diameter) seen with full resolution data (Figure 3.35). The longest dimension of the materials is usually less than 50 km, however materials from a number of pits merge at 4.5° N, 333.2° E (Figure 3.35). Isolated flow materials show no relief on Magellan imagery. Some materials are topographically controlled by wrinkle ridges. (e.g. at 3.1° N 332.3° E). In the V31 quadrangle, the unit overlies homogeneous and regional plains materials (Figure 3.36), and lineated and mottled plains.

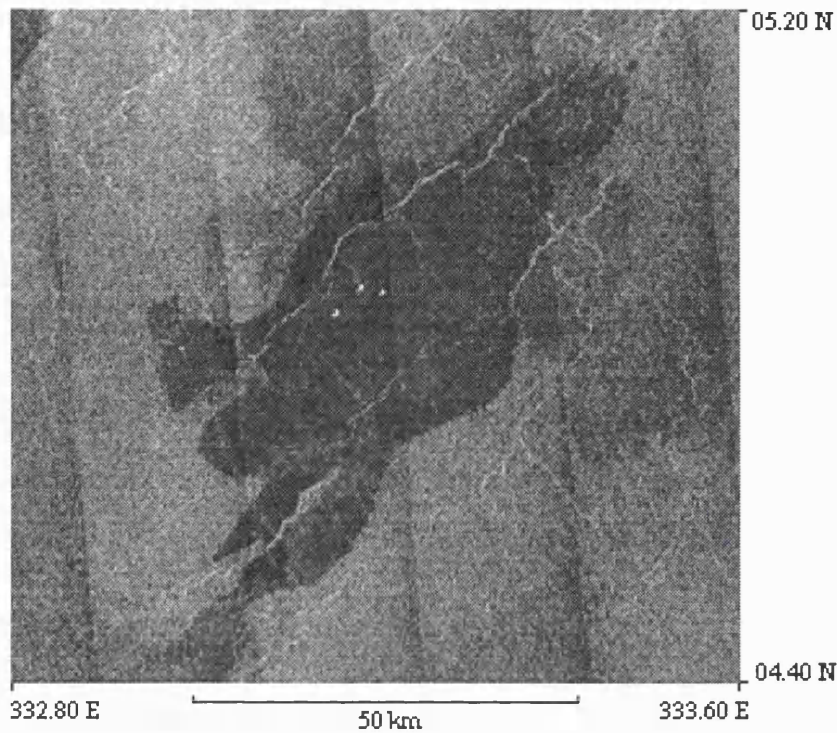


Figure 3.35 Example of the Isolated flow unit (*f*). The three radar-bright pits situated to the west of the centre of the radar-dark flows are interpreted to be the source. The flows superpose both the Guinevere regional and homogeneous plains. The flow material are interpreted to be relatively smooth owing to the weak radar backscatter, and must have been emplaced relatively rapidly with little surface disruption. The style of volcanism is thought to be analogous to eruptions from basaltic shields observed in Iceland (C1-MIDR.00N333;1 browse).

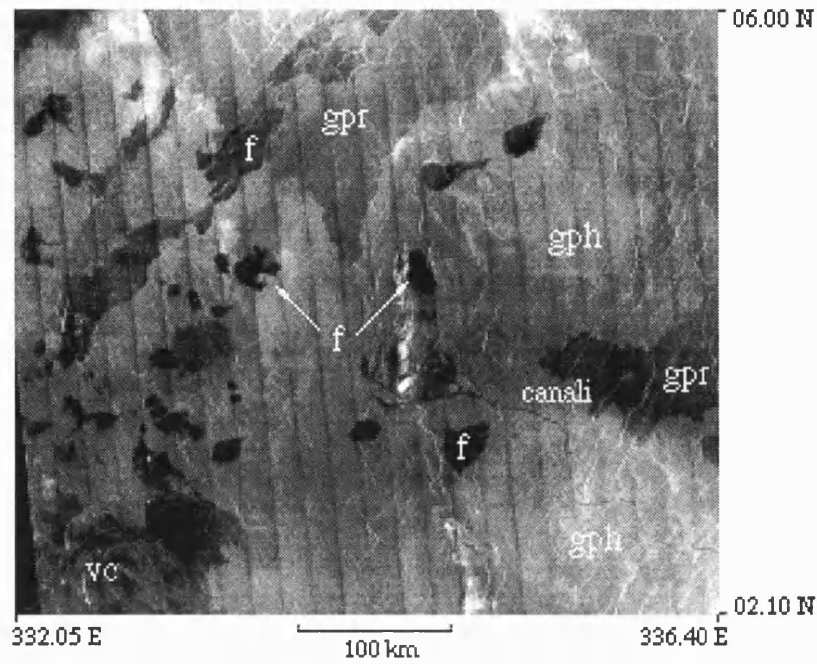


Figure 3.36 Isolated flow units (*f*) seen overlying on plains materials of southern Guinevere Planitia. Sati canali is marked in the SE portion of the image. The radar-dark, delta-shaped flow material seen at the western end of Sati is situated at a greater elevation than the canali themselves. The image also shows the backscatter difference between the regional (*gpr*) and homogeneous (*gph*) plains (C1-MIDR.00N333;1 browse).

Interpretation

The small isolated flow materials are considered to be the manifestation of local areas of melting, producing volcanoes lacking edifices. Instead, flow materials originate from pits which lie at or near the surrounding surface level. The materials are interpreted as smooth, owing to a weak radar backscatter, and hence the crusts of these flows are probably relatively undeformed. Since wrinkle ridges can control the flow materials, it is inferred that the materials were relatively fluid when erupted. The low viscosity of the erupted material would also explain the lack of edifice construction.

3.4.7 Volcanic Centre -vc, and Sif and Gula Materials -s, g

Volcanic centres (vc) constitute materials which originate from an edifice (typically between 15 and 40 km in diameter), which may extend up to 200 km from the source (mean apron extent is approximately 100 km). Two prominent examples occur in V19: Evaki tholus (37.51⁰ N, 342.17⁰ E) and Toci tholus (29.50⁰ N, 355.29⁰ E, Figure 22). Evaki and Toci materials are superimposed on Sedna regional plains materials. Evaki has a summit which has a number of pits and domes. Two E-W elongated pits (less than 4 km in length) occur on the southern flank. The summit is surrounded by flow materials with a digitate appearance, extending up to 160 km from the central summit peak.

Toci exhibits a prominent circular central peak with two central depressions, the smaller (4 km in diameter) being partially nested within the larger (10 km in diameter). A concentric series of fractures which measure 35 km in diameter surround the summit. To the SW, a number of fracture sets intersect to form a polygonal pattern. A finer fabric radiates to the SE from the centre of the volcano. As mentioned earlier, synthetic stereo data show that flows from Toci have been warped by uplifting since the southern flow apron flows 'uphill'. The warping is interpreted to

be associated the uplift of Western Eistla Regio (*Stofan et al.*, 1995). Flow materials extend in a semi-radial fashion away from the summit reaching up to 180 km (to the SW) and have a relatively constant radar return only slightly greater than Sedna regional plains materials. A number of volcanic centres are contained within the lineated and mottled plains materials (see V31 map) typified by edifices with a summit caldera and radial flows.

Two larger volcanic centres, Sif and Gula Montes (*s* and *g*) occur within V31. The volcanoes are defined by a prominent radial extension of flow materials (with a mean distance greater than 300 km) which originate from central edifices identified in topographic data. The flow materials overlie the regional plains materials of Guinevere and Sedna Planitia. The two large shield volcanoes display complex eruption histories recorded by flow units of varying radar backscatter and morphology. A full account of the stratigraphy and interpretation of Sif and Gula Montes is presented in Chapter 5.

Interpretation

Volcanic centres identified within the mapping quadrangle are interpreted as volcanoes with a central conduit. The mean diameter of the flow aprons associated with these volcanoes are marginally greater than 100 km and hence may be called large volcanoes according to the classification of *Head et al.* (1992). Multiple phases of magma extrusion and withdrawal are considered responsible for the calderas and summit structures observed at some volcanic centres (e.g. Toci), analogous to caldera formation on Earth.

Sif and Gula Montes are interpreted as large central volcanoes associated with the topographic highland of Western Eistla Regio. While the volcanoes are considered to have formed from volcanic construction by the effusion of magma contained within a reservoir (Chapter 5), the highland on which they are situated (Western Eistla Regio) is referred to as a volcanic rise. Some of the topographic expression of Western Eistla Regio is considered the

result of processes other than volcanic construction, for instance thermal support (*Senske et al.*, 1992; *Stofan et al.*, 1995, Figure 3.37).

3.4.8 Coronae

Coronae are described as dominantly circular structures consisting of an annulus of concentric ridges and/or fractures with either a topographically positive or negative interior and a peripheral rim and/or trough (*Barsukov et al.*, 1986; *Head et al.*, 1992; *Stofan et al.*, 1991, 1992, 1997). Nine coronae lie within the area defined by the V19 and V31 quadrangles with others occurring elsewhere within Guinevere Planitia.

Coronae contained within the mapping quadrangles have various units associated with them including flows, volcanoes and edifice fields. As coronae are of considerable importance in the stratigraphy and overall geological processes on Venus, the next chapter has been set aside to present the results of a study of coronae from the V31 mapping quadrangle, two of which overlap into V19 (to the north) and one into V43 (to the south). The units associated with coronae in the mapping areas are described in detail there.

Interior units of coronae include volcanic edifices with associated flow materials (see Heng-o Corona, V31) edifice fields, some of which also have associated flow materials (e.g. Benten Corona, V31), and plains materials. The age of interior units varies considerably (discussed in Chapter 4). Many coronae have extensive flow materials associated with them (e.g. Benten Corona, V31) which can extend for 1 to 2 corona radii from the rim and/or annulus (*Magee-Roberts and Head*, 1993; *Stofan and Smrekar*, 1996). In many cases, the flow materials may be further subdivided into units based on radar characteristics, morphology, and spatial extent. Such extensive units are important when considering the composition and stratigraphy of the plains.

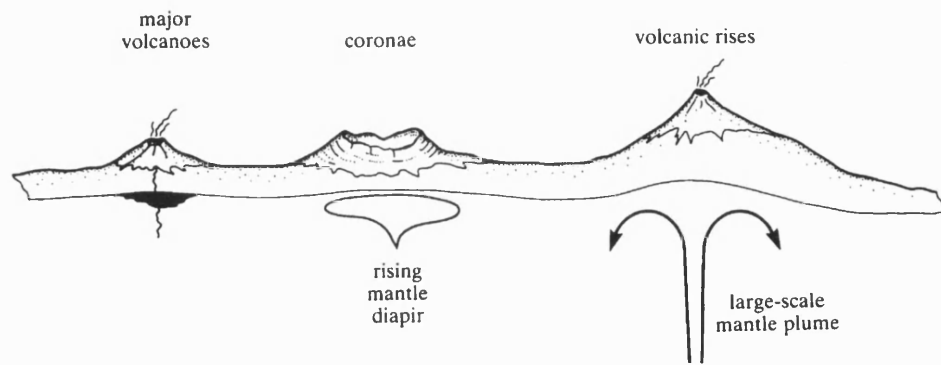


Figure 3.37 Different scales of melting and convection considered responsible for the formation of hot-spot related volcanism on Venus. Large shield volcanoes (left) are associated with large bodies of magma. Large-scale mantle plumes are considered responsible for volcanic rises such as Western Eistla Regio (the site of Sif and Gula). Intermediate between the two are coronae. After *Stofan et al. (1992)*.

Interpretation

The volcanic units and tectonic features associated with coronae are interpreted as the result of initial diapiric upwelling and early stage volcanism, impingement of the diapir against the underside of the lithosphere, and final gravitational relaxation and late stage volcanism as the diapir cools and loses buoyancy (Stofan *et al.*, 1991, 1997; Squyres *et al.*, 1992). A detailed description of the proposed three stage model of corona evolution is presented in Chapter 2 (2.6.1). Regarding stratigraphy, new observations from coronae in V31 show considerable evidence of a protracted history ranging from before to after local regional plains emplacement. A full treatment of corona evolution and stratigraphy is presented in Chapter 4.

3.4.9 Great Flow Fields

An example of a great flow field is Neago Fluctus, which extends into the northern sector of V19, and consists of a suite of flow units of varying morphologies and radar backscatter properties (Appendix V). The total assemblage covers an area of 744,000 km² with its longest dimension measuring approximately 2000 km. The assemblage is subdivided into four stratigraphic units (Arvidson *et al.*, 1992; and Lancaster *et al.*, 1995) Neago Fluctus flow units 1 to 4, *nf1* to *nf4* (Figure 3.38).

The bulk of flows associated with Neago Fluctus originate from N-S trending graben associated with the southern margin of Clotho Tessera (Lancaster *et al.*, 1995). *Nf3* is most extensive (approximately 167,000 km²) and has the strongest radar return (Appendix V). *Nf4* has the weakest radar return and smallest spatial extent and can be traced to a small cluster of edifices to the north of V19. The edifices are superimposed on older Neago Fluctus units. *Nf3*, *Nf2* and *Nf1* are deformed by wrinkle ridges (Figure 3.39).

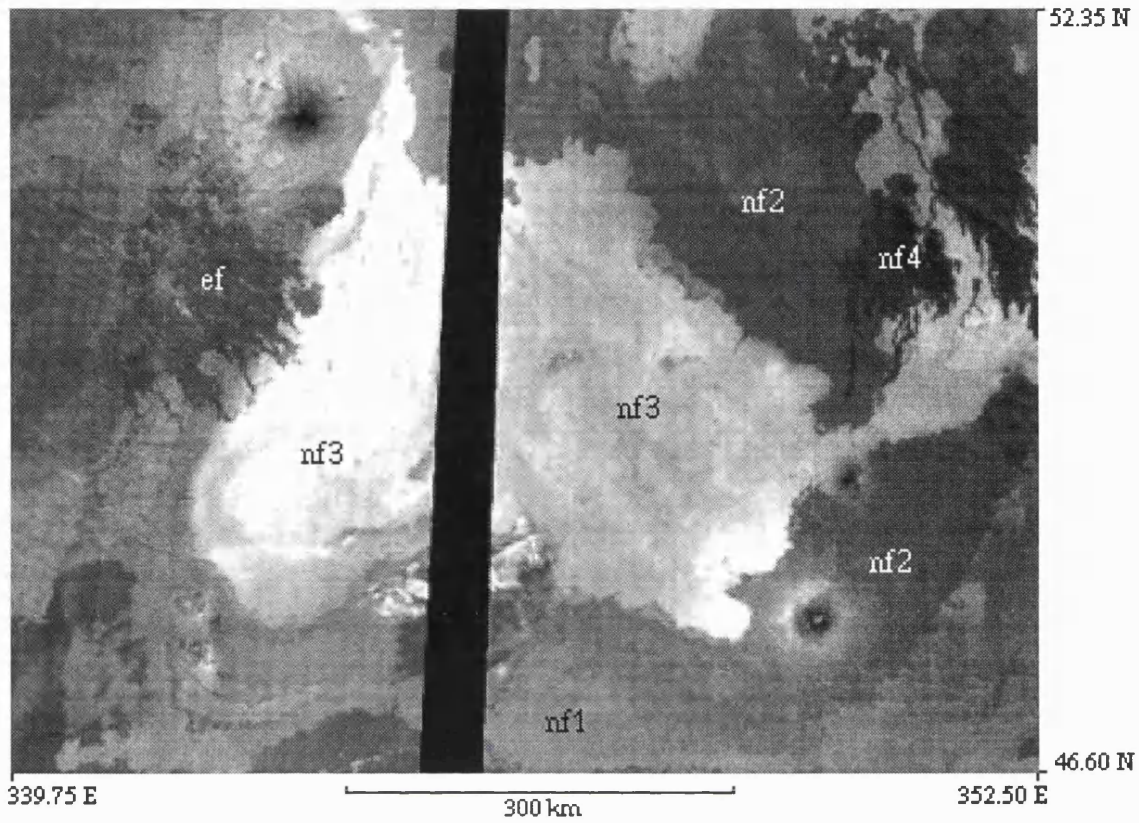


Figure 3.38 Neago Fluctus superposed on northern Sedna regional plains. This great flow is composed of four main units (*nf1*, oldest to *nf4*) which have considerably different radar characteristics (C1-MIDR.45N350;1 browse).

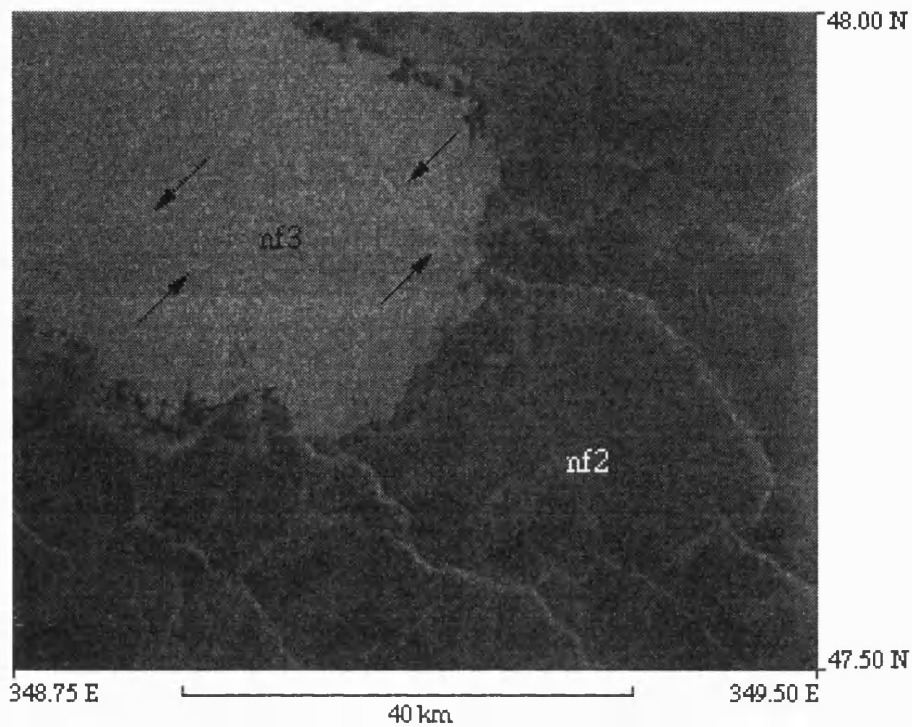


Figure 3.39 Wrinkle ridges clearly cut Neago Fluctus flow 2 materials (*nf2*) and extend into *nf3*, but are difficult to observe as the flows have a similar backscatter to the ridges. Neago Fluctus postdates regional plains materials and belongs to the Atla Group within the global stratigraphic model described by Basilevsky and Head (C1-MIDR.45N350;1 framelet 20).

Interpretation

Neago Fluctus is classified by *Lancaster et al.* (1995) as a great flow field. Great flow fields are recognised by an area greater than 50,000 km² and are typically a few hundred thousand km² in extent (*Guest et al.*, 1992; *Head et al.*, 1992; *Lancaster et al.*, 1992, 1995). Great flow fields are relatively common on Venus, are typically associated with rift zones, and are interpreted as extensive volcanic flow materials. *Lancaster et al.* (1995) noted that a lesser number of great flows originate from volcanoes, coronae and edifice fields interpreted to be younger than the background (regional) plains.

The association of great flow fields with rift-related settings strongly indicates conditions of lithospheric extension and thinning (*Magee-Roberts et al.*, 1993). Great flow fields which are connected to smaller local centres of volcanism (coronae, and large shields) may originate from isolated plumes (*Lancaster et al.*, 1995). An in-depth study of Mylitta Fluctus (55° S, 355° E) by *Roberts et al.* (1992) estimated that here the flow units erupted at between 10⁴ and 10⁶ m³ s⁻¹, with typically a duration of a few days to a few months. These calculations were based on the extrapolation of terrestrial flow lengths versus effusion rates (*Walker*, 1973). While the results represent a first order estimate, and do not allow for periods of inactivity between emplacement of flow episodes, the values are similar to estimates of eruption rate and duration obtained for units within the Roza Member of the Columbia River Basalts (*Shaw and Swanson*, 1970; *Swanson et al.*, 1975). Hence it is considered that great flows on Venus are analogous to major units within terrestrial flood basalt provinces.

3.4.10 Impact and Surficial Crater Materials

V19 and V31 contain a total of 16 and 21 craters, with 5 and 6 surficial 'splotch' impacts respectively. The crater average density for the combined area of the two quadrangles ($14.683 \times 10^6 \text{ km}^2$) is 1 crater per $3.97 \times 10^5 \text{ km}^2$. Including splotches, the average density equals 1 impact related feature per $3.12 \times 10^5 \text{ km}^2$.

Surficial splotch impacts typically have a weak interior radar backscatter surrounded by stronger returning materials. The deposits have diffuse boundaries and are approximately circular. Impact craters within the study area range in size from approximately 5 km to 100 km in diameter (measured from the crater centre to the distal edge of the mean ejecta apron).

For craters ≥ 30 km in diameter, three units may be distinguished: central peak materials (*cp*), crater floor materials (*cf*) and ejecta materials (*ce*). Craters smaller than 35 km are marked *ce* only. Both *ce* and *cp* have strong radar returns with a mottled hummocky appearance. Crater ejecta materials may have deposits with a flow-like morphology extending beyond the main ejecta margin (e.g. Cunitz, V31, 14.40° N , 350.80° E , Figure 3.40). The flow materials may be topographically controlled (e.g. Enid, V31, 16.40° N ; 352.20° E). Crater floor materials typically have a weak radar backscatter. The crater floor materials of Cunitz show a pervasive fabric of ridges with approximately 2 km spacing (Figure 3.40). Surrounding many impact craters are radar dark or bright haloes some of which are parabolic in shape. In some cases the distribution of the dark haloes is controlled by surface features such as wrinkle ridges. Except where bounded by topographic obstacles, these haloes have indistinct boundaries.

Of the 37 craters within the mapping area, one is tectonically modified by fractures (Rhoda, V31, 11.50° N , 347.70° E), and one embayed by flow materials (Heidi, V31, 20.36° N , 350.10° E) interpreted to originate from Sif Mons or a nearby volcanic centre. Where a relation can be established, crater materials typically postdate wrinkle ridge formation. No correlation between unit and

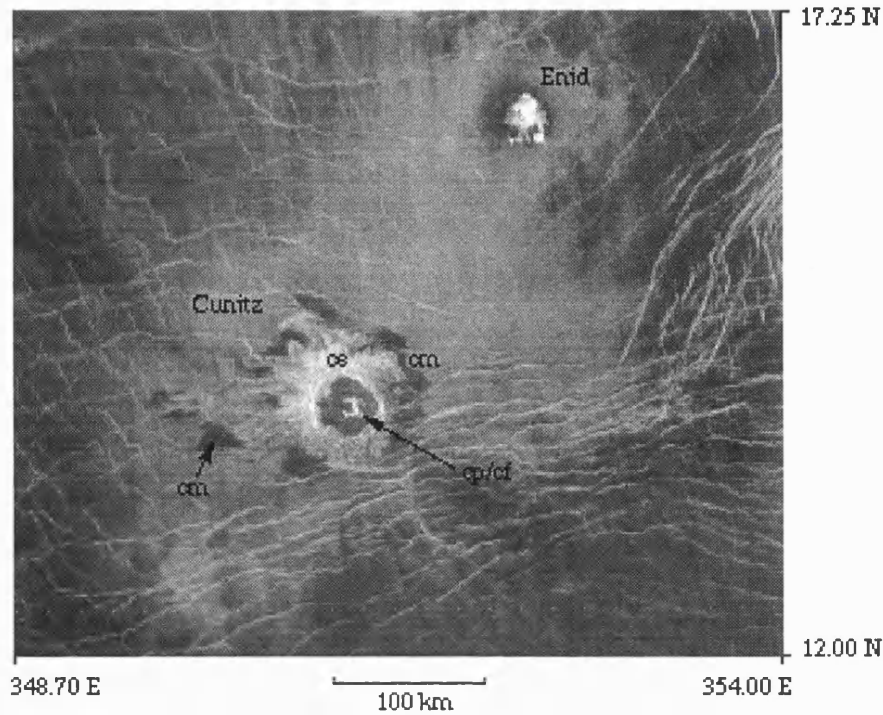


Figure 3.40 Cunitz and Enid craters. Cunitz is surrounded by a radar-bright surficial deposit, ce - crater ejecta materials (which include flow-like materials to the west of the impact), cm - crater margin materials, cp - central peak materials and cf - crater floor materials. Enid is surrounded by a local radar-dark halo and has materials which are topographically controlled by the local regional plains fabric (south of the crater) (CI-MIDR.15N352;1 browse).

crater density is observed.

Interpretation

Apart from Heidi and Rhoda, the craters within the mapping quadrangles are interpreted to be locally young features. However, as with tessera, an age relation between individual craters cannot be established. The average density of impact related features within the mapping quadrangles is similar to that for the global surface area of Venus, calculated as 1 crater related feature per 3.38×10^5 km² (calculated using 1333 impact related features identified by *Strom et al.* (1994) from 98% of the surface of Venus).

Splotch impacts are interpreted to be surface materials disturbed by the incoming shockwave of a bolide which either formed a crater too small to be detected by the Magellan SAR radar, or which failed to create a crater owing to bolide disintegration and/or vaporisation before impact (*Schultz, 1992*). Radar bright and dark parabolic haloes are considered to have formed from crater fallout materials (*Schultz, 1992; Campbell et al., 1992*). Flow materials associated with ejecta and the interior floors of the larger craters (e.g. Cunitz, Benton and Hellman) are interpreted as melt materials formed during and shortly after impact (*Schultz, 1992*). The interior fabric seen within Cunitz is considered to have formed by the cooling and subsequent contraction of floor melt materials.

3.5 A quantitative Measure of the Amount of Materials Associated with an Identifiable Source

From the suite of units identified within the study area, a quantitative measure of the percentage of plains materials which can be attributed to a volcanic or tectonic source was calculated. To achieve this, the study area (Guinevere and Sedna Planitiae) C2 photoproducts were divided into 33 10^0 by 10^0 boxes. The total area of the 33 boxes is 32.41×10^6 km² and represents 7% of the

venusian surface, an area similar to that analysed by *Basilevsky and Head* (1995a, 1995b, 1996, 1997) and *Basilevsky et al.* (1997) in their global stratigraphic model. In each box an estimate of the percentage of materials which could be attributed to a source was noted. The categories for sources were: edifices and edifice fields, intermediate volcanoes (with a mean diameter approximately <200 km), large volcanoes, coronae, and great flows associated with extensional deformation. For each box, the percentage of materials hidden by impact crater materials and by structural modification was estimated. All materials which could not be confidently traced to a source were summed and recorded as unidentified flow materials (UFM). The use of full resolution data and synthetic stereo helped to aid source identification. The results of the study are presented in Tables 3.2 and 3.3 and graphically in Figure 3.41.

Neglecting materials obscured by impact materials and structures, it is shown that approximately 40% of materials within the study area can be traced to a source. The greatest contribution comes from small edifices and edifice fields, followed by larger volcanoes (both large shields, such as Sif and Gula and smaller central volcanoes) and coronae. The percentage here is considered to be an underestimate since some materials had well defined flow morphologies but could not be confidently traced to a source, for instance where a flow has later materials superimposed on it.

Clearly the statistics of this area may not be representative of Venus as a whole. This fact may be illustrated with materials attributed to coronae. While the plains of Guinevere and Sedna contain some coronae, *Stofan et al.* (1997) state that coronae most commonly occur along chasmata systems. It is probable that in the vicinity of chasmata, the degree of plains materials which can be attributed to coronae will be greater. This theory is supported by a preliminary investigation of the Ulfrun Regio which contains a greater number of coronae. Within 18 10⁰ by 10⁰ boxes, 30% of materials in the Ulfrun area (~ 15⁰N, 225⁰E) originate from coronae (Brian, per. comms.) and 63% of observed materials are

Box No.	Lat/ Long	¹ CM	² VC	³ LS	⁴ EF	Coronae	⁵ Ex+GF	⁶ STR	Data Gap	⁷ UFM
1	-10 350	10	10	0	15	10	0	7	15	33
2	-10 340	3	0	0	40	0	0	3	17	37
3	-10 330	3	0	0	20	0	0	1	25	51
4	-10 320	0	0	0	0	0	0	0	100	0
5	-10 310	5	0	35	5	0	0	1	10	44
6	00 350	15	20	0	5	10	0	5	3	42
7	00 340	12	0	5	10	0	0	3	15	55
8	00 330	5	7	0	10	0	0	3	25	50
9	00 320	3	0	0	0	0	0	0	80	17
10	00 310	0	0	35	0	25	0	3	25	7
11	10 350	3	0	15	10	0	0	2	3	67
12	10 340	2	5	10	10	12	0	3	10	52
13	10 330	5	0	0	5	25	0	7	3	55
14	10 320	30	0	0	0	0	0	0	30	40
15	10 310	5	0	0	50	25	0	0	5	20
16	20 350	3	10	40	3	10	0	8	5	21
17	20 340	15	15	5	10	10	0	15	15	15
18	20 330	10	0	0	25	0	0	5	3	47
19	20 320	3	10	0	12	0	0	5	30	50
20	20 310	0	0	0	28	18	0	5	0	49
21	30 350	8	0	0	20	0	0	10	5	57
22	30 340	1	10	0	30	0	0	6	15	38
23	30 330	1	0	0	30	0	0	20	0	49
24	30 320	10	0	0	5	10	0	7	28	40
25	30 310	2	10	0	7	30	0	15	3	33
26	40 350	1	0	0	10	8	15	17	2	48
27	40 340	1	0	0	5	0	45	3	10	36
28	40 330	0	5	0	30	0	1	7	2	55
29	40 320	1	0	0	25	0	0	2	30	42
30	40 310	3	15	0	20	7	0	10	1	44
31	40 300	0	0	10	20	5	20	20	2	23
32	40 290	4	0	30	7	0	30	5	0	24
33	40 280	0	0	40	8	0	25	10	0	17

¹ Crater materials - percentage of area within box obscured by craters and associated materials. Underlying materials cannot be identified.

² Central volcanoes with a mean radial flow field of approximately 100 km

³ Central volcanoes with a mean radial flow field greater than 100 km (e.g. Sif and Gula Montes).

⁴ Edifice Fields and edifices, edifices smaller than approximately 10 km.

⁵ Great flows (as defined by Lancaster *et al.* 1995), associated with extensional structures.

⁶ Structures - Percentage corresponds to sum of *all* forms structure within box

⁷ Unidentified flow materials - materials to which a source could not be confidently attributed.

Lat. long. corresponds to lower right hand corner of each box

Table 3.2 Percentages of materials which can be associated with a source from 33 10⁰ by 10⁰ boxes covering Guinevere and Sedna Planitia. The percentage of structure, data gap and crater materials are also given.

	Crater Materials	Volcanic Centres	Large Shields	Edifice Fields	Coronae	¹ Extension + GF	Structure	Data Gap	² UFM
Total % of materials in the 33 boxes	4.88	3.55	6.82	14.24	6.21	4.12	6.12	15.67	38.12
% after data gap subtraction	5.79	4.20	8.08	16.89	7.37	4.89	7.26	-----	45.20
Total surface of 33 boxes (10⁶ km²)	32.408	32.408	32.408	32.408	32.408	32.408	32.408	32.408	32.408
Total surface area of materials in 33 boxes (10⁶ km²)	1.876	1.361	2.618	5.474	2.388	1.585	2.353	-----	14.648

¹ Great flows (as defined by Lancaster *et al.* 1995), associated with extensional structures.

² Unidentified flow materials - materials to which a source could not be confidently attributed.

Table 3.3 Quantitative measure of materials within Guinevere and Sedna Planitiae calculated as a percentage and surface area.

Surface areas for each box latitude were calculated using spherical trigonometry.

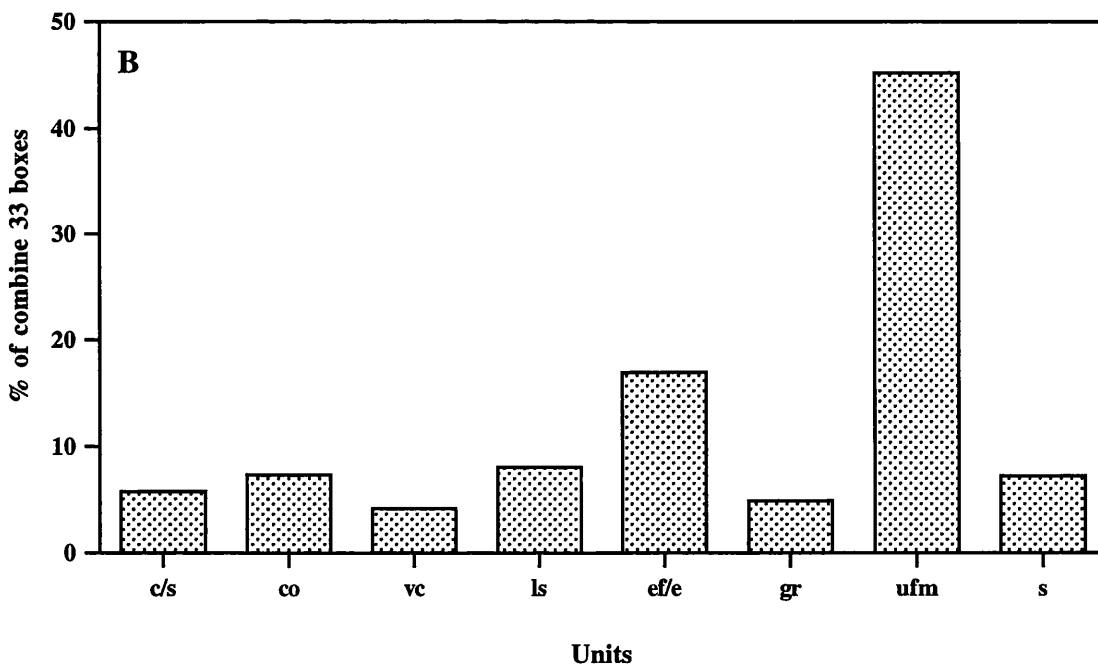
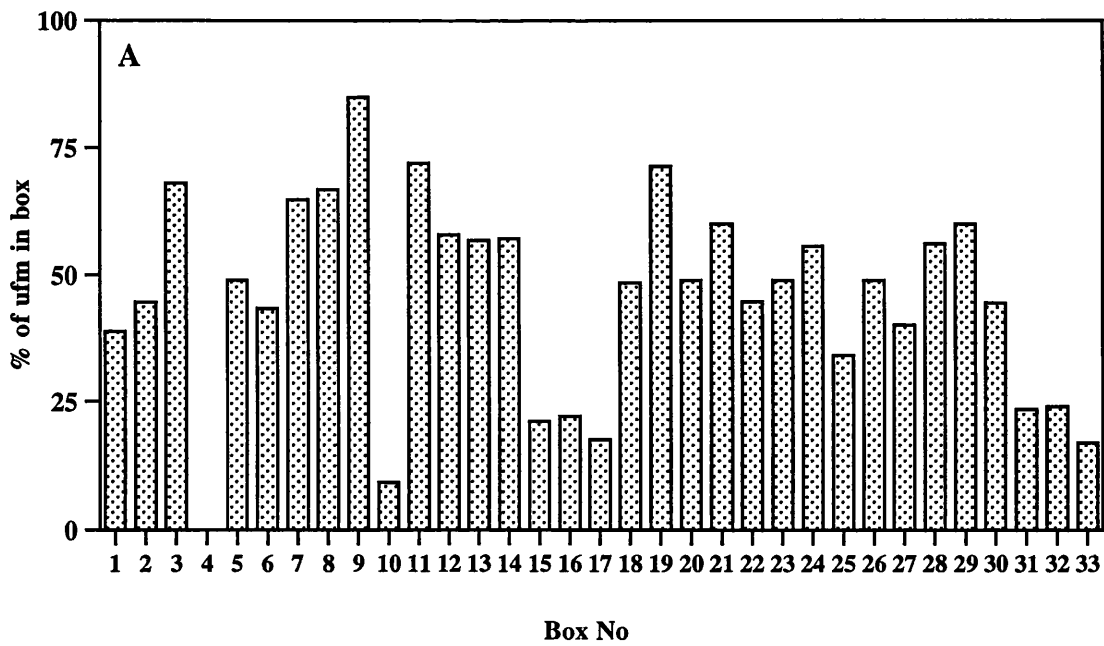


Figure 3.41 A shows the percentage of unidentified flow materials in each of the 33 boxes. B shows the cumulative total of flow materials attributed to a volcanic landform seen in the 33 boxes.

seen to originate from a volcanic landform. Hence here, coronae are important sources of plains materials. There is still some debate concerning a distinction between volcanoes and coronae (*Stofan et al.*, 1992, 1997) and so the percentage associated with each landform may depend on individual interpretation. However, the qualitative study is generally useful in accounting for the bulk of materials which have an identified origin. The significance of these observations regarding stratigraphy are discussed below.

3.6 Stratigraphic Observations from Guinevere and Sedna Planitiae

The stratigraphic conclusions, based on the observations presented above from Guinevere and Sedna Planitiae, are summarised below. Stratigraphic correlation charts for V31 and V19 are shown in Figures 3.42 and 3.43 respectively.

1. The oldest materials in the area are interpreted as Tessera and deformed plains, but this does not imply all the outcrops are the same age. Both units are embayed by lineated and mottled, and regional plains, for instance tessera in the area 40° N 356° E (Figure 3.14). However, the age of tessera and deformed plains units relative to one another cannot be established and a considerable time period may exist between the formation of different outcrops of these units (see discussion below).

2. The lineated and mottled plains are interpreted to represent relatively old plains materials which have experienced multiple phases of deformation. The materials are deformed by at least two phases of wrinkle ridges one of which is restricted to this unit. Furthermore, ridge belts which do not deform younger surrounding materials are observed. Other sets of deformation not represented in younger plains materials are observed. The time duration represented by the lineated and mottled plains is not clear.

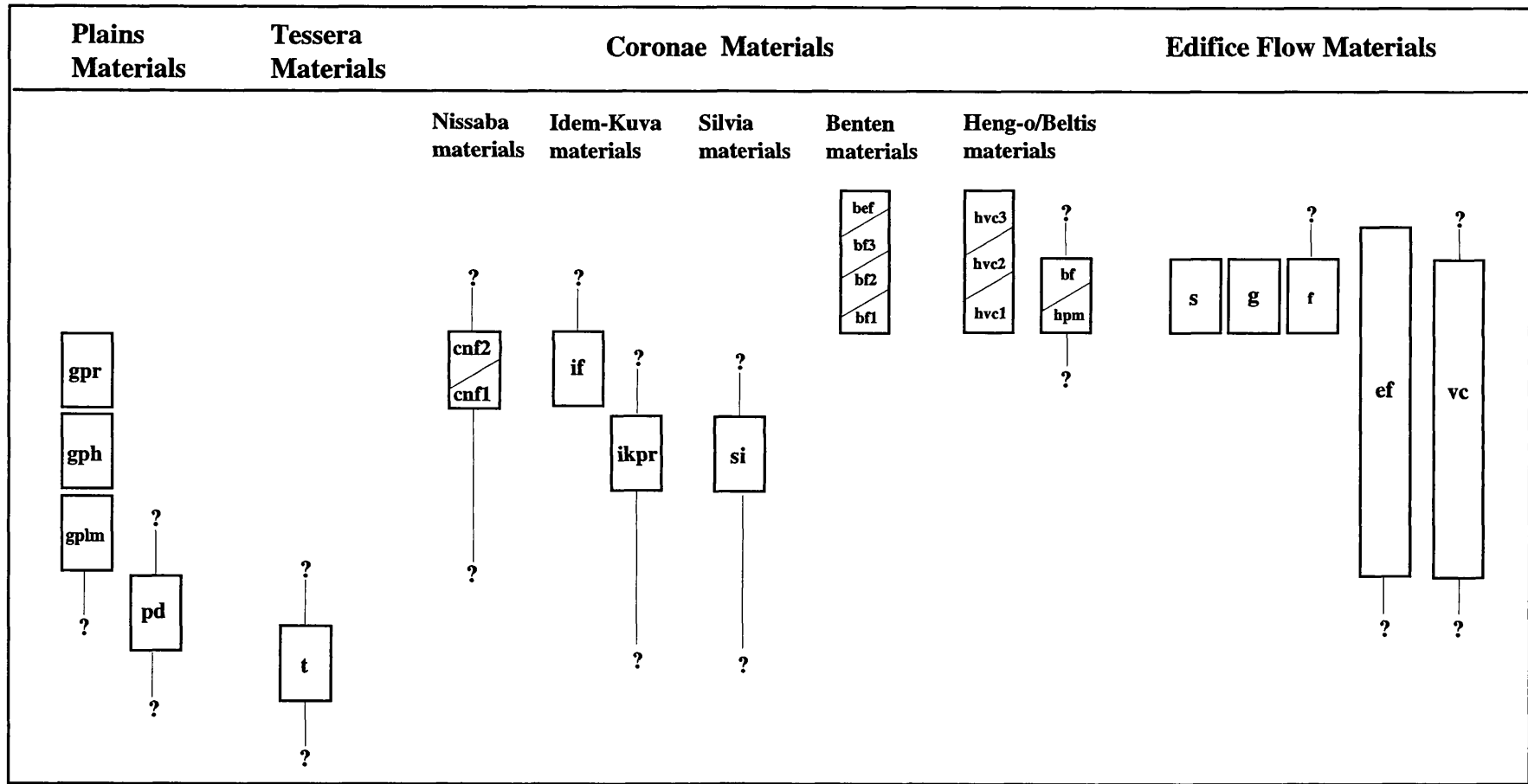


Figure 3.42 Unit Correlation Chart for units of V31 Sif Mons Quadrangle. The chart is based on unit observations solely from the V31 quadrangle.

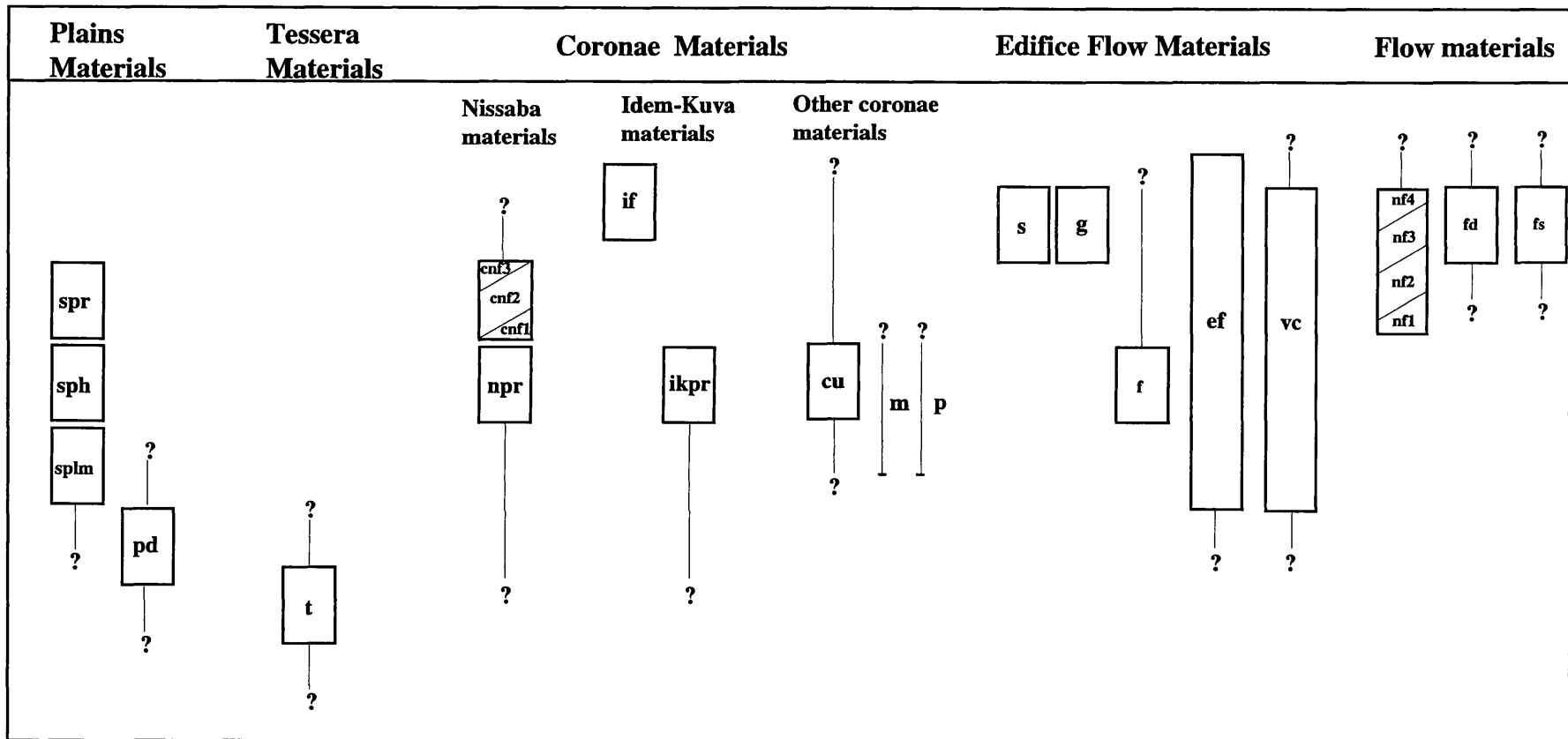


Figure 3.43 Unit Correlation Chart for units of V19 Sedna Planitia Quadrangle. The chart is based on unit observations solely from the V19 quadrangle. *m* and *p* show the position of Mesca and Purandi Coronae which have no flow materials associated with them.

3. The regional and homogeneous plains embay the mottled and lineated plains. Homogeneous plains are typically embayed and hence predate the more extensive regional plains. Both units are deformed by a younger series of wrinkle ridges and ridge belts than those which deform the lineated and mottled plains.

4. The formation of edifice fields is considered to have occurred over a relatively long period of time. Edifice fields pre- and postdate regional plains materials, coronae and large shield volcanoes.

5. Prominent flow materials from large shields (e.g. Sif and Gula Montes), coronae (e.g. Benten, Idem-Kuva) and great flow materials (Neago Fluctus) are typically superimposed on the regional plains units. The wrinkle ridges which deform the homogeneous and regional plains materials also deform the above flow materials locally. While flow materials associated with coronae are typically young (superimposed on regional plains materials), some coronae in V31 show protracted histories (Chapter 4), with initial stages postdating regional plains emplacement.

6. In the study area, approximately 40% of materials can be traced to a source (edifice fields, coronae, large shield volcanoes etc.). These landforms are of different ages.

7. The youngest materials are deposits associated with impact craters. The crater density within the mapping quadrangles is similar to that calculated for the whole planet. A stratigraphic relation cannot be established between individual craters.

3.7 Comparison of Stratigraphic Observations of Guinevere and Sedna Planitiae with the Global Stratigraphy Model

The model of global stratigraphy proposed by *Basilevsky and Head* (1994, 1995a, 1995b, 1996, 1997) and *Basilevsky et al.* (1997) is described in detail in Chapter 2 (2.2-2.4). The model suggests distinct periods during which specific types of volcanic and tectonic activity occurred on a global scale. How do the stratigraphic conclusions from Guinevere and Sedna Planitiae compare with this model?

The directional nature of the model is not supported by observations from Guinevere and Sedna Planitiae. The stratigraphic relations between volcanic units and structures suggest a non-directional history is prevalent within the study area; the same volcanic and deformational processes have occurred more than once over time. The evidence for a non-directional stratigraphy is now discussed in context with the proposed global stratigraphy model.

3.7.1 Evidence for Repeated phases of Volcanism

Throughout Guinevere and Sedna Planitiae (and Venus in general) various styles of volcanism are identified (*Head et al.*, 1991, 1992; *Copp and Guest*, 1995, 1997). The global stratigraphy model places styles of volcanism in specific geological periods: the Atla Period contains all volcanism associated with large shield volcanoes, great flows and coronae, the Rusalka Period contains all volcanism which gave rise to the plains. Observations made during this work show that the same style of volcanism occurs at different times in the history of Venus described below:

Edifice fields and edifices

First, consider the stratigraphy of edifice fields. Edifice fields clearly pre and postdate regional plains formation, as well as large volcanoes and coronae. Olosa Colles (18.5° N, 354° E, Figure 3.29) postdates regional plains, while others are embayed by regional plains materials (e.g. around 39.0° N, 350.5° E, Figure 3.33).

The same situation occurs with small volcanic edifices. Small volcanic edifices are ubiquitous within the lineated and mottled plains materials, and are considered responsible in part for the construction of these plains. Other small edifices postdate lineated and mottled, and regional plains materials, for instance the Isolated flow materials (labelled *f* in the quadrangle maps, Figure 3.36, V31) and the small edifices identified with full resolution data in areas of regional plains materials (*Copp and Guest, 1995, 1997*). Hence, it is considered these younger volcanoes are the result of similar volcanic processes to those which formed edifices in the lineated and mottled plains, and that edifice field and small edifice formation is not restricted to any stratigraphic period.

Intermediate and large volcanoes

Intermediate and large volcanoes are considered relatively young within the Basilevsky and Head global stratigraphic model, confined to the Atla Period, subsequent to regional plains formation. While volcanoes do postdate regional plains materials (e.g. Toci and Evaki tholi, V19, Figure 3.22), volcanic centres within Guinevere lineated and mottled plains materials are embayed by regional plains materials. Further evidence for intermediate and/or large volcanic construction prior to regional plains emplacement is inferred from embayed circular structures seen elsewhere on Venus (Figures 3.44 and 3.45). The circular structures are upstanding, with interior depressions analogous to summit calderas. The largest identified occurs in Aino Planitia (Figure 3.44). The exposed section of this volcano measures 41 km in diameter and is surmounted by a caldera 18.5 km in diameter. Concentric fractures associated with the volcano summit are embayed by materials analogous to regional plains materials.

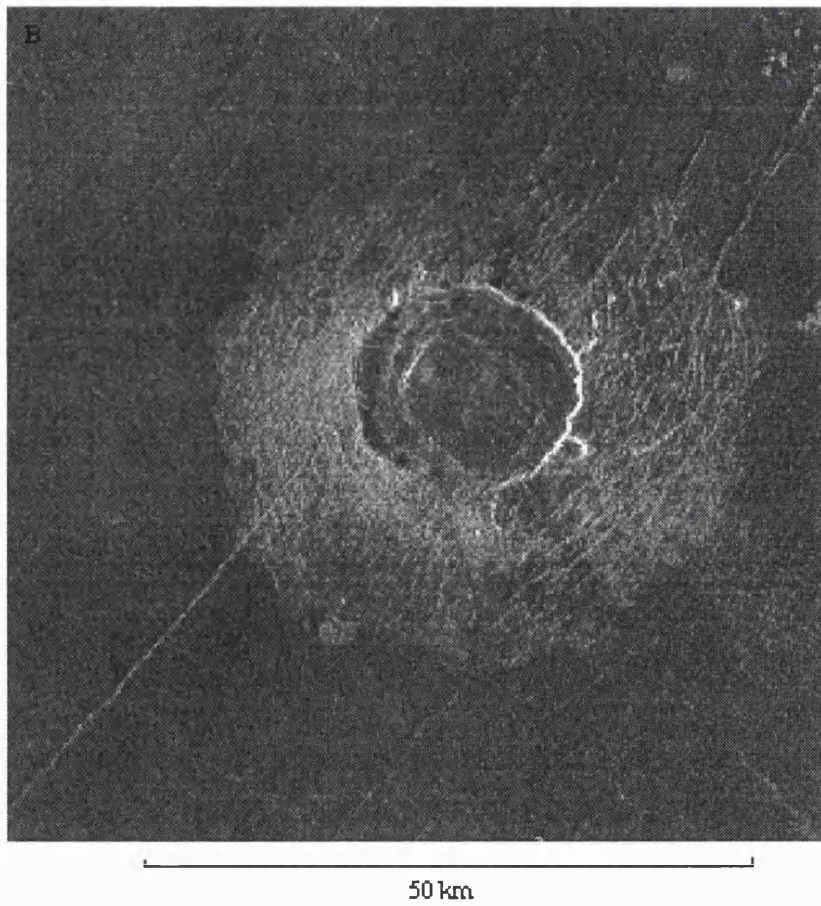
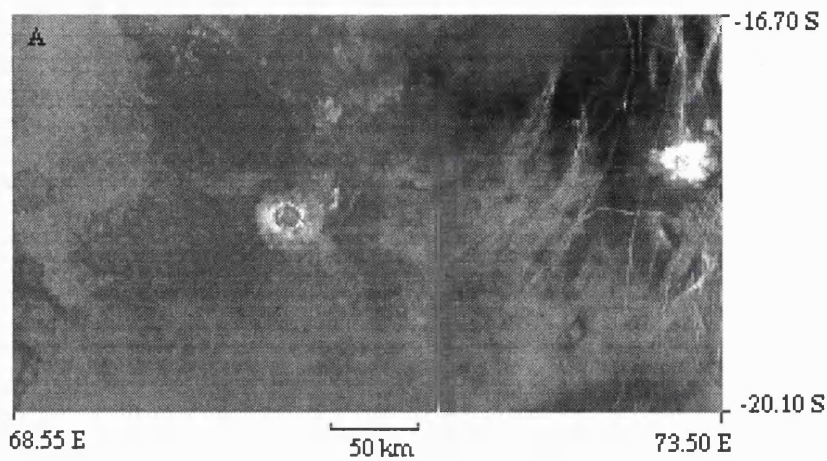


Figure 3.44 Example of buried large edifice in Aino Planitia. A shows plain materials surround the volcano summit, no associated flow materials are observed. B shows the volcano is clearly embayed by younger plains materials. Concentric deformation associated with the volcano summit is embayed by plains materials, e.g. the northern flank (C1-MIDR15S.077;1 A - browse, B - framelets 41 and 42).

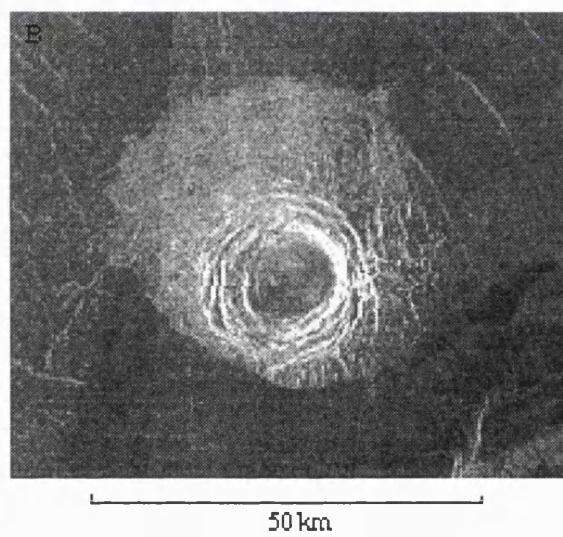
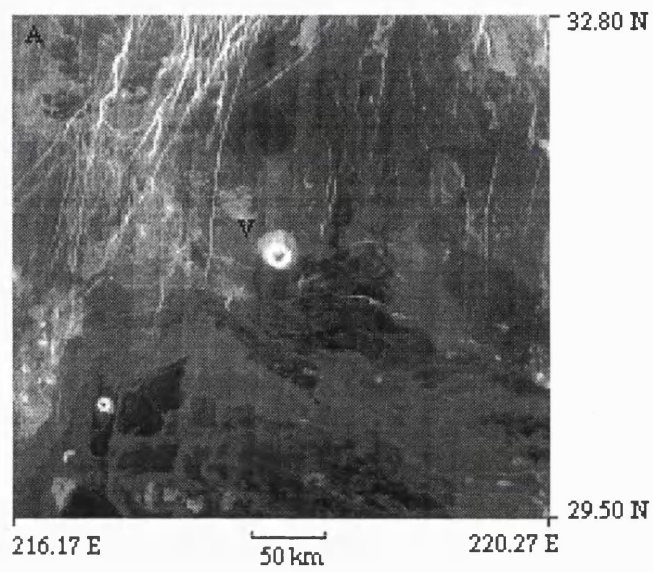


Figure 3.45 Example of buried volcano in Ganiki Planitia. A shows the local geology, a mixture of regional plains and more recent flows. B shows the northern flank of the volcano is embayed by regional plains materials, and the southern flank by the more recent flows (C1-MIDR.30N225;1, A- browse B - framelet 26).

Guest and Stofan (1997) state, using observations by *Copp et al.* (1996, 1997), that although the flow materials of Sif and Gula Montes (Chapter 5) postdate the local regional plains (*gpr*), the topographic rim of Heng-o corona deforms similar regional plains materials, and hence must be younger. Since materials associated with the two volcanoes and corona do not overlap, the stratigraphic relation between them cannot be found. Heng-o corona may be younger than the two shield volcanoes.

Plains

In considering the stratigraphy of plains materials, it is important to identify their source. The quantitative study discussed in 3.5 shows a significant amount of plains materials may be attributed to volcanic and/or tectonic landforms including edifice fields, intermediate and large volcanic centres, rifts and coronae. Particularly significant is the contribution from edifice fields and small edifices. The sources described above are shown here to occur throughout the observed stratigraphy within the study area. It is considered then, that plains materials have different ages because the sources from which they originate have formed at different times. Regional plains materials with unidentified sources can show flow boundaries (e.g. in *spr*, V19). This observation implies layering of materials indicative of repetitive volcanic processes. It is considered that the homogeneous and regional plains materials represent similar styles of volcanism acting over a protracted period of time. A similar situation is observed with Aino Planitia described by *Guest and Stofan* (1997). Here, the plains are interpreted to have formed from numerous superimposed flood lavas which have varying surface textures.

The earlier lineated and mottled plains materials are considered to have undergone periods of construction, formed by the amalgamation of materials from small edifices, clusters of small edifices and larger volcanic sources. From the study area, evidence exists for a progressional accumulation of volcanic materials, with edifices and associated materials extruded onto

the local regional plains to form new units.

Great flows

In identifying great flow fields, *Lancaster et al.* (1995) noted that the bulk originate from rifts. However as with plains materials, some sources of great flows include volcanoes, edifice fields and coronae. Furthermore, *Lancaster et al.* (1995) state that the great flow fields were identified by their pristine morphology. As explained at the beginning of this chapter, radar backscatter is dependent on surface roughness. Flow fields with similar radar backscatters are likely to be difficult to distinguish. *Guest and Stofan* (1997) cite observations of flow margins within the regional plains by *Crown et al.* (1994) as examples of great flows which have the same radar backscatter and which formed at different times.

3.7.2 Evidence for Repeated phases of Deformation

As with volcanic activity, structural fabrics identified within Guinevere and Sedna Planitiae imply a non-directional rather than directional nature to deformational processes. The observations contradict those cited in the global stratigraphic model of Basilevsky and Head.

Tesserae

Based on embayment observations, tessera is commonly cited as the oldest local unit when mapping on Venus (e.g. *Bindschadler and Head*, 1989; *Ivanov and Basilevsky*, 1993; *Greeley et al.*, 1994; *Copp and Guest*, 1995, 1997; *Tapper and Guest*, 1997). Within the global stratigraphy model, tessera is used as a global time-stratigraphic marker (the Fortunian) and is considered the result of a global period of deformation called tesseration (*Ivanov and Head*, 1995, 1996; *Basilevsky and Head*, 1995a, 1995b). However, tesserae are defined by their structural characteristics which are not necessarily an absolute age criterion.

By way of a terrestrial analogy, before absolute dating of rocks was possible, relative ageing was established using the principles of superposition and cross-cutting relations, similar to mapping techniques used with Magellan data today. Crystalline metamorphic rocks were identified as the oldest materials at separate localities and thus mapped as one age. From more careful stratigraphic studies (and later, the advent of absolute dating methods) it was shown that metamorphic rocks span the whole stratigraphic age of the Earth, and of course, are currently forming today (*Hansen and Willis, 1996*). A similar situation should be considered with tesserae on Venus. For example, there is no way of knowing the age relation between Manzan-Gurme tesserae and tesserae elsewhere on the planet.

Ridge belts

Within the global stratigraphy model, deformational processes responsible from the production of ridge belts are considered by Basilevsky and Head to be confined to the Lavinia Period, preceding the Rusulka regional plains forming period. Ridge belts within the study area do not conform to this stratigraphic restriction. Examples both pre and postdate regional plains materials. Zorile Dorsa (Figure 3.19) is confined to lineated and mottled plains materials, while the ridge belt located at 38.5° N, 329.5° E, (Figure 3.23) postdates regional and homogeneous plains materials. Hence, the formation of ridge belts has been repetitive.

Wrinkle ridges

Another global compressional event proposed by *Basilevsky and Head* (1995a, 1995b), *Head and Basilevsky* (1996), and *Basilevsky et al.* (1997) is represented by wrinkle ridge structures, which are claimed to be confined to the Rusulka Period. As with ridge belts, observations from units within Guinevere and Sedna Planitiae suggest more than one period of wrinkle ridge formation (Figures 3.15 and 3.16). Lineated and mottled plains materials contain a set of older wrinkle ridges which do not deform the younger regional plains (*Copp and Guest,*

1995); hence a period of wrinkle ridge formation took place prior to regional plains emplacement, before the Rusulka Period.

Flow materials belonging to the Atla Period which are superimposed on the regional plains are considered not to have experienced wrinkle ridge deformation (*Basilevsky and Head* 1995a, 1995b; *Basilevsky et al.*, 1996, 1997). Yet wrinkle ridges deform flow units of Neago Fluctus (Figures 3.38 and 3.39), materials to the NE of an unnamed corona at 9.5° N, 315.05° E, and flows at 04°S, 311°E, which originate from a central volcano. Other work has also shown that wrinkle ridge formation was not globally contemporaneous. *McGill* (1993) found that wrinkle ridges have different distribution and intersection patterns on a global scale. This observation suggests different regional stress regimes in the crust occurred at different times.

Coronae

Perhaps the greatest (incorrect) assumption of the global stratigraphic model relates to the formation of coronae and associated structure and volcanism. Recall from Chapter 2 (2.3) that an 'idealised' sequence of corona development is suggested by Basilevsky and Head, with the various stages of formation (represented by the same structure at each corona) occurring at the same time throughout the history of Venus. Observations of coronae within the V31 mapping quadrangle tell a very different story and show that coronae can have a protracted history; stages of corona formation are not specific to any period of geological time (Chapter 4).

3.8 Resurfacing Models and Venusian Stratigraphy

Two models were described in Chapter 2 (2.5) to explain the crater retention age of the surface of Venus (500-300 Ma); the global (catastrophic) resurfacing model (GRM), and the equilibrium resurfacing model (ERM). Observations from Guinevere and Sedna Planitiae provide evidence for repetitive

volcanic and deformation processes.

Based on this observation, the equilibrium model proposed by *Phillips et al.* (1992) is more applicable than the global resurfacing model followed by dramatically reduced volcanism. The conclusion is supported by recent observations at Anio Planitia (*Stofan and Guest, 1996; Guest and Stofan, 1997*) where further repetitive resurfacing is considered responsible for the interfingering of plains materials.

3.9 Summary and Conclusions

Geological maps for V31 Sif Mons, and V19, Sedna Planitia quadrangles (Venus) have been constructed using the Magellan data sets. Mapping of the quadrangles, and a more areally extensive investigation covering Guinevere and Sedna Planitiae, has resulted in the identification of numerous units and structures. The bulk of the units are interpreted as volcanic in origin, and may be associated with volcanic and tecto-volcanic landforms (volcanoes, shield fields, rifts and coronae). Both compressional and extensional deformation have resulted in widespread fabrics of varying scales. The relations between the structures and units within the study area (Guinevere and Sedna Planitiae) are used to construct a stratigraphy which, in turn, tests the global stratigraphic model of Basilevsky and Head and resurfacing models, described in Chapter 2 (2.2-2.4).

In the study area, tesserae and small outcrops of deformed plains are considered the oldest units, as both are embayed by subsequent plains materials. The lineated and mottled plains are considered a consequence of the amalgamation of volcanic materials associated with numerous small edifices, and local flows. The unit has experienced considerably more deformation than younger plains materials. Embaying the lineated and mottled plains materials are the homogeneous, and regional plains materials. All three plains units are deformed by sets of wrinkle ridges. More than one phase of wrinkle ridge deformation is

observed.

Volcanic units are also associated with coronae, local concentrations of small edifices (shield fields) and central volcanoes which vary in size. The most prominent flows from these sources postdate the regional plains. However, new observations presented here suggest the volcanic landforms have a protracted history. A quantitative study on a broad scale shows a significant amount (~40%) of plains materials may be attributed to volcanic landforms within Guinevere and Sedna Planitiae.

The new observations show the stratigraphy of the study area does not conform with the global stratigraphy model proposed by Basilevsky and Head. In contrast to the directional nature of their model, similar volcanic and deformation processes have occurred at different times within the study area. While some of these processes may be more dominant at certain times (for example the formation of tessera), the processes are not restricted to any particular time frame. The non directional nature of stratigraphy observed here favours a resurfacing model similar to the equilibrium resurfacing originally proposed by *Phillips et al.* (1992), rather than a rapid resurfacing event (*Strom et al.*, 1994).

Chapter 4

New insights into corona evolution on Venus

4.1 Introduction

Coronae consist of concentric annuli of ridges and/or graben (*Barsukov et al.*, 1986; *Stofan et al.*, 1992; *Squyres et al.*, 1992). Most have a circular or ovoidal planform shape, with maximum diameters of 65 to 2100 km. The topography of coronae varies, with most having a raised rim (*Stofan et al.*, 1992, 1997). Volcanism is nearly always associated with coronae, the amount and style of which varies both spatially and temporally (*Stofan et al.*, 1992; *Head et al.*, 1992; *Roberts and Head*, 1993).

As described in Chapter 2 (2.6.1) and 3 (3.4.8), a number of models have been presented to account for the morphology and formation of coronae. However, current models do not explain the many variations in morphology which are observed (*Stofan et al.*, 1992; *Stofan and Smrekar*, 1996). Coronae occur in a number of tectonic environments including volcanic rises, the plains and, most commonly, along chasmata systems (*Stofan et al.*, 1997). Chapter 2 (2.6.1) describes three stages of corona evolution inferred from previous observations. Theoretical models have been developed to explain these observations (*Stofan and Head*, 1990; *Stofan et al.*, 1992; *Squyres et al.*, 1992).

In this study, five coronae contained within the Sif Mons mapping quadrangle (V31) were observed to test models of corona formation and global stratigraphy (Figure 4.1). Two coronae overlap into the Sedna Planitia mapping quadrangle (V19) and one with V43, south of V31. *Stofan et al.* (1997) have shown that corona characteristics, such as topography and morphology, are globally random. Using full-resolution Magellan Synthetic Aperture Radar (SAR) data, the five coronae were mapped and their relations with surrounding units established. The mapping techniques follow the guidelines of *Tanaka et al.*

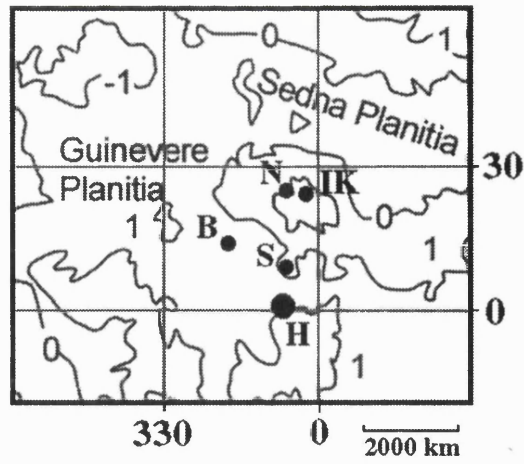


Figure 4.1 Location Map for the five coronae in V31. Contour interval is 1 km. IK - Idem Kuva Corona, N - Nissaba Corona, B - Benten Corona, H - Heng-o Corona, S - Silvia Corona.

(1994). From the observations, it is argued that these coronae formed over an extensive period of time, and that coronae have a more complex history than the simple three stage model previously proposed (*Stofan and Head, 1990; Stofan et al., 1992; Squyres et al., 1992*). This has important implications for modelling the origin of coronae and constructing a global stratigraphy for Venus described in Chapter 2 (2.2-2.4).

4.2 Observations of coronae in Guinevere and Sedna Planitia

The five coronae described are Idem-Kuva, Nissaba, Benten, Heng-o and Silvia. The margins of these and many coronae show two scales of deformation: (1) a broad (25-120 km across), usually discontinuous, topographic ridge with or without a surrounding trough; and (2) closely spaced (5-15 km) arcuate fractures, graben and/or ridges. Throughout this chapter, the zone of closely-spaced structures is defined as the annulus, following previous practice (*Barsukov et al., 1986*) and the broader scale ridge and trough structures as rim topography. The two scales of deformation can show important information regarding the formation and stratigraphy of a corona and hence often need to be discussed individually. The section below describes the geological history of each corona, then its relation with surrounding units.

4.2.1. Idem-Kuva Corona

Idem-Kuva (25° N, 358° E, Figures 4.2 and 4.3) is situated immediately north of the large shield volcano Gula Mons in Western Eistla Regio. It is classified by *Stofan et al. (1992)* as having a concentric morphology dominated by volcanism. The corona measures approximately 280 km in diameter based on the outer most extent of concentric structures. It is circular in plan view, with a 600 meters high central domical region which is 100

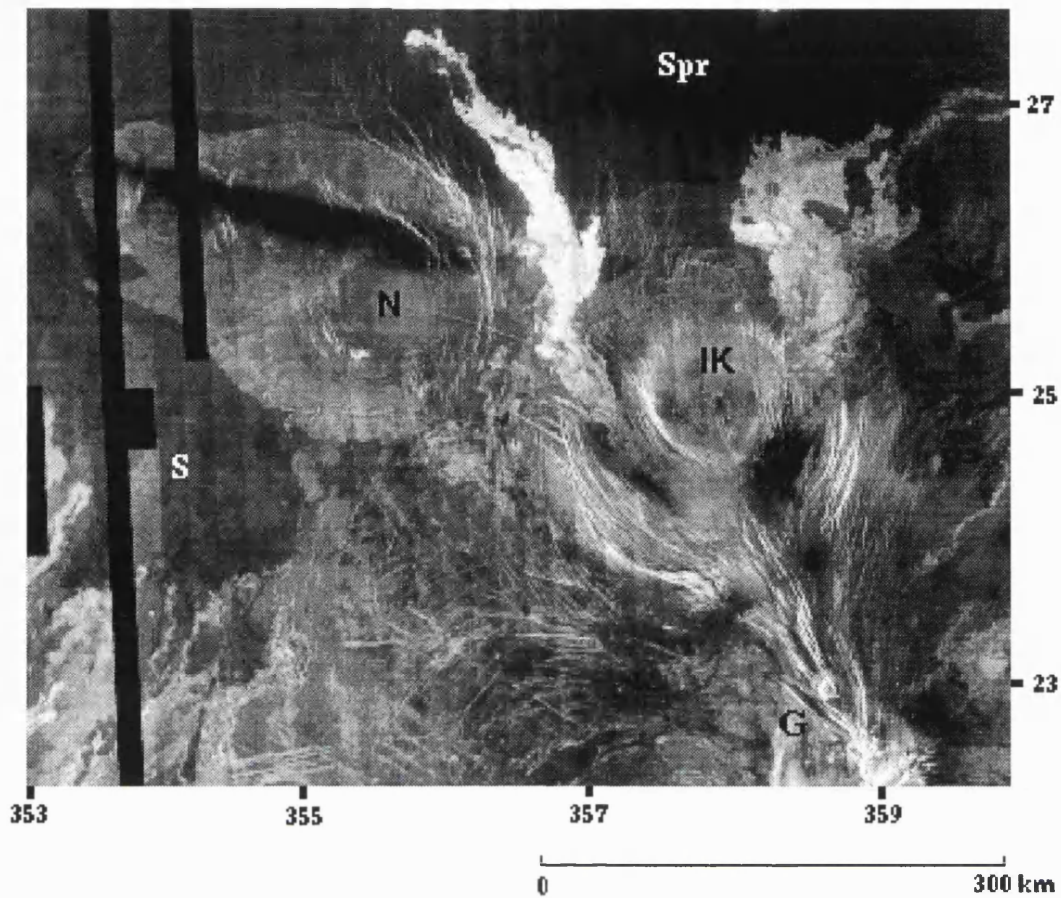
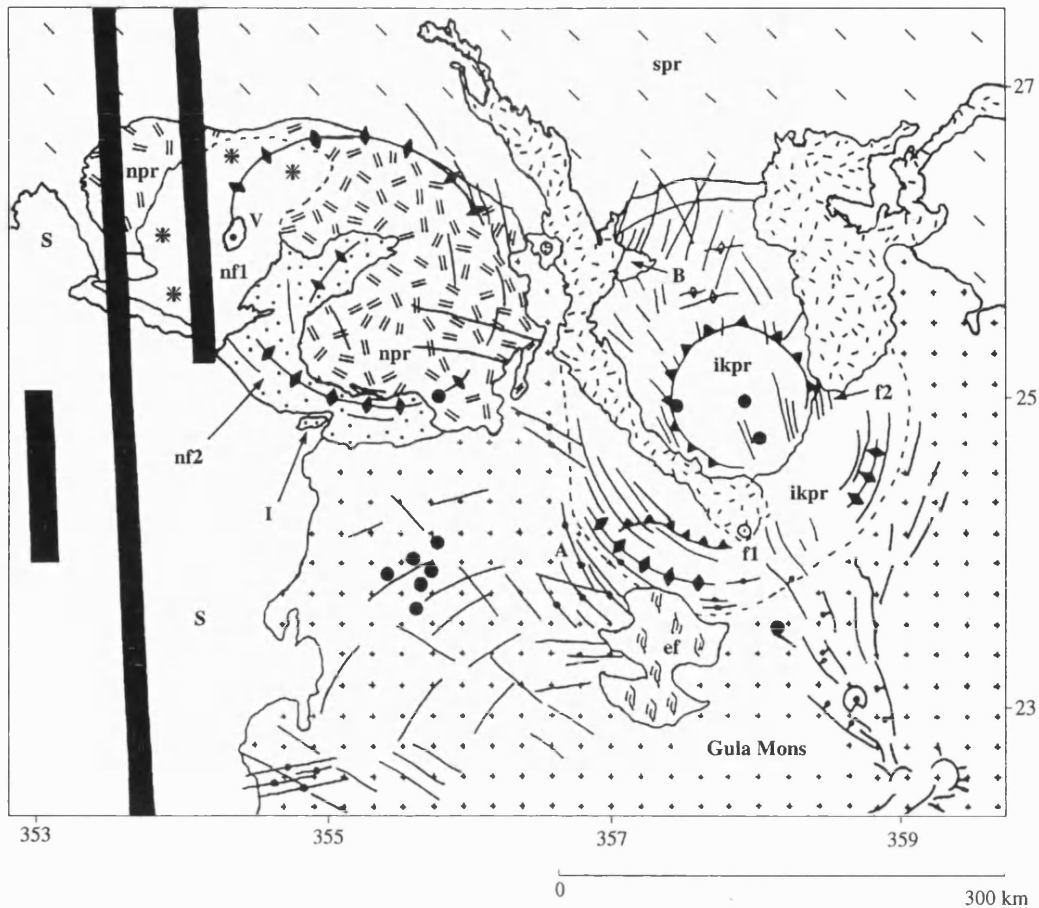


Figure 4.2 Magellan image of Idem-Kuva (IK) and Nissaba Coronae (N). Nissaba Corona shows little annulus deformation compared with Idem-Kuva. The southern annulus of Idem-Kuva cuts into, and hence postdates, the northern flank of Gula Mons (G). In the north, both coronae are embayed by local regional plains materials (*spr*). However, two flows with relatively strong radar backscatter (associated with Idem-Kuva) postdate the plains materials. S marks flow materials from Sif Mons (taken from C1-MIDR 30N351).



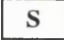



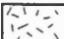

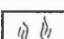

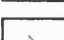



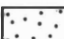



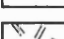

- | | | | |
|---|--|---|--|
|  | Sif Flow Materials |  | Graben |
|  | Gula Flow Materials |  | Volcanic Edifices <15 km |
|  | Idem-Kuva Flow Materials |  | Volcanic Edifices >15 km |
|  | ef - Edifice Field |  | Small scale fractures and ridges |
|  | spr- Sedna Regional Plains Materials |  | Large scale rim topography: Ridges |
|  | nf2 - Nissaba Flow Materials 2 |  | Scarp |
|  | nf1 - Nissaba Flow Materials 1 |  | Impact crater |
|  | ikpr - Idem-Kuva Relict Plains Materials |  | Approximate boundary of ikpr materials |
|  | npr - Nissaba Relic Plains Materials |  | Wrinkle ridges |

Figure 4.3 Sketch map of Idem-Kuva and Nissaba Coronae. The approximate boundary between Idem-Kuva relict plains materials (ikpr) and flow materials from Gula Mons is shown with a dashed line. Possible origins for the Idem-Kuva flow materials are marked f1 and f2. Graben at A are off-set from the main topographic deformation. Materials at B are interpreted as regional plains materials (spr). I indicates an inlier of Nissaba flow materials (nf2).

km across (Figures 4.4 and 4.5) (*Senske et al.*, 1992). The central domical region has a minor inner depression, the rim of which is delineated by narrow, radial graben. The highest part of the central rise is to the west, where a small central volcano (< 10 km in diameter) is situated (Figure 4.3). Two radar bright, digitate flows extend to the north of Idem-Kuva. The SW flow appears to originate from a small edifice situated at approximately 24.3° N, 358° E, while the eastern flow originates from graben located at approximately 24.5° N, 358.5° E (marked f1 and f2 respectively, Figures 4.2, 4.3 and 4.6).

The rim topography of Idem-Kuva (the large-scale concentric structure) consists of a well developed inner trough and ridge to the south, but only a very shallow inner trough and minor ridge to the north; it has no outer trough (Figures 4.4 and 4.5). The SW rim shows an inner 'terraced' topography which coincides with an annulus of arcuate graben concentric to the central mound of Idem-Kuva. The graben which form the annulus are prominent to the SW and SE, on the inner sloping margins of the corona's trough and, to a lesser extent, on the outer margin of the ridge. Some arcuate graben, associated with the SW annulus of Idem-Kuva, do not coincide with the larger scale topographic rim but are clearly offset outboard (marked A, Figure 4.3, and Figure 4.7). Furthermore, these graben have a different trend to the topographic rim. To the north of the central dome of Idem-Kuva, concentric graben are less pronounced and are considerably shorter (typically less than 25 km) with reduced widths in comparison to those to the SW and SE. The presence of arcuate graben which do not conform to the topographic rim of Idem-Kuva (marked A, Figure 4.3, and Figure 4.7), and the terracing of the SW rim on its inner side are interpreted as evidence of more than one phase of annulus formation.

The oldest materials of Idem-Kuva are relict upstanding plains materials (Idem-Kuva relict plains, *ikpr*, Figures 4.3 and 4.8). The relict plains are interpreted as either materials related to an early phase of volcanism associated with Idem-Kuva, or uplifted old plains materials which underlie younger regional

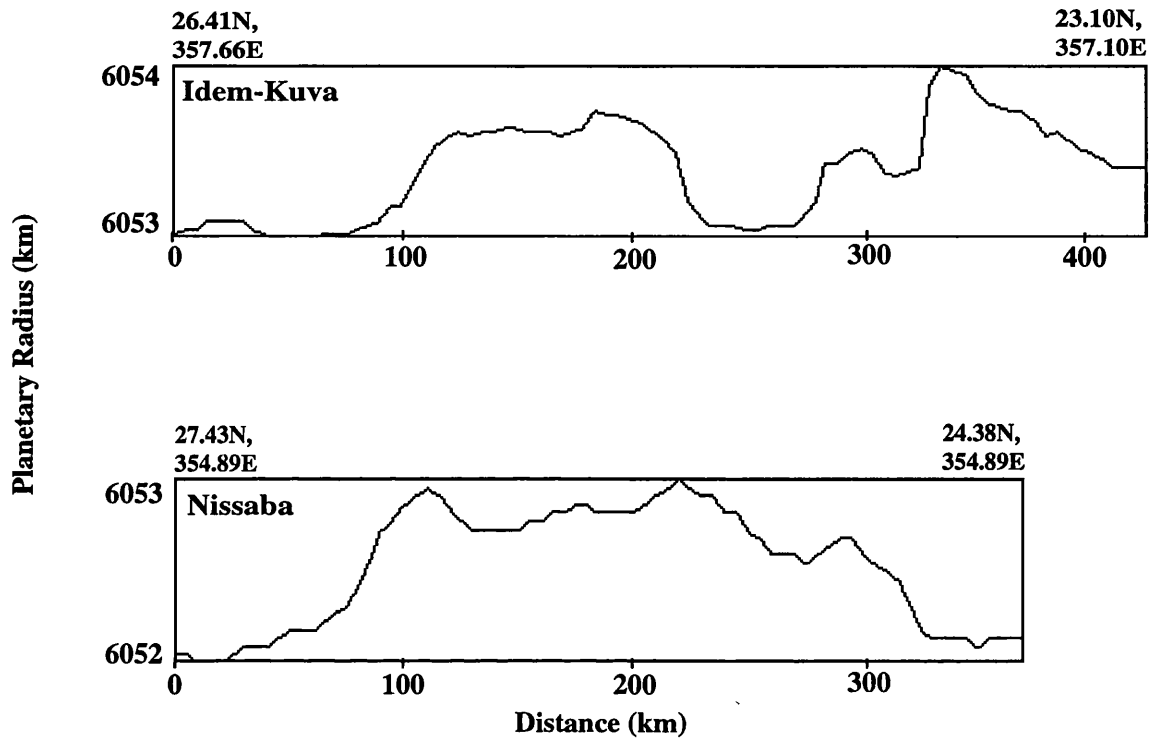
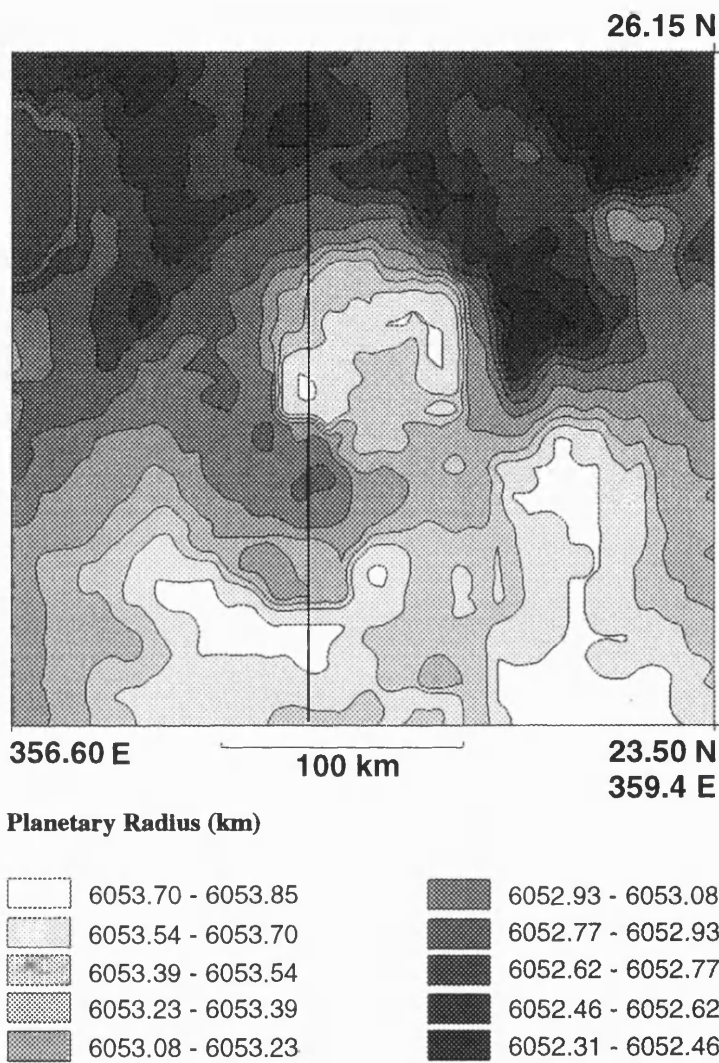


Figure 4.4 Topographic profiles of Idem-Kuva and Nissaba Coronae. These and other profiles were constructed from the Global Topographic Data Record (GTDR). Idem-Kuva has a prominent central rise while Nissaba has a central depression.



**Figure 4.5 Topographic map of Idem-Kuva Corona.
 Line corresponds to topographic profile in Figure 4.4.**

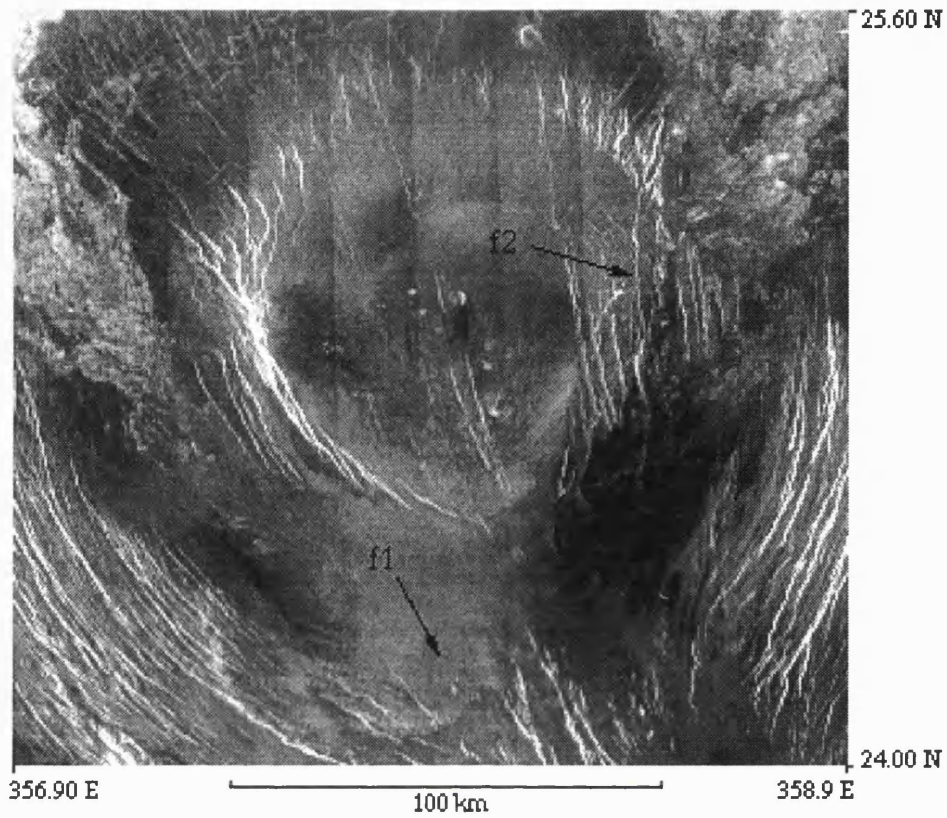


Figure 4.6 Interior of Idem-Kuva showing the location of the probable sources of flow materials *f1* (a volcanic edifice, arrowed) and *f2* (graben, arrowed). The image is centred on the interior upstanding dome seen in topographic data (F-MIDR.25N357;1 browse).

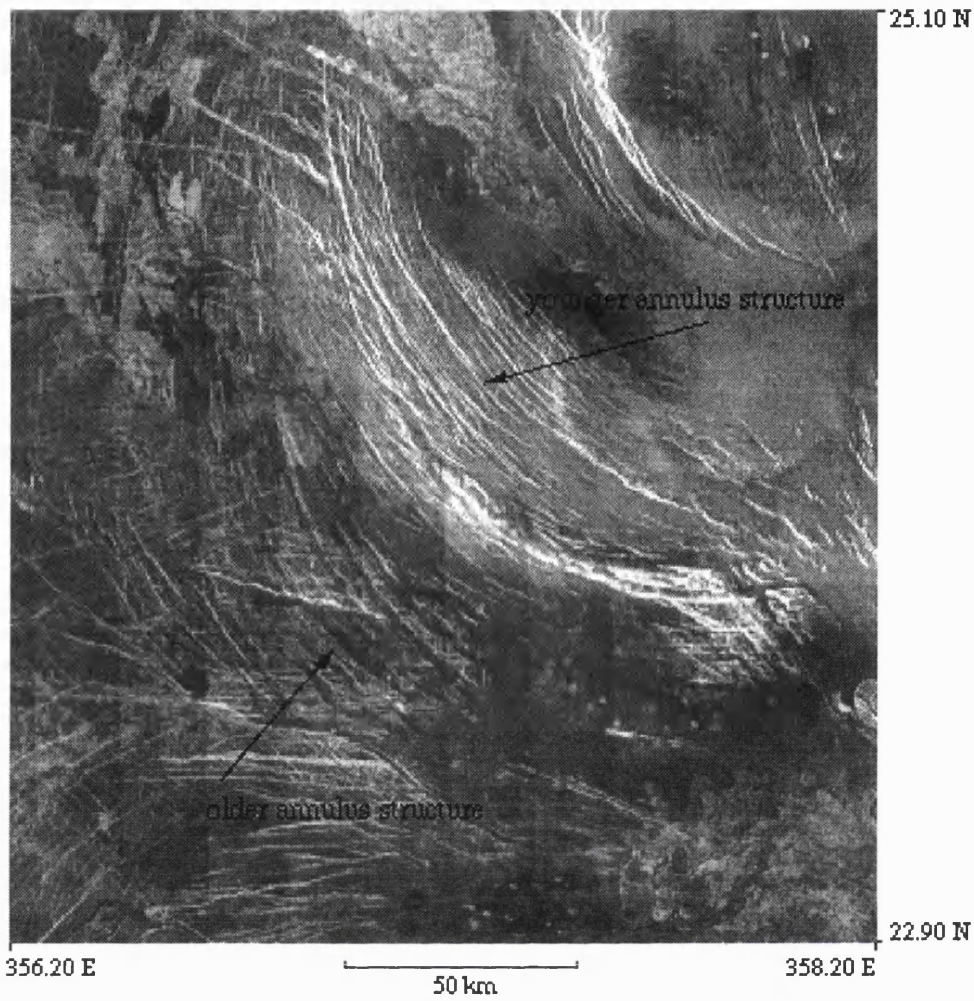


Figure 4.7 SW section of Idem-Kuva Corona. The image shows annulus structures (graben) which are the result of two distinct phases of deformation. The older structures are offset outboard and do not have the same trend as the large-scale topographic rim of Idem-Kuva (F-MIDR.25N357;1 browse).

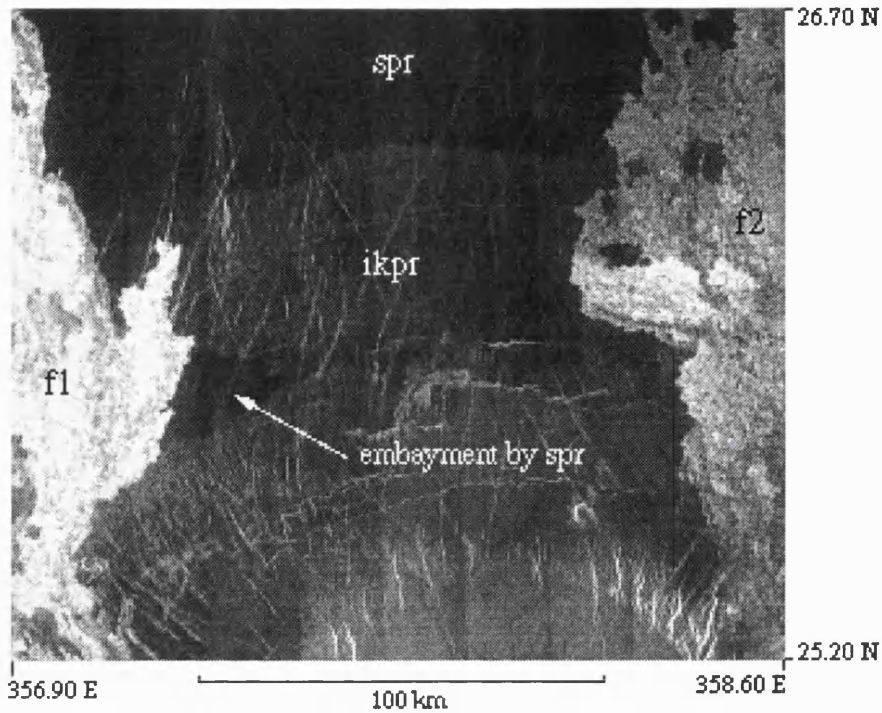


Figure 4.8 The northern section of Idem-Kuva Corona. Sedna regional plains materials (*spr*) embay Idem-Kuva relict plains (*ikpr*) which have undergone more deformation. The arrow shows Sedna regional plains materials which have breached the outer topographic rim structure. This material has flowed into, and is controlled by, the inner topographic trough of Idem-Kuva. The two radar-bright flow units associated with this corona are also labelled (*f1* and *f2*) (F-MIDR.25N357;1 browse).

plains materials (*Copp and Guest, 1995, 1997*). Three principal phases of deformation associated with corona formation have deformed the relict plains materials; the oldest is represented by arcuate graben forming the prominent SW and SE annulus. A second phase of deformation produced the closely spaced radial graben fabric to the NW of the central rise. This fabric postdates the concentric graben which form the annulus. Finally, an extensional fabric consisting of graben trend NW and NE, and are seen to cross each other. This fabric is interpreted to be the youngest, based on the observed cross-cutting relations.

Overlying on structures associated with the three sets of extensional structures are the two radar-bright flows, indicating that some volcanism has occurred after annulus formation at this corona. These two flows represent the most recent event in the formation of Idem-Kuva. The flows follow the topography of the corona, curving inwards to the north as they flow into the shallow northern annular trough, showing that the rim topography of Idem-Kuva had formed before this volcanism.

Relation with surrounding units

Idem-Kuva, has a complex stratigraphic relation with the regional plains materials. The northern edge of the corona displays a sharp contact with Sedna regional plains materials (unit *spr*, Figure 4.3) which overlie Idem-Kuva materials. Sedna regional plains materials (*spr*) breached the minor northern concentric ridge of the corona, resulting in partial flooding of the concentric trough on the NW side (marked B, Figure 4.3 and labelled in Figure 4.8). This flooding occurred after extensional tectonics deformed the Idem-Kuva relict plains materials (*ikpr*). Regional plains materials were subsequently overlain by two radar-bright flows from Idem-Kuva, indicating that the formation of Idem-Kuva both pre and postdate local plains materials (marked f1 and f2 in Figure 4.8).

As discussed previously, the southern topographic rim of Idem-Kuva is marked by a dense fabric of concentric graben (Figure 4.7). This fabric is seen to cut flows on the northern

margin of Gula Mons, clearly postdating them. This observation differs from Central Eistla Regio, where coronae apparently predate large volcanic edifices (McGill, 1994) Thus, contrary to observations made by Senske *et al.* (1992) and Senske and Stofan (1993), it is clear that Idem-Kuva, at least in part, postdates Gula Mons. Furthermore, graben interpreted to be related to Guor Linea cut the northern summit of Gula Mons and extend to the NW, where they merge with the annulus structure of Idem-Kuva. Hence, Idem-Kuva is considered, in part, younger than Gula Mons.

The above observations indicate that Idem-Kuva has a complex history, originating before and continuing after the emplacement of regional plains materials as well as materials on the north flank of Gula Mons.

4.2.2 Nissaba Corona.

Nissaba Corona (26° N, 355° E) lies directly NW of Idem-Kuva in Western Eistla Regio (Figure 4.2). The corona's topography is irregular in plan view, with a central circular plateau and smaller topographic high to the NW (Figures 4.4 and 4.9). The NW-SE axis measures approximately 320 km, with a N-S axis of 220 km.

To the west and SW, the central rise is surrounded by a trough, which shallows to the east. Outside the trough, to the SW, is a broad ridge which curves into the central region of Nissaba. The ridge is discontinuous around the corona. No outer trough is observed.

Nissaba shows less annulus deformation than Idem-Kuva, with the annulus again being defined by small-scale structures in comparison to the larger scale rim topography. The annulus only partly coincides spatially with the rim topography. A fine scale annulus fabric is seen in the vicinity of 25.3° N, 354.6° E as well as two long graben which cut flows on the southern margin (Figure 4.10). A later phase of deformation which may or may not be associated with annulus formation is represented by prominent, semi-concentric graben which occur along the east and NE margin

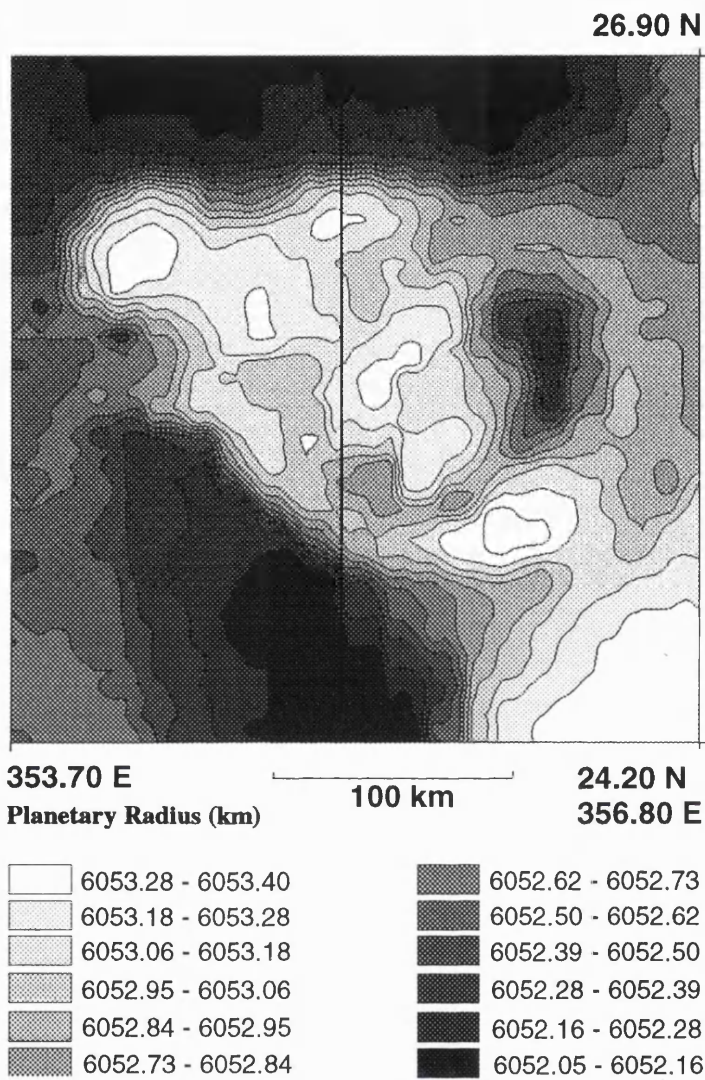


Figure 4.9 Topographic map of Nissaba Corona.
Line corresponds to topographic profile in Figure 4.4.

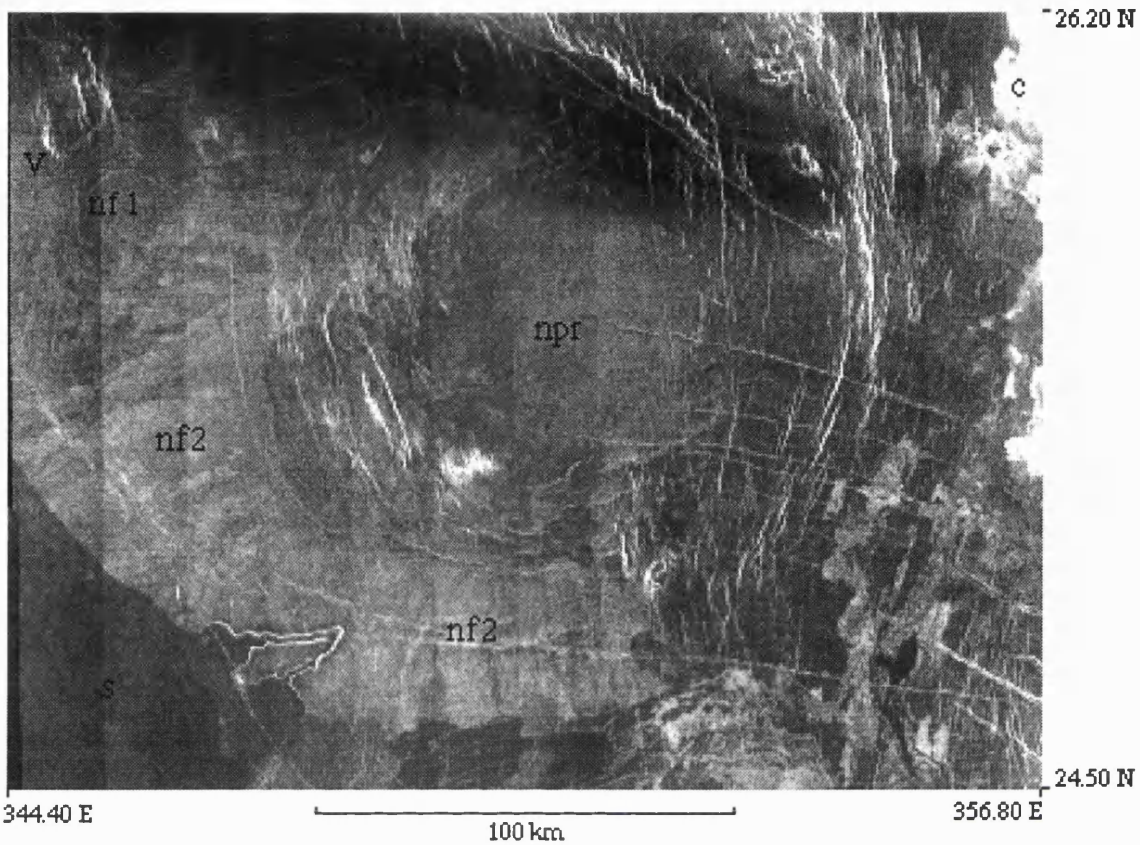


Figure 4.10 Nissaba Corona. The central area of Nissaba Corona consists of relict plains materials (*npr*). To the SW, flow materials (*nf2*) cover the large-scale topographic rim and are overlain by flow materials from Sif Mons (*s*). An earlier volcano (marked *V*) is responsible for an earlier flow apron (*nf1*). The dark streak at the top of the image is surficial materials associated with the crater marked *c* (F-MIDR.25N357;1 browse).

of Nissaba and extend into Sedna Planitia to the north.

An extensive apron of flows (Nissaba flow unit, *nf2* Figures 4.3 and 4.10) is seen on the west, SW and southern topographic rim of the corona. The flows originate from fractures that surround a circular depression within Nissaba. The flows are up to 100 km long and are radial to the central rise of the corona. A central volcano at 26.0° N, 354.5° E (marked V, Figure 4.10) has a radial, ill defined flow apron (*nf1*) which covers a significant portion of Nissaba's NW section.

As at Idem-Kuva, the oldest unit is plains material, seen within the corona (Nissaba relict plains materials, marked *npr*, Figures 4.3 and 4.10). Although considerably less deformed than the relict plains of Idem-Kuva, these materials are interpreted as having undergone a similar phase of initial uplift. The volcano (marked V, Figure 4.10) postdates the relict plains and is itself postdated by the more extensive apron of flows on the western and southern ridge. The flows which drape the western and southern ridge of Nissaba are interpreted as the youngest volcanic materials.

In summary, the annulus deformation is considerably less pronounced than that of Idem-Kuva. Its structures cut the southern and western flows and thus postdate them. The youngest features associated with Nissaba are the semi-concentric graben along the eastern and NE margin of the corona. The structures postdate not only the formation of the rim and annulus of Nissaba, but also the emplacement of the regional plains through which they cut. Volcanism has occurred throughout the history of the corona.

Relation with surrounding units.

The corona is embayed by local regional plains materials (which constitute Sedna Planitia) to the north, NW and NE. Embayment of Nissaba by the materials of Sedna Planitia suggests that at least part of the formation sequence of the corona began before the deposition of these plains material, or contemporaneous with it. On the basis of a similar mottled

appearance and deformational characteristics, it is considered that the Nissaba relict plains materials may represent an uplifted plains unit stratigraphically older than the regional plains materials which form extensive areas of Guinevere and Sedna Planitiae, described in Chapter 3 (*Copp and Guest*, 1995, 1997).

The south and SW ridge of Nissaba corona acts as a topographic barrier to Sif and Gula flow materials, and thus existed before emplacement of these flows. Furthermore, there is a small inlier of Nissaba material surrounded by Sif flow materials (marked *I*, Figure 4.3). To the SW, flows which erupted from fractures associated with Nissaba (*nf2*, Figure 4.3) are overlain by Sif Mons flow materials. However, at the southern margin of the corona, Nissaba flow materials have a more ambiguous relation with surrounding units. Some Nissaba flow lobes may postdate adjacent early Sif or Gula Montes materials, suggesting that Nissaba late-stage volcanism may postdate emplacement of some Sif and Gula materials.

Nissaba is cut by approximately E-W trending graben that are associated with Idem-Kuva. This places the formation of Nissaba before this later stage deformation of Idem-Kuva.

4.2.3 Benten Corona.

Benten Corona (Figure 4.11), 14.2° N, 341° E, is classified as an asymmetrical corona with extensive volcanism (*Stofan et al.*, 1992). On the basis of mapping presented here, the volcanic materials are divided into four distinct units. These are Benten flows 1, 2, and 3, and Benten edifice field materials, (labelled *bf1*, *bf2*, *bf3* and *bef* respectively in Figure 4.12). The corona has a kidney shaped interior with a maximum diameter of 320 km, and is partly surrounded by a prominent broad outer arcuate ridge on its eastern and NE margin. The annulus of compressional ridges is dominantly on the inward facing slope of the broad arcuate ridge (Figure 4.12).

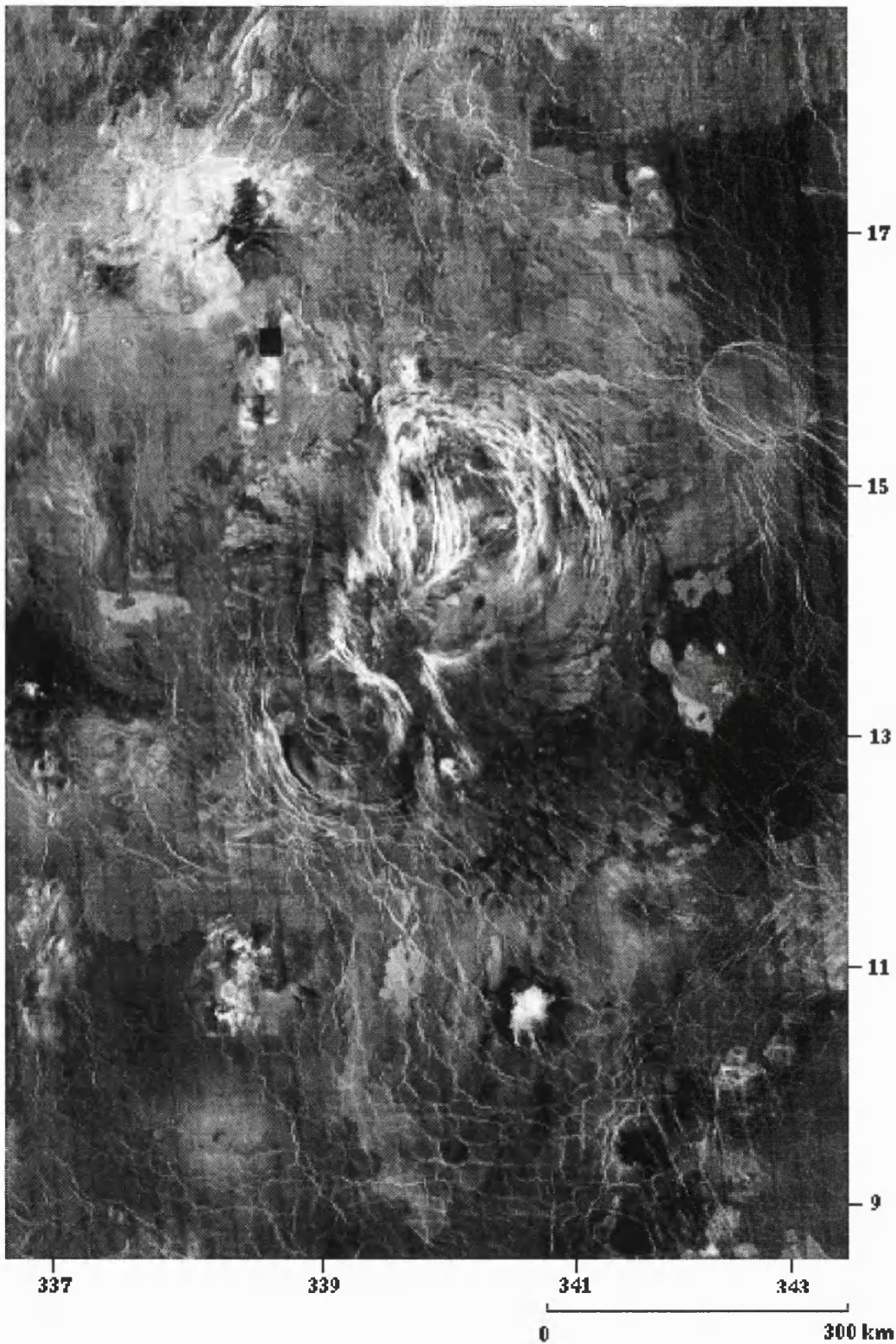


Figure 4.11 Magellan image of Benten Corona and associated flow materials. The circular feature at the top of the image is Chiun Corona (portion of C1-MIDR 15N335).

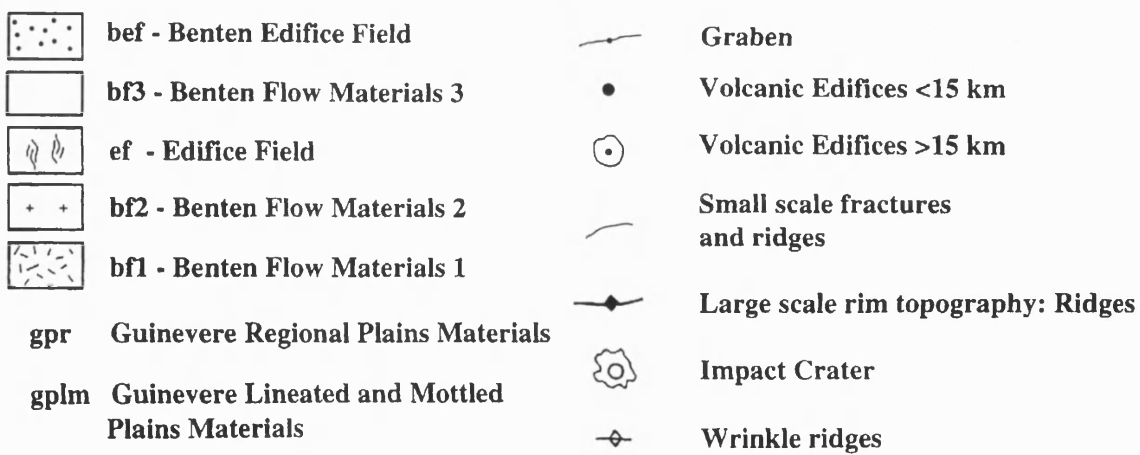
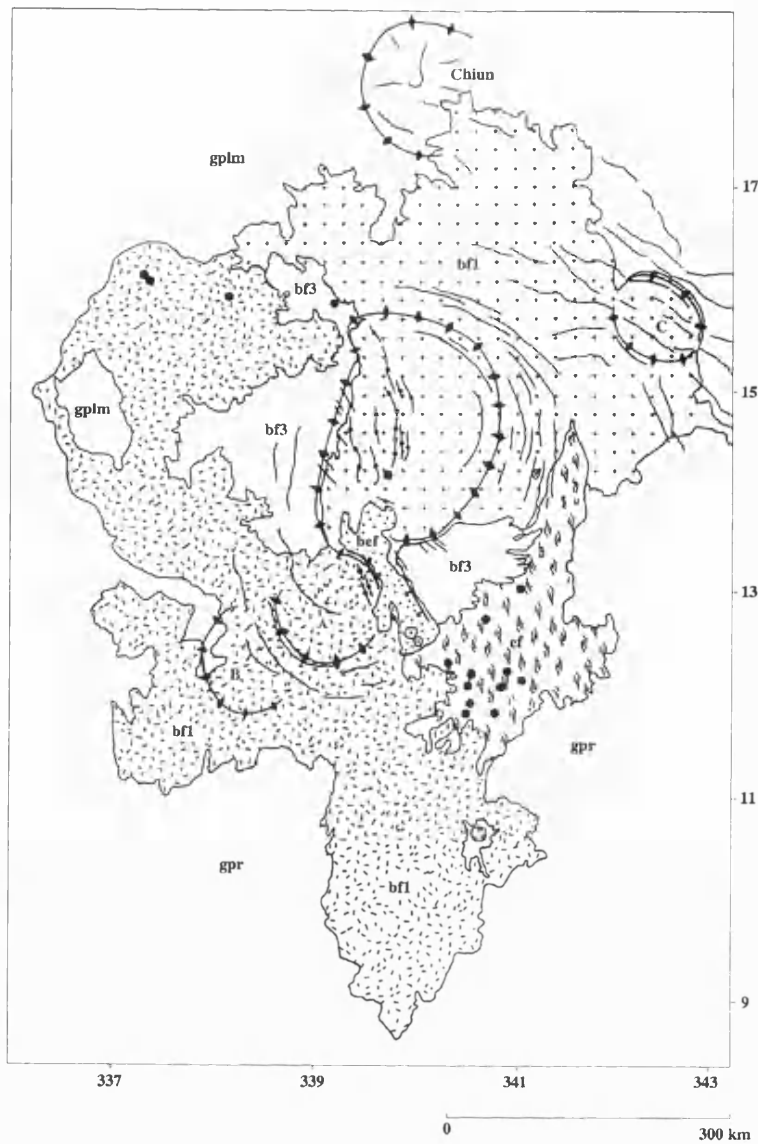


Fig. 4.12 Sketch map of Benten Corona. A, B and C mark the location of smaller coronae mentioned in the text. Three distinct flow units are associated with Benten Corona.

The southern end of the arcuate ridge terminates at the edge of a flooded graben which is 50 km wide and at least 110 km long. The margins of the graben are delineated by a series of smaller NW-SE trending graben. The corona's western margin is composed of a linear ridge trending NNE cross-cut by numerous graben oriented radially to the corona. Bente lacks a prominent outer trough (Figures 4.13 and 4.14).

The interior of Bente is an irregular hollow which is lower than the outer arcuate ridge of the corona, but at a greater elevation than the surrounding plains (Figures 4.13 and 4.14). The floor of the hollow is undulating and deformed by an extensive N-S trending graben system (Figure 4.15). These graben are partly embayed by the Bente edifice field unit (*bef*, Figures 4.12 and 4.15) at the southern margin of the central depression. To the SE, Bente edifice field materials are topographically confined within the large graben. No evidence of early stage radial deformation is observed at Bente Corona.

The formation of Bente is interpreted to have begun with substantial volcanism. Two of the three principal flow units, Bente flow 1 (*bf1*) and Bente flow 2 (*bf2*), are interpreted to be the consequence of early voluminous phases of volcanism occurring before or coeval with the formation of the annulus, because the annulus and topographic ridge deform both of these flow materials. Bente flow 2 materials form the northern interior floor of Bente. After the formation of the annulus, a third less extensive phase of volcanism resulted in the emplacement of digitate flows (Bente flow 3, *bf3*) to the east and west of Bente. *Bf3* materials are inferred as the youngest of the three exterior flow units. They overlie the annulus structure, and are topographically controlled by the large scale ridge. The flows come from relatively young radial graben located on the western and SE margins the corona. The Bente edifice field unit postdates *bf3* and is interpreted as the youngest unit.

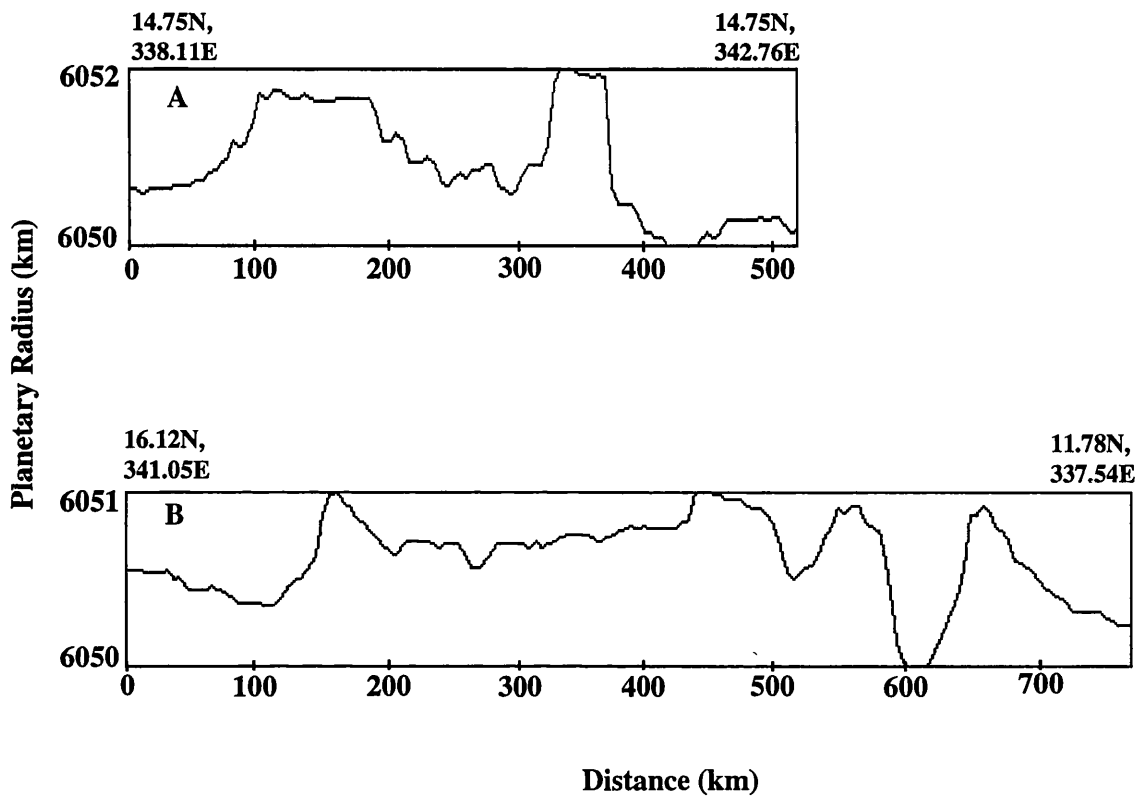
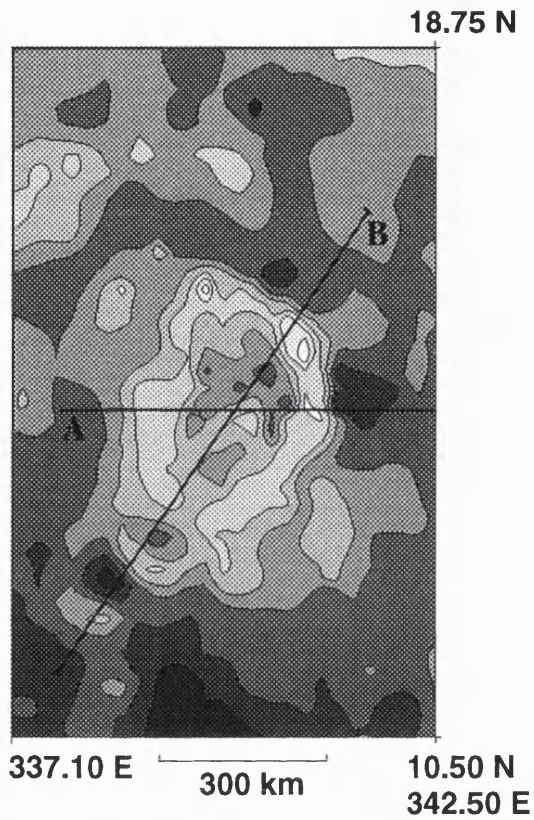


Figure 4.13 Topographic profiles of Benten Corona. Profile A shows an E-W section highlighting Benten's central depression and prominent eastern ridge topography. Profile B also shows the central depression and the two smaller coronae to the SW marked A and B in Figure 4.12.



Planetary Radius (km)

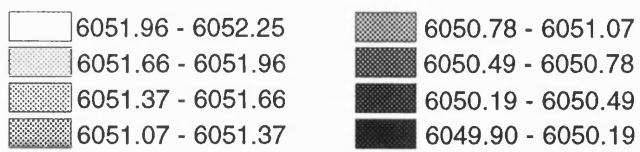


Figure 4.14 Topographic map of Benten Corona. Lines A and B correspond to topographic profiles A and B in Figure 4.13.

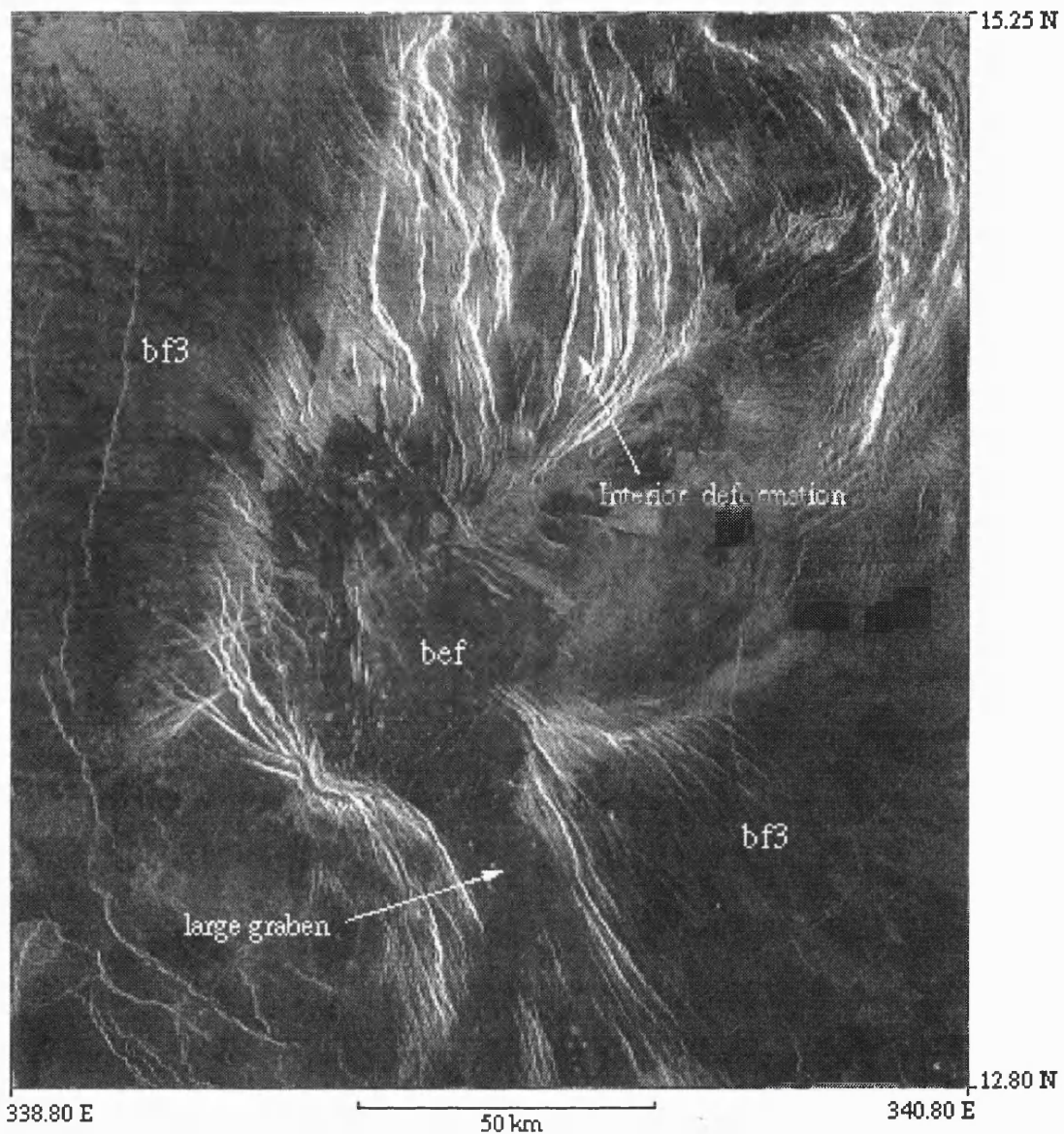


Figure 4.15 Central region of Benten Corona. The interior structure is mainly graben which have been embayed by flow materials from an edifice field (*bef*). The flows from *bef* flood the large NW-SE trending graben. In the SE and NW corners of the image, *bf3* flows are seen (F-MIDR.15N340;1 browse).

Relation with surrounding units

The large-scale flow units associated with Benten Corona (*bf1* and *bf2*) are superimposed on the regional plains materials of Guinevere Planitia (unit *gpr*, Figure 4.12) to the south, and older Guinevere lineated and mottled plains (unit *gplm*, Figure 4.12) to the NW. The flows also overlie *gplm* materials to the NW, for example in the vicinity of 16° N, 337° E. To the SW of Benten lies an extensive edifice field, with numerous edifices and associated flow materials. Flows from the edifice field are superimposed on Benten flow 1 materials, but are overlain by Benten flow 3 materials.

Topographic data show four smaller coronae (all less than 150 km in diameter) near Benten Corona (Figure 4.12, marked Chiun Corona, and unnamed coronae A, B and C). The largest of the these coronae, Chiun, lies to the north and has a diameter of 130 km. It has a depressed interior. Corona A has an ovoid shape with a prominent SW topographic rim in the form of a ridge. This ridge displays less deformation than the main ridge of Benten; the deformation is mainly confined to the outer facing slope.

Chiun, and the three smaller coronae, may or may not be related to Benten. However, Chiun must have existed prior to the extrusion of Benten flow 2 materials, since they embay Chiun deformational structures. In contrast, the unnamed corona deforms Benten flow 2 materials thus post dating them.

The observations indicate Benten flow materials are younger than the surrounding plains materials which constitute Guinevere Planitia. Whether Benten Corona began forming before the regional plains of Guinevere Planitia is not known; older units may have been subsequently covered by younger plains materials. Flow units associated with Benten Corona record a sequence indicative of varying amounts and styles of volcanic activity with time. The style of volcanism has changed from voluminous flood lavas to a less extensive digitate flow morphology with a variable backscatter, similar to the sequence observed at other coronae (*Stofan and Smrekar, 1996*). The changing style and magnitude of volcanism is indicative of a gradual depleting of the magma

reservoir.

4.2.4 Heng-o Corona.

Heng-o Corona in southern Guinevere Planitia (2.0° N, 355.5° E) is the second largest corona on Venus with a mean diameter of 965 km. It was originally classified as an older, isolated corona with a medium amount of associated volcanism (*Stofan et al.*, 1992, 1997). Heng-o extends from the V31 quadrangle into the V43 quadrangle to the south (*Greeley et al.*, 1994).

Heng-o is approximately circular in plan view and has varying amounts of deformation around its margin (Figures 4.16 and 4.17). The simplest large-scale rim structure is on the western side. Here the large-scale rim topography is composed of a ridge, which has little elevation above the floor of the corona (typically less than 600 metres) and which has a narrow band (typically 12 km across) of lineations along the summit. No inner or outer trench is observed here.

The southern topographic rim is a double ridge and trough (Figures 4.18 and 4.19). The outer ridge displays an annulus of two sets of intersecting graben (Figure 4.20). Both sets terminate at the summit of the outer ridge and are not seen within the troughs. The double ridge and trough topography and associated cross-latticed graben annulus decrease to the west and NW along the margin. To the east and SW, fragments of old embayed graben and ridge structures are observed (Figure 4.17, marked A and B, and Figure 4.21).

The northern rim topography is demarcated by a prominent ridge with an inner and outer trough (Heng-o Chasma, Figures 4.18, 4.19 and 4.22). Annulus deformation in the form of compressional ridges is concentrated approximately half way up the north facing flank of the ridge. Continuing up the ridge, narrower concentric ridges are observed. The main ridge rises approximately 1 km above the local topography. The crest of the ridge displays another fabric which is made up of thin lineations oriented radially to the corona.

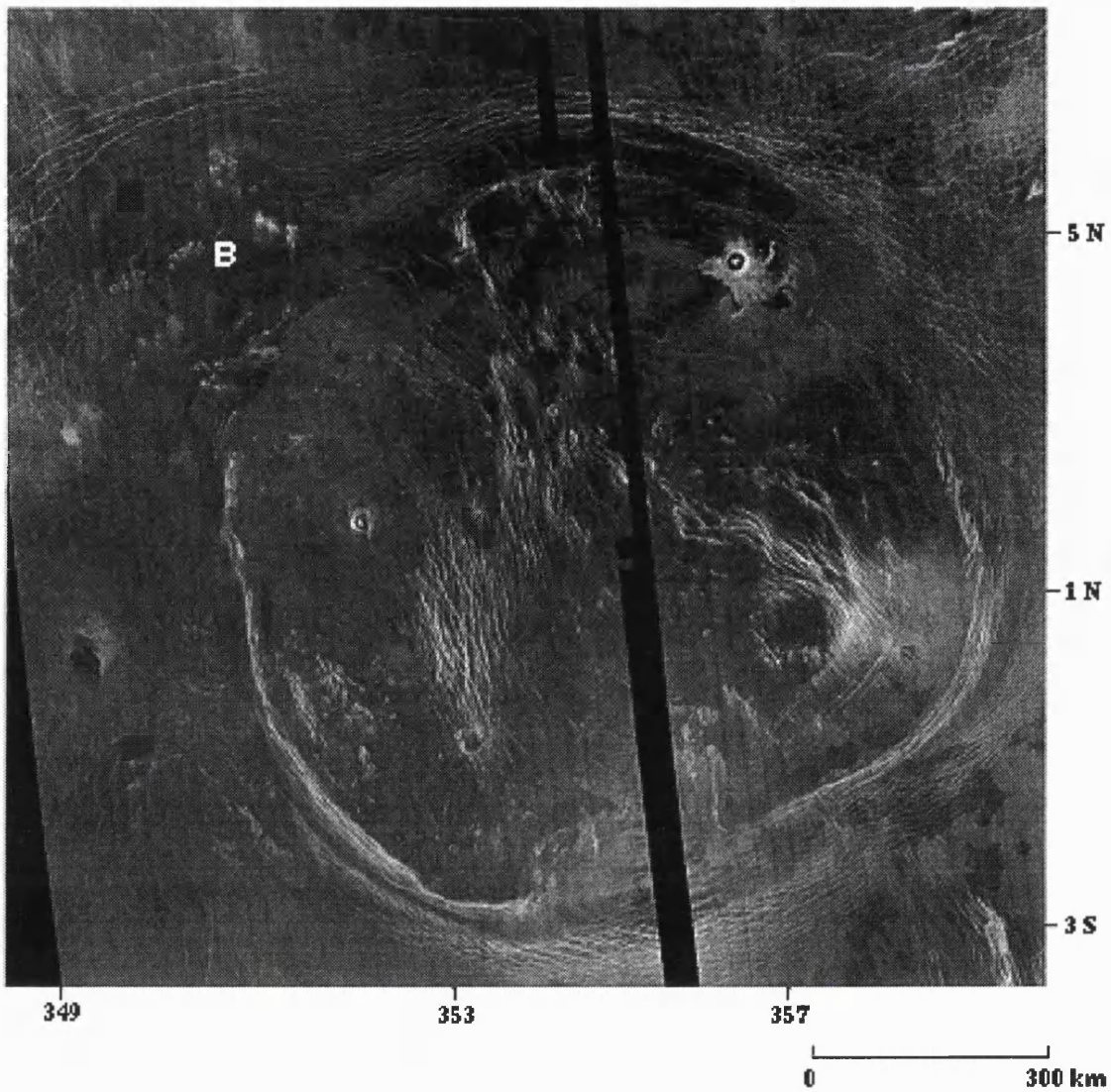


Figure 4.16 Magellan image of Heng-o and Beltis Coroneae (B). The topographic rim of Heng-o deforms the local regional plains. An extensive flow field lies to the west and is thought to originate from Beltis Corona (to the NW of Heng-o) and the western annulus of Heng-o. Three volcanic centres of different ages lie within the annulus of Heng-o (portion of C1-MIDR 00N352).

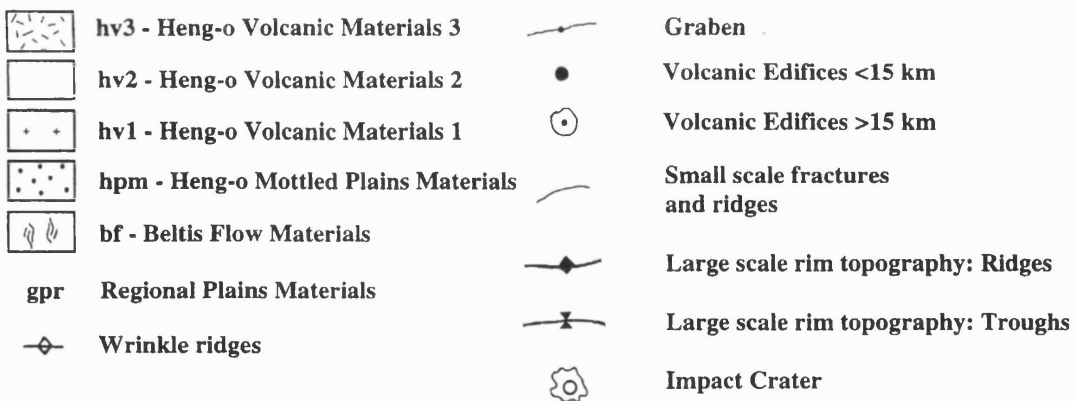
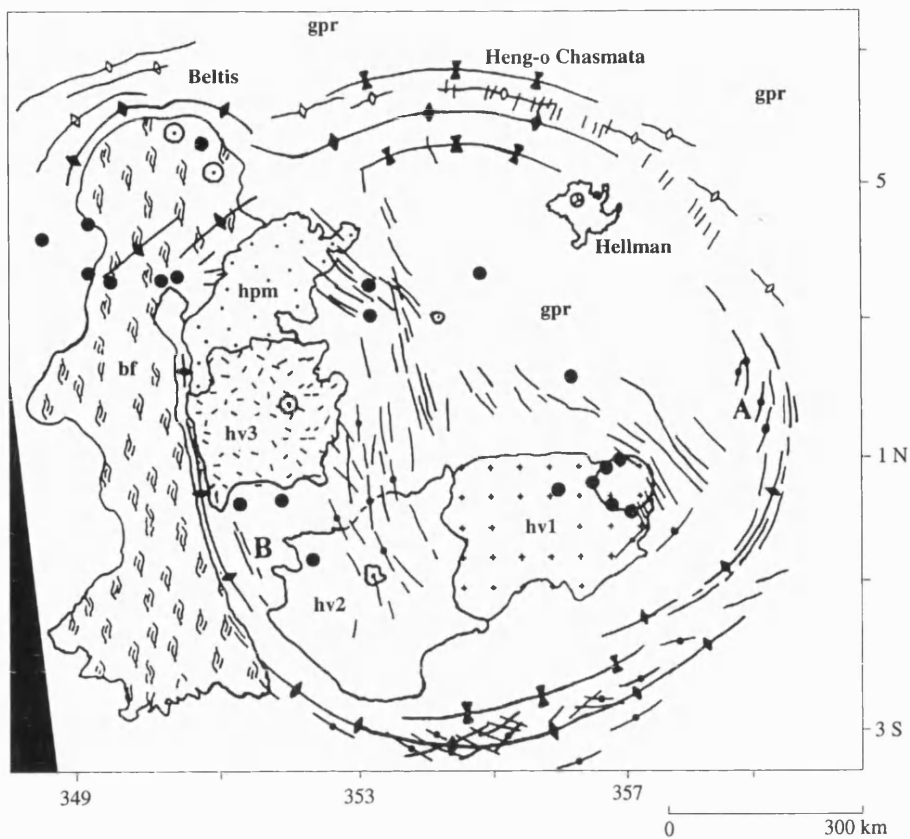


Fig. 4.17. Sketch map of Heng-o and Beltis Coronae. The interior of Heng-o Corona has three distinct volcanic centres. A and B indicate areas of older deformation which may be representative of an older annulus-forming event.

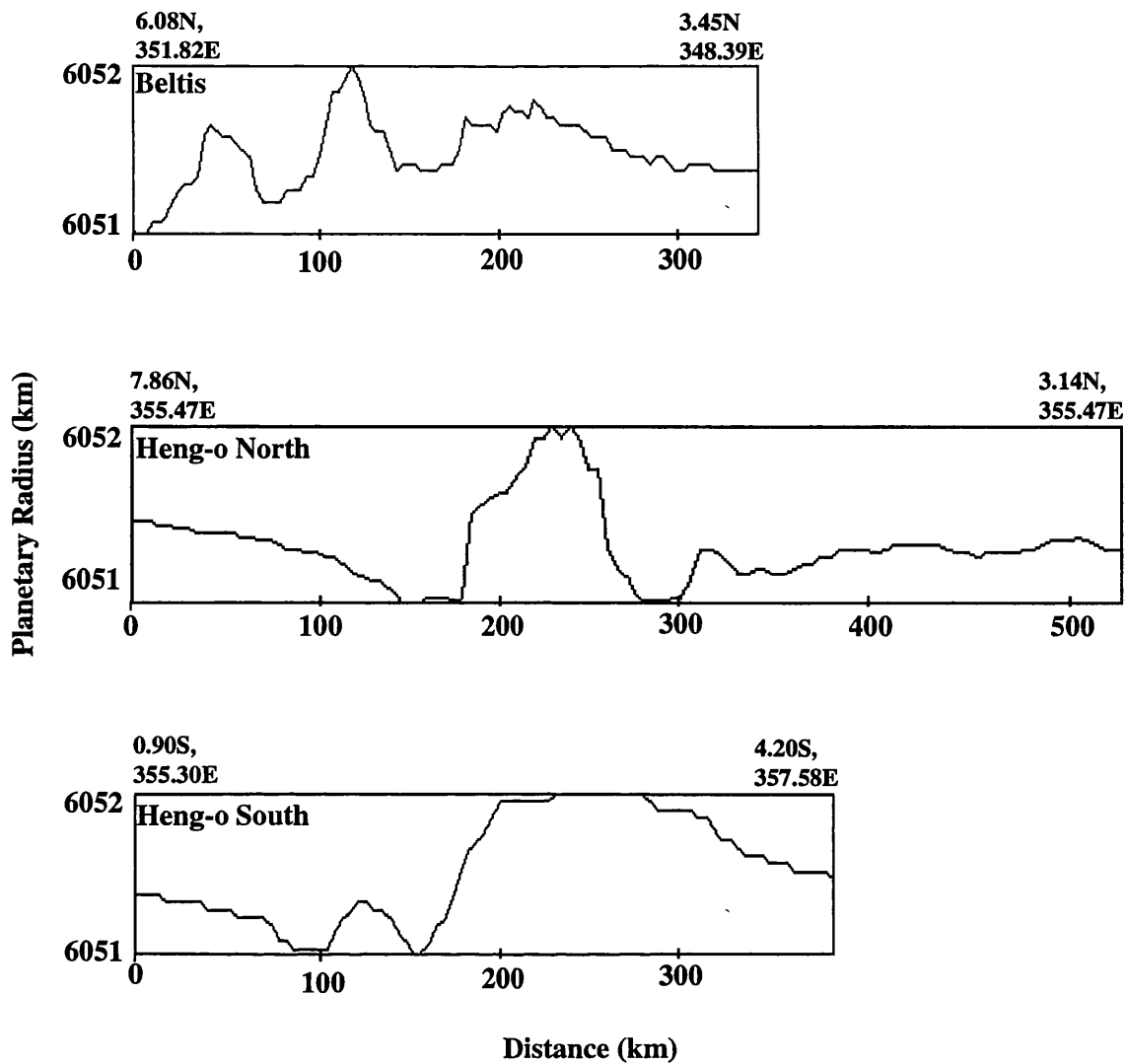


Figure 4.18 Topographic profile of Beltis Corona and the northern and southern rim of Heng-o Coranae. Beltis Corona shows a complex interior topography. The northern rim of Heng-o displays both an outer and inner trough while the southern rim topography of Heng-o shows two inner troughs separated by a ridge.

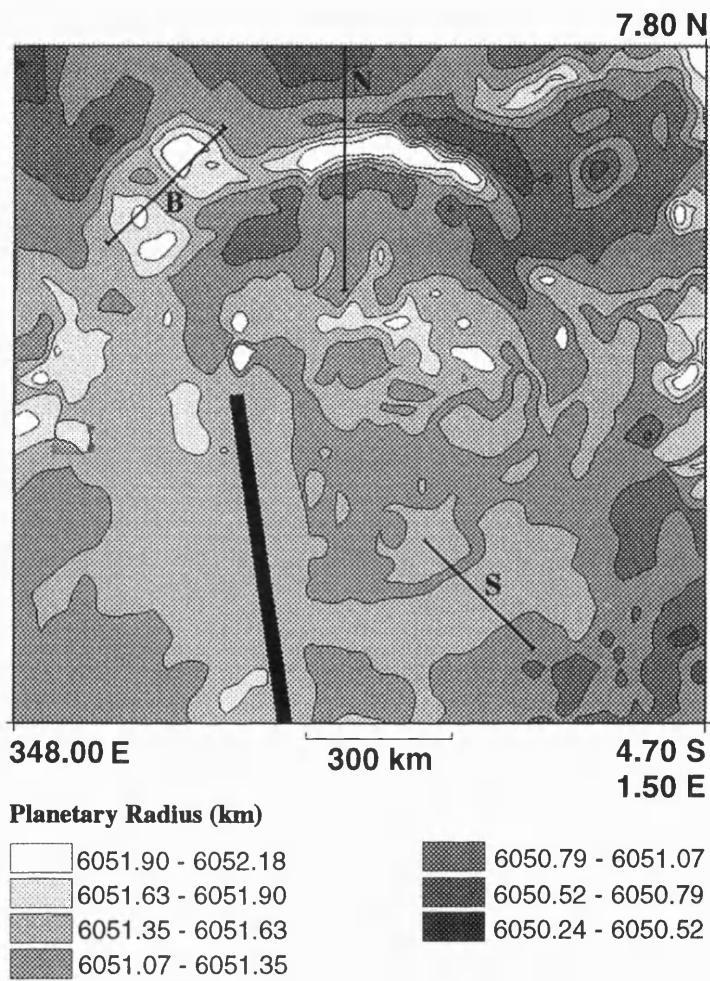


Figure 4.19 Topographic map of Heng-o and Beltis Coroneae. Topographic profiles are marked by lines. N, S correspond to the northern and southern section of Heng-o Corona and B to Beltis Corona, see Figure 4.18.

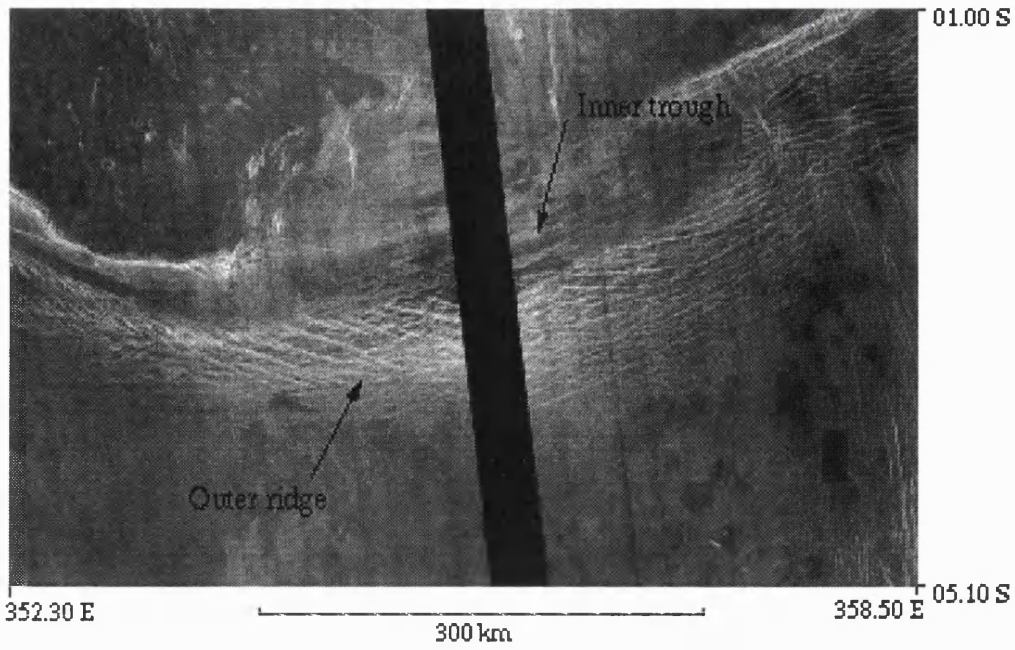


Figure 4.20 Image showing the southern margin of Heng-o Corona. The corona shows a marked inner and outer trough with crossing annulus structure which coincides with the outer rim topography. Figure 4.18 shows the topography along a cross-section take through this area (C1-MIDR).

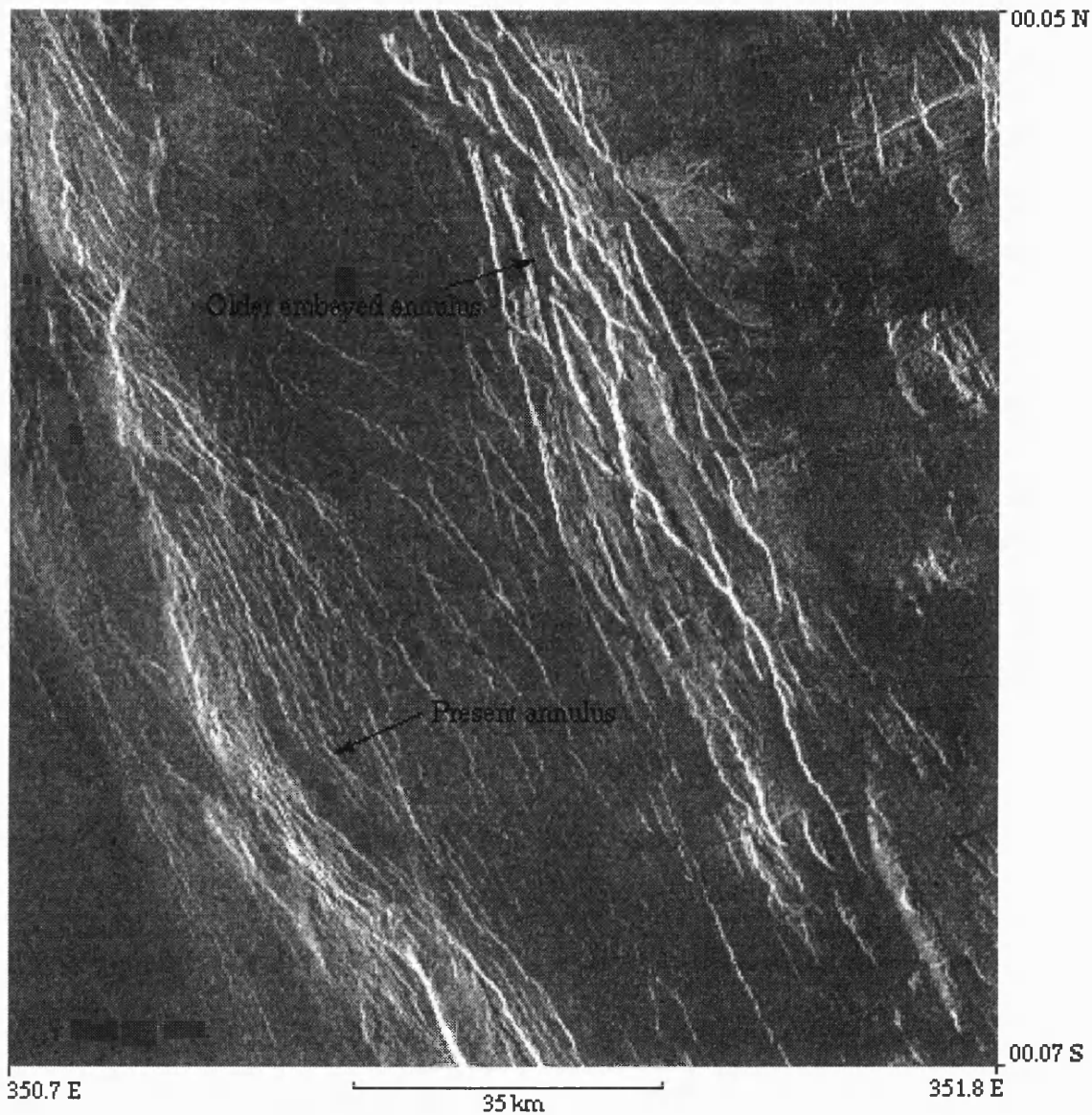


Figure 4.21 Two phases of annulus deformation are seen at the SW rim of Heng-o Corona. The inner annulus structures represent an earlier phase of deformation, and have subsequently been embayed. The outer structures are considered to represent a later phase of annulus deformation. It is considered from this observation that coronae may have a protracted history, with more than one phase of annulus formation (C1-MIDR00N352;1 framelet 28).



Figure 4.22 The northern rim of Heng-o Corona. The concentric wrinkle ridges form the annulus of Heng-o and are situated on the outer northern slope of the large-scale topographic rim (Heng-o Chasma). The rim topography and annulus deform the regional plains materials, hence the corona is considered relatively young (C1-MIDR.00N352;1 browse).

A number of volcanic centres lie within the rim of Heng-o, including central volcanoes, and small shields and cones. There are three major central volcanoes (Heng-o volcanic centres, 1, 2, and 3, labelled *hv1*, *hv2* and *hv3*, Figure 4.17). *Hv1* is an edifice at least 100 km across with a 60 km diameter caldera deformed by intense NW trending graben. Associated with this volcano are clusters of small shields. *Hv1* materials are overlain by flows from *hv2* (Figure 4.17) which itself is cut by NNE trending fractures. These fractures formed after the set which trend NW, and cut *hv1* materials. Both fracture sets are oriented obliquely to the rim and annulus and do not parallel regional plains structure. *Hv3* has a prominent apron of flow materials, the distal margins of which are superimposed on the fractures that cut the volcano *hv2*.

From observations, the stratigraphy of Heng-o involves a number of phases of volcanism and deformation, but the bulk of the corona appears to be composed of regional plains materials. Heng-o volcanic centre 1 is interpreted as the oldest volcanic unit (*hv1*, Figure 4.17). *Hv2* formed next, followed by *hv3*; each phase of volcanism probably overlapped in time. The two belts of deformation which cut *hv1* and *hv2* are oblique to and do not cut the rim topography of Heng-o, hence it is difficult to establish their relation to Heng-o.

How do the above phases of volcanism relate to the annulus and topographic rim formation of Heng-o? The large volcano *hv1* situated in the SE quadrant of the corona apparently formed during the early stages of corona formation, since it is deformed by graben confined within the corona. An age relation between *hv1* materials and the annulus cannot be established since they do not coincide. The SW margin of materials associated with volcano *hv2* appear to be topographically controlled by the rim of Heng-o. The western volcano *hv3*, appear to have flows which bank up against the western ridge, hence postdating its formation.

Relation with surrounding units

Heng-o is relatively rare among coronae in that it occurs distant from chasmata or large topographic rises (*Stofan et al.*, 1997). The relation that the rim of Heng-o has with the surrounding materials is critical in establishing its stratigraphic position. To the north and south it is possible to trace regional Guinevere plains materials (unit *gpr*, Figure 4.17) over the rim topography inward towards the centre of the corona; the rim topography clearly deforms the plains materials, and hence is younger at these locations. Older structures proximal to the main rim topography are concentric and are embayed by regional plains materials (Figure 4.17, A and B, and Figure 4.21). These materials are interpreted to represent an earlier annulus at Heng-o, suggesting that, as at Idem-Kuva, more than one phase of annulus formation has occurred. While some minor volcanism associated with *hvl* postdates the regional plains, the age relation between the plains and *hvl* is obscured by dense fracturing which cuts both units.

The northern rim topography described above terminates to the NW at a smaller corona. Averaging 375 kilometres in diameter, Beltis Corona (provisional IAU name) is defined by semi-circular rim topography in the form of a ridge. The rim topography lacks annulus deformation. The floor of Beltis is undulating (Figure 4.18) and displays a number of different styles of volcanism including calderas and numerous small edifices. Volcanic deposits extend from Beltis Corona (*bf*, Figure 4.17) to the NW margin of Heng-o. The flows postdate the regional plains materials and are topographically controlled by the western rim topography of Heng-o. However, it is apparent that structures associated with the SW margin of Heng-o have cut the flow materials and hence postdate them. This represents further evidence for multiple stage annulus formation at Heng-o.

While it is not possible to precisely establish the earliest phase of the development of Heng-o, it is apparent that the present topographic rim and annulus are younger than previously suggested (*Sandwell and Schubert*, 1992). As with the other

coronae in this study, Heng-o has a complex structural and volcanic history rather than representing a discrete event in time.

The style of interior volcanism has remained constant over time, i.e. three phases of volcanism have each produced an edifice with associated flow materials. This is in contrast to the evolution in volcanic style seen at other coronae (e.g. Benten Corona).

4.2.5 Silvia Corona

Silvia Corona (provisional IAU name), 12.5° N, 355.5° E (Figures 4.23 and 4.24) has a mean diameter of 300 km and is approximately circular in plan view. The corona has a prominent northern and southern topographic rim in the form of ridges (Figures 4.25 and 4.26). Lower topographic ridges are observed to the east and west; no internal or external trough is observed. The interior stands higher than the regional plains and has a highly irregular undulating topography (Figures 4.25 and 4.26). Interior materials have a mottled appearance in the radar image. Weakly defined concentric fractures coincide with the northern and NW rim topography.

In contrast to the other coronae studied here, no corona related volcanism is seen superimposed on regional plains material and little evidence exists for any interior volcanism, except for a few small (< 10 km) calderas. However, it is conceivable that any early stage volcanism has been superimposed by the surrounding regional plains. No prominent early interior deformation is observed. The interior is interpreted as older plains materials which have been uplifted prior to the formation of the topographic rim by which they are deformed. The regional plains which surround the corona embay the older internal materials and are also deformed by rim topography (Figure 4.23). A number of wrinkle ridges which are pervasive throughout the regional plains are seen to cross part of the western margin of Silvia and hence are presumed to have formed after or contemporaneously with the corona rim (McGill, 1994).

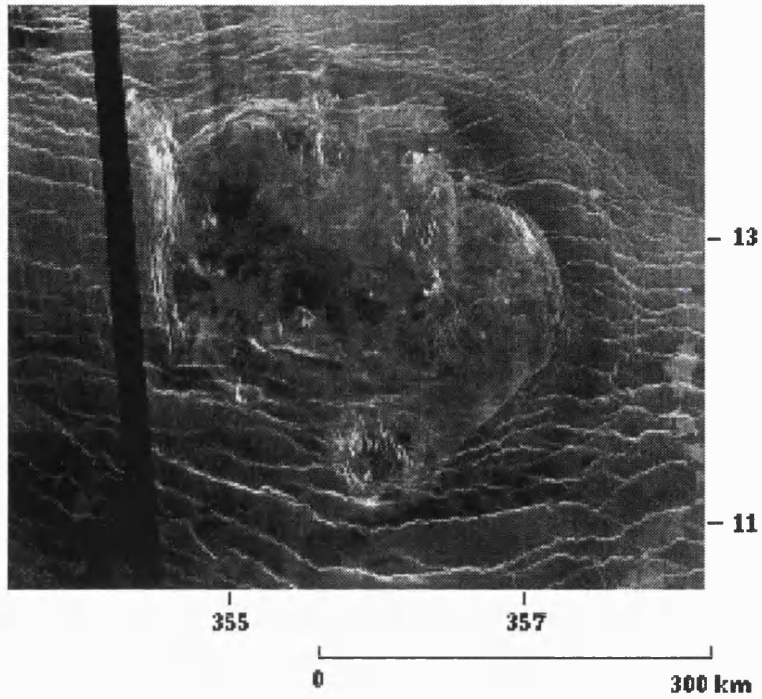
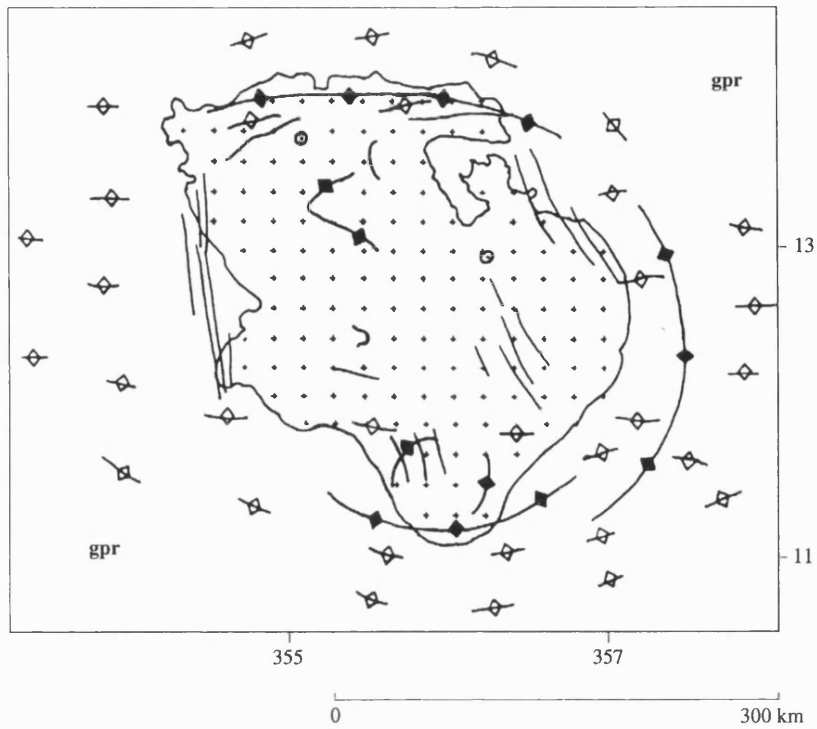


Figure 4.23 Magellan image of Silvia Corona. The interior of the corona is composed of elevated relict plains which have been embayed by the younger regional plains. Little volcanism is associated with the formation of the corona (portion of C1-MIDR 15N352).



- | | |
|--|------------------------------------|
| Silvia Relict Plains Materials | Volcanic Edifices <15 km |
| gpr Guinevere Regional Plains Materials | Volcanic Edifices >15 km |
| Wrinkle ridges | Small scale fractures and ridges |
| | Large scale rim topography: Ridges |

Fig. 4.24 Sketch map of Silvia Corona. The centre of the corona is interpreted as older relic plains materials. Silvia Corona lacks small scale annulus structures and volcanism.

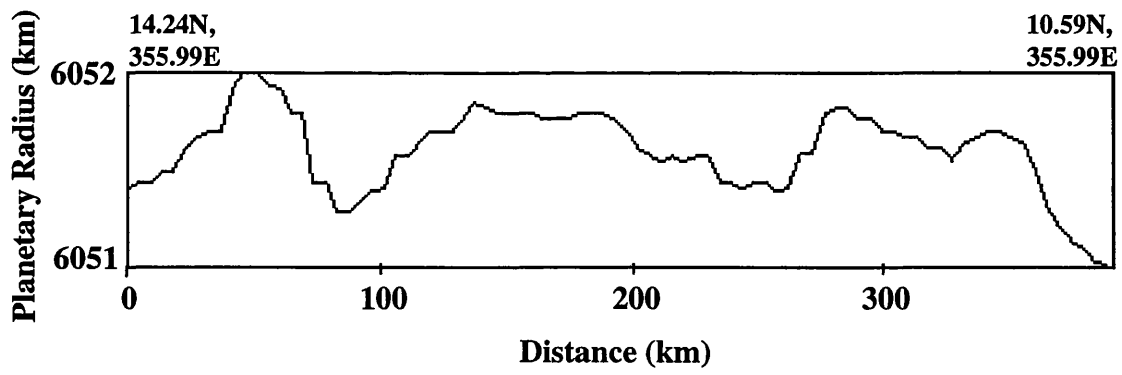


Figure 4.25 Topographic profile of Silvia Corona. The corona interior is higher than surrounding regional plains materials.

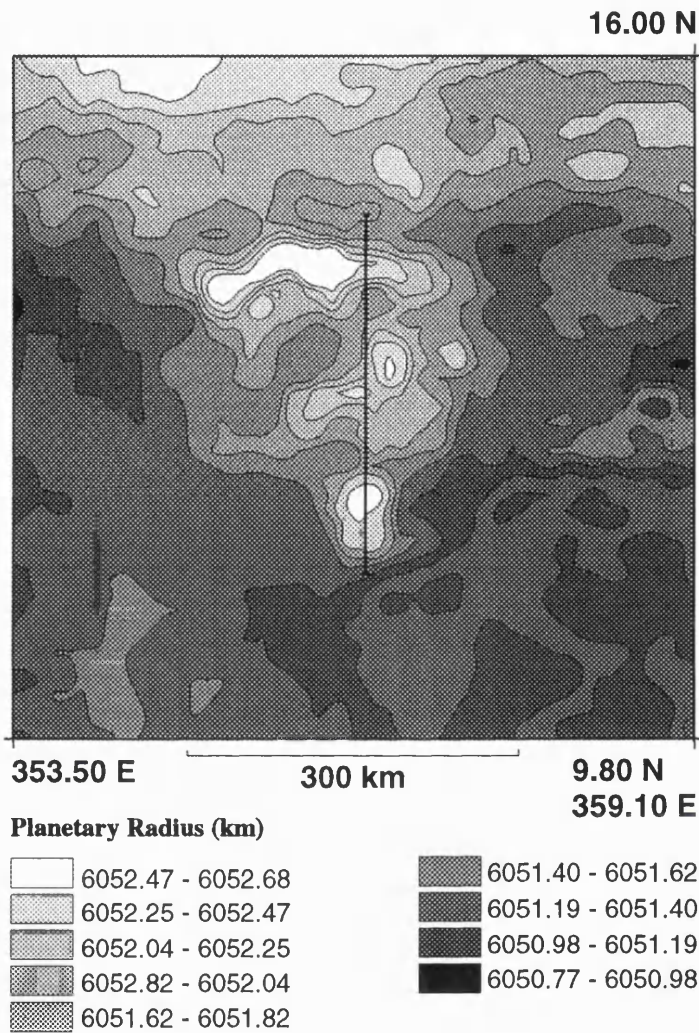


Figure 4.26 Topographic map of Silvia Corona.
Line corresponds to topographic profile in Figure 4.25.

From the above observations it is considered that Silvia Corona began forming prior to the emplacement of the regional plains materials of Guinevere Planitia. A period of initial uplift has resulted in the preservation of older plains materials within the corona's interior which were subsequently embayed by regional plains materials. Deformation continued after regional plains emplacement, with the formation of a discontinuous topographic ridge and weak fractures seen to coincide with the northern rim topography. No late stage volcanism is observed.

4.3 Implications for corona evolution.

Most models of corona formation are based on a three stage sequence (*Stofan and Head, 1990; Stofan et al., 1992; Squyres et al., 1992*). While this three-stage sequence is a useful generalisation and does apply well to some individual features, some coronae have a much more complex, and currently unmodelled, evolution. *Stofan (1995)* described the variations of corona topography, and noted that current models do not account for all the topographic forms observed. How well does the current three-stage evolutionary sequence of corona formation proposed by *Stofan and Head (1990)* fit the five coronae studied here?

4.3.1 Stage 1: Uplift and interior deformation

Initially coronae are proposed to go through a sequence of uplift with interior deformation and volcanism (*Stofan and Head, 1990; Stofan et al., 1992; Squyres et al., 1992*). The coronae studied here have interiors which have been modified by varying amounts of deformation; Benten and Heng-o show the greatest amount of interior deformation, while Idem-Kuva, Nissaba and Silvia show relatively little. However, the timing of deformation is not always associated with the initial formation of the corona. For example, the interior deformation at Benten postdates rim

topography formation.

Idem-Kuva, Nissaba, and Silvia Coronae all contain materials which are interpreted to be older than the regional plains materials surrounding them. These materials are interpreted to be uplifted and subsequently deformed by later stages of corona development. No evidence is seen for preserved early-stage uplifted materials at Heng-o Corona. Although early-stage extensional features are present, the interior of Heng-o is not higher than the surrounding plains. This is considered to indicate that Heng-o has not undergone uplift at any stage in its evolution. At Benten Corona, no early-stage deformational features or materials are identified. Benten does have a large amount of associated volcanism. While Benten may have experienced some amount of uplift, volcanic construction could account for the bulk of its topography. The initial phase of corona formation has been modelled as a rising diapir with uplift and radial extension (*Stofan et al.*, 1991; *Janes et al.*, 1992); the new observations presented here indicate that uplift can occur, but in widely varying amounts, and that early-stage interior faulting does not occur at all coronae.

The amount of early stage volcanism identified at each corona varies considerably. Benten Corona has two extensive flow fields which were subsequently deformed by annulus formation. Heng-o has a less extensive amount of early stage volcanism in the form of large edifices. Idem-Kuva, Nissaba and Silvia Coronae do not have exposed old volcanic units, but are embayed by regional plains materials that may cover early-stage corona flows.

4.3.2 Stage 2: Annulus formation

The formation of the annulus and possibly a surrounding trough is associated with the second stage of corona formation (*Stofan and Head*, 1990; *Stofan et al.*, 1992, *Squyres et al.*, 1992). All five coronae have some degree of annulus deformation, and as with interior deformation, the amount and style differs considerably between coronae and within an individual corona.

The deformation is predominantly graben, although compressional ridges occur, for example on the eastern ridge of Benten. Evidence also exists for more than one annulus forming event at Idem-Kuva and Heng-o Coronae. These observations imply a more complex sequence of events, with annulus formation possibly occurring in multiple events not necessarily confined to the middle or late stages of corona evolution. Late-stage radial graben observed at Benten postdate the annulus and may reflect a secondary phase of uplift (e.g. *Stofan and Smrekar, 1996*).

Coronae are defined by their concentric annulus of ridges and/or graben (*Barsukov et al., 1986*). However, most coronae also have an annular rim of raised topography. How does the annulus deformation relate to the larger scale topographic ridges and troughs, and in particular, which came first? The two scales of deformation are thought to occur contemporaneously during the middle stage of corona evolution, however the precise timing is ambiguous. No evidence from observations of combined topographic and SAR data of the five coronae resolve the timing to a greater accuracy, although as stated above, more than one phase of annulus formation and a protracted topographic rim history is apparent at some coronae. At others, the topographic rim formed with little or no associated small-scale deformation structures (e.g. Silvia). Initial work by *Tapper (1997)* suggests that there may be a large number of circular features with an annular rim but lacking concentric ridges and/or fractures, suggesting that the number of coronae on Venus has been underestimated.

4.3.3 Stage 3: Corona relaxation and the correlation of coronae relief with age

Previous work suggested that coronae interpreted to be older have low relief and late-stage volcanism (*Stofan and Head, 1990*). All the coronae, apart from Silvia, have associated volcanism that postdates annulus formation. However, observations of topographic profiles for the five coronae in the study area show

no correlation between age, absolute relief and the complexity of relief. Furthermore, the amount of relief at each corona studied here is similar and does not show great variation, typically 1 km or less. Heng-o has low relief, the main annulus deforms the youngest major plains unit, and hence postdates it, thus the corona is interpreted to be relatively young. Idem-Kuva, which began formation prior to the regional plains, has greater relief than Heng-o. Therefore, based on this limited study, there is little evidence to suggest that relief can be used to characterise any particular stage of corona evolution, contrary to *Sandwell and Schubert* (1992). At the coronae studied here, the amount of relief at any individual feature is more strongly controlled by the amount of deformation and/or volcanic construction that has taken place. For example at Benten, volcanism is probably a significant contributor to topography, while at Heng-o and Idem-Kuva, topography is probably the dominant product of uplift or annular deformation rather than construction. *Janes and Squyres* (1995) demonstrated that corona topography could be supported by isostatic buoyancy and flexure of the lithosphere, consistent with the observation here that height is not a reliable indicator of corona age.

The last two stages of corona evolution have been modelled as the formation of a plateau followed by gravitational relaxation (*Stofan et al.*, 1991; *Janes et al.*, 1992; *Janes and Squyres*, 1995). With the exception of Benten, none of the coronae studied here has a plateau shape. Some have an upraised rim (Heng-o), while others have a ridge encircling an inner dome-shaped topographic high (Idem-Kuva, Nissaba). This diversity in corona morphology is seen on a global scale (*Stofan et al.*, 1997). In addition, formation and relaxation of a plateau have also been called upon to form the corona annulus (*Stofan et al.*, 1991; *Janes et al.*, 1992; *Janes and Squyres*, 1995). However, corona annuli exist in coronae with widely varying topographic forms. From the above observations, it is interpreted that the plateau stage may not be as significant as proposed previously, and may not occur at all coronae. Furthermore, widely varying corona topographic forms and

multiple stage annulus formation provide evidence that some coronae go through a more complex evolutionary process than previously suggested. A few of the shapes of coronae could be explained by the stalling of a neutrally buoyant diapir (*Koch and Manga, 1996*). However, *Smrekar and Stofan (1997)*, who include the effects of pressure and temperature-dependent viscosity, pressure-release melting, and a residuum layer in their upwelling model, can model the complete diversity of corona forms, as well as explain multiple stage annulus formation observed at some coronae in this study.

4.4 Implications for corona stratigraphy on Venus

As described in Chapter 2, some workers have suggested a specific age of formation for coronae on Venus using both local stratigraphic relations (*Basilevsky and Head, 1994, 1995a, 1995b, Basilevsky et al., 1997*) and crater density statistics (*Price and Suppe, 1994; Namiki and Solomon, 1994; Price et al., 1996*). The application of these global models to specific areas is considered below.

4.4.1 Dating coronae using local stratigraphic relations.

Basilevsky and Head (1994, 1995a, 1995b) and *Basilevsky et al. (1997)* have defined three stratigraphic units associated with coronae based on observations from 36 randomly distributed sites (Chapter 2, 2.3). Each unit is characterised by the structure present. The oldest unit as classified by *Basilevsky and Head (1994, 1995a, 1995b)* and *Basilevsky et al. (1997)* is interior radial or chaotic deformation interpreted to form early in the development of coronae (COdf). The ridges of corona annuli (COar) form the second global unit, and the youngest unit, (COaf), is made up of fractures of corona annuli. *Basilevsky and Head (1994, 1995a, 1995b)* and *Basilevsky et al. (1997)* argue that each of the stages of corona evolution represented by these three units is

normally contemporaneous on a global scale. No similar simplistic relations are observed between structural deformation and time at the five corona studied here. For example, two of the coronae in V31 show evidence of more than one phase of annulus formation. Some corona annuli are younger than the regional plains (e.g. Heng-o) while others are older (e.g. Nissaba). Similarly, interior deformation is not always relatively old at the coronae studied here (e.g. Benten). The different stages of corona evolution were not simultaneous in this region, nor were the same processes repeated at a single corona. The results here indicate that it may be premature to establish global stratigraphic units for coronae; the initial proposed scheme of *Basilevsky et al.* (1997) is not consistent with observations of coronae in V31.

From detailed mapping, it is established that three (Nissaba, Idem-Kuva and Silvia) of the five coronae began forming before the materials of the regional plains in the study area were deposited. Deformation and volcanism at Idem-Kuva has continued after the formation of Gula Mons. While some coronae may predate large shields (*McGill*, 1994), the study here indicates that simplistic relations between the relative ages of coronae and large volcanoes (i.e. *Price et al.*, 1996; *Namiki and Solomon*, 1994) should be used with caution.

4.4.2 Dating coronae using crater statistics

Phillips et al. (1992) calculated that the minimum area needed to produce statistically meaningful crater densities for a planet which has 891 craters is approximately 5×10^6 km². Only Artemis Corona is large enough to meet this criterion. In order to overcome the problem of corona surface areas being too small to produce meaningful ages using crater densities, an area-weighted mean was used in the dating model of *Price et al.* (1996). As *Price et al.* state, this is inherently problematic because where the surface areas of coronae are combined, any range in ages will be smoothed. Hence, although an average age for coronae has been

calculated, the shape of the age distribution curve and its span are not known. A further problem is that of the 319 coronae observed on Venus, 89% of the population contain no impact craters (*Namiki and Solomon, 1994*).

The average age for coronae calculated by *Price et al. (1996)* is 120 ± 115 Ma, compared with an age of approximately 300 Ma for the plains. However, it is shown here that coronae formation both pre and postdates the regional plains units (e.g. Idem-Kuva). The five coronae studied here have complex geological histories indicating that they formed over long periods of time. Thus, although calculating an average age for coronae using global crater densities is possible, the use of the results may be misleading, firstly because an individual corona can have a long life span, and secondly because coronae have formed at different times in the history of Venus. Detailed stratigraphic studies are necessary to correctly determine the relative ages of coronae.

The *Price et al. (1996)* model assumes that cratering is spatially random and rate-constant since the emplacement of the plains, and that volcanism and tectonism occurred 'simultaneously and instantaneously within a terrain'. While the first assumption may hold, the second is a substantial idealisation which *Price et al. (1996)* recognise, but still employ. The long period of extrusion of flows associated with Benten is an example that this second assumption is not the case at every corona.

Even if the issue of averaging ages is neglected, in order to calculate a meaningful crater density for coronae, it is of utmost importance to map all the materials which are associated with each corona. *Namiki and Solomon (1994)* obtained crater densities for coronae by counting the number of craters which fell within the annulus. As *Price et al. (1996)* indicate, errors in mapping can have a significant effect on the crater density and hence age of a unit; a reduction in area by as little as 10% for the combined area of large volcanoes can result in the crater density of the unit being overestimated by a factor of 2. Therefore, if large sheet flows which are associated with many coronae (*Stofan and Smrekar, 1996*) are not accounted for, grossly incorrect ages will be

calculated. The quantitative study of plains materials in Chapter 3 further highlights the probability of a greater amount of materials being associated with coronae (and other volcanic landforms) than previously considered.

4.5 Summary and Conclusions

While the previously proposed three-stage model for corona evolution is useful, corona evolution can be much more complex. It is shown here that not all coronae undergo initial uplift, nor do all coronae go through a plateau-forming stage. Annulus formation was previously thought to occur during the second stage of corona formation, however, evidence for multiple annuli at Idem-Kuva and Heng-o Coronae suggests that it could occur early in the evolution of the coronae, and go through multiple cycles. In addition, annulus formation and rim topography formation do not necessarily coincide in space and time, again indicating that both large and small-scale deformational processes at coronae can be protracted and may not be confined to a single stage.

The amount and style of volcanism associated with the coronae studied here varies considerably. Predicted early stage volcanism is not observed at Idem-Kuva, Nissaba or Silvia Coronae. Benten Corona has multiple phases of volcanism, with a decrease in volume and change in style over time. Heng-o apparently lacks voluminous early-stage volcanism, and is dominated by central edifice-style volcanism.

Furthermore, the use of global-scale stratigraphic units at coronae is problematic; coronae in the region studied did not form simultaneously, did have a complex, protracted history, and were not affected by the same processes in the same order. This study also highlights the potential problems in applying globally-derived average ages to individual coronae. Continued detailed mapping studies of Venus are required to accurately determine the relative ages of coronae.

Chapter 5

A geological investigation of Sif and Gula Montes

5.1 Introduction

Using new data from the Magellan spacecraft (full resolution FMAPs, synthetic stereo images, and ancillary data, described in Appendix I), a study of the morphology of Sif and Gula Montes, and associated materials was conducted to determine styles of eruptive activity, and internal plumbing and evolution. The volcanoes were mapped using normal photogeological techniques adapted for radar images (*Tanaka et al.*, 1994), with surface textures of lava flows interpreted using radar backscatter characteristics.

Sif and Gula Montes are situated on the topographic rise of Western Eistla Regio, an elongate (3200 km by 2000 km) domical upland, rising 1.8 km above the plains (*Campbell et al.*, 1989; *Campbell and Campbell* 1990; *Senske et al.*, 1992; *Stofan et al.*, 1995, Figure 5.1). Western Eistla Regio is part of the more extensive upland of Eistla Regio in the equatorial region of Venus. The upland is classified as a volcano-dominated rise (*Stofan et al.*, 1995), and is interpreted to be the manifestation of a mantle plume (*Schaber*, 1982; *Kozak and Schaber*, 1989; *Grimm and Phillips*, 1992; *Senske et al.*, 1992; *Bindschadler et al.*, 1992b; *Smrekar*, 1994; *Stofan et al.*, 1995).

Although Sif and Gula Montes formed adjacent to one another, their morphology and associated flow materials show a number of differences. Sif Mons (22° N, 352° E) is broadly circular in plan view and has a mean diameter of 350 km. Gula Mons (22° N, 359° E) is elliptical in plan view with a mean diameter of 450 km. The summits of Sif and Gula stand at 2.0 km and 3.2 km respectively above the local topography. Sif is surmounted by a prominent caldera, while Gula has a rift zone which terminates at both ends in modified calderas.

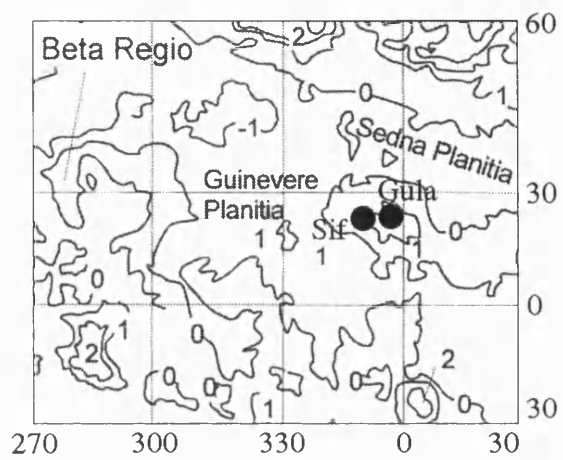


Figure 5.1 Location map for Sif and Gula Montes

Both volcanoes are surrounded by a suite of flow units, the greatest extent of which is more than 700 km from the main edifices. The number and morphology of the flow units differ between each volcano (Figure 5.2).

Two relatively well understood terrestrial basaltic volcanoes, Mount Etna (Sicily) and Kilauea (Hawaii) are used as analogs to understand how Sif and Gula Montes developed and, in particular, to explain the morphological differences observed between them. The study of Sif and Gula Montes can be used to test and compare models of large volcano formation on Venus and Earth described in Chapter 2 (2.6). Before descriptions and interpretations are presented, important constraints in using radar to study lava flows are discussed.

5.2 Constraints on the Identification and Interpretation of Volcanic Materials using Radar

Studies of terrestrial volcanoes using airborne and orbital radar are well documented (e.g. *Evans*, 1978; *Elachi*, 1980; *Farr et al.*, 1981, 1983; *Fielding et al.*, 1986; *Greeley and Martel*, 1988; and *Gaddis et al.*, 1989). The identification of lava flows from radar images on the basis of their planimetric shapes (elongate, lobate morphology and often radial distribution about a central edifice often with a summit depression) is widely accepted (*Ford et al.*, 1989). The main purpose of these studies has been to establish techniques and baselines which can be used to investigate remote volcanoes on Earth, as well as interpret radar data from other planets, in particular Venus.

A number of constraints apply when using radar images to interpret lava flow surface texture and hence emplacement mechanisms. The constraints may be subdivided into two categories: (1) radar instrument constraints, which include radar wavelength, geometry and resolution; and (2) surficial constraints, which include surface textural characteristics.

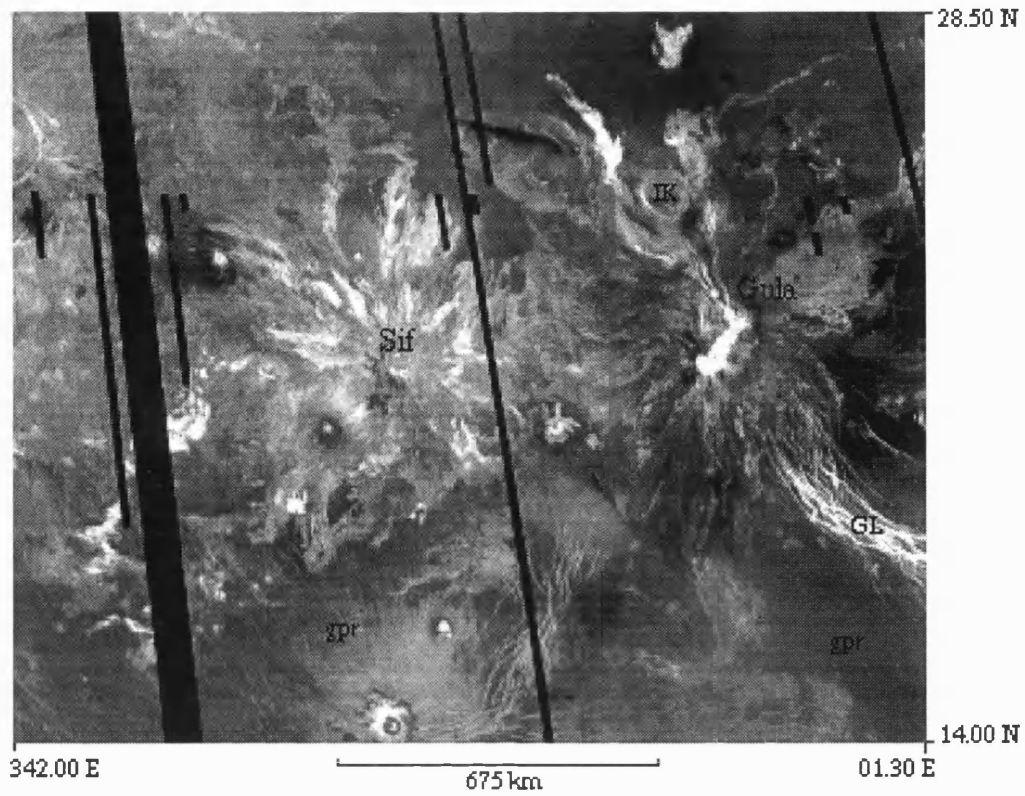


Figure 5.2 Sif and Gula Montes situated on the rise of Western Eistla Regio. IK = Idem Kuva Corona, GL = Guor Linea fracture belt. (C2-MIDR30N335;2 browse).

The constraints are outlined below, illustrated with examples from field observations and radar data of Mt. Etna (Sicily). Mt. Etna was imaged using the Space Shuttle's SIR-C Radar which had a resolution of 12.5 m in two radar wavelengths: C-band (6 cm) and L-band (23 cm). The HH polarisation of the C band is most similar to the Magellan SAR instrument.

5.2.1 Radar Instrument Constraints

Radar Wavelength

Within a radar image, the brightness of an individual lava flow, or compound flow field, is controlled mainly by the large-scale topographic slope (rms slopes) and the surface roughness at radar wavelengths (*Elachi et al.*, 1980; *Pettengill et al.*, 1992; *Ford et al.*, 1989; *Campbell*, 1995). Rms slope values represent the standard deviation of surface height variations on lava flows typically on the order of 10 to 100's of meters; broad-scale surface morphology can be inferred from these data. Small-scale surface roughness, at scales much smaller than the spatial resolution of radar, controls the overall brightness of the radar image at wavelength scales (*Ford et al.*, 1989). The longer the wavelength of the radar, the rougher the surface must be for significant backscatter to occur. The Magellan SAR radar had a fixed wavelength of 12.6 cm and hence a bright return at wavelength scales denotes a surface which is rough at multiples of 12.6 cm.

Radar Geometry

Brightness variations in radar images are influenced by variations in the look angle and/or the direction of illumination (*Ford et al.*, 1989). For instance, with incidence angles less than about 25° , smoother surfaces have greater backscatter than rougher surfaces in Magellan SAR data (*Farr*, 1993). The Magellan SAR radar had a look angle which varied from 14° to 45° depending on latitude. Flow assemblages at widely different

latitudes (hence viewed at different look angles) may have different radar returns which must be accounted for before inferring and comparing surface roughness (Appendix I). This is not a problem with the discrimination of Sif and Gula flow materials, as the look angle is relatively constant (approximately 43° to 45°). Right looking data were not used in this study as it is of poor quality.

Radar Resolution

A constraint of any remote sensing instrument in discriminating surface features is its limiting resolution. *Gaddis et al.* (1989) describes the difficulty in separating individual terrestrial pahoehoe flows at Kilauea using SIR-B radar images with a resolution of approximately 25 m. The resolution of Magellan SAR data (120 m at best) will limit the ability to identify individual lava flows and surface structures at Sif and Gula Montes.

5.2.2 Surficial Constraints

Adjacent flow units of similar surface textures

Adjacent flows units which have the same (or similar) rms slope and/or surface roughness properties are likely to be difficult to distinguish using radar data. For example, flows with similar surface textures are likely to have similar radar characteristics. This will make the separation of the individual flows difficult. Furthermore, non-volcanic deposits with similar radar properties to adjacent flow materials will also hinder discrimination of the flow.

An example is noted from the Mt. Etna study. The 1983, 1985, and 1991-93 flows all have a relatively strong radar return in both C and L bands owing to their relatively rough surface texture (Table 5.1, Figure 5.3). However, the 1991-93 flow cannot be distinguished from surrounding materials in SIR-C radar images as both materials have a similar surface roughness, and radar

backscatter. In contrast, the 1983 and 1985 flow materials overlies ash deposits. The ash deposits have a significantly weaker radar return (owing to a smoother surface texture) than the relatively rough aa surfaces of the 1983 and 1985 flow materials (Table 5.1, Figure 5.3). As a consequence, the radar backscatter contrast is great and the 1983 and 1985 flows are easily delineated against the ash deposits. An implication of the above observation is that the age of a lava flow cannot be related to radar backscatter; the 1983 flow is more prominent than the 1991-93 flow in radar images, but it is older.

A lava flow may vary considerably in surface texture along its length and width. For example pahoehoe and aa can be found as parts of the same lava flow (*Macdonald, 1953*). Without supplementary field observations, misinterpretation may arise in the subdivision of a discrete flow from radar observations owing to a change in texture and subsequent changes in radar backscatter. Conversely, although the 1983 flow is composed of a mixture of both aa and pahoehoe surfaces (*Guest et al., 1987*), the variation in texture is not apparent from SIR-C radar images.

The identification and discrimination between aa and pahoehoe lava

Previously, some authors have classified lava flows on Venus as either aa or pahoehoe, based on radar backscatter (e.g. *Campbell and Campbell, 1992*). However, this classification using radar data alone (as is the case for Venus) may be misleading. Field observations undertaken here of lava surface textures on Mt. Etna serve to highlight this problem.

Lavas which surround Mt. Etna include several historic flows that are mainly of pahoehoe texture (*Guest et al., 1984*). Of these the radar characteristics of the 1614-24 and 1651 flows are of particular interest. Pahoehoe flows are considered to have smoother surface textures than aa flows, and hence are expected to represent relatively dark areas in radar images (*Ford et al., 1989*). However, the 1614-24 and 1651 pahoehoe flows have a

Name of Flow	¹ CHH (λ - 6 cm)	¹ LHH (λ - 23 cm)	² Look Angle, θ
1983 - aa flow			
Proximal	-15.44 (-25.20, -08.30)	-05.20 (-13.01, -00.63)	49.06
Middle	-14.85 (-21.56, -10.36)	-05.99 (-12.17, -01.16)	49.10
Distal	-14.66 (-19.12, -07.96)	-05.76 (-10.23, -01.19)	49.21
1985 - aa flow			
Proximal	-16.38 (-24.25, -09.79)	-07.12 (-13.41, -01.67)	48.87
Distal	-12.99 (-19.30, -08.38)	-04.66 (-09.14, 00.00)	48.70
1991-1993 - aa/ slab	-16.25 (-24.52, -10.64)	-06.95 (-13.32, -02.33)	49.90
Summit ash	-21.69 (-27.06, -15.89)	-04.53 (-10.50, 00.00)	48.38
1614-1624 - pahoehoe			
Proximal	-17.06 (-24.47, -09.58)	-04.24 (-11.85, 00.00)	48.10
Middle	-14.92 (-23.14, -07.79)	-02.93 (-09.93, 00.00)	47.98
Distal	-12.64 (-20.25, -05.94)	-01.45 (-06.70, 00.00)	47.84
1651 - pahoehoe			
Proximal	-15.07 (-20.09, -07.94)	-04.42 (-09.76, 00.00)	47.58
Middle	-14.07 (-19.82, -07.95)	-03.56 (-07.91, 00.00)	47.44
Distal	-15.02 (-26.71, -08.86)	-03.29 (-12.89, 00.00)	47.39

¹ Values are in linear dB format, mean (min, max) values are shown.

² Look angle corresponds to the centre of sample box.

Table 5.1 Comparison of SIR-C data for selected flows at Mt. Etna.

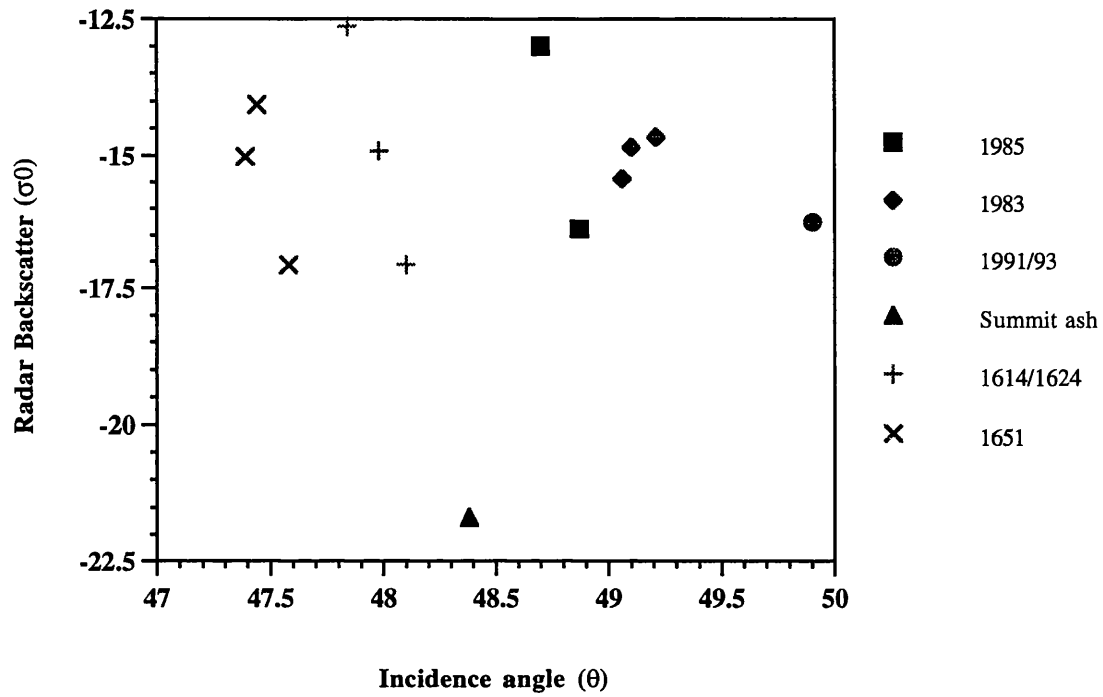


Figure 5.3 Radar backscatter for selected flows at Mt. Etna

relatively strong radar return and appear radar bright at both C and L bands of SIR-C data (see Table 5.1, Figure 5.3). Such a strong radar backscatter is indicative of a comparatively rough surface texture analogous to aa. What surface morphology is responsible for the unexpected strong radar return?

Field observations show the flows are composed of tumuli which coalesce to form chaotic areas of tilted crustal slabs, typically less than 1 m thick (*Guest et al.*, 1984). The tumuli and slabs result in a medium to large scale surface roughness which accounts for the strong radar return, indicated from the radar images. The surface texture of the flows is explained by their emplacement mechanism. The 1614-24 flow was emplaced from a long-duration flank eruption. A consequence of the long duration eruption was the formation of a number of lava terraces (*Romano and Guest*, 1979; *Guest et al.*, 1984). The crusts of the terraces experienced deformation from exogenic and endogenic processes as they cooled. Molten lava under pressure forced the crust up to form tumuli and mega-tumuli structures. The 1651 flow experienced a similar emplacement. It is conceivable that similar processes have occurred with flows on Venus. Such a flow may be incorrectly interpreted as aa lava.

Modification by surficial deposits

Returning to observations from Venus, FMAP data show the role of surficial deposits from impact craters is important in modifying radar backscatter from the surface. Impact crater deposits can significantly alter the radar properties of geological features, in particular flow surfaces. The deposits are particularly good at enhancing fine scale deformation contained in a flow field; this aids in delineation of the fabric. Conversely, surficial impact crater deposits can mask flow boundaries, (hence delineation becomes more difficult) and hinders textural interpretation by mantling the surface of the lava flow. Materials deposited on some Gula flows from Annia Faustina crater have resulted in the flows having a weaker radar backscatter (Figures 5.2 and 5.5).

In conclusion, when using radar data to identify and interpret the styles of emplacement of volcanic materials on Venus, the above constraints must be considered. In particular, it may be misleading to label venusian flows with classical terrestrial nomenclature (i.e. pahoehoe and aa, first introduced by *Dutton*, 1884) based on radar data alone. The last conclusion is drawn from comparisons between field observations and radar images of Mt. Etna flows. With the above constraints in mind, the flow units of Sif and Gula Montes were mapped and compared.

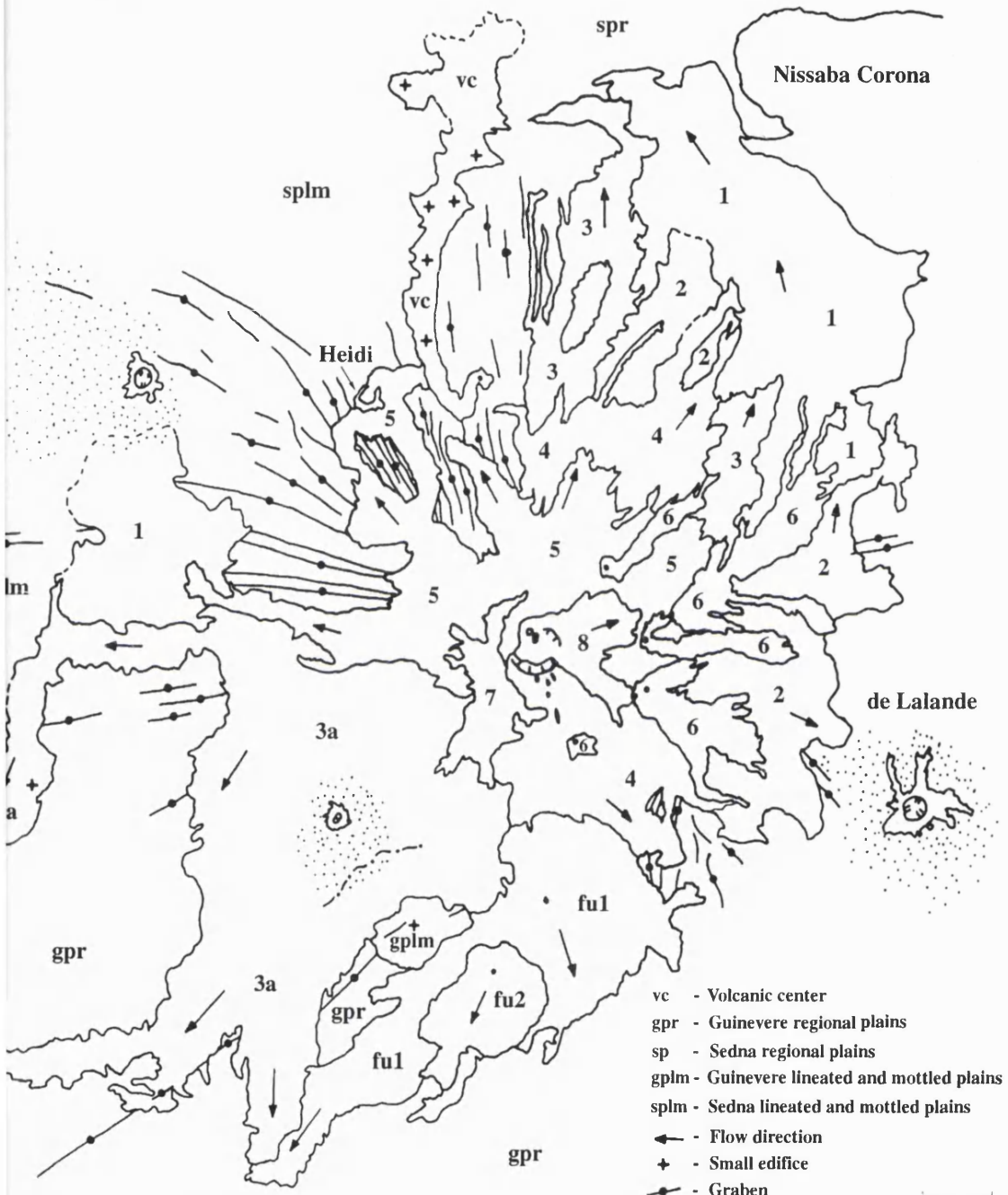
5.3 Description and Interpretation of Volcanic Units of Sif and Gula Montes

Sif and Gula Montes flows are divided into 8 and 4 map units respectively (Figures 5.4 and 5.5). Radar backscatter and ancillary data for sample areas of each unit are presented in Table 5.2. Figure 5.6 shows the radar backscatter of sample areas for each flow unit identified at Sif and Gula Montes. The morphology, inferred surface texture, and dimensions of the different flow materials at each volcano are used to infer a number of emplacement mechanisms, many of which are considered similar to those observed at terrestrial volcanoes. These include sheet, tube-fed, channel-fed, flank eruptive and possible pyroclastic flow emplacement mechanisms.

5.3.1 Sheet Flows

Common to both volcanoes are materials which have a weak, homogeneous radar backscatter, labelled Unit 1 (see Table 5.2). Ancillary data imply the surface of the flow materials to be relatively smooth; rms slope values are less than the global mean of 2.84°. At Sif Mons, Unit 1 materials are areally extensive (typically thousands of square kilometres), have a sheet-like morphology, and terminate with broad lobate flow fronts which overlie the local regional plains materials (Figure 5.7).

27.00 N



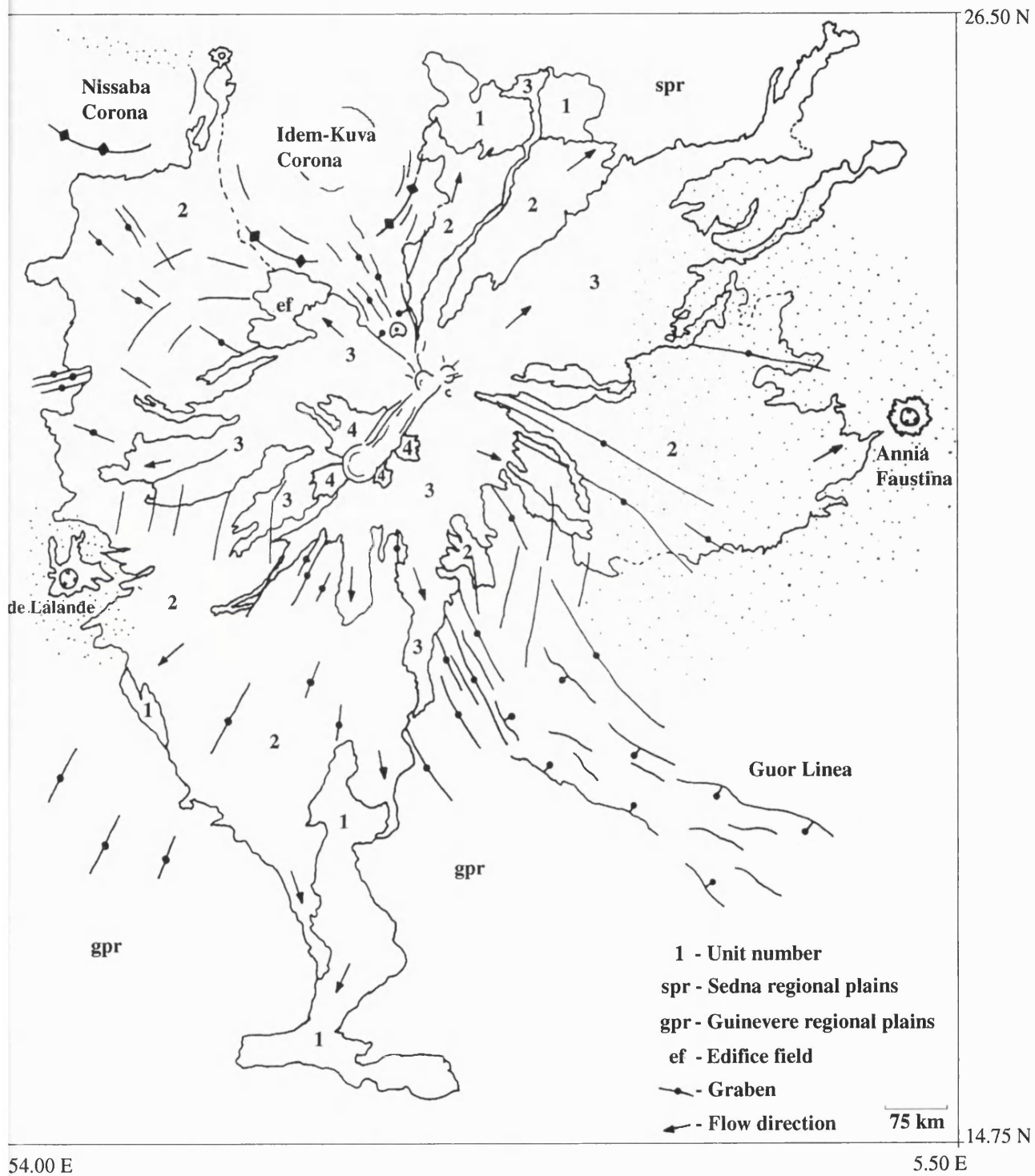
- vc - Volcanic center
- gpr - Guinevere regional plains
- sp - Sedna regional plains
- gplm - Guinevere lineated and mottled plains
- splm - Sedna lineated and mottled plains
- ← - Flow direction
- + - Small edifice
- - Graben
- - - - Channel

100 km

17.00 N

50 E

355.75 E



Location data for sample areas of Sif Mons units.

Unit	Lat	Long	Δ(m)	N	Angle	Radius (km)
1	25.080, 25.330 N;	352.470, 353.200 E	225	47400	43.8	6052.274 (6052.232, 6052.325)
2	24.190, 24.270 N;	352.390, 352.590 E	225	9152	44.1	6052.295 (6052.270, 6052.337)
3a	25.060, 25.150 N;	351.560, 352.090 E	225	6862	43.8	6052.240 (6052.225, 6052.255)
3b	18.220, 18.260 N;	345.030, 345.150 E	225	2430	45.2	6050.961 (6050.952, 6050.974)
3b	19.590, 20.170 N;	346.480, 346.560 E	225	7579	45.0	6051.566 (6051.543, 6051.597)
3b	18.480, 18.580 N;	349.070, 349.200 E	225	7326	45.2	6051.803 (6051.767, 6051.821)
3b	19.090, 19.190 N;	349.320, 349.420 E	225	6160	45.2	6051.983 (6051.961, 6052.003)
3b	20.570, 21.170 N;	349.520, 350.500 E	225	67575	44.8	6052.259 (6052.168, 6052.428)
4	23.160, 23.290 N;	352.110, 352.380 E	225	20706	44.3	6052.377 (6052.363, 6052.387)
5	22.190, 22.330 N;	351.340, 352.240 E	225	42688	44.4	6053.162 (6052.658, 6053.535)
5	22.160, 22.270 N;	350.430, 351.060 E	225	14960	44.6	6052.662 (6052.592, 6052.795)
6	21.300, 21.340 N;	352.530, 353.000 E	225	2030	44.7	6053.008 (6052.800, 6053.179)
6	21.010, 21.100 N;	352.590, 353.190 E	225	10868	44.7	6052.714 (6052.597, 6052.838)
6	22.020, 22.090 N;	353.040, 353.190 E	225	6844	44.6	6052.583 (6052.575, 6052.597)
6	21.480, 21.420 N;	353.010, 353.150 E	225	5292	44.6	6052.677 (6052.578, 6052.793)
7	20.560, 21.020 N;	351.040, 351.120 E	225	3294	44.8	6052.537 (6052.452, 6052.655)
7	21.510, 24.540 N;	351.040, 351.060 E	225	352	44.6	6052.486 (6052.168, 6053.246)
8	21.370, 21.460 N;	351.400, 351.460 E	225	3648	44.7	6053.720 (6053.541, 6053.864)
8	21.240, 21.450 N;	352.030, 352.160 E	225	16038	44.7	6053.662 (6053.461, 6053.974)
fd	18.380, 19.120 N;	351.210, 351.390 E	225	36305	45.2	6052.185 (6052.128, 6052.309)
fd	19.100, 19.580 N;	352.000, 358.586 E	225	65772	45.0	6052.388 (6052.259, 6052.625)
fd	19.450, 19.500 N;	351.010, 351.140 E	225	4059	45.0	6052.479 (6052.346, 6052.720)

Table 5.2 Radar data for flow units at Sif and Gula Mons

Radar data for Sif Mons units.

Unit	σ_0 (dB)	θ_{rms} (deg)	ρ Fresnel	Emissivity	ϵ_s ϵ_r
1	-18.31 (-23.35, -13.54)	2.10 (1.40, 2.70)	0.142 (0.125, 0.155)	0.806 (0.802, 0.812)	3.9, 6.3
2	-11.16 (-15.00, -7.00)	3.07 (2.10, 4.20)	0.106 (0.100, 0.130)	0.841 (0.820, 0.859)	3.3, 5.1
3a	-11.21 (-18.55, -6.55)	1.79 (1.30, 3.00)	0.144 (0.125, 0.180)	0.818 (0.814, 0.821)	3.7, 5.9
3b	-10.13 (-16.33, -6.73)	2.87 (2.60, 3.30)	0.101 (0.095, 0.115)	0.861 (0.857, 0.864)	2.9, 4.5
3b	-10.18 (-17.84, -6.64)	2.70 (1.90, 4.50)	0.098 (0.075, 0.115)	---	---
3b	-10.11 (-14.31, -6.70)	1.18 (0.90, 1.60)	0.145 (0.115, 0.175)	0.817 (0.811, 0.824)	3.6, 5.9
3b	-16.67 (-21.69, -11.09)	2.46 (2.20, 2.70)	0.110 (0.105, 0.115)	0.831 (0.825, 0.835)	3.4, 5.4
3b	-12.43 (19.40, -6.00)	2.21 (1.00, 4.00)	0.154 (0.120, 0.220)	0.802 (0.782, 0.812)	3.9, 6.5
4	-15.35 (-21.26, -10.07)	2.41 (2.00, 2.80)	0.139 (0.130, 0.155)	0.803 (0.792, 0.815)	3.9, 6.5
5	-12.43 (-18.73, -6.13)	2.74 (2.10, 3.50)	0.109 (0.090, 0.135)	0.820 (0.811, 0.836)	3.6, 5.8
5	-14.52 (-20.76, -2.96)	3.35 (2.10, 5.60)	0.160 (0.145, 0.235)	0.810 (0.799, 0.829)	3.8, 6.2
6	-9.30 (-14.58, -5.58)	2.40 (1.60, 3.00)	0.129 (0.105, 0.160)	0.780 (0.775, 0.788)	4.3, 7.4
6	-12.73 (-18.40, -6.20)	2.88 (2.40, 3.40)	0.119 (0.105, 0.140)	0.788 (0.777, 0.797)	4.2, 7.1
6	-10.65 (-17.56, -5.96)	2.64 (2.60, 2.70)	0.144 (0.140, 0.145)	0.773 (0.770, 0.778)	4.5, 7.7
6	-11.92 (-16.96, -7.77)	2.05 (1.60, 2.70)	0.158 (0.150, 0.165)	0.779 (0.777, 0.783)	4.4, 7.4
7	-20.26 (-25.20, -11.60)	1.67 (0.9, 2.50)	0.164 (0.115, 0.200)	0.788 (0.782, 0.797)	4.2, 7.0
7	-18.45 (-22.56, -14.96)	2.64 (1.10, 4.90)	0.143 (0.095, 0.180)	0.810 (0.781, 0.831)	3.8, 6.2
8	-13.72 (-18.97, -8.57)	2.49 (2.20, 2.90)	0.140 (0.100, 0.160)	0.819 (0.809, 0.831)	3.6, 5.9
8	-12.73 (-17.98, -4.38)	2.71 (2.20, 3.70)	0.128 (0.105, 0.155)	0.786 (0.777, 0.795)	4.2, 7.1
fu	-17.41 (-23.50, -8.72)	2.06 (1.40, 2.60)	0.134 (0.085, 0.190)	0.796 (0.790, 0.803)	4.0, 6.7
fu	-16.38 (-23.26, -8.09)	1.88 (0.70, 4.20)	0.130 (0.100, 0.210)	0.812 (0.768, 0.829)	3.7, 6.1
fu	-11.71 (-15.26, -7.66)	2.86 (2.10, 4.00)	0.159 (0.145, 0.175)	0.803 (0.800, 0.805)	3.9, 6.4

Table 5.2 Cont.

Location data for sample areas of Gula Mons units.

Flow unit	Lat	Long	Δ (m)	N	Angle	Radius (km)
1	16.040, 16.110 N;	357.490, 358.070 E	225	8178	45.5	6051.880 (6051.844, 6051.953)
2	19.450, 20.000 N;	357.260, 357.540 E	225	30645	45.0	6052.559 (6052.510, 6052.638)
2	17.000, 17.360 N;	357.500, 358.040 E	225	32718	45.4	6052.240 (6052.151, 6052.298)
2	17.320, 17.480 N;	357.280, 357.460 E	225	17520	45.4	6052.321 (6052.303, 6052.332)
2	19.300, 19.520 N;	356.000, 356.170 E	225	22833	45.0	6052.459 (6052.441, 6052.486)
2	23.020, 23.480 N;	000.460, 001.230 E	225	87932	44.2	6052.912 (6052.758, 6053.065)
2	25.560, 26.050 N;	004.010, 004.060 E	225	2774	43.6	6051.422 (6051.340, 6051.487)
2	24.410, 24.550 N;	004.290, 004.360 E	225	5616	43.9	6051.640 (6051.634, 6051.645)
3	21.070, 21.300 N;	359.000, 359.340 E	225	45666	44.7	6053.321 (6052.948, 6053.742)
3	22.240, 22.290 N;	360.170, 360.340 E	225	5000	44.6	6053.132 (6053.117, 6053.146)
3	20.400, 20.490 N;	358.100, 358.160 E	225	3021	44.8	6052.793 (6052.772, 6052.827)
3	20.580, 21.040 N;	358.010, 358.100 E	225	3332	44.8	6053.018 (6052.854, 6053.257)
3	21.280, 21.470 N;	356.230, 356.430 E	255	23088	44.7	6052.570 (6052.528, 6052.593)
3	21.280, 21.470 N;	356.230, 356.430 E	225	17442	44.6	6052.884 (6052.877, 6052.893)
3	21.300, 21.560 N;	000.210, 000.360 E	225	19584	44.7	6052.831 (6052.710, 6053.010)
4	22.100, 22.200 N;	358.010, 358.040 E	225	2418	44.6	6053.387 (6053.290, 6053.542)
4	21.210, 21.270 N;	357.510, 358.040 E	225	4128	44.7	6053.135 (6052.883, 6053.686)
Summit	21.320, 21.460 N;	358.140, 358.280 E	255	11877	44.7	6054.003 (6053.875, 6054.334)
Summit	22.250, 22.360 N;	359.000, 359.110 E	225	7482	44.6	6054.492 (6054.246, 6054.700)

Table 5.2 Cont.

Radar data for Gula Mons units.

Unit	σ_0 (dB)	θ_{rms} (deg)	ρ_{Fresnel}	Emissivity	ϵ_s ϵ_r
1	-16.94 (-22.00, -10.60)	2.55 (1.90, 3.20)	0.098 (0.095, 0.105)	0.822 (0.816, 0.827)	3.5, 5.7
2	-21.35 (-26.86, -11.46)	1.65 (1.30, 2.00)	0.146 (0.120, 0.185)	0.814 (0.805, 0.824)	3.7, 6.0
2	-15.89 (-22.37, -8.37)	1.53 (0.70, 2.30)	0.113 (0.100, 0.130)	0.817 (0.802, 0.828)	3.6, 5.9
2	-15.80 (-23.16, -9.36)	1.55 (1.30, 1.90)	0.108 (0.100, 0.115)	0.828 (0.826, 0.830)	3.4, 5.5
2	-19.48 (-24.48, -9.27)	1.72 (1.40, 2.10)	0.110 (0.100, 0.125)	0.810 (0.808, 0.812)	3.7, 6.2
2	-15.45 (-26.04, -6.68)	4.47 (1.30, 8.20)	0.078 (0.050, 0.105)	0.855 (0.830, 0.890)	3.0, 4.7
2	-11.67 (-18.10, -4.69)	2.25 (1.60, 3.10)	0.090 (0.075, 0.115)	0.830 (0.815, 0.854)	3.5, 5.5
2	-12.19 (-19.58, -4.18)	1.96 (1.80, 2.10)	0.056 (0.050, 0.065)	0.895 (0.890, 0.899)	2.5, 3.6
3	-13.20 (-20.82, -7.62)	2.57 (2.50, 2.60)	0.129 (0.120, 0.140)	0.798 (0.797, 0.798)	4.0, 6.7
3	-14.92 (-19.60, -10.20)	3.11 (2.50, 4.20)	0.130 (0.115, 0.155)	0.792 (0.785, 0.795)	4.1, 6.9
3	-15.80 (-23.38, -8.17)	2.17 (2.00, 2.50)	0.130 (0.120, 0.150)	0.800 (0.797, 0.804)	3.9, 6.5
3	-19.28 (-24.56, -9.56)	1.89 (1.50, 2.40)	0.166 (0.145, 0.175)	0.796 (0.790, 0.802)	4.1, 6.7
3	-17.27 (-25.98, -7.60)	3.67 (2.70, 4.50)	0.145 (0.125, 0.190)	0.784 (0.775, 0.790)	4.3, 7.2
3	-16.75 (-23.56, -10.76)	2.55 (2.40, 2.80)	0.128 (0.125, 0.145)	0.783 (0.780, 0.786)	4.3, 7.2
3	-17.45 (-25.17, -9.98)	3.09 (2.30, 3.60)	0.129 (0.105, 0.145)	0.785 (0.782, 0.789)	4.2, 7.2
4	-23.40 (-27.76, -17.56)	1.79 (1.50, 2.20)	0.231 (0.200, 0.275)	0.784 (0.781, 0.787)	4.3, 7.2
4	-22.92 (-28.38, -15.98)	2.43 (1.80, 4.50)	0.200 (0.155, 0.290)	0.786 (0.760, 0.799)	4.2, 7.1
Summit	-4.88 (-16.57, 8.42)	2.36 (1.60, 3.80)	0.164 (0.140, 0.190)	0.726 (0.698, 0.746)	5.7, 10.0
Summit	-8.25 (-19.76, 3.44)	3.47 (2.30, 4.30)	0.189 (0.145, 0.230)	0.698 (0.682, 0.714)	6.5, 11.7

Table 5.2 cont.

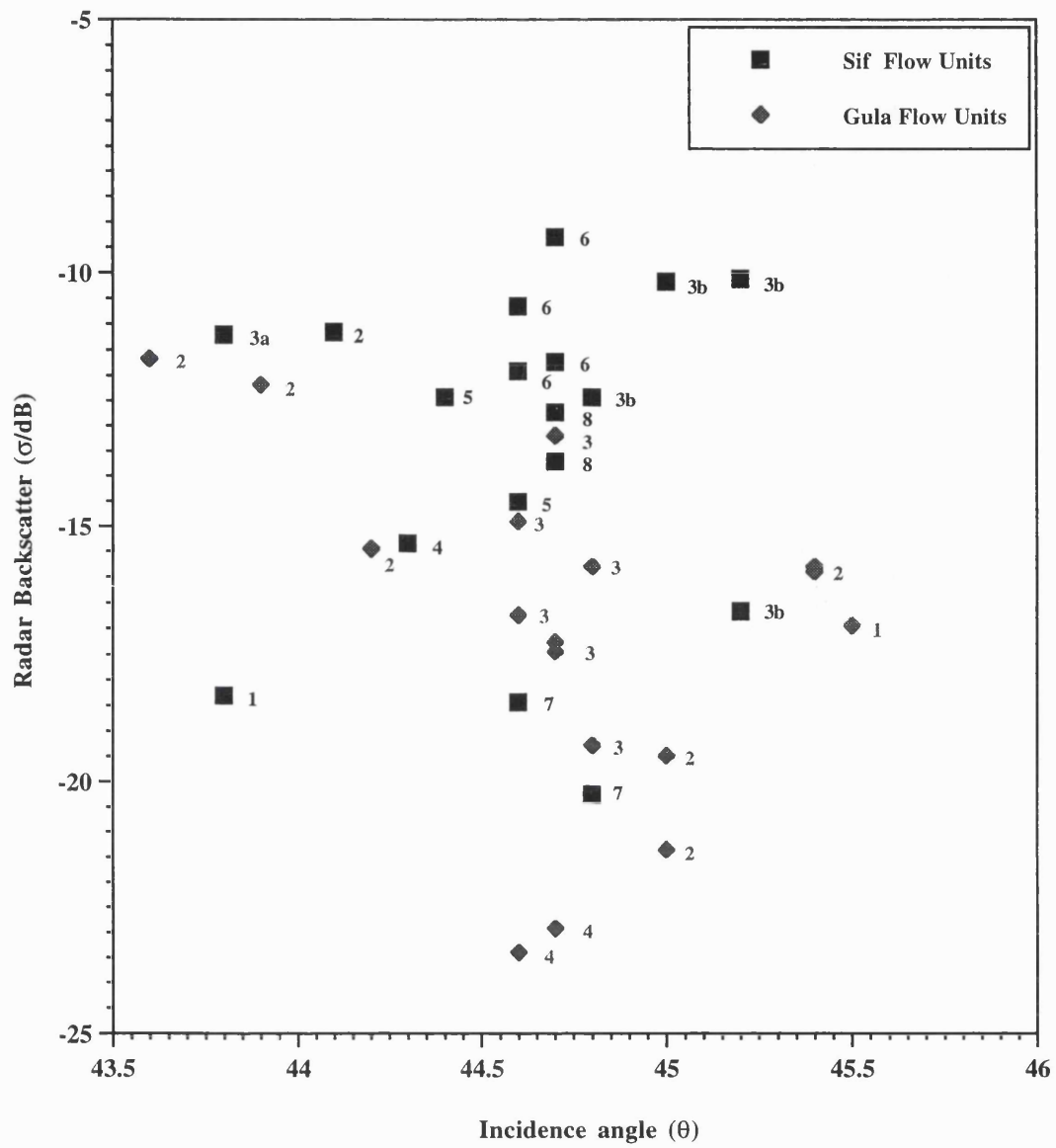


Figure 5.6 Radar backscatter for Sif and Gula Montes flow units.

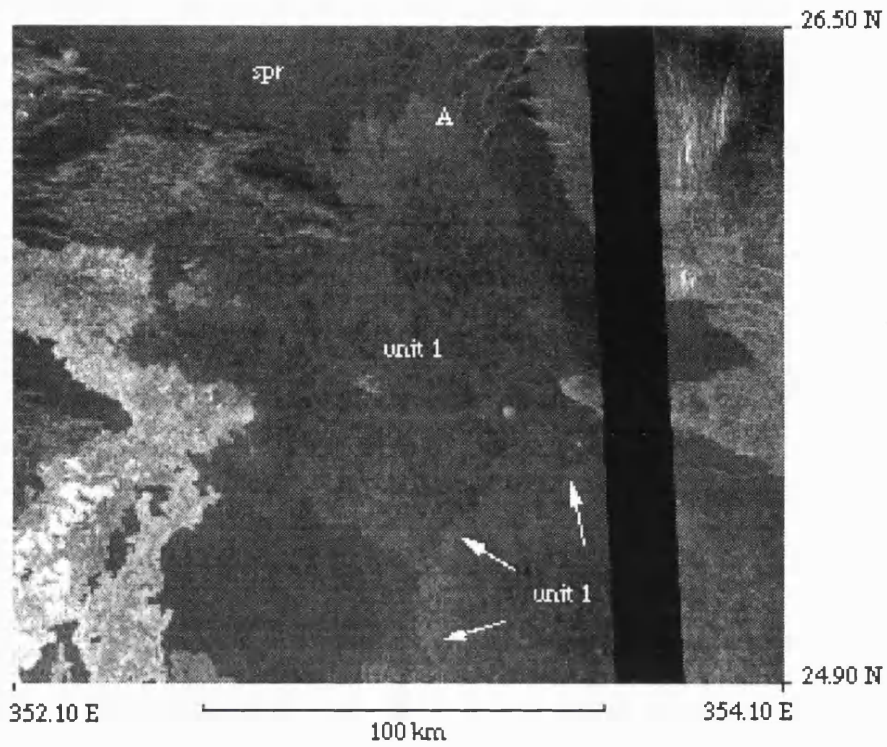


Figure 5.7 Unit 1 flow materials. These flow materials have a simple sheet-like morphology, with a relatively weak radar backscatter. Arrows show the weakly defined flow front which overlies an earlier Unit 1 flow. At A, the contact between Unit 1 and the Sedna Regional Plains materials is observed; Unit 1 overlies wrinkle ridges. Each flow field is typically 100 km across (F-MIDR.25N351;1 browse).

Weakly defined interior flow fronts show that broad individual sheet-flows overlie each other (e.g. in the vicinity of 25.50° N, 353.35° E, Figure 5.7). Surface structure is lacking. Flows associated with Unit 1 overlie (and so postdate) wrinkle ridge structures that deform the local regional plains (e.g. seen in the region of 26.30° N, 353.15° E, Figure 5.7).

The Unit 1 materials of Gula Mons are less well exposed, show more flow structure, and appear more mottled than Unit 1 materials at Sif Mons. The materials are deformed by wrinkle ridges at 16.5° N, 357° E (Figure 5.8).

Eruptive Style

Radar characteristics of the Unit 1 materials imply a relatively smooth, constant surface texture at 12.6 cm and rms-slope scales. What eruptive style do these observations imply? The type of surface texture which develops on a lava flow depends on a number of factors, in particular, for a given rheology, on the thickness of the crust and the amount and rate of shear the crust experiences (*Guest et al.*, 1995, 1996). A flow which comes to rest before the formation of a surface crust is likely to later develop a crust which undergoes practically no shear deformation, hence is likely to be smooth (hence relatively radar dark). A thin crust which develops while the flow is still moving may deform into ropes, typical of pahoehoe textures seen at terrestrial volcanoes. Thicker crusts may break into slabs, and with continued cooling and consequential crustal thickening, produces block and clinker crusts associated with terrestrial aa (*Guest et al.*, 1995, 1996).

Observations from Mt. Etna (*Sparks and Pinkerton*, 1978) and Hawaii (*Roland and Walker*, 1990) show pahoehoe and aa form by low and high effusion rates respectively, but this may not be the case with flows on Venus. It is considered that the formation of an extensive uniform smooth lava crust on Venus (similar to that of Unit 1) may be achieved by more rapid effusion rates in comparison to those on Earth, with the crust forming after the eruption ceases.



Figure 5.8 Gula Mons Unit 1 flow materials. The materials overlie the Guinevere regional plains materials but appear to be deformed by wrinkle ridges which deform the regional plains (C1MIDR.15N352;1 Framelet 26).

The ambient temperature and pressure on Venus may aid in the emplacement of such rapid extensive flows; flows on Venus are predicted to be generally longer with thinner crusts (*Head and Wilson, 1986*).

The morphology, areal extent, and inferred surface texture of Unit 1 flows (particularly at Sif Mons) are analogous to terrestrial basaltic flows. Furthermore, the observed dielectric coefficient for Unit 1 (3.9 to 6.3 see Table 5.2) is consistent with terrestrial material of basaltic composition (*Ulaby et al., 1990; Campbell, 1995*). At Etna, early stage volcanism is represented by extensive basaltic flows, for instance early tholeiitic basalts (*Cristofolini, 1973; Rittmann, 1973*). While the materials of Unit 1 are established as being older than subsequent overlying flows, it is not possible to determine if they represent initial volcanism; preceding flows may have been covered by Unit 1 materials.

Other volcanoes show similar relatively early units. Sapas Mons (8.5⁰ N, 188.0⁰ E, *Keddie and Head, 1994*), Sekmet Mons (44.2⁰ N, 240.8⁰ E, *Edmunds, 1995*), four large shields in Dione Regio (*Keddie and Head, 1995*), and Kali Mons (9.3⁰ N, 29.3⁰ E) all display early materials typified by a relatively weak backscatter and a homogeneous surface texture (inferred from radar data). The materials are areally extensive and have been extruded onto local regional plains materials. At Kali Mons the flow thickness is considered relatively thin as the materials are topographically controlled by wrinkle ridges locally.

5.3.2 Compound Flow Fields of Sif and Montes

Overlain on the Unit 1 materials of Sif and Gula Montes are a sequence of compound flow fields (mapped in Figures 5.4 and 5.5). Terrestrial compound lava flows are defined as those which are divisible into smaller individual flows, in comparison to simple flows which are not divisible (*Walker, 1971*). The materials of Unit 1 (described above) are interpreted as dominantly simple flows, full resolution data show them to be discrete and extensive.

The bulk of subsequent flow units at Sif and Gula Montes are considered as compound flows. Full resolution data show the flow fields consist of many individual flows. However, as stated above, care should be taken when applying this classification to Venusian volcanic materials as the age relation between flows is often difficult to establish owing to the limited resolution of 120 meters, and complications arising from identification and interpretation using radar data.

5.3.3 Sif Mons

Units 2 and 3 of Sif Mons display a range of morphologies and radar backscatter values which imply varying surface textures and emplacement mechanisms (Figure 5.9). The bulk of units are distinguished by a considerably greater radar return in comparison with Unit 1 materials. Many flows show greater aspect ratios (aspect ratio is defined here as the ratio of the length to width of the flow as seen in planimetric form), and consequently have a pronounced digitate appearance (Figure 5.9). The distal margins of some flows are topographically controlled by pre-existing structures, for example linear structures interpreted as graben located at 24.70° N, 351.60° E (Figure 5.10). Flows associated with Unit 3a extend the greatest distance, approximately 700 km from Sif Mons.

A radar-dark sinuous channel (20.0° N, 350.0° E) enhanced by superficial crater materials, occurs in Unit 3b (Figure 5.11). Magellan resolution hampers the identification of this feature, however, its sinuous nature and radar bright inner right wall is indicative of a depression. The channel has a relatively constant width (3 km) which can be traced for approximately 60 km, and terminates downslope in a fan of flow materials with a strong radar backscatter.

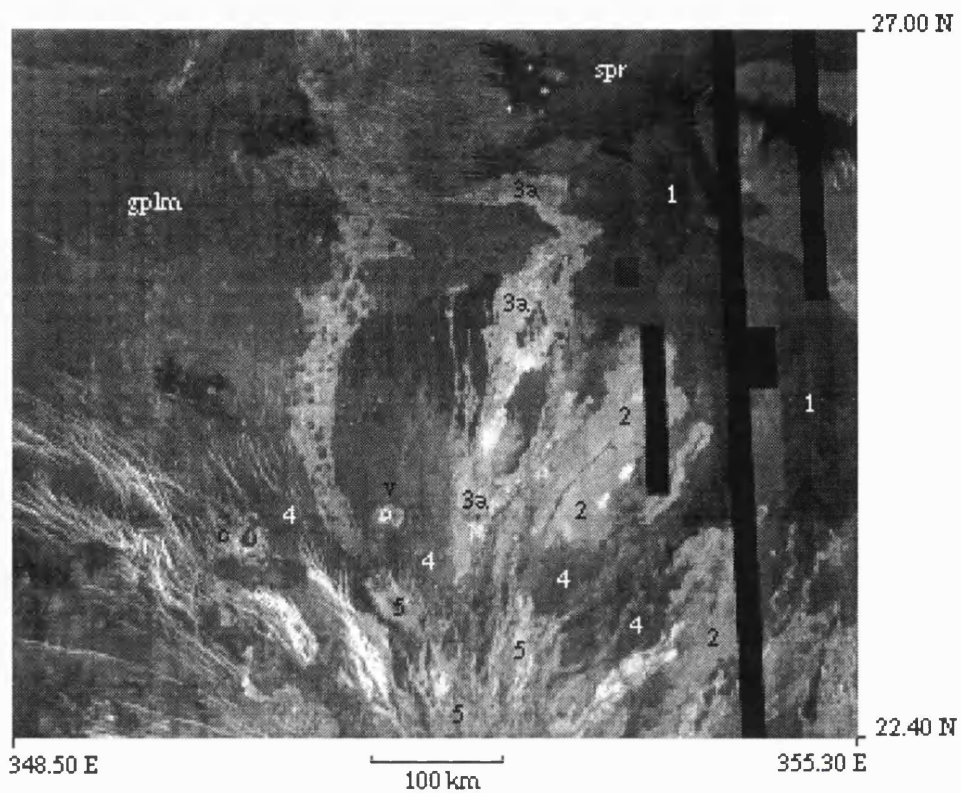


Figure 5.9 Flow units observed on the northern flank of Sif Mons. Numbers correspond to flow units described in the text. Note the diversity of morphology and radar backscatter of these materials. C marks an embayed crater. V marks a small volcano, considered the source of the flow unit to the west (extending north) with a relatively strong radar return (C1-MIDR351;1 browse).

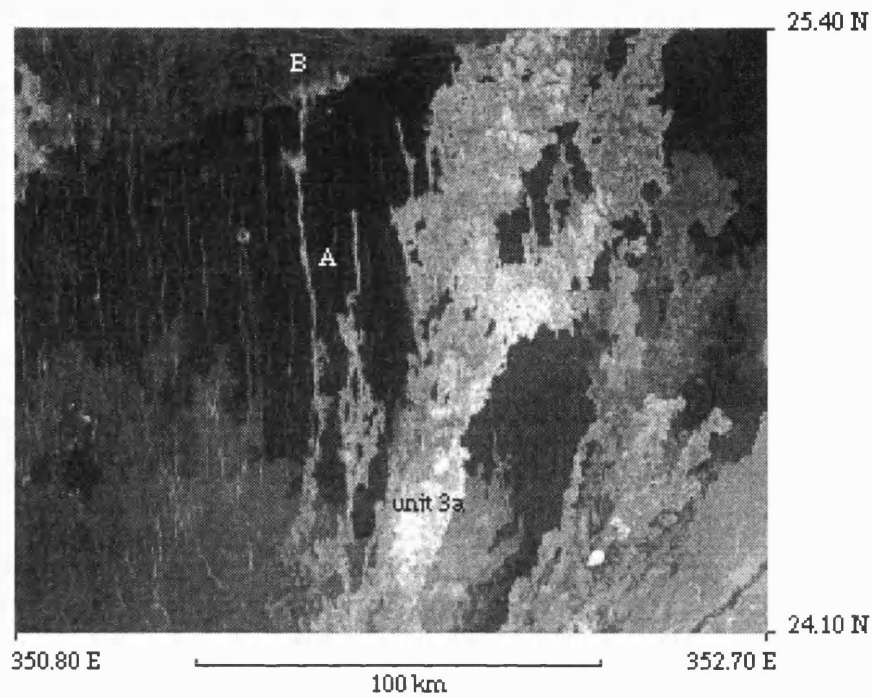


Figure 5.10 Controlled flows of Unit 3a. A shows flows which have been captured and channelled by fractures (graben) which trend N-S. At B, the flow is ponded against the topographic barrier of lineated and mottled plains materials (C-MIDR.25N351;1 browse).

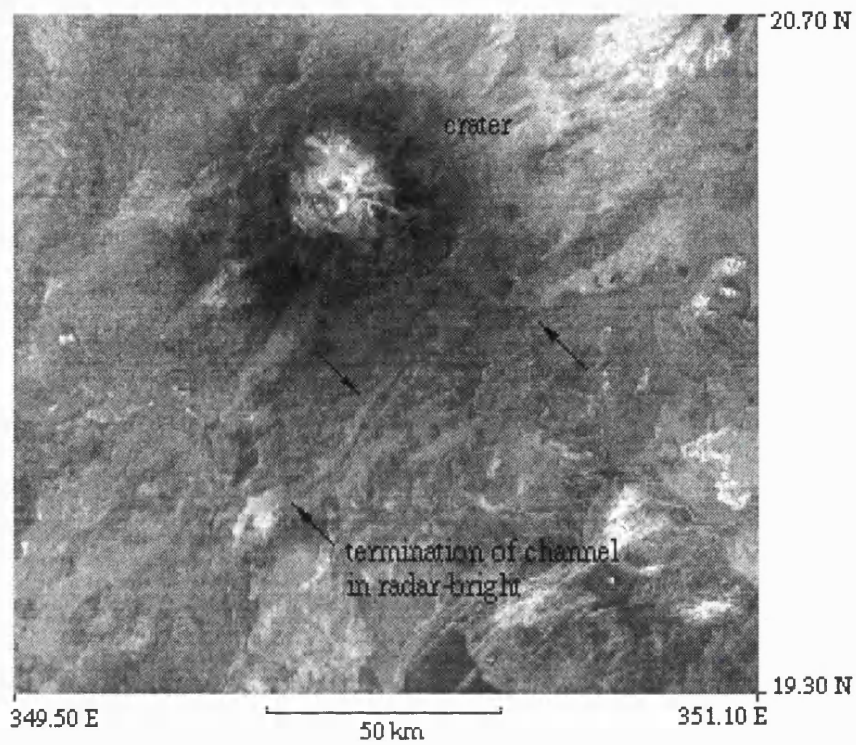


Figure 5.11 Identification of a channel within the flow materials of Unit 3b. The channel has been enhanced by the surficial deposit from the nearby crater (F1-MIDR.20N351;1 browse).

Units 4, 5 and 8 show variable morphologies, which range from sheets to more sinuous flows which have lobate and digitate margins (Figures 5.8 and 5.12). Within a western flow of Unit 5, full resolution FMAP data show a line of oval depressions or pits, 25 km long, which range between 450 and 600 metres in diameter (Figure 5.13). The pits parallel the direction of flow. No resolvable extruded materials are associated with the pits.

5.3.4 Gula Mons

In contrast to the number of Sif Mons units described above, only two major units are identified which overlie Unit 1 materials of Gula Mons (labelled Units 2 and 3 Figure 3.5). The radar characteristics and morphology of these two units are relatively similar. Radar images show the bulk of flows have a pronounced mottled appearance (Figures 5.14 and 5.15). Flow materials of Unit 2 have highly dendritic, sinuous morphologies frequently delineated by radar-bright margins. Unit 3 materials show a sheet-like structure on the order of 10s of kilometres proximal to the summit, however, their morphology changes downslope to flows which have greater aspect ratios and dendritic flow fronts; the change in morphology typically occurs near the lower break of slope at the foot of the main edifice.

Captured flows are identified at Gula Mons, associated with extensional structures of Gour Linea and SW graben which extend from near the summit of the volcano (Figure 5.14). At 22.0⁰ N, 359.1⁰ E a sinuous flow crosses NE-SW trending graben, approximately 1.2 km wide, and materials have flowed downslope along the graben and emerged from the terminus of the graben some 25 km to the SW. The flows are cut by bright linear and curve-linear features which have lengths on the order of 100s of kilometres (Figure 5.5).

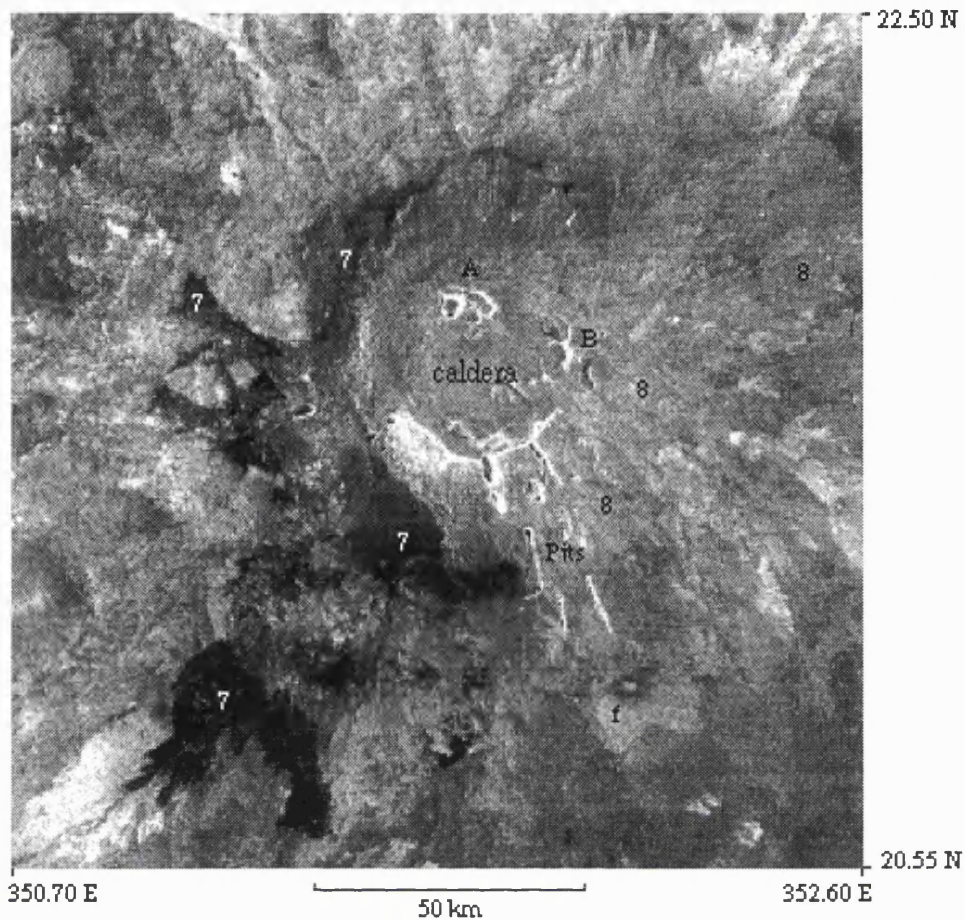


Figure 5.12 The summit region of Sif Mons. A and B mark smaller nested calderas within the main caldera. All but the southern region of the main caldera has been breached by flows. Units 7 and 8 are marked. Unit 7 has the weakest radar backscatter of all Sif flow materials and is interpreted to have a smooth surface, possibly of pyroclastic origin. Unit 8 is interpreted as compound flow materials; the most recent materials identified at Sif Mons. f marks a flank eruptive site (F-MIDR20N351;1 browse).

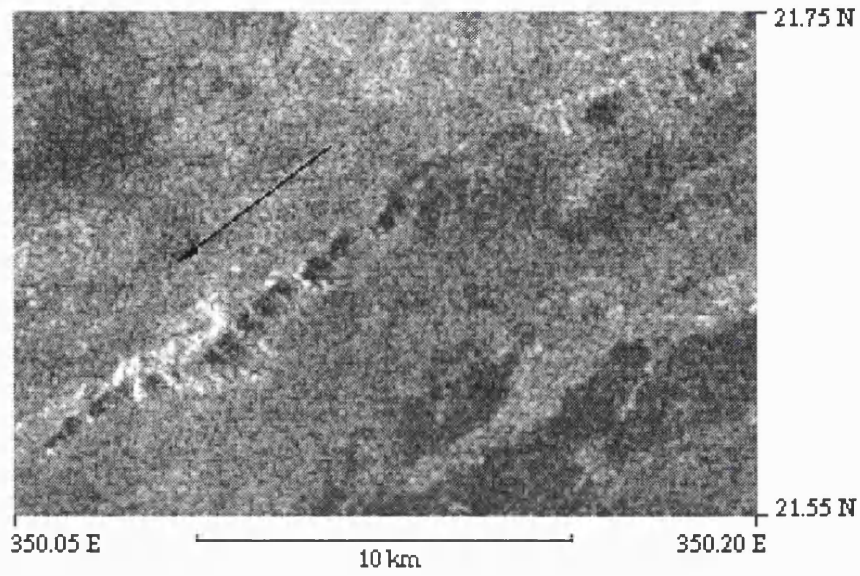


Figure 5.13 Site of possible collapsed lava tube seen within Unit 5 of Sif Mons. Approximately 23 depressions (skylights) are observed (between 450m and 600m in diameter) and extend for approximately 20 km (F-MIDR.20N351;1 Framelet 11).

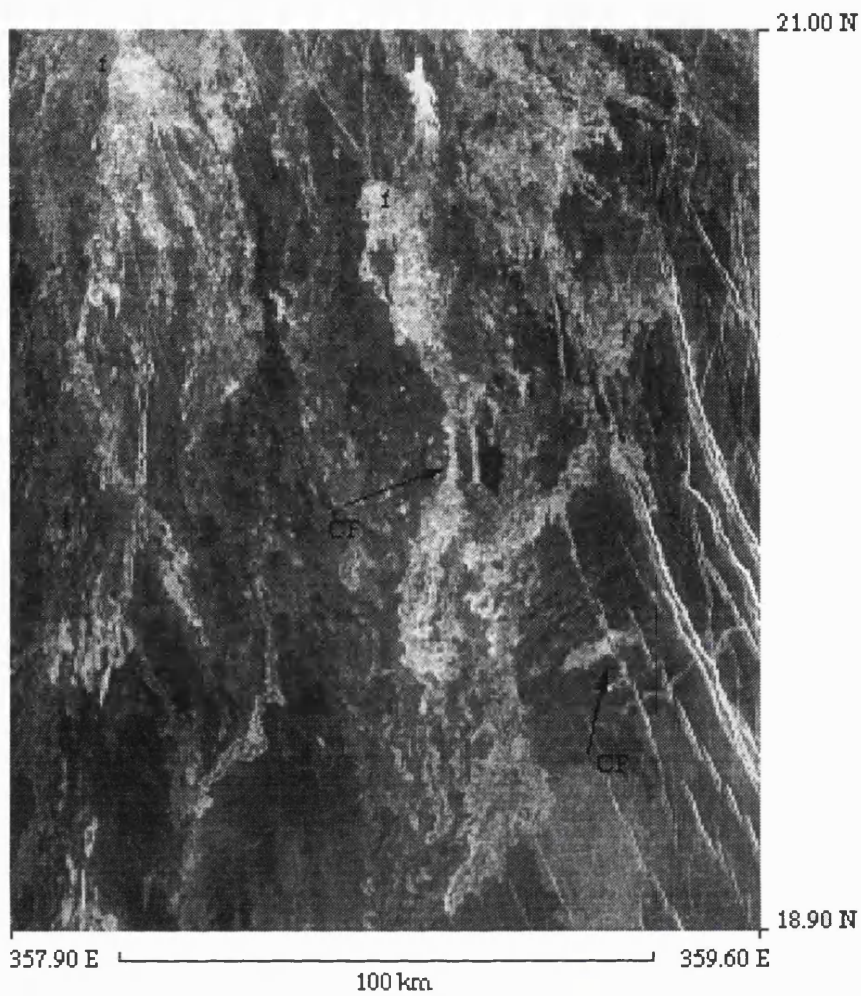


Figure 5.14 Digitate flows located on the southern flank of Gula Mons. CF show flows captured by graben associated with Guor Linea, f mark sites of possible flank eruptive sites (F-MIDR.20N357;1 browse).

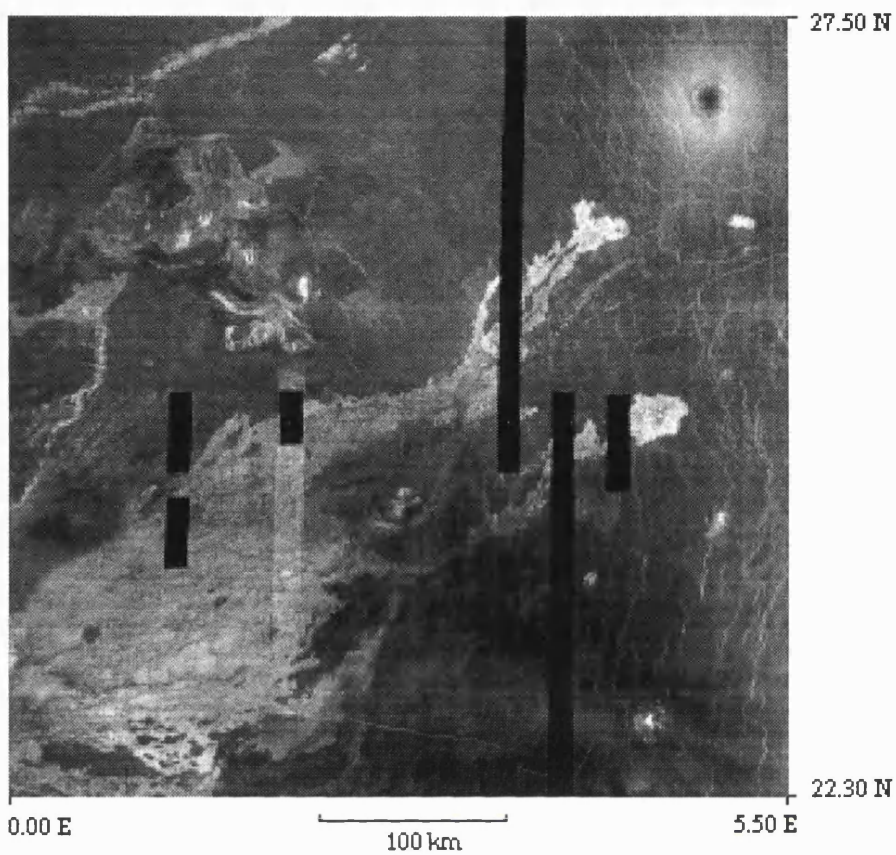


Figure 5.15 Compound flow field seen to the NE of Gula Mons. The flows have a mottled appearance, sinuous morphology and do not show a great variation in radar backscatter (C1MIDR.30N009, Browse).

Eruptive styles

What eruptive styles may be inferred from the observations at Sif and Gula? Empirical data from Mt. Etna show that whether a flow is compound or simple may be linked primarily to the rate of extrusion and duration of eruption; a low rate, long duration eruption favours compound flow formation, while a high rate, short duration eruption favours simple flow formation (*Walker*, 1967, 1971). Furthermore, *Walker* (1971) suggests that the critical extrusion rate at which a compound flow forms over a simple flow is controlled by viscosity, with greater viscosity giving rise to more compound style flow units.

If similar processes described by *Walker* (1971) are applicable to large venusian volcanoes, the observed change from simple flows (Unit 1) to compound flows at Sif and Gula Montes, may indicate an initial high effusion rate followed by lower effusion rates. Sif Mons shows a stratigraphic sequence which consists of less extensive flows over time. An evolving magma may explain a change in viscosity and observed flow morphology seen at Sif Mons.

Interpretation of structures within individual flows suggests both channel and tube-fed emplacement mechanisms have occurred at Sif Mons. The line of pits within Unit 5 resembles aerial photographs of Sullivan's Cave and Bear Trap lava tubes in the Eastern Snake River Plains volcanic province, Idaho, USA (*Greeley and King*, 1977). Here, the pits represent segments of roof collapse along the tube. A similar interpretation may explain the pits in Unit 5 (Sif Mons). No associated effusive materials preclude the surface manifestation of a dyke.

Swanson (1973) showed the transport of lava from tube-fed flows at Kilauea (1969-1971 eruption) was almost isothermal, cooling at a rate of about 1°C per kilometre. Such a cooling rate combined with an adequate volume of lava can produce long tube fed flows at very low effusion rates (approximately 12 km long for an effusion rate of 4 m³/s). A survey of Mauna Loa by *Greeley et al.* (1976), concluded that more than 80% of exposed lava flows at least partly involved flow emplacement through lava tubes and

channels. However at Hawaii, many such flows are terminated when they meet the chilling effect of the sea. If the flows were allowed to cool to their solidus, such eruptions might form flows 200 km long, provided they remained tube-fed (*Swanson, 1973, Malin, 1980*). Hence the longer flow lengths observed at many venusian volcanoes, in comparison with terrestrial volcanoes (*Schaber, 1990*) may be a consequence of tube-fed emplacement. However, flows at Sif and Gula Mons are considered to be channel fed as well as tube fed.

5.3.5 Flank Eruptive Sites at Sif Mons

Flank eruptive sites are common at terrestrial volcanoes (*Wadge et al., 1975, 1977; Fisk and Jackson, 1971*). Throughout its history, numerous flank eruptions have occurred at Mt. Etna, owing to the lateral extension of dykes which transport magma away from the central caldera (*Wadge, 1975, 1977; Chester et al., 1985*).

Contrary to the conclusion that large venusian volcanoes lack flank eruptive sites (*Keddie and Head, 1994*), Sif Mons offers evidence for just such a style of eruption. Identified on the eastern flank of Sif Mons are six relatively small flow fields which radiate fan-like from small edifices (<5 km in diameter) surmounted by summit pits (Figure 5.16). The materials which compose the fans have a relatively strong radar backscatter and are mottled in the imagery (Figure 5.16). Ancillary data show the materials are relatively rough at rms scales (Table 5.2). Flows within the fields have a dendritic, sinuous morphology. Topographic data show the location of the small edifices correspond with the break of slope of the main edifice of Sif, measured approximately 100 km from the centre of the summit.

The pits, from which the fan shaped flows originate, are surrounded by a diffuse, radar-dark deposit. The dark deposits are topographically controlled, the minimum extension of the material occurs up-slope, while greatest extension (a maximum of 8 km) occur downslope of the pits.

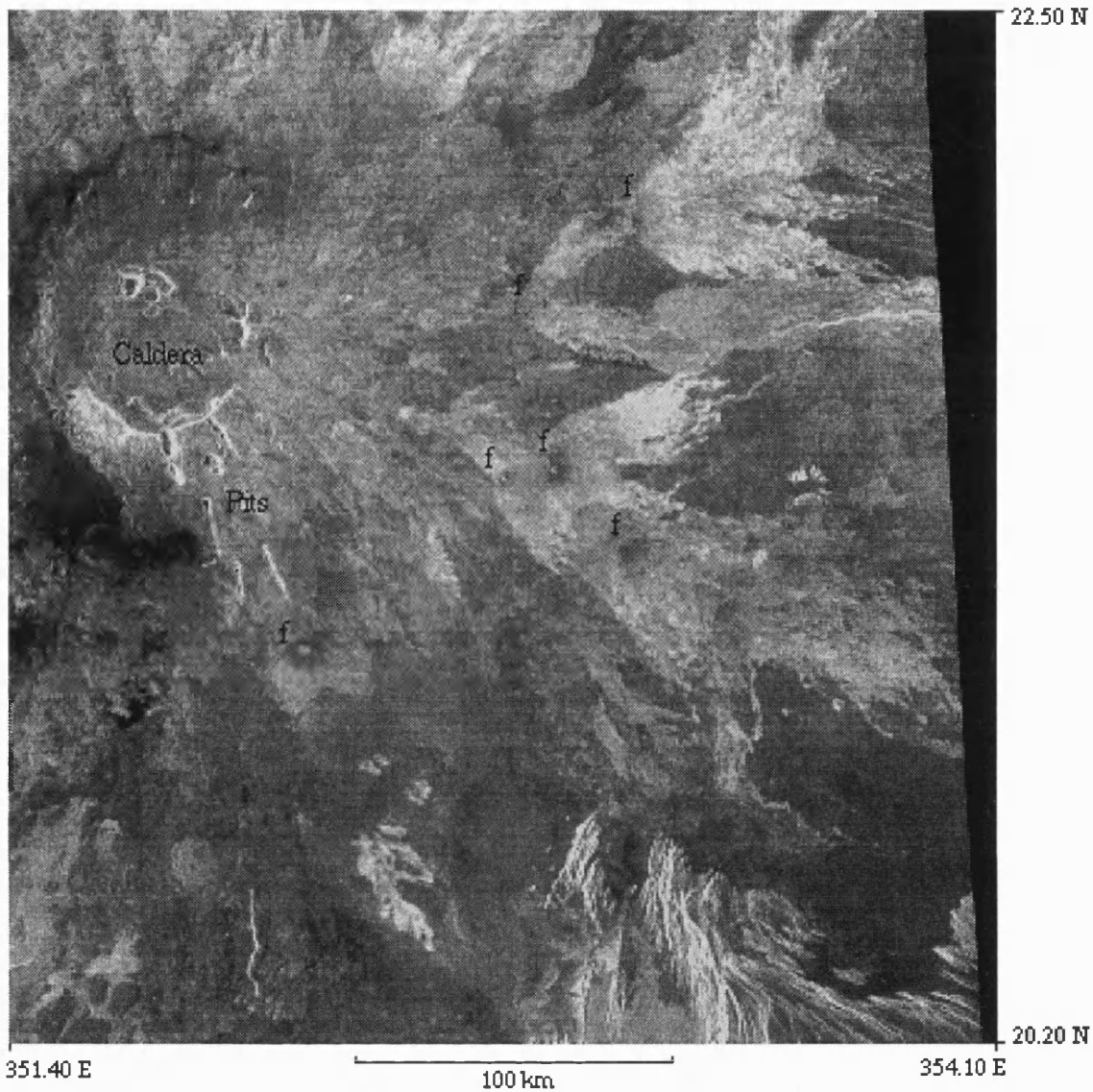


Figure 5.16 Location of interpreted flank eruptive sites (f) on the eastern flank of Sif Mons. The sites are identified by a small bright pit, surrounded by diffuse topographically controlled materials which have a weak radar backscatter. Flow fields are associated with the pits, and show a digitate morphology at their termination. The flow materials have a strong radar backscatter (F-MIDR.20N351;1 browse).

Eruptive style

The radar-bright fan-shaped deposits of Unit 6 are interpreted as the product of flank eruptions. The smaller, radar-dark topographically controlled materials which surround the pits of the small edifices are interpreted as thin, relatively fine-grained pyroclastic deposits. In comparison, Gula Mons has only two possible flank eruption sites located in the vicinity of 358.30° E, 21.85° N (Figure 5.14). No diffuse materials surround these sites.

The lack of flank eruptive sites at Gula Mons is considered to be a consequence of different internal plumbing, discussed later in the chapter. The emplacement of undifferentiated flow materials (Unit fu1 and fu2) which lie approximately 300 km from the summit of Sif (351.30° E, 19.20° N) are interpreted as either materials originating from either flank eruptive sites, or from separate volcanic centres.

5.3.6 Diffuse Volcanic Materials near the Summits of Sif and Gula Montes

Located near the summits of both volcanoes are materials which display a similar morphology and radar backscatter, labelled Unit 7 (Sif Mons, Figure 5.12) and Unit 4 (Gula Mons, Figure 5.17). The units have the weakest radar backscatter of materials seen at both volcanoes. They have a prominent mottled surface appearance in radar images. The boundaries of the units are irregular, lobate, and in places, diffuse. The materials are topographically controlled. Full resolution data show a weakly defined striated texture contained within Unit 7 materials closest to the summit of Sif Mons. Similar deposits are observed near the summits of other large shield volcanoes including Kunapipi Mons (86.0° E, 33° S) and Sapas Mons (*Keddie and Head, 1994*).

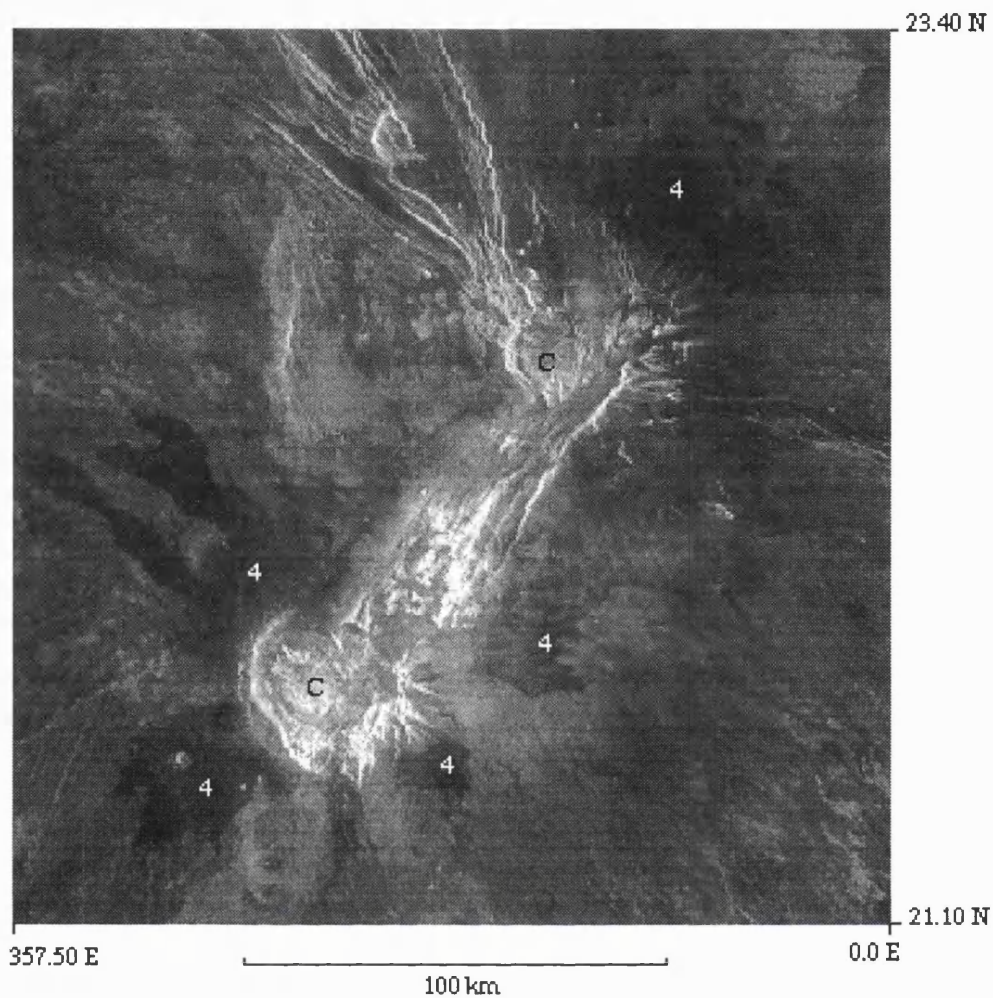


Figure 5.17 The summit region of Gula Mons. Two modified calderas (marked C) are joined by a series of fractures interpreted to represent a rift. Unit 4 (marked 4) has the weakest radar backscatter of all Gula Mons materials and is analogous to Unit 7 near the summit of Sif Mons (C2-MIDR.30N335;2 framelet 40).

Eruptive style

Based on radar and ancillary data, *Keddie and Head*, (1994), interpreted the materials at Sapas Mons as 'young' mass-wasting deposits which surround two summit domes. The materials at Sapas have a strong emissivity and weak reflectivity, contrary to most materials near the summits of high volcanoes, which typically show the reverse, considered symptomatic of in-situ weathering (*Pettengill et al.*, 1988; *Klose et al.*, 1992). Unlike the materials near the summit of Sapas, those at Sif and Gula Montes have a strong reflectivity and complementing weak emissivity, hence may have undergone weathering. Furthermore, they have a considerably greater areal extent.

An alternative interpretation proposed here is that the materials may represent pyroclastic deposits. Pyroclastic deposits at Kilauea (*Gaddis et al.* 1989) and Mt. Etna (compare linear dB values in Tables 5.1 and 5.2 and Figures 5.3 and 5.6) have similar radar characteristics to Unit 7 and 4 of Sif and Gula Montes. The pyroclastic deposits at the terrestrial volcanoes represent materials which have the weakest radar backscatter and locally display a mottled appearance in radar data. Units 4 and 7 are interpreted as having similar smooth surface textures to those at Mt. Etna and Kilauea, and may have formed from similar styles of eruptive activity.

Units 7 and 4 may represent welded pyroclastic deposits similar to those predicted by *Kieffer* (1995, see Chapter 2, 2.6.3). In contrast to pyroclastic deposits on Earth, pyroclastic flows are predicted to travel greater distances on Venus owing to the hotter ambient temperature (*Head and Wilson*, 1986; *Kieffer*, 1995). Such a mechanism would account for the materials being topographically controlled, and may explain the observations of striations which parallel the long-axis of the materials. The striations may have arisen from flow emplacement.

5.4 Comparison of Flow Materials at Sif and Gula Montes

The observations from radar data of Sif and Gula Montes presented above show that the materials which compose the two volcanoes have both similarities and differences. In common, the first identified flow materials are relatively smooth and extensive, interpreted as a relatively rapid voluminous extrusive event. Second, both volcanoes have a sequence of units which overlie Unit 1 materials. The bulk of these units are interpreted as compound flows. Third, the two volcanoes have relatively young diffuse materials located near their summits. However, the contrasts in the flows at each volcano outnumber the similarities, summarised below:

1. It is noted that many Gula Mons flows are considerably longer and have a greater sinuosity than those at Sif.
2. Materials within individual flow units show a greater variation in radar backscatter and morphology at Sif Mons.
3. A greater diversity of radar backscatter and morphology is observed at Sif Mons when flow units are compared with each other.
4. Six flank eruptive sites are identified at Sif Mons. Flank eruptive sites are generally lacking at Gula Mons.

The differences outlined above are considered a result of different internal and evolutionary styles of the two volcanoes. Before considering the differences, the gross morphology and summit structure of the volcanoes are discussed.

5.5 Description and Comparison of the Gross Morphology and Summit Structure of Sif and Gula Montes

Perhaps the most distinctive contrast between Sif and Gula Montes is their gross morphology and summit structure. Synthetic stereo images show Sif has an approximate conical shape, while Gula is more elongate, with its long axis trending NE-SW. Both volcanoes have pronounced central edifices with relatively high angles of slope in comparison to their distal flanks (Figures 5.18 and 5.19). The slope angle is reduced abruptly approximately 100 km and 150 km from the summits of Sif and Gula respectively.

While the diameter of Mt. Etna is considerably smaller than the venusian volcanoes, (~40 km compared with 350 km and 450 km for Sif and Gula respectively), the variation of flank slope is similar. Mt. Etna has concave slopes rising from the base at $<5^{\circ}$ increasing to $<10^{\circ}$ below 1800 m. However, the cone of the volcano has slopes of 20° or more (*Guest, 1982*). The consequence is a volcanic edifice which has a relatively steep cone surrounded by much shallower sloping flanks. Measurements of the southern flank of Sif Mons show distal flank slopes of between 0.15° and 0.25° , while the slope of the cone is approximately ten times greater: a marked break in slope is observed (Figure 5.18). The distal flanks of Gula Mons are typically 0.2° , with the slopes of the central edifice varying between 2° and 3.5° (Figure 5.19).

Guest and Murray (1979) and *Guest (1982)* suggest the steeper sided summit region of Mt. Etna probably owes its form to numerous eruptions near the summit region, resulting in greater edifice construction than the outer flanks which, by comparison, form from less frequent flank eruptions. A similar process at Sif and Gula Montes may explain the steep prominent cone and shallower flank morphology.

The summit of Sif Mons is surmounted by a circular depression 40 km in diameter, interpreted as a caldera (*Campbell et al., 1989; Campbell and Campbell, 1990; Senske et al., 1992*). The main caldera has a prominent southern rim from which a series of small (<1.7 km in diameter) linear pits extend to the SE

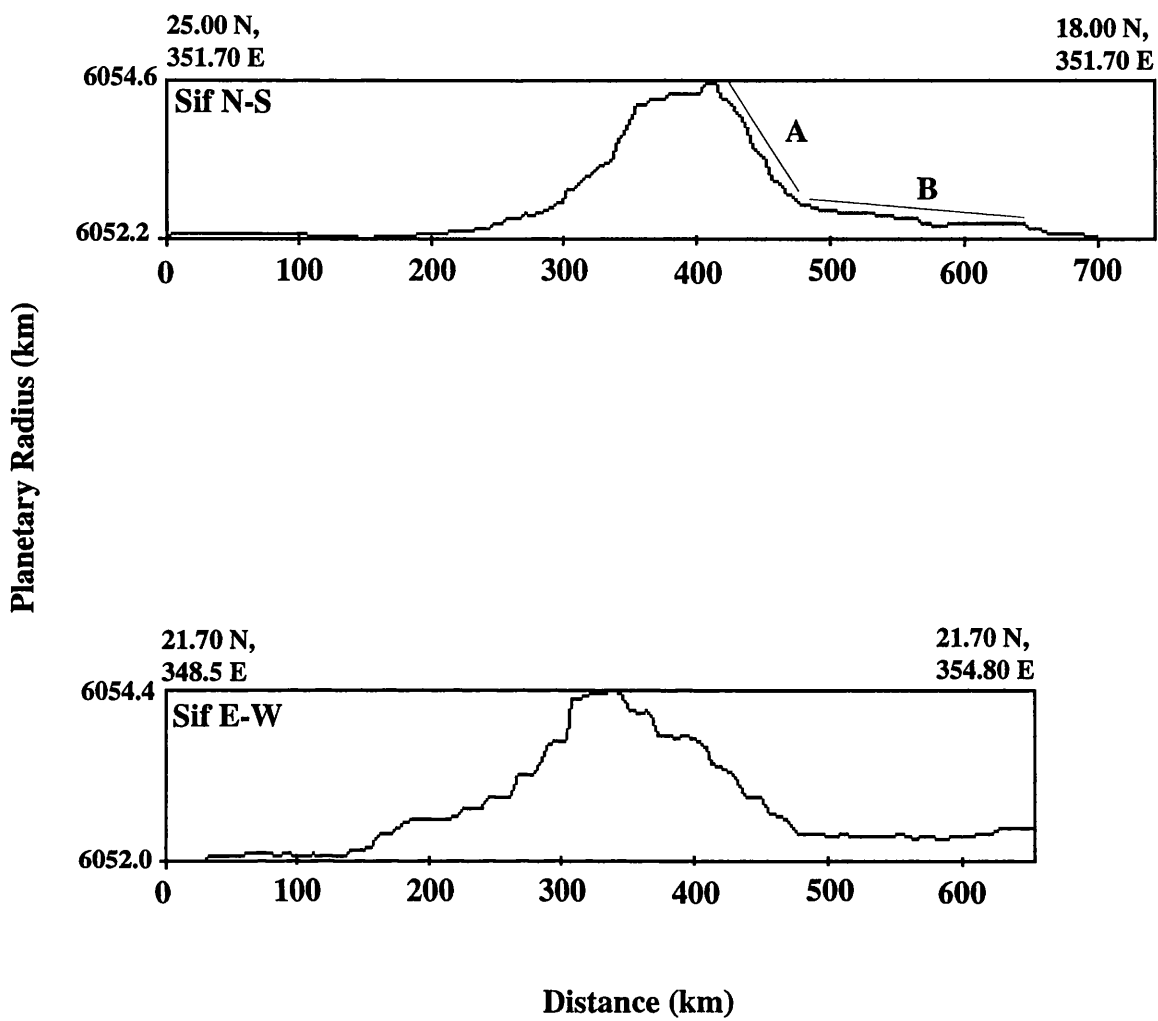


Figure 5.18 Topographic profiles of Sif Mons. The slope of the central edifice (A) is considerable greater than the outer flanks (B). A similar situation is observed at Mt. Etna.

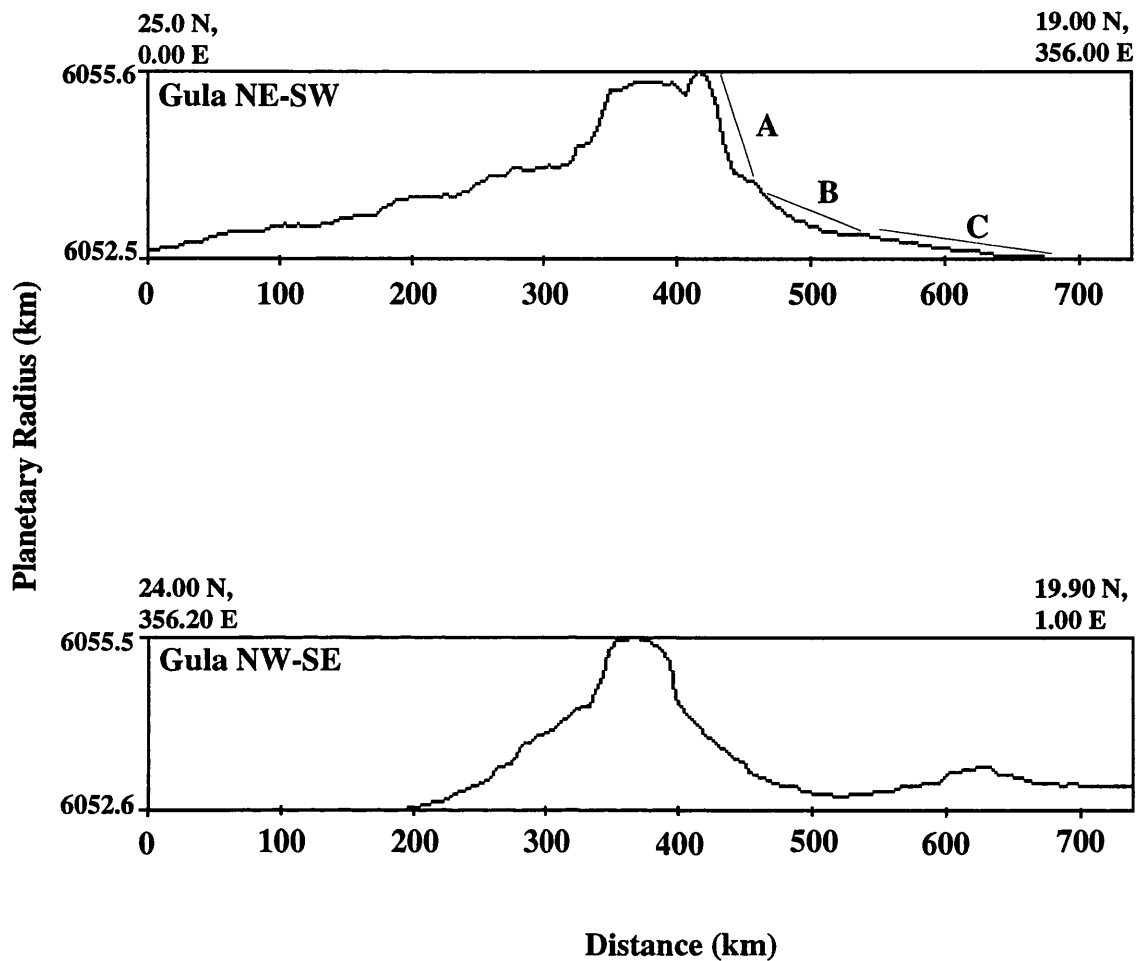


Figure 5.19 Topographic profiles of Gula Mons. Three distinctive breaks in slope are identified by A, B and C. The main slope of the edifice is approximately 10 times greater than the flanks of the volcano.

for approximately 50 km (Figure 5.12). The northern, western and eastern sections of the main caldera rim are lower and less well defined. Unit 8 flow materials originate from two interior nested calderas approximately 10 km in diameter (Figure 5.12) and breach all but the southern section of the main caldera.

In contrast, the summit of Gula is demarcated by an upstanding zone of NE-SW trending fractures. The fracture zone (~155 km long and 35 km wide) terminates at each end in a circular and arcuate landform (Figure 5.17). Topographic data show both circular structures have centres which appear upstanding. The SW structure is higher and covers a larger surface area than the NE structure. The NE caldera has a number of small semi-circular collapse structures associated with it (<15 km in diameter). Both fracture zone and circular structures have a strong radar backscatter.

As with terrestrial volcanoes, observations of summit structures at Sif and Gula Montes may be used to infer internal processes. Calderas on Earth form by collapse in three ways: (1) explosive eruptions which result in the rapid evacuation of magma; (2) by the amalgamation of minor intrusions (dykes) which result in an increased density and lead to subsidence; and (3) owing to magma withdrawal from a high level reservoir. The presence of a large caldera and subsequent smaller nested caldera at the summit of Sif is significant in indicating phases of magma withdrawal from a reservoir over time.

The fracture zone at the summit of Gula Mons is considered analogous to rift zones associated with terrestrial volcanic centres for instance Kilauea, albeit on a larger scale at Gula. The circular features are interpreted as calderas which have subsequently been modified and possibly contain lava domes. Hence, two styles of summit structure are observed at Gula, modified calderas and a primary rift zone. Along with flow morphology, the contrasting summit structures observed at Sif and Gula imply different magma storage and stress regimes for each volcano which have occurred over time, which are now discussed.

5.6 The Internal Dynamics and Evolution of Sif and Gula Montes.

From observations of the morphology and interpreted eruptive and emplacement mechanisms of Sif and Gula flow materials, inferences may be made regarding the internal dynamics and evolution of the two volcanoes. These inferences may be used to explain the morphological differences observed between the two volcanoes.

5.6.1 Edifice Morphology and Summit Structure

Why do the two adjacent volcanoes have different edifice and summit morphologies? *Fiske and Jackson* (1972) concluded from material modelling and observations of Hawaiian volcanoes that the local structure and stress regime can play an important role in determining the shape and magma movement within an edifice. First, the geometry of a volcano can be controlled by the regional structure, and second, magma emplacement and movement may be constrained by the stress orientations in a pre-stressed volcano (*Fiske and Jackson, 1972*).

Gula Mons is situated on an extensional rift zone (Gour Linea, Figures 5.1 and 5.5) which strikes NW-SE. Gour Linea predates the bulk of materials from Gula Mons. Furthermore, Gula Mons abuts Idem-Kuva Corona (Figure 5.20). The corona is interpreted to have a protracted history, which post and predates the volcano (Chapter 4, 4.2.1). It is considered here that the initial morphology and subsequent extrusion of flow materials from Gula Mons may have been controlled by the stresses imposed from either Gour Linea or Idem-Kuva Corona, or both. In consequence, the edifice of Gula is elongated in planimetric view and is surmounted by a rift zone which trends in the same direction as the volcano's long axis.

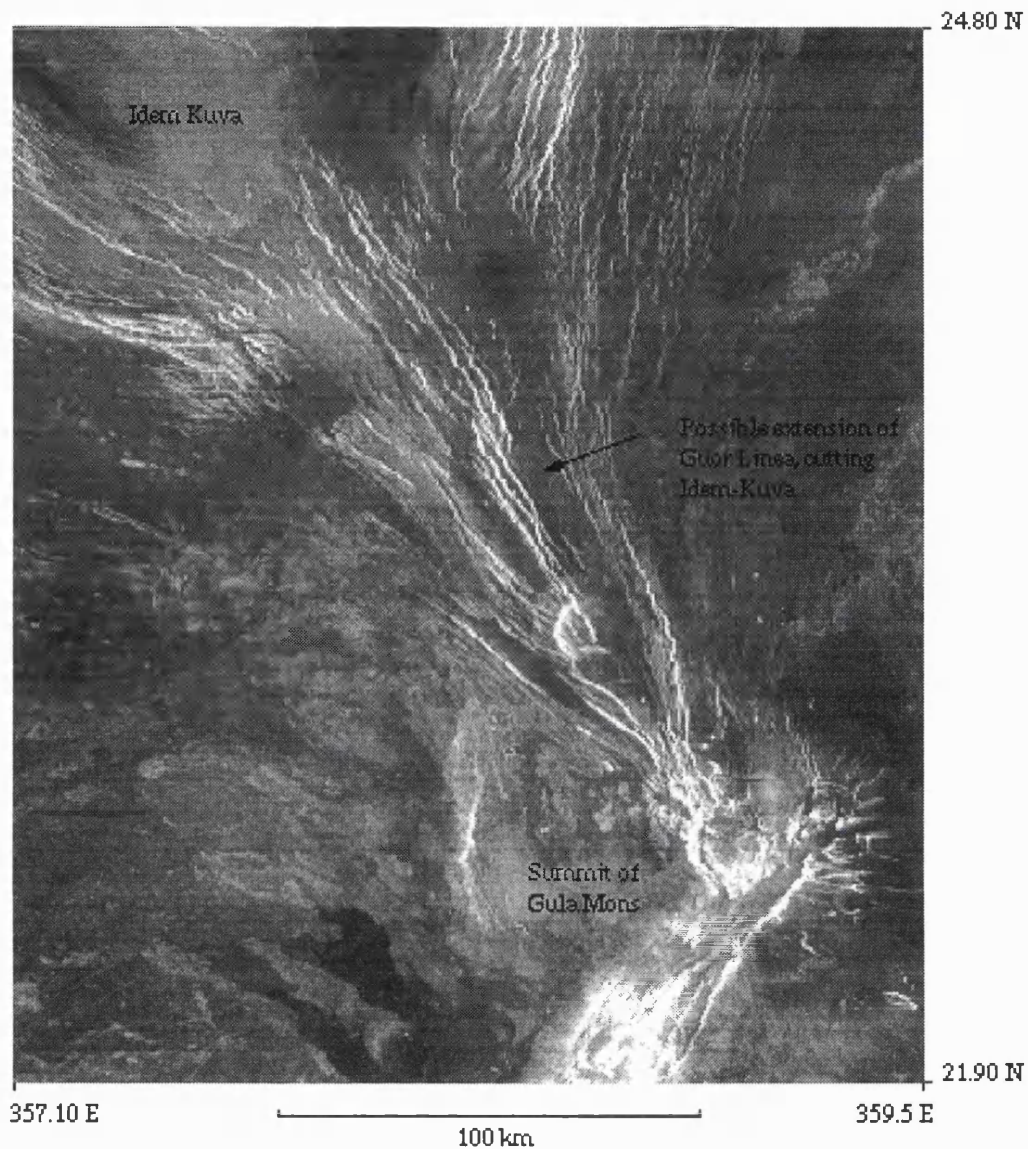


Figure 5.20 The NE flank of Gula Mons is constrained by Idem-Kuva Corona. The gross morphology and summit structure of Gula Mons is considered to be the result of contemporaneous growth of the two volcanic landforms. The NW-SE trending fractures may represent an extension of Guor Linea, and are seen to cut Idem-Kuva Corona (C2-MIDR.30N335;2 framelet 40).

In contrast, Sif Mons is interpreted to have developed relatively uninhibited by regional structure or stress regimes. Consequently, the edifice is approximately circular surmounted by a prominent circular caldera indicative of high-level storage of magma during the volcano's history.

5.6.2 Comparative Flow Morphology

Processes which have resulted in the observed differences between flow morphologies at Sif and Gula Montes may be analogous to the explanation for temporal variation in flow morphology identified at Mt. Etna by *Hughes et al.* (1990). Examination of historic flows from 1750 to the present at Mt. Etna show two distinct morphologic categories: those which are relatively narrow and sinuous, and those which have considerably broader dimensions.

The distribution of the two categories is seen to be sectorial; the broad flows are confined to the eastern sector, while the western and northern flanks contain the long narrow flows. *Hughes et al.* (1990) state that the different flow morphologies are the product of different eruption rates. Typically, the broad flows which occur on the eastern flank of Mt. Etna, are associated with low effusion, long duration eruptions (*Wadge*, 1981). In contrast, the narrow long flows on the western and northern flanks are considered to be the product of relatively greater effusion rates of shorter duration.

It is considered that the difference in eruption style reflects interactions between the volcanic system and the regional and localised gravitational stress fields (*Hughes et al.*, 1990). The unsupported eastern flank of Mt. Etna shows evidence of seaward gravitation (*Guest et al.*, 1984) which produces the dilation of fissures. Owing to fissure dilation, eruption rates are longer and flows broader on this flank. In contrast, the western and northern flanks are buttressed against the Peloritani Mountains and so fissures dilate less easily. Consequently, effusion rates are greater but shorter, and more sinuous flow morphologies occur.

The above terrestrial observation may relate directly to different flow morphologies of Sif and Gula Mons. Similar control of effusion rates and duration may have occurred (or is occurring) at Gula Mons owing to buttressing by Idem-Kuva Corona. In common with the western and northern flows of Mt. Etna, Gula Mons has long sinuous compound flow morphologies seen within Units 2 and 3 (Figures 5.14 and 5.15) In contrast, Sif Mons has broader, shorter flows, similar to those observed on the eastern flank of Mt. Etna, a consequence of low effusive, longer duration eruptions uninhibited by the stresses associated with buttressing.

5.6.3 Internal Plumbing and Evolution

How is magma transported and stored within Sif and Gula Montes? The observation of a prominent caldera complex at the summit of Sif Mons suggests that repetitive intrusion and withdrawal of magma has occurred. Furthermore, evidence for drainage is shown by the flank eruptive sites situated along an arc at the base of the central edifice. It is considered here that magma is transported to a relatively high-level storage reservoir which resides (or has resided) within the volcanic pile of Sif Mons.

Similar internal plumbing is considered for terrestrial volcanoes. Geodetic and seismic data from Hawaiian volcanoes indicate the bulk of intrusive activity occurs within their volcanic piles. Hawaiian shield volcanoes (e.g. Kilauea), also display flank eruptive sites throughout their history (*Fiske and Jackson, 1972*). *Wadge* (1975, 1977) identifies numerous flank eruptions associated with Mt. Etna and suggests they are a consequence of the failure of the central conduit (the Chasm). The failure occurs by fracturing resulting in the horizontal propagation of a vertical fissure which drains the Chasm periodically.

What size was/is the reservoir beneath Sif Mons? *Ryan et al.* (1983) investigated the diameter of collapsed structures at Kilauea and noted that at least one was closely correlated with the horizontal dimension of the underlying reservoir. *Keddie and Head*

(1994) stated that when estimating the size of an underlying reservoir, the stresses which give rise to a caldera may only be associated with its shallowest portion. Hence, for Sif Mons, the 40 km caldera may be indicative of a magma reservoir with a minimum horizontal dimension of similar proportions. This is considerably larger than terrestrial basaltic volcano magma reservoirs, but smaller than those associated with large shield volcanoes on Mars (*Crumpler et al.*, 1996).

In contrast, the lack of a large central caldera at Gula Mons may suggest that, owing to internal stresses, high-level magma reservoir storage at this volcano is infrequent, and that the magma resides mainly beneath the edifice. However, some indication of temporal high-level magma is inferred by the observation of the two small calderas at each end of the rift. In considering the internal plumbing and evolution of Gula, attention is drawn to the conclusions of *Guest and Duncan* (1981) and *Duncan and Guest* (1982) from Mt. Etna.

The eruptive history of Mt. Etna shows a marked dichotomy between pre and post-1669 eruptions (*Guest and Duncan*, 1981, *Duncan and Guest*, 1982). Pre-1669 eruptions were more voluminous and are petrographically distinct from post-1669 eruptions. Larger plagioclase phenocrysts in the pre-1669 lavas are indicative of a period of high level storage whereas post-1669 magmas have much smaller phenocrysts and are interpreted to have risen directly from a magma reservoir between 20 and 25 km below sea-level. The changes in internal plumbing are considered to be a consequence of changes in the local and/or regional stress patterns. Based on the geodetic and petrographic studies of Mt. Etna, *Guest and Duncan* (1981) concluded that there is no simple model of volcano plumbing which can be applied to central basaltic volcanoes; a long-lived volcano may display numerous eruption episodes and yet have changing styles of plumbing throughout its history. The observed rift and calderas at the summit of Gula imply similar complex changes of internal plumbing at this venusian volcano with time.

5.6.4 An Evolutionary Model for Sif and Gula

Incorporating the observations and interpretations discussed above, an evolutionary model for Sif and Gula Montes may be summarised. It is evident that Sif has had distinct phases of formation, resulting in an edifice which, in general, shows a sequence of flows which are considered younger near the summit, similar to that observed at Sapas Mons (*Keddie and Head, 1994*). The first identified volcanism is represented by the voluminous flows (Unit 1), on which subsequent compound flow units were extruded. The flow units have become less extensive over time.

This observation may be explained by two processes. First, a decrease in eruption volume owing to increasing hydrostatic pressure over the time required to erupt magma from the summit caldera. Second, shorter summit eruptions have become dominant over flank eruptions. The latter process has been used to describe the morphology of Mt. Etna, as discussed in 5.5. If such a process has occurred, the relative age between the distal and summit flow materials of Sif Mons may be great.

The presence of the caldera is indicative of magma storage within a reservoir followed by drainage. Flank eruptions indicate lateral magma emplacement has also occurred during the history of Sif. It is considered that the magma reservoir for Sif Mons has remained within the volcanic pile.

In contrast, while Gula Mons show flows which are considered younger nearer the summit than those on the lower flanks, less variation in flow morphology is observed with time in comparison with Sif. The first identified flow materials exposed at Gula Mons are sheet flows, similar to Sif Mons. The subsequent flows of Gula Mons are considered to be the product of a magma reservoir which erupted materials through a volcanic pile controlled by the regional structure and the resulting stresses. These stresses are considered responsible for the elongate morphology and summit rift structure, and resulted in effusion rates which gave rise to long sinuous flows which compose the observed flow fields.

The storage of magma within the volcanic pile of Gula is considered to be intermittent. While two modified calderas are seen, the dominant summit structure is a feature analogous to a rift. The suggestion here that the magma source of Gula lies at greater depth may be supported by the greater height of the volcano. Magmas located at depth are subjected to greater hydrostatic pressure. Greater pressure can result in magma being pushed higher within a central conduit, resulting in the construction of a comparatively taller edifice.

5.7 Implication for Models of Large Shield Volcanism on Venus

How do the observations and interpretations presented here compare with predictions of models of venusian volcanic activity discussed in Chapter 2? Based on numerical modelling, *Head and Wilson* (1992) concluded that for edifices less than approximately 2.5 km in elevation, the magma reservoir will not enter the edifice. However, the prominent nested summit calderas of Sif imply periods of magma storage within the volcanic pile, analogous to the Hawaiian volcanoes. Furthermore, the identification of what are interpreted as flank eruptive sites suggests that magma may have drained from within the volcano in a similar fashion to the drainage of the Chasm at Mt. Etna (*Wadge*, 1975, 1977). Sif Mons stands only 2 km above the local topography and so, according to the Head and Wilson model should lack a magma reservoir within the volcanic pile.

In comparison, Gula stands 3.2 km above the local topography and does not have a well developed nested caldera system. Instead, its summit is demarcated by a prominent rift. It is considered here that the storage of magma within the volcanic pile has been lacking, or at best intermittent. Hence, the Head and Wilson model of magma reservoir position and neutral buoyancy zones does not adequately explain the structures at Sif and Gula Montes. The local structure and internal stress regime of a volcano

may play a greater role in the movement and storage of magma than direct environmental conditions, as in the case of Gula.

A further view on the position of magma reservoirs is presented by *McGovern and Solomon* (1997) in light of recent modelling. Large shield volcanoes on the Earth and Mars typically have a flexural moat which surrounds them, induced by volcanic loading. The lack of flow materials seen controlled by troughs around large venusian shields has led *McGovern and Solomon*, (1995, 1997) to suggest that flexural moats associated with venusian edifices are filled in. On Earth, lithosphere flexure typically leads to surficial circumferential faulting and moat formation. However, moats on Venus are predicted to fill during formation by flooding from extrusive materials (*McGovern and Solomon*, 1997). Such a method of construction is considered to have implications for the position of magma reservoirs. The model presented by *Head and Wilson* (1992) neglects the depth of the volcanic pile filling the flexural depression. When this accumulation of edifice material (which resides below the surrounding topography) is taken into consideration, it results in a greater overall thickness of the volcanic pile.

In calculating the greater edifice height, *McGovern and Solomon* (1997) suggest the magma reservoir is likely to reside within the volcanic pile. Hence, although a volcano such as Sif Mons stands 2 km above the local topography, the true thickness of the volcanic pile is greater. The model of volcanic construction proposed by *McGovern and Solomon* (1997) may account for the fact that Sif lies below the threshold considered necessary for magma to reside within a volcanic pile (~2.5 km, *Head and Wilson*, 1992) and yet shows landforms and eruptive styles indicative of magma residing within the edifice.

The prediction that lateral migration of venusian magma reservoirs dominates over vertical migration is considered to produce larger calderas (where applicable) and significant lateral dyke propagation, a consequence of a predominant lateral stress regime (*Head and Wilson*, 1992). The observations from Sif and Gula support these predictions. Sif has a large caldera (~40 km) by

terrestrial standards, implying a large magma reservoir. Gula Mons has a number of bright lineaments which radiate from the summit (Figures 5.2, 5.13). The radial features are considered to be the surface manifestations of dykes, similar to those identified by *McKenzie et al.* (1992). Furthermore, the observation of flank eruptive sites located at a horizontal distance of approximately 100 km from the summit of Sif Mons implies that dykes or dyke swarms have transported magma laterally for a considerable distance, greater than observed at most volcanoes on Earth.

A greater horizontal dimension of the magma reservoir is also considered responsible for the observed large height to basal ratio of venusian volcanoes (*Head and Wilson, 1992*). Sif and Gula are no exception to this observation and lateral movement of magma may explain their large diameters and shallow slopes. The ambient atmospheric conditions are predicted to lead to longer lava flows (*Head and Wilson, 1986*) and hence a greater mean diameter. Lava tubes are considered an effective method of transporting lava on Earth (*Swanson et al., 1973; Greeley et al., 1976*). If tube fed flows on venusian volcanoes occur (supported by the observation of what is interpreted as a tube fed flow at Sif Mons), this style of emplacement may result in lava reaching greater distances from the source, as the lava is thermally insulated.

Pyroclastic eruptions are considered to be inhibited on Venus owing to the great atmospheric density (*Head and Wilson, 1986, Chapter 2*). However, possible pyroclastic activity near the summits of Sif and Gula Montes, (Units 7 and 4 Sif and Gula respectively) and diffuse materials associated with flank eruptive sites (Unit 6 at Sif Mons) support the theory that bubble coalescence, or the formation of a chilled carapace, could result in volatile concentration and eventual pyroclastic eruptions on Venus (*Garvin et al., 1982; Fagents, 1994*).

5.8 Summary and Conclusions

Sif and Gula Montes represent two large shield volcanoes on Venus, which average 350 km and 450 km in diameter respectively. The two edifices stand 2 and 3.2 km above the surrounding topography of Western Eistla Region, a rise 1.8 km above the surrounding plains.

Magellan radar observations are used to interpret the flow materials and structures associated with the two volcanoes, which in turn help to infer their volcanic evolution and internal plumbing. However, the use of radar may lead to a number of misinterpretations regarding flow delineation, classification (based on inferred surface roughness) and stratigraphy. Examples of potential misinterpretations are highlighted from the comparison of field observations and SIR-C radar of Mt. Etna. From the observations it is considered inappropriate to use terrestrial lava flow classifications when discussing flow on Venus. Furthermore, stratigraphy of flow units should be analysed with care as radar backscatter is unlikely to relate to the flow age.

Detailed observations and mapping show 8 and 4 flow units associated with Sif and Gula respectively. Evidence exists for compound and single flows which have sheet, channel fed, tube fed, flank erupted and pyroclastic emplacement mechanisms. Sif Mons is considered to have at least 6 flank eruptive sites, contradicting the previous conclusion that venusian volcanoes lack this style of eruption (*Keddie and Head, 1994*). The flank eruptions are interpreted as a consequence of drainage of an internal magma reservoir (through lateral dykes) within the volcanic pile.

While the two volcanoes formed adjacent to each other, Sif and Gula show a number of differences between their flow field morphology, gross morphology and summit structure. By using analogies from terrestrial volcanoes (Kilauea and Mt. Etna) it is considered here that stress regimes within the volcanoes have been different during their evolution.

Gula Mons abuts Idem-Kuva Corona which is interpreted to have a protracted history (Chapter 4, 4.2.1). Furthermore, it sits on Gour Linea, an extensive rift which predates the bulk of materials associated with Gula. The evolution of Gula Mons, and consequential flow and edifice morphology are considered to have been controlled by stress regimes which occur within the volcanic pile and local surrounding materials. In contrast, Sif Mons owes its approximate circular shape and relatively broader flow morphology to a more unrestricted growth regime.

Numerical models predict that neutral buoyancy zones generally remain below the volcanic pile of volcanoes on Venus (*Head and Wilson, 1992*). However, it is considered here that the position of any magma reservoir may be at least partly controlled by the stresses within, and surrounding, the volcano. Furthermore, the model predicted larger calderas and greater lateral intrusion manifested by dykes, both a consequence of predicted greater lateral spreading of magma. These predictions are consistent with the large caldera which surmounts Sif Mons, as well as numerous (approximately radial) lineaments associated with both volcanoes, considered the surface manifestation of dykes.

Chapter 6

Conclusions

The detailed studies presented in this thesis, utilising the latest data from the Magellan mission, have led to a number of new conclusions which have important implications for understanding the geology of Venus. This final chapter summarises the achievements of the work, discusses the implications of the findings in a broader geological context, and suggests direction for further work.

The bulk of the surface of Venus we see today is probably older than 500 Ma. Magellan images have shown that geological processes on the planet have been extremely dynamic. This is not a surprising observation since Venus is of similar dimensions as the Earth and is expected to have a comparable heat budget, hence one would expect a similar level of geological activity on Venus as on Earth. However, the processes of volcanism and deformation inferred from features on the venusian surface show the geological processes contrast considerably from those seen on other terrestrial planets. In order to understand fundamental geological questions, such as the mechanism of heat loss on Venus, we need to unravel the geological processes which have occurred on the planet with time. This thesis has added more work by investigating the stratigraphy of Guinevere and Sedna Planitiae, and by testing evolutionary models of specific volcanic landforms (coronae and large shield volcanoes) using observations drawn from detailed mapping within the study area.

As with any branch of science, models are typically created in order to simplify and characterise processes which have resulted in an observed end product or products. Models of venusian geology explain processes which have not been directly observed, and are built around static observations of surface landforms and their relations with each other. Hence the models are particularly dependent on accurate observations. A major

conclusion from the work presented in this thesis is that as better data have become available, more detailed observations show previous models are too simple to explain fully geological processes that have occurred on Venus. In particular, models proposed for global stratigraphy and coronae formation on Venus have tended to compartmentalise events, suggesting processes which act in a directional fashion. The directional nature of these models are now widely accepted within the general understanding of venusian geology and have been extrapolated into a global context. It is hoped the work presented here (and pending publications e.g. *Copp et al.* 1997b, *Copp and Guest*, 1997) will dispel this way of thinking, for it is considered a superficial view of understanding venusian geology.

First consider the stratigraphy of Venus as a whole. The stratigraphic model proposed by *Basilevsky and Head* (1994, 1995a, 1995b, 1996), *Head and Basilevsky* (1996) and *Basilevsky et al.* (1996, 1997) implies a strongly directional stratigraphic history (described in Chapter 2, 2.2-2.4). The model contains periods of extensional and compressional tectonism which are considered to have occurred on a global scale, together with distinct styles of volcanic activity, resurfacing the planet at different times. Subsequently, global volcanism has dwindled to local volcanism. Applying this model globally means each style of volcanism and structural landform can easily be accounted for within the stratigraphy since the process which gave rise to it is specific to a period of geological history. Is this really how Venus works? And if so, why? An explanation for the directional nature is not provided by the authors of the model.

The directional nature of the global stratigraphic model does not apply to Guinevere and Sedna Planitia (Chapter 3). The study area from which the observations come from covers approximately 7% of the planet, a similar area to that considered by the global stratigraphy model. Unlike the areas considered by *Basilevsky and Head*, the planitiae represent a contiguous area rather than smaller individual areas of the planet. Observations made here show a more complex stratigraphic history. The picture

that emerges is one of styles of volcanism and deformation which have occurred on more than one occasion and which are not restricted to any specific time period.

A considerable amount of plains materials is associated with volcanic landforms; landforms which are shown here to be of different ages. The implications are that Venus may well have a non-directional stratigraphic history more akin to that of the Earth. The global stratigraphic model, while serving as a start in constructing a time frame from processes which have acted on Venus, does not adequately explain the observations seen within the study area here. Furthermore, other recent detailed studies support this conclusion (*Guest and Stofan, 1997*).

A considerable problem with most previous models which explain venusian stratigraphy and volcanic processes is that they appear to have been constructed without reference to stereo and full resolution FMAP imagery. Adding a third dimension to observations (using stereo data) shows considerably more complexity in the evolution of individual volcanic landforms on Venus. This is shown in Chapter 4, where stereo imagery and full resolution (FMAP) data are used to interpret coronae evolution in the Sif Mons quadrangle V31 (*Copp et al., 1997a*).

For some time, the evolution of coronae has been explained by a simple three stage model designed to fit previous observations. As with the global stratigraphic model, the processes and resultant landforms associated with coronae were compartmentalised within the model; a specific process occurring at each corona formed similar features at the same time. Each corona was considered to undergo initial uplift and volcanism accompanied by interior, radial extensional deformation. This stage was followed by the formation of an annulus of either ridges or graben or both, and ended with the reduction of topographic relief and continued volcanism. This model was acceptable because it was inferred from observations made at that time.

However, stereo imagery shows this model does not apply to all coronae. Coronae studied here are considered to have a more complex evolution inferred from the relation of structures and

volcanism associated with them (Chapter 4); these new observations cannot be explained fully by the previous three-stage corona model of evolution. The processes which have resulted in their present morphologies are not restricted to any particular period of time (as suggested by the stratigraphic model of Basilevsky and Head) and have occurred repeatedly at some coronae. Furthermore, the coronae studied have protracted histories (e.g. Heng-o and Idem-Kuva).

The implications of these observations are important for two reasons. First, they strongly support the general argument of the thesis, that the global stratigraphy of Venus is non-directional and does not fit a compartmental history. Second, the observations of coronae presented here must be accounted for within any subsequent models developed to explain corona formation.

The multi-stage annulus formation, annulus and topographic rim relations, and the protracted histories seen at coronae studied here (in particular Idem-Kuva and Heng-o Coronae) have been used to test a new corona model by *Smrekar and Stofan* (1997). The model predicts upwelling with delamination at the edge of a rising plume head and deformation of a pre-existing depleted mantle layer. When run over a time period in the order of 100s of millions of years, the model shows the evolution of topography over the lifetime of an upwelling plume can produce the full range of topographic forms of coronae. *Smrekar and Stofan* (1997) consider the delamination process an effective way of heat loss on Venus. The inferred protracted history of coronae (shown in Chapter 4) implies that if the delamination model is applicable, coronae are important mechanism of heat loss on Venus over an extended period of geological time.

A second prominent landform on Venus are the large volcanic shields (Chapter 5). Unlike coronae, which appear unique to Venus, a considerable amount can be learnt about large venusian volcanoes by comparing them with large shields on Earth. The approach has proved useful in understanding the volcanic processes and evolution of Sif and Gula Montes (Chapter 5). As on Earth, venusian volcanoes are constructed by a series of

eruptions and subsequent emplacement of lava flows. Establishing the stratigraphy and emplacement mechanisms of the flow materials is important as it provides information about the evolution and internal plumbing of the volcano.

At present, the geologist only has radar data with which to observe venusian volcanism and a number of constraints must be taken into consideration when trying to establish the evolution of large volcanoes using these data. It is critical to consider how flow units are represented in radar data. The comparative study between SIR-C data and field observations at Mt. Etna (Chapter 5) showed potential misinterpretation can easily occur and that it is unwise to use the same terrestrial classification of lava flow morphology on Venus.

Observations from full resolution data show that the emplacement mechanisms of flows which surround large shield volcanoes are similar to those observed at terrestrial volcanoes. The observation of flank eruptive sites are particularly important as they are indicative of either drainage from a magma reservoir contained within the volcanic pile or the propagation of dykes through the volcanic pile to the flank of the volcano. Despite the inhibiting environmental conditions, materials which are analogous to pyroclastic deposits at terrestrial volcanoes show that explosive volcanism may occur on Venus.

While models have been proposed for the morphology of large shield volcanoes on Venus controlled by the position of the neutral buoyancy zone of magmas (*Head and Wilson, 1992*), observations here imply that large shield evolution is more complex. The development of large volcanoes is considered here to be partly controlled by internal stresses and stresses associated with the regional geological setting on Venus as on Earth.

Further work

The observations within the thesis have significantly contributed to the understanding of venusian geology. However, further observations and quantitative work focusing on the contributions of volcanic landforms are needed to further refine models of stratigraphy and volcanic processes. The completion of investigating the 62 venusian quadrangles will allow a detailed stratigraphic picture to emerge. However, this is a long term project. In the meantime, investigations of a more local nature will be useful in understanding stratigraphy. A comparison of plains areas with areas that incorporate volcanism from rifts and coronae, is considered particularly useful in establishing the amount of resurfacing by these tecto-volcanic landforms. Careful attention should be paid towards the stratigraphic positions of volcanic landforms; a quantitative study in which the stratigraphy of these landforms can be constructed will aid in resolving the directional versus non-directional stratigraphic arguments. Establishing the density and timing of broad scale structures will be useful in further refining and testing the conclusions of this work.

The thesis highlights the fact that the evolution of some coronae are not consistent with previous models of formation. Five coronae were studied in detail from V31. These represent a small fraction of the coronae identified in the survey by *Stofan et al.* (1992) and more recently *Tapper* (1997). To fully understand the evolution and stratigraphic significance of coronae, the following relations should be established at each corona: (1) the nature of interior materials along with the degree and timing of any interior and exterior deformation. Observations of interior materials will help establish the degree and timing of uplift versus volcanic construction; (2) the relation between annulus and topographic rim, which will help to determine the amount and timing of crustal flexure; (3) the amount of volcanism and its stratigraphic relation with annulus and rim structure; and (4) the relation of the corona and any associated flow materials with surrounding units. These observations will allow us to test further the

evolution and stratigraphic relations of individual components of coronae as well as coronae evolution in a global context.

With venusian large shields, observations of the relations of flow units will further help to constrain emplacement mechanisms (e.g. tube and channel fed flows and the identification of potential pyroclastic deposits) and give further information on the evolution of the volcano. In particular, attention should be paid to volcano morphology and summit structure as a function of altitude. These observations may be used to further test the modelled positions of the neutral buoyancy zones of magmas associated with large volcanoes. The establishment of the volcanic history of further large volcanoes will permit a more detailed comparison of volcanoes in different geological settings, and allow an assessment of the importance of setting in controlling the formation and evolution of volcanoes on Venus.

References

- Arkani-Hamed, J., and M. N. Toksoz, Thermal evolution of Venus, *Phys. Earth Planet. Inter.*, 34, 232-250, 1984.
- Arkani-Hamed, J., G. G. Schaber, and R. G. Strom, Constraints on the thermal evolution of Venus inferred from Magellan data, *J. Geophys. Res.*, 98, 5,309-5,315, 1993.
- Arkani-Hamed, J., On the thermal evolution of Venus, *J. Geophys. Res.*, 99, 2,019-2,033, 1994.
- Arvidson R. E., R. Greeley, M. C. Malin, R. S. Saunders, N. Izenberg, J. J. Plaut, E. R. Stofan and M. K. Shepard, Surface modification of Venus as inferred from Magellan Observations of Plains, *J. Geophys. Res.*, 97, 13,303-13,317, 1992.
- Arvidson, R. E., J. J. Plaut, R. F. Jurgens, R. S. Saunders, and M. A. Slade, Geology of southern Guinevere Planitia, Venus, based on analyses of Goldstone radar data, *Proc. 20th Lunar Planet Sci. Conf.*, Houston: Lunar and Planetary Institute, 557-572, 1990.
- Aubele J. C., J. W., Head, L. S. Crumpler, and J. E. Guest, Fields of small volcanoes on Venus (Shield Fields): Characteristics and implications (abstract), *Lunar Planet. Sci.*, XXIII, 47-48, 1992.
- Aubele, J. C., and E. N. Slyuta, Small domes on Venus: Characteristics and origin, *Earth, Moon, and Planets*, 50/51, 493-532, 1990.
- Aubele, J. C., Stratigraphy of small volcanoes and plains terrain in Vellamo Planitia - Shimti Tessera region, Venus (abstract), *Lunar Planet. Sci.*, XXVI, 59-60, 1995.

- Aubele, J. C., Stratigraphy of small volcanoes and plains terrain in Vellamo Planitia, Venus (abstract), *Lunar Planet. Sci.*, XXV, 45-46, 1994.
- Avduevsky, V. S., N. F. Borodin, V. P. Burtzev, V. Malkvo Ya., M. Marov, S. F. Morozov, M. K. Rozhdestvensky, R. S. Romanov, S. S. Solkolov, V. G. Fokin, Z. P. Cheryomukhina, and V. I. Shkirina, Measurements of atmosphere parameters during the descent of probes to the surface of a planet, *Institute of Space Research, Akad. Nauk. SSSR, Pr-278*, p. 13-14, 1976b.
- Avduevsky, V. S., S. L. Vishnevetsky, I. A. Golov, Yu. Ya. Karpeisky, A. D. Lavro, V. Ya. Likhushin, M. Ya. Marov, D. A. Mel' Nikov, N. I. Pomogin, N. N. Pronina, K. A. Razin, V. G. Fokin, Measurements of wind velocity on the surface of Venus during operation of stations Venera 9 and 10, *Cosmic Research* 14, 622-625, 1976a.
- Barsukov, V. L., A. T. Basilevsky, G. A. Burba, N. N. Bobinna, V. P. Kryuchkov, R. O. Kuz'min, O. V. Nikolaeva, A. A. Pronin, L. B. Ronca, I. M. Chernaya, V. P. Shashkina, A. V. Garanin, E. R. Kushky, M. S. Markov, A. L. Sukhanov, V. A. Kotel'nikov, O. N. Rzhiga, G. M. Petrov, Yu. N. Alexandrov, A. I. Sidorenko, A. F. Bogomolov, G. I. Skrypnik, M. Yu. Bergman, L. V. Kudrin, I. M. Bokshstein, M. A. Kronrod, P. A. Chochia, Yu. S. Tyuflin, S. A. Kadnichansky, and E. L. Akim, The geology and geomorphology of the Venus surface as revealed by the radar images obtained by Veneras 15 and 16. *Proc. of the Sixteenth Lunar and Planet. Sci. Conf., Part 2, J. Geophys. Res.*, 91, D378-D398, 1986.
- Barsukov, V. L., A. T. Basilevsky, R. O. Kuz'min, A. A. Pronin, V. P. Kruchkov, O. V. Nikolayeva, I. M. Chernaya, G. A. Burba, N. N. Bobina, V. P. Shashkina, M. S. Markov, and A. L. Sukhanov, Preliminary evidence on the geology of Venus from radar measurements by the Venera 15 and 16 probes, *Geokhimiya*, 12, 1811-1820, 1984.

- Barsukov, V. L., Venus geology, geochemistry, and geophysics: research results from the USSR, edited by V. L. Barsukov, A. T. Basilevsky, V. P. Volkov and V. N. Zharkov, Univ. of Ariz. Press, Tucson, pp. 412, 1992.
- Barsukov, V. L., Y. A. Surkov, L. P. Moskaleva, O. P. Shcheglov, V. P. Kharyukova, O. S. Mavelyan, and V. G. Perminov, Geochemical studies of the surface of Venus by "Venera-13 and 14". *Geochemistry*, 7, 899-920, 1982.
- Basilevsky, A. T., Age of rifting and associated volcanism in Atla, Regio, Venus, *Geophys. Res. Lett.*, 20, 883-886, 1993.
- Basilevsky, A. T., and J. W. Head, Global stratigraphy of Venus: Analysis of a random sample of thirty-six test areas, *Earth, Moon, Planets*, 66, 285-336, 1995a.
- Basilevsky, A. T., and J. W. Head, Preliminary stratigraphic basis for geologic mapping of Venus, (abstract), *Lunar Planet. Sci.*, XXV, 65-66, 1994.
- Basilevsky, A. T., and J. W. Head, Regional and global stratigraphy of Venus: A preliminary assessment and implications for the geologic history of Venus, (abstract), *Lunar Planet. Sci.*, XXVII, 69-71, 1996.
- Basilevsky, A. T., and J. W. Head, Regional and global stratigraphy of Venus: A preliminary assessment and implications for the geologic history of Venus, *Planet. Space Sci.*, 1,523-1,533, 1995b.
- Basilevsky, A. T., and J. W. Head, The geology of Venus, *Annu. Rev. Earth Planet. Sci.*, 16, 295-317, 1988.

- Basilevsky, A. T., B. A. Ivanov., G. A. Burba, I. M. Chernaya, V. P. Krvuchkov, O. V. Nikolaeva, D. B. Campbell, and L. B. Ronca, Impact craters of Venus: A continuation of the analysis of data from the Venera 15 and 16 spacecraft, *J. Geophys. Res.*, 92, 12,869-12,901, 1987.
- Basilevsky, A. T., G. A. Burba, and V. P. Kryuchkov, Stratigraphy of venusian plains: Comparison of Price [1995] and Basilevsky and Head [1995] units (abstract), *Lunar Planet. Sci.*, XXVII, 73-74, 1996.
- Basilevsky, A. T., J. W. Head, G. G. Schaber, and R. G. Strom, The resurfacing history of Venus, in *Venus II*, edited by S. W. Bougher, D. M. Hunten, and R. J. Phillips, Univ. of Ariz. Press, in press, 1997.
- Basilevsky, A. T., O. V. Nikolaeva, and C. M. Weitz, Geology of the Venera 8 landing site region from Magellan data: Morphological and geochemical considerations, *J. Geophys. Res.*, 97, 16,315-16,335, 1992.
- Basilevsky, A. T., R. O. Kuzmin, O. V. Nikolaeva, A. A. Pronin, L. B. Ronca, V. S. Avduevsky, G. R. Uspensky, Z. P. Cheremukhina, and V. V. Semenchenko, The surface of Venus as revealed by the Venera landings, *Geol. Soc. Am. Bull.*, 96, 137-144, 1985.
- Basilevsky, A. T., The structure of the Ishtar Terra central and eastern parts and some tectonic problems of Venus, NASA TM-88508, Translation of "Stroyeniye tsentral'noy i vostochnoy chastey zemli ishtar i nekotoryye problemy tektoniki venery," *Geotektonika*, 4, 42-53, 1986.
- Batson R. M., R. L. Kirk, K. Edwards, and H. F. Morgan, Venus cartography, *J. Geophys. Res.*, 99, 21,173-21,183, 1994.

- Bindschadler, D. L., A. DeCharon, K. K. Beratan, S. E. Smrekar, and J. W. Head, Magellan observations of Alpha Regio: Implications for formation of complex ridged terrains on Venus, *J. Geophys. Res.*, *97*, 13,563-13,577, 1992a.
- Bindschadler, D. L., and J. W. Head, Characterisation of Venera 15/16 geologic units from Pioneer Venus reflectivity and roughness data, *Icarus*, *77*, 3-20, 1989.
- Bindschadler, D. L., and J. W. Head, Tessera terrain, Venus: Characterisation and models for origin and evolution, *J. Geophys. Res.*, *96*, 5,889-5,907, 1991.
- Bindschadler, D. L., G. Schubert, and W. M. Kaula, Coldspots and hotspots: Global tectonics and mantle dynamics of Venus, *J. Geophys. Res.*, *97*, 13,495-13,532, 1992b.
- Blackburn, E. A., L. Wilson, and J. S. R. Sparks, Mechanisms and dynamics of Strombolian activity, *J. Geol. Soc. London*, *132*, 429-440, 1976.
- Bond, P., Space probes unveil Venus, *Astronomy Now*, *8*, vol.10, 45-49, 1994.
- Bullock, M, A., D. H. Grinspoon, and J. W. Head, Venus resurfacing rates: Constrains provided by 3-D Monte Carlo simulations, *Geophys. Res. Lett.*, *20*, 2,147-2,150, 1993.
- Campbell B., A. and D. B. Campbell, Western Eistla Regio, Venus: Radar properties of volcanic deposits, *Geophys. Res. Lett.*, *17*, 9, 1,353-1,356, 1990.
- Campbell, B. A., Merging Magellan emissivity and SAR data for analysis of Venus surface dielectric properties, *Icarus*, *112*, 187-203, 1994.

- Campbell, C. B., D. A. Senske, J. W. Head, A. A. Hine, and P. C. Fisher, Venus southern hemisphere: Geologic character and age of terrains in the Themis-Alpha-Lada Region, *Science*, 251, 180-183, 1991.
- Campbell, D. B., and B. A. Burns, Earth-based radar imagery of Venus, *J. Geophys. Res.*, 85, 8,271-8,281, 1980.
- Campbell, D. B., J. W. Head, A. A. Hine, J. K. Harmon, D. A. Senske, and P. C. Fisher, Styles of volcanism on Venus: New Arecibo high resolution radar data, *J. Geophys. Res.*, 246, 373-377, 1989.
- Campbell, D. B., N. J. S. Stacy, and A. A. Hine, Venus: Crater distributions at low northern latitudes and in the southern hemisphere from New Arecibo observations. *Geophys. Res. Lett.*, 17, 9, 1,389-1,392, 1990.
- Campbell, D. B., N. J. S. Stacy, W. I. Newman, R. E. Arvidson, E. M. Jones, G. S. Musser, A. Y. Roper, and C. Schaller, Magellan observations of extended impact crater related features on the surface of Venus. *J. Geophys. Res.*, 97, 16,249-16,277, 1992.
- Campbell, D. B., R. B. Dyce, and G. H. Pettengill, New radar image of Venus, *Science*, 193, 1,123-1,124, 1976.
- Campbell B. A., Use and interpretation of Magellan quantitative data in Venus mapping, 2nd ed., Centre for Earth and planetary studies, *Washington D.C.*, 1995.
- Cattermole, P. J., *Venus: The geological story*, London, UCL Press, pp. 250, 1994.
- Chester, D. K., A. M. Duncan, J. E. Guest, and C. R. J. Kilburn, Mount Etna: The anatomy of a volcano, Chapman and Hall Ltd., pp. 403, 1985.

- Coffin, M. F., and O. Eldholm, Large igneous provinces: Crustal structure, dimensions, and external consequences, *Rev. Geophys.*, 32, 1, 1994.
- Coffin, M. F., and O. Eldholm, Scratching the surface: Estimating dimensions of large igneous provinces, *Geology*, 21, 515-518, 1993.
- Coffin, M. F., and O. Eldholm, Volcanism and continental break-up: A global compilation of large igneous provinces, in *Magmatism and the causes of continental break-up*, edited by B. C. Storey, T. Alabaster and R. J. Pankhurst, *Geol. Soc. Spec. Pub.*, 68, pp. 17-30, 1992.
- Colin L., The Pioneer Venus Program, *J. Geophys. Res.*, 85, 7,575-7,598, 1980.
- Copp D. L., and J. E. Guest, Sif Mons quadrangle, V31; Venus, U.S. Geological Atlas of Venus, *U.S. Geol. Surv.*, 1997, in press.
- Copp D. L., J. E. Guest, and E. R. Stofan, New insights to coronae formation: Mapping on Venus, *J. Geophys. Res.*, 1997b, in press.
- Copp, D. L., and J. E. Guest, Geology of the Sif and Gula Quadrangle of Venus (abstract), *Lunar and Planet. Sci.*, XXVI, 283-284, 1995.
- Copp, D. L., J. E. Guest, and E. R. Stofan, Observations of selected coronae from venusian quadrangles V31 and V19, (abstract), *Lunar and Planet. Sci.*, XXXVIII, 1997a.
- Cristofolini, R., Recent trends in the study of Etna, *Phil. Trans. R. Soc. Lond. A.* 274, 17-35, 1973.

- Crown, D. A., E. R. Stofan, and J. J. Plaut, Geology of the Guinevere Planitia quadrangle of Venus, (abstract), *Lunar Planet. Sci.*, XXV, 301-302, 1994.
- Crumpler, L. S., J. C. Aubele, D. A. Senske, S. T. Keddie, K. P. Magee and J. W. Head, Volcanoes and Centres of Volcanism on Venus, in *Venus II*, edited by S. W. Bougher, D. M. Hunten, and R. J. Phillips, Univ. of Ariz. Press, Tucson, in press, 1997.
- Crumpler, L. S., J. W. Head, and J. C. Aubele, Calderas on Mars: characteristics, structures and associated flank deformation, in; *Volcano Instability on the Earth and Other Planets*, edited by W. J. McGuire and A. P. Jones, Geol. Soc. special publication, 110 pp. 307-348, 1996.
- Decker, R. W., R. Y. Koyanagi, J. J. Dvorak, J. P. Lockwood, A. T. Okamura, K. M. Yamashita, and W. R. Tanigawa, Seismicity and surface deformation of Mauna Loa volcano, Hawaii, *EOS 64*, 545-547, 1983.
- Donahue, T. M., and J. B. Pollack, Origins and evolution of the atmosphere of Venus, in *Venus* edited by D. M. Hunten, L. Colin, T. M. Donahue and V. I. Moroz, pp. 1,003-1,036, University of Arizona Press, Tuscon, 1983.
- Donahue, T. M., J. H. Hoffman, R. R. Hodges. Jr., and A. J. Watson, Venus was wet: a measurement of the ratio of D to H, *Science*, 216, 630-633, 1982.
- Duncan, A. M., and J. E. Guest, Mount Etna: Variations in its internal plumbing, *Geophysical Surveys*, 5, 213-227, 1982.
- Dutton, C. E., Hawaiian volcanoes, *U.S. Geol. Surv., 4th Annu. Rep.*, 75-219, 1884.

- Edmunds, M. S., A geologic analysis of Sekmet Mons, Venus using Magellan radar data, (abstract), *Lunar and Planet. Sci.*, XXVI, 361-362, 1995.
- Elachi, C., Spaceborne imaging radar: Geologic and oceanographic Applications, *Science*, 209, 1,073-1,082, 1980.
- Evans, D. L., Radar observations of a volcanic terrain: Askja Caldera, Iceland, JPL publication 78-81, *Jet Propulsion Laboratory*, Pasadena, California, 1978.
- Fagents, S. A., and L. Wilson, Vulcanian explosive eruptions: A mechanism for localised pyroclastic dispersal on Venus, *Lunar Planet. Sci.*, XXV, 1994.
- Farr, T. G., and N. Engheta, Quantitative comparisons of radar image, scatterometer, and surface roughness data from Pisgah Crater, California, *I.E.E.E. Int. Geoscience and Remote Sensing Symp. Digest*, 2.1-2.6, 1983.
- Farr, T. G., C. Elachi, M. Daily, and R. Blom, Image radar observations of volcanic features in Medicine Lake Highland, California, *I.E.E.E. Int. Geoscience and Remote Sensing Symp. Digest*, 872-877, 1981.
- Farr, T. G., Radar interactions with geologic surfaces, in *Guide to Magellan image interpretation*, J. P. Ford, J. J. Plaut, C. M. Weitz, T. G. Farr, D. A. Senske, E. R. Stofan, G. Michaels and T. J. Parker, JPL Publication 93-24, *Jet Propulsion Laboratory*, Pasadena, California, pp. 148, 1993.
- Fielding, E. J., W. J. Knox, Jr., and A. L. Bloom, SIR-B radar imagery of volcanic deposits in the Andes, *I.E.E.E. Int. Geoscience and Remote Sensing*, GE-24, 582-589, 1986.

- Fiske R. S., and E. D. Jackson, Orientation and growth of Hawaiian volcanic rifts: the effect of regional structure and gravitational stresses, *Proc. R. Soc. Lond., A.*, 329, 299-326, 1972.
- Florensky, C. P., A. T. Basilevsky, G. A. Burba, O. V. Nikolaeva, A. A. Pronin, V. P. Volkov, and L. B. Ronca, First panoramas of the venusian surface, *Proc. 8th Lunar Planet Sci. Conf.*, Houston: Lunar and Planetary Institute, 2,655-2,664, 1977b.
- Florensky, C. P., A. T. Basilevsky, V. P. Kryuchkov, R. O. Kuz'min, O. V. Nikolaeva, A. A. Pronin, I. M. Chernaya, Yu. S. Tyuflin, A. S. Selivanov, M. K. Naraeva, and L. B. Ronca, Venera 13 and Venera 14: Sedimentary rocks on Venus, *Science*, 221, 57-59, 1983.
- Florensky, C. P., L. B. Ronca, A. T. Basilevsky, G. A. Burba, O. V. Nikolaeva, A. A. Pronin, A. M. Trakhtman, V. P. Volkov, and V. V. Zazetsky, The surface of Venus as revealed by Soviet Venera 9 and 10, *Geo. Soc. of America*, 88, 1,537-1,545, 1977a.
- Ford, J. P., R. G. Blom, J. A. Crisp, C. Elachi, T. G. Farr, R. S. Saunders, E. E. Theilig, S. D. Wall, and S. B. Yewell, Spaceborne Radar Observations: A Guide for Magellan Radar Image Analysis, JPL Publication 89-41, *Jet Propulsion Laboratory*, Pasadena, California, pp. 126, 1989.
- Ford, J. P., and J. J. Plaut, Magellan image data, in *Guide to Magellan image interpretation*, J. P. Ford, J. J. Plaut, C. M. Weitz, T. G. Farr, D. A. Senske, E. R. Stofan, G. Michaels and T. J. Parker, JPL Publication 93-24, *Jet Propulsion Laboratory*, Pasadena, California, pp. 148, 1993.

- Ford, J. P., Magellan image data, in *Guide to Magellan image interpretation*, J. P. Ford, J. J. Plaut, C. M. Weitz, T. G. Farr, D. A. Senske, E. R. Stofan, G. Michaels and T. J. Parker, JPL Publication 93-24, *Jet Propulsion Laboratory*, Pasadena, California, pp. 148, 1993.
- Ford, P. G. and D. A. Senske, The radar scattering characteristics of Venus landforms, *Geophys. Res. Ltrs.*, 17, 9, 1,361-1,364, 1990.
- Ford, P. G., and G. H. Pettengill, Venus topography and kilometre-scale slopes, *J. Geophys. Res.*, 97, 13,103-13,114, 1992.
- Gaddis L. R., P. J., Mougini-Mark, R. Singer, and V. Kaupp, Geologic analyses of Shuttle Imaging Radar (SIR-B) data of Kilauea Volcano, Hawaii, *Geol. Soc. Amer. Bulletin*, 101, 317-332, 1989.
- Garvin J. B., J. W. Head, and L. Wilson, Magma vesiculation and pyroclastic volcanism on Venus, *Icarus*, 52, 365-372, 1982.
- Garvin, J. B., J. W. Head, M. T. Zuber, and P. Helfenstein, Venus: The nature of the surface from Venera panoramas, *J. Geophys. Res.*, 89, 3,381-3,399, 1984.
- Garvin, J. B., P. J. Mougini-Mark, and J. W. Head, Characterisation of rock populations on planetary surfaces: Techniques and a preliminary analysis of Mars and Venus, *Moon and Planets*, 24, 355-387, 1981.
- Garzanti, E., Himalayan ironstones, "superplumes," and the breakup of Gondwana, *Geology*, 21, 105-108, 1993.
- Gilmore, M. S., M. A. Ivanov, J. W. Head, and A. T. Basilevsky, Duration of tessera deformation on Venus, *J. Geophys. Res.*, 102, 13,357-13,368, 1997.

- Goldstein, R. M., Preliminary Venus radar results, *Radio Sci.*, 69D, 1,623-1,625, 1965.
- Goldstein, R. M., R. R. Green, and H. C. Rumsey, Venus radar brightness and altitude images, *Icarus*, 36, 334-352, 1978.
- Goldstein, R. M., R. R. Green, and H. C. Rumsey, Venus radar images, *J. Geophys. Res.*, 81, 4,807-4,817, 1976.
- Goldstein, R. M., Radar studies of Venus, in *Moon and Planets*, edited by A. Dollfus, pp 126-131, North-Holland, Amsterdam, 1967.
- Greeley R., and J. S. King, Volcanism of the Eastern Snake River plains, Idaho: A comparative planetary geology guidebook, edited by Greeley R., and J. S. King, NASA CR 154621, Washington D.C., *National Aeronautics and Space Administration*, p 308, 1977.
- Greeley, R., and J. R. Martel, Radar observations of basaltic lava flows, Craters of the Moon, Idaho, *Int. J. Remote Sensing*, 9, 1,017-1,085, 1988.
- Greeley, R., D. Storm, and C. Wilbur, Frequency distance of lava tubes and channels on Mauna Loa volcano, Hawaii, *Geol. Soc. Amer. Abs.*, 8, 892, 1976.
- Greeley, R., J. R. Marshall, and R. N. Leach, Microdunes and other aeolian bedforms on Venus: Wind tunnel simulations, *Icarus*, 60, 152-160, 1984.
- Greeley, R., K. Bender, and D. Senske, The Carson quadrangle, Venus, (abstract), *Lunar Planet. Sci.*, XXV, 463-464, 1994.

- Greeley, R., R. E. Arvidson, C. Elachi, M. A. Geringer, J. J. Plaut, R. S. Saunders, G. Schubert, E. R. Stofan, E. J. P. Thouvenot, S. D. Wall, and C. M. Weitz, Aeolian features on Venus: Preliminary Magellan results, *J. Geophys. Res.*, 97, 13,319-13,345, 1992.
- Grimm, R. E., and R. J. Phillips, Anatomy of a Venusian hot spot: Geology, gravity, and mantle dynamics of Eistla Regio, *J. Geophys. Res.*, 97, 16,035-16,054, 1992.
- Guest J. E., C. R. J. Kilburn, H. Pinkerton, and A. M. Duncan, The evolution of lava flow fields: observations of the 1981 and 1983 eruptions of Mount Etna, Sicily, *Bull. Volcanol.*, 49, 527-540, 1987.
- Guest, J. E., and A. M. Duncan, Internal Plumbing of Mount Etna, *Nature*, 290, 584-586, 1981.
- Guest, J. E., and E. R. Stofan, A planet in search of a paradigm: The nature of the venusian stratigraphical record, submitted to *J. Geophys. Res.*, 1997.
- Guest, J. E., and J. B. Murray, An analysis of hazard from Mount Etna volcano, *Journ. Geol. Soc.*, 136-3, 347-354, 1979.
- Guest, J. E., C. Wood, and R. Greeley, Lava tubes, terraces and megatumuli on the 1614-24 pahoehoe lava flow field, Mount Etna, Sicily, *Bull. Volcanoe.*, 47-3, 635-648, 1984.
- Guest, J. E., M. G. Lancaster, and D. L. Copp, Speculations on Lava flow textures on Venus, *Lunar Planet. Sci.*, XXVI, 529-530, 1995.
- Guest, J. E., M. G. Lancaster, D. L. Copp and E. R. Stofan, Emplacement mechanics for great lava flows on the plains of Venus: Slow vs Fast (abstract), in *Chapman Conference on Long lava flows*, 16-18, Edited by P. J. Stephenson and P. W.

- Whitehead, James Cook University of North Queensland, 1996.
- Guest, J. E., M. H. Bulmer, J. C. Aubele, K. Beratan, R. Greeley, J. W. Head, G. Michaels, C. Weitz, and C. Wiles, Small volcanic edifices and volcanism in the plains of Venus, *J. Geophys. Res.*, 97, 15,949-15,966, 1992.
- Guest, J. E., Styles of eruption and flow morphology on Mt. Etna, *Mem. Soc. Geol. It.*, 23, 49-73, 1982.
- Hagfors T., Relations between rough surfaces and their scattering properties as applied to radar astronomy, in *Radar Astronomy*, edited by J. V. Evans and T. Hagfors, pp. 187-218, McGraw-Hill, New York, 1968.
- Hagfors, T., Backscattering from an undulating surface with applications to radar returns from the Moon, *J. Geophys. Res.*, 69, 3,779-3,784, 1964.
- Hagfors, T., Remote probing of the Moon by infrared and microwave emissions and by radar, *Radio Sci.*, 2, 445-465, 1970.
- Hansen, V. L., and J. J. Willis, Structural analysis of a sampling of tesserae: Implications for Venus geodynamics, *Icarus*, 123, 296-312, 1996.
- Head J. W., and A. T. Basilevsky, Sequence of tectonic deformation in the history of Venus: Evidence from global stratigraphic relations, (abstract), *Lunar Planet. Sci.*, XXVII, 511-512, 1996.
- Head, J. W., and L. Wilson, Magma reservoirs and neutral buoyancy zones on Venus: implications for the formation and evolution of volcanic landforms, *J. Geophys. Res.*, 97, 3,877-3,903, 1992.

- Head, J. W., and L. Wilson, Volcanic processes on Venus, (abstract) *Lunar Planet. Sci.*, XIII, 312-313, 1982.
- Head, J. W., and S. C. Solomon, Tectonic evolution of the terrestrial planets, *Science*, 213, 62-76, 1981.
- Head, J. W., D. B. Campbell, C. Elachi, J. E. Guest, D. P. McKenzie, R. S. Saunders, G. G. Schaber, and G. Schubert, Venus volcanism: initial analysis from Magellan data, *Science*, 252, 276-288, 1991.
- Head, J. W., K. Magee, S. Keddie, M. Gilmore and A. Yingst, Geology of the Lavinia Planitia area, Venus, *Lunar Planet. Sci.*, XXV, 529-530, 1994.
- Head, J. W., L. S. Crumpler, J. C. Aubele, J. E. Guest, and R. S. Saunders, Venus volcanism: Classification of volcanic features and structures, associations, and global distribution from Magellan data, *J. Geophys. Res.*, 97, 13,153-13,197, 1992.
- Head, J. W., R. W. Vorder Bruegge, and L. S. Crumpler, Venus Orogenic belt environments: Architecture and origin, *Geophys. Res. Lett.*, 17, 9, 1,337-1,340, 1990.
- Head, J., and W. L. Wilson, Volcanic processes and landforms on Venus: Theory, predictions and observations, *J. Geophys. Res.*, 91, 9,407-9,446, 1986.
- Herrick, R. R., and R. J Phillips, Blob tectonics: A prediction for western Aphrodite Terra, Venus, *Geophys. Res. Lett.*, 17, 2,129-2,132, 1990.
- Herrick, R. R., and R. J. Phillips, Implications of a global survey of venusian impact craters, *Icarus*, 111, 387-416, 1994.

- Herrick, R. R., N. Izenberg, and R. G. Phillips, Comment on "The global resurfacing on Venus" by R. G. Strom, G. G. Schaber, and D. D. Dawson, *J. Geophys. Res.*, 100, 355-359, 1995.
- Herrick, R. R., Resurfacing history of Venus, *Geology*, 22, 703-706, 1994.
- Herrick, R. R., The three ages of Venus, (abstract), *Lunar Planet. Sci.*, XXIV, 645-646, 1993.
- Hoffman, J. H., R. R. Hodges, T. M. Donahue, and M. B. McElroy, Composition of the Venus lower atmosphere from the Pioneer Venus mass spectrometer, *J. Geophys. Res.*, 85, 7,882-7,890, 1980a.
- Hoffman, J. H., V. I. Oyama, and U. von Zahn, Measurements of the Venus lower atmosphere composition: A comparison of results. *J. Geophys. Res.*, 85, 7,871-7,881, 1980b.
- Hughes, J. W., J. E. Guest, and A. M. Duncan, Changing styles of effusive eruption on Mount Etna, in *Magma Transport and Storage*, edited by M. P. Ryan, 386-406, John Wiley and Sons Ltd, 1990.
- Hunt G. E., and P. Moore, The planet Venus, Faber and Faber, pp 207, 1982
- Ivanov, B. A., and J. W. Head, Sequence of events in tessera formation, Northern Ovda Region, (abstract), *Lunar Planet. Sci.*, XXVI, 691-692, 1995.
- Ivanov, B. A., and J. W. Head, Tessera terrain on Venus: A summary of global distribution, characteristics, and relation to surrounding units from Magellan data, *J. Geophys. Res.*, 101, 14,816-14,908, 1996.

- Ivanov, B. A., and J. W. Head, Tessera terrain on Venus: Global characterisation from Magellan data, (abstract), *Lunar Planet. Sci.*, XXIV, 691-692, 1993.
- Ivanov, M. A., A. T. Basilevsky, V. P. Kryuchkov, and I. M. Chernaya, Impact craters on Venus: Analysis of Venera 15/16 data, *Proc. of the Sixteenth Lunar and Planet. Sci. Conf., J. Geophys. Res.*, 91, 423-430, 1986.
- Ivanov, M. A., and A. T. Basilevsky, Coronae and the major shields on Venus: Comparisons of their areas, basal altitudes and areal distribution, *Earth, Moon, Planets*, 50/51, 409-420, 1990.
- Ivanov, M. A., and A. T., Basilevsky, Density and morphology of impact craters on tessera terrain, Venus, *Geophys. Res. Lett.*, 20, 2,579-2,582, 1993.
- Izenberg, N. R., R. E. Arvidson, and R. J. Phillips, A first-order model for impact crater degradation on Venus, (abstract), *Lunar Planet. Sci.*, XXIV, 703-704, 1993.
- Janes D. M., and S. W. Squyres, Viscoelastic relaxation of topographic highs on Venus to produce coronae, *J. Geophys. Res.*, 100, 21,173-21,187, 1995.
- Janes, D. M., S. W. Squyres, D. L. Bindschadler, G. Baer, G. Schubert, V. L. Sharpton, and E. R. Stofan, Geophysical models for the formation and evolution of coronae on Venus, *J. Geophys. Res.*, 97, 16,055-16,067, 1992.
- Kasting J. F., Runaway and moist greenhouse atmospheres and the evolution of Earth and Venus, *Icarus*, 74, 472-494, 1988.
- Keddie S. T., and J. W. Head, Sapas Mons, Venus: Evolution of a large shield volcano, *Earth, Moon, Planets*, 65, 129-190, 1994.

- Keddie S. T., and J. W. Head, Volcanic edifices on Dione Regio rise, Venus, *J. Geophys. Res.*, 100, 11,729-11,754, 1995.
- Kieffer, S. W., Numerical models of caldera-scale volcanic eruptions on Earth, Venus and Mars, *Science*, 269, 1,385-1,391, 1995.
- Klose, K. B., J. A. Wood, and A. Hashimoto, Mineral equilibria and the high radar reflectivity of Venus mountain tops, *J. Geophys. Res.*, 97, 16,353-16,369, 1992.
- Koch D. H., and M. Manga, Neutrally buoyant diapirs: A model for Venus coronae, *Geophys. Res. Lett.*, 23, 3, 225-228, 1996.
- Koch, D. M., A spread drop model for plumes on Venus, *J. Geophys. Res.*, 99, 2,035-2,052, 1994.
- Kozak R. C., and G. G. Schaber, New evidence for global tectonic zones on Venus, *Geophys. Res. Lett.*, 16, 175-178, 1989.
- Kryuchkov, V. P., Ridge belts: Are they compressional or extensional structures? *Earth, Moon, Planets*, 50/51, 471-492, 1990.
- Lancaster, M. G., J. E. Guest, and K. M. Roberts, Great lava flow fields on Venus, *Icarus*, 118, 69-86, 1995.
- Lancaster, M. G., J. E. Guest, K. M. Roberts and J. W. Head, "Great" lava fields on Venus, (abstract), *Lunar Planet. Sci.*, XXIV, 753-754, 1992.
- Larson, R. L., Geological consequences of superplumes, *Geology*, 19, 963-966, 1991b.
- Larson, R. L., Latest pulse of Earth: Evidence for a mid-Cretaceous superplume, *Geology*, 19, 547-550, 1991a.

- Macdonald, G. A., Pahoehoe, aa, and block lava, *Am. J. Sci.*, 251, 169-191, 1953.
- Magee Roberts, K., J. E. Guest, J. W. Head, and M. G. Lancaster, Mylitta Fluctus, Venus: Rift-related, centralised volcanism and the emplacement of large volumes flow units, *J. Geophys. Res.*, 97, 15,991-16,015, 1992.
- Malin, M. C., Lengths of Hawaiian lava flows, *Geology*, 8, 306-308, 1980.
- Masursky, H., E. Eliason, P. G. Ford, G. E. McGill, G. H. Pettengill, G. G. Schaber, and G. Schubert, Pioneer Venus radar results: Geology from images and altimetry, *J. Geophys. Res.*, 85, 8,232-8,260, 1980.
- McGill, G. E., Hotspot evolution and Venusian tectonic style, *J. of Geophys. Res.*, 99, 23,149-23,161, 1994.
- McGovern, P. J., and S. C. Solomon, Factors affecting the growth, development, and structure of large volcanoes on Venus (abstract), *Lunar Planet. Sci.*, XXVI, 939-940, 1995.
- McGovern, P. J., and S. C. Solomon, Filling of flexural moats around large volcanoes on Venus: Implications for volcano structure and global magmatic flux, *J. Geophys. Res.*, 102, 16,303-16,318, 1997.
- McKenzie, D., J. M. McKenzie and R. S. Saunders, Dike emplacement on Venus and Earth, *J. Geophys. Res.*, 97, 15,997-15,991, 1992.
- Mian, Z. U., and D. C. Tozer, No water, no plate tectonics: convective heat transfer and the planetary surfaces of Venus and Earth, *Terra Nova*, 2, 455-459, 1990.

- Morgan, W. J. and R. J. Phillips, Hotspot heat transfer: Its application to Venus and implications to Venus and Earth, *J. Geophys. Res.*, 88, 8,305-8,317, 1983.
- Muhleman, D. O., Radar scattering from Venus and the Moon, *Astron. J.*, 69, 34-41, 1964.
- Namiki, N., and S. C. Solomon, Impact crater densities on volcanoes and coronae on Venus: Implications for volcanic resurfacing, *Science*, 265, 929-933, 1994.
- Neukum, G., The cratering rate in the Earth-Moon system over the past 3 b.y. and in recent times, *Lunar Planet. Sci. Conf.*, XIX, 850-851, 1988.
- Nikolayeva, O. V., Geochemistry of the Venera 8 material demonstrates the presence of continental crust on Venus, *Earth, Moon, Planets*, 50/51, 329-342, 1990.
- Parfitt, E. A., and J. W. Head, Buffered and unbuffered dike emplacement on Earth and Venus: Implications for magma reservoir size, depth, and rate of magma replenishment, *Earth, Moon, Planets*, 61, 249-281, 1993.
- Parmentier, E. M., and P. C. Hess, Chemical differentiation of a convecting planetary interior: Consequences for a one plate planet such as Venus, *Geophys. Res. Lett.*, 19, 2,015-2,018, 1992.
- Pettengill, G. H., D. B. Campbell, and H. Masursky, The surface of Venus, *Scientific American*, 243, 2, 54-65, 1980a.
- Pettengill, G. H., E. Eliason, P. G. Ford, G. B. Lorient, H. Masursky, and G. E. McGill, Pioneer Venus radar results: Altimetry and surface properties, *J. Geophys. Res.*, 85, 8,261-8,270, 1980b.

- Pettengill, G. H., P. G. Ford, and B. D. Chapman, Venus: Surface electromagnetic properties, *J. Geophys. Res.*, 93, 14,881-14,892, 1988.
- Pettengill, G. H., P. G. Ford, and R. J. Wilt, Venus surface radiothermal emission as observed by Magellan, *J. Geophys. Res.*, 97, 13,091-13,102, 1992.
- Pettengill, G. H., P. G. Ford, W. T. K. Johnson, R. K. Raney, and L. A. Soderblom, Magellan: Radar Performance and Data Products, *Science*, 252, 260-265, 1991.
- Phillips R. J., and V. L. Hansen, Venus now and then, (abstract), *Lunar Planet. Sci.*, XXVIII, 1,105-1,106, 1997.
- Phillips R. J., R. E. Arvidson, J. M. Boyce, D. B. Campbell, J. E. Guest, G. G. Schaber, and L. A. Solderblom, Impact craters on Venus: Initial analysis from Magellan, *Science* 252, 288-297, 1991b.
- Phillips, R. J., R. E. Grimm, and M. C. Malin, Hot-spot evolution and the global tectonics of Venus, *Science*, 252, 651-658, 1991a.
- Phillips, R. J., R. F. Raubertas, R. E. Arvidson, I. C. Sarkar, R. R. Herrick, N. Izenberg, and R. E. Grimm, Impact craters and Venus resurfacing history, *J. Geophys. Res.*, 97, 15,923-15,948, 1992.
- Plaut, J. J., The non-SAR experiments, in *Guide to Magellan image interpretation*, J. P. Ford, J. J. Plaut, C. M. Weitz, T. G. Farr, D. A. Senske, E. R. Stofan, G. Michaels and T. J. Parker, JPL Publication 93-24, *Jet Propulsion Laboratory*, Pasadena, California, pp. 148, 1993.
- Pollack, J. B., and D. C. Black, Implications of the gas compositional measurements of Pioneer Venus for the origin of planetary atmospheres, *Science*, 205, 56-59, 1979.

- Price, M. H., and J. Suppe, Mean age of rifting and volcanism on Venus deduced from impact crater densities, *Nature*, 372, 756-759, 1994.
- Price, M. H., G. Watson, J. Suppe, and C. Brankman, Dating volcanism and rifting on Venus using impact crater densities, *J. Geophys. Res.*, 101, 4,657-4,671, 1996.
- Richards, M. A., R. A. Duncan, and V. E. Courtillot, Flood basalts and hotspot tracks: Plume heads and tails, *Science*, 246, 103-107, 1989.
- Rittmann, A., Structure and evolution of Mount Etna, *Phil. Trans. R. Soc. Lond. A* 274, 5-16, 1973.
- Roberts, K. M., and J. W. Head, Large-scale volcanism associated with coronae on Venus: Implications for formation and evolution *Geophys. Res. Lett.*, 20, 1,111-1,114, 1993.
- Romano, R. and J. E. Guest, Volcanic geology of the summit and northern flank of Mount Etna, Sicily, *Bull. Soc. Geol. It.*, 98, 189-215, 1979.
- Rowland, S. K. and G. P. L. Walker, Pahoehoe and aa in Hawaii: volumetric flow rate controls the lava structure, *Bull. Volcanol.*, 52, 615-628, 1990.
- Ryan, M. P., Elasticity and contractancy of Hawaiian olive tholeiite and its role in the stability and structural evolution of subcaldera magma reservoirs and rift systems, in *Volcanism in Hawaii*, edited by R. W. Decker, T. L. Wright, and P. Stauffer, *U.S. Geol. Surv. Prof. Pap.*, 1350, 1,395-1,447, 1987b.

- Ryan, M. P., J. Y. K. Blevins, A. T. Okamura, and R. Y. Koyanagi, Magma reservoir subsidence mechanics: Theoretical summary and application to Kilauea volcano, Hawaii, *J. Geophys. Res.*, 88, 4,147-4,181, 1983.
- Ryan, M. P., Neutral buoyancy and the mechanical evolution of magmatic systems, in *Magmatic processes: Physico-chemical principles*, *Spec. Pub. 1*, edited by B. O. Mysen, pp. 259-287, *Geochem. Soc.*, 1987a.
- Sandwell, D. T. and G. Schubert, Flexural ridges, trenches, and outer rises around coronae on Venus. *J. Geophys. Res.*, 97, 16,069-16,083, 1992.
- Saunders, A. J. Spear, P. C. Allin, R. S. Austin, A. L. Berman, R. C. Chandlee, J. Clark, A. V. DeCharon, E. M. DeJong, D. G. Griffith, J. M. Gunn, S. Hensley, W. T. K. Johnson, C. E. Kirby, K. S. Leung, D. T. Lyons, G. A. Michaels, J. Miller, R. B. Morris, A. D. Morrison, R. G. Piereson, J. F. Scott, S. J. Shaffer, J. P. Slonski, E. R. Stofan, T. W. Thompson, and S. D. Wall, Magellan mission overview, *J. Geophys. Res.*, 97, 13,067-13,090, 1992.
- Saunders, R. S., and G. H. Pettengill, Magellan: Mission Summary. *Science*, 252, 247-249, 1991.
- Saunders, R. S., and M. C. Malin, Geologic interpretation of new observations of the surface of Venus, *Geophys. Res. Lett.*, 4, 11, 546-549, 1977.
- Saunders, R. S., R. E. Arvidson, J. W. Head, G. G. Schaber, E. R. Stofan, and S. C. Solomon, An Overview of Venus Geology, *Science*, 252, 249-252, 1991.
- Schaber G. G. and R. C. Kozak, Morphologies of ten venusian shields between lat. 30⁰ N and 90⁰ N, (abstract), *Lunar and Planet. Sci.*, XX, 954-955, 1989.

Schaber, G. G., E. M. Shoemaker, and R. C. Kozak, The surface age of Venus, *Solar System Res.*, 21, 89-94, 1987.

Schaber, G. G., R. G. Strom, H. J. Moore, L. A. Soderblom, R. L. Kirk, D. J. Chadwick, D. D. Dawson, L. R. Gaddis, J. M. Boyce, and J. Russell, Geology and distribution of impact craters on Venus: What are they telling us?, *J. Geophys. Res.*, 97, 13,257-13,301, 1992.

Schaber, G. G., Venus: Limited extension and volcanism along zones of lithospheric weakness, *Geophys. Res. Lett.*, 9, 499-502, 1982.

Schaber, G. G., Venus: Quantitative analyses of terrain units identified from Venera 15/16 data and described in open-file report 90-24. Open-File Report 90-468, Dept. of the Interior, U.S. Geological Survey, 1990.

Schaber, G. G., Volcanism on Venus as inferred from the morphometry of large shields, *21 st Proc. Lunary and Planet. Sci. Conf.*, Houston: Lunar and Planetary Institute, 3-11, 1991.

Schultz, P. H., Atmospheric effects on ejecta emplacement and crater formation on Venus from Magellan, *J. Geophys. Res.*, 97, 16,183-16,248, 1992.

Self, S., L. Wilson, and I. A. Nairn, Vulcanian eruption mechanisms, *Nature*, 277, 440-443, 1979.

Self, S., Th. Thorddarson, L. Keszthelyi, G. P. L. Walker, K. Hon, M. T. Murphy, P. Long, and S. Finnemore, A new model for the emplacement of Columbia River Basalts as large, inflated pahoehoe lava flow fields, *Geophys. Res. Lett.*, 23, 2,689, 2692, 1996.

Senske, D. A., and E. R. Stofan, Geologic Mapping on Venus in *Guide to Magellan image interpretation*, J. P. Ford, J. J. Plaut, C. M. Weitz, T. G. Farr, D. A. Senske, E. R. Stofan, G. Michaels and T. J. Parker, JPL Publication 93-24, *Jet Propulsion Laboratory*, Pasadena, California, pp. 148, 1993.

Senske, D. A., D. B. Campbell, E. R. Stofan, P. C. Fisher, J. W. Head, N. Stacy, J. C. Aubele, A. A. Hine, and J. K. Harmon, Geology and tectonics of Beta Regio, Guinevere Planitia, Sedna Planitia, and Western Eistla Regio, Venus: Results from Arecibo image data, *Earth, Moon, Planets*, 55, 163-214, 1991a.

Senske, D. A., G. G. Schaber, and E. R. Stofan, Regional topographic rises on Venus: Geology of western Eistla Regio and comparison to Beta Regio and Atla Regio, *J. Geophys. Res.*, 97, 13,395-13,420, 1992.

Senske, D. A., Geology of the Venus equatorial region from Pioneer Venus radar imaging, *Earth, Moon, Planets*, 50/51, 305-328, 1990.

Senske, D. A., J. W. Head, E. R. Stofan, and D. B. Campbell, Geology and structure of Beta Regio, Venus: Results from Arecibo radar imaging, *Geophys. Res. Lett.*, 18, 1,159-1,162, 1991b.

Shaw, H. R., and D. A. Swanson, Eruption and flow rates of flood basalts, in *Proc. Second Columbia River Basalt Symposium*, edited by E. H. Gilmour and D. Stradling, pp 271-299, Cheney, Eastern Washington State College Press, 1970.

Smrekar, S. E., and E. R. Stofan, Coupled upwelling and delamination: A new mechanism for coronae formation and heat loss on Venus, submitted to *Science*, 1997.

Smrekar, S. E., Evidence for active hotspots on Venus from analysis of Magellan gravity data, *Icarus*, 112, 2-26, 1994.

- Solomon, S. C., and J. W. Head, Mechanisms for lithospheric heat transport on Venus: Implications for tectonic style and volcanism, *J. Geophys. Res.*, 87, 9,236-9,246, 1982.
- Solomon, S. C., and J. W. Head, Fundamental Issues in the Geology and Geophysics of Venus, *Science*, 252, 252-260, 1991.
- Solomon, S. C., S. E. Smrekar, D. L. Bindschadler, R. E. Grimm, W. M. Kaula, G. E. McGill, R. J. Phillips, R. S. Saunders, G. Schubert, S. W. Squyres, and E. R. Stofan, Venus tectonics: An overview of Magellan observations, *J. Geophys. Res.*, 97, 13,199-13,255, 1992.
- Sparks, R. S. J. and H. Pinkerton, Effect of degassing on rheology of basaltic lava, *Nature*, 276, 385-386, 1978.
- Squyres, S. W., D. M. Janes, G. Baer, D. L. Bindschadler, G. Schubert, V. L. Sharpton, and E. R. Stofan, The morphology and evolution of coronae on Venus, *J. Geophys. Res.*, 97, 13,611-13,634, 1992.
- Stofan E. R., S. E. Smrekar, D. L. Bindschadler, and D. A. Senske, Large topographic rises on Venus: Implications for mantle upwelling, *J. Geophys. Res.*, 100, 23,317-23,327, 1995.
- Stofan, E. R., and J. E. Guest, Geology of the Aino Planitia Quadrangle (V46): Relative timing of tectonism and volcanism, (abstract), *Lunar Planet. Sci.*, XXVII, 1,277-1,278, 1996.
- Stofan, E. R., and J. W. Head, Coronae of Mnemosyne Regio: Morphology and origin, *Icarus*, 83, 216-243, 1990.
- Stofan, E. R., and S. E. Smrekar, New insights into corona evolution on Venus: Implications for models of origin, (abstract), *Lunar Planet. Sci.*, XXVII, 1,279-1,280, 1996.

- Stofan, E. R., Coronae on Venus: Topographic variations and correlations between morphology and regional setting, *Lunar Planet. Sci.*, XXVI, 1,361-1,362, 1995.
- Stofan, E. R., D. L. Bindschadler, J. W. Head, and E. M. Parmentier, Corona structures on Venus: Models of origin, *J. Geophys. Res.*, 96, 20,933-20,946, 1991.
- Stofan, E. R., V. H. Hamilton, D. M. Janes, and S. E. Smrekar, Coronae on Venus, Morphology and Origin, in *Venus II*, edited by S. W. Bougher, D. M. Hunten, and R. J. Phillips, Univ. of Ariz. Press, Tucson, in press, 1997.
- Stofan, E. R., V. L. Sharpton, G. Schubert, G. Baer, D. L. Bindschadler, D. M. Janes, and S. W. Squyres, Global distribution and characteristics of coronae and related features on Venus: Implications for the origin and relation to mantle processes, *J. Geophys. Res.*, 97, 13,347-13,378, 1992.
- Strom R. G., G. G. Schaber, and D. D. Dawson, The global resurfacing of Venus, *J. Geophys. Res.*, 99, 10,899-10,926, 1994.
- Strom, R. G., G. G. Schaber, D. D. Dawson, and R. L. Kirk, Reply, *J. Geophys. Res.*, 100, 23,361-23,365, 1995.
- Strom, R. G., Parabolic features and the erosion rate on Venus, (abstract), *Lunar Planet. Sci.*, XXIV, 1,371-1,372, 1993.
- Surkov, Yu. A., F. F. Kirnozov, V. N. Glazov, A. G. Dunchenko, L. P. Tatsy, and O. P. Sobornov, Uranium, thorium, and potassium in the Venusian rocks at the landing sites of Vega 1 and 2, *Proc. of the Seventeenth Lunar and Planet. Sci. Conf.*, Part 2, *J. Geophys. Res.*, 92, E537-E540, 1987.

- Surkov, Yu. A., L. P. Moskalyova, V. P. Kharyukova, A. D. Dudin, G. G. Smirnov and S. E. Zaitzeva, Venus rock composition and the Vega 2 landing site, *Proc. of the Sixteenth Lunar and Planet. Sci. Conf.*, Part 2, *J. Geophys. Res.*, 91, 212-218, 1986.
- Surkov, Yu. A., V. L. Barsukov, L. P. Moskalyova, V. P. Kharyukova, and A. L. Kemurdzhian, New data on the composition, structure, and properties of Venus rock obtained by Venera 13 and 14. *Proc. of the fourteenth Lunar and Planet. Sci. Conf.*, Part 2, *J. Geophys. Res.*, 89, 393-402, 1984.
- Swanson, D. A., Pahoehoe flows from the 1969-1971 Mauna Ulu eruption, Kilauea Volcano, *Hawaii. Geol. Soc. Am. Bull.*, 84, 615-626, 1973.
- Swanson, D. A., T. Wright, and R. Helz, Linear vent systems and estimated rates of magma production and eruption for the Yakima basalt on the Columbia Plateau, *Am. J. Sci.*, 275, 877-905, 1975.
- Syluta, E. N., and M. A. Kreslavsky, Intermediate (20-100 km) sized volcanic edifices on Venus, (abstract), *Lunar and Planet. Sci.*, XXI, 1,174-1,175, 1990.
- Tackley, P. J., and D. J. Stevenson, The production of small venusian coronae by Rayleigh-Taylor instabilities in the uppermost mantle, (abstract), *Eos, Trans, AGU*, 72, 287, 1991.
- Tanaka, K. L., The Venus geologic mappers' handbook, 2nd ed., *U. S. Geol. Surv.*, open file report 94-438, p 50, 1994.
- Tapper, S. W and J. E. Guest, Geology of the Scarpellini (V33) quadrangle of Venus, (abstract) *Lunar Planet. Sci.*, XXVIII, 1997.

- Tapper, S. W., A survey and investigation of 'stealth' coronae on Venus: Distribution, morphology and stratigraphy, (abstract) *Lunar Planet. Sci.*, XXVIII, 1997.
- Thornhill, G. D., Theoretical modelling of eruption plumes on Venus, *J. Geophys. Res.*, 98, 9,107-9,111, 1993.
- Tolan, T. L., S. P. Reidel, M. H. Beeson, J. L. Anderson, K. R. Fecht and D. A. Swanson, Revisions to the estimates of areal extent and volume of the Columbia River Basalt Group, *Geol. Soc. Am., Spec. Pap.*, 239, 1-20, 1989.
- Turcotte, D. L., An episodic hypothesis for venusian tectonics, *J. Geophys. Res.*, 98, 17,061-17,068, 1993.
- Turcotte, D. L., How does Venus lose heat?, *J. Geophys. Res.*, 100, 16,931-16,940, 1995.
- Tyler, G. L., P. J. Ford, D. B. Campbell, C. Elachi, G. H. Pettengill, and R. A. Simpson, Magellan: Electrical and physical properties of Venus' surface, *Science*, 252, 265-270, 1991.
- Tyler, G. L., R. A. Simpson, M. J. Maurer, and E. Holmann, Scattering properties of the venusian surface: Preliminary results from Magellan, *J. Geophys. Res.*, 97, 13,115-13,139, 1992.
- Ulaby, F. T., T. H. Bengal, M. C. Dobson, J. R. East, J. B. Garvin and D. L. Evans, Microwave dielectric properties of dry rocks, *I.E.E.E. Int. Geoscience and Remote Sensing*, 28, 3, 325-335, 1990.
- Wadge, G., G. P. L Walker, and J. E. Guest, The output of the Etna volcano, *Nature*, 255, 385-387, 1975.
- Wadge, G., The storage and release of magma on Mt. Etna, *J. Volcanol. Geotherm. Res.*, 2, 361-384, 1977.

- Wadge, G., The variation of magma discharge during basaltic eruptions, *J. Volcanol. Geotherm. Res.*, 11, 139-168, 1981.
- Walker, G. P. L., Compound and simple lava flows and flood basalts, *Bull. Volcanologique, Tome XXXV-3*, 579-590, 1971.
- Walker, G. P. L., Lengths of lava flows, *Phil. Trans. R. Soc. Lond., A*, 274, 107-118, 1973.
- Walker, G. P. L., Thickness and viscosity of Etnean lavas, *Nature*, 213, 484-485, 1967.
- Wall, S. D., S. L. McConnell, C. E. Leff, R. S. Austin, K. K. Beratan, and M. J. Rokey, User guide to the Magellan synthetic aperture radar images, NASA reference publication 1356, *Jet Propulsion Laboratory*, Pasadena, California, pp. 205, 1995.
- Weitz, C. M., and A. T. Basilevsky, Magellan observations of the Venera and Vega landing site regions, *J. Geophys. Res.*, 98, 17,069-17,097, 1993.
- Wilhelms, D. E., Geologic mapping, in *Planetary Mapping*, edited by R. Greeley and R. M. Batson, Cambridge University Press, 1990.
- Wilson, L., and J. W. Head, A comparison of volcanic eruption processes on Earth, Moon, Mars, Io, and Venus, *Nature*, 302, 663-669, 1983.
- Wilson, L., and J. W. Head, Factors controlling the structures of magma chambers in basaltic volcanoes, (abstract), *Lunar Planet. Sci.*, XXI, 1,343-1,344, 1990.
- Young, C., editor, The Magellan Venus explorers guide, JPL Publication 90-24, *Jet Propulsion Laboratory*, Pasadena, California, pp. 197, 1990.

Appendices

Appendix I - Magellan Radar Products: Acquisition and Reduction

1. Magellan Data Acquisition

Magellan radar data were obtained by a 'burst mode' operation process in which the sensor acquired SAR, altimetric and radiometric data sequentially in batches several times each second (Figure 1). The bursts were interleaved with the returning pulses from the surface received by the HGA. The acquisition of data commenced when Magellan was located above the north pole with the HGA pointed towards the venusian surface, traversing from north to south (Figure 2), each observation period lasted 37.2 minutes. After each 37.2 minute mapping phase, Magellan was rotated and the HGA aimed to playback the recorded radar data to a Deep Space Network station on Earth. After completion of playback and spacecraft housekeeping data, Magellan was rotated to orientate the HGA ready for the next mapping phase (Figure 2).

Owing to the area of new terrain observed in equatorial latitudes being much greater than at the poles, it was possible to map high latitudes on alternating orbits with an acceptable margin of overlap, resulting in reduced redundancy and maximising spatial coverage. During the first mapping cycle (Cycle 1), mapping commenced at the north pole continuing to approximately 57° . The next mapping orbit started at 70° north and extended to 74° south. These styles of orbits were alternated. Magellan completed 7.3 orbits in 24 hours, each orbit lasting 3.259 hours (*Saunders and Pettengill, 1991; Ford, 1993*).

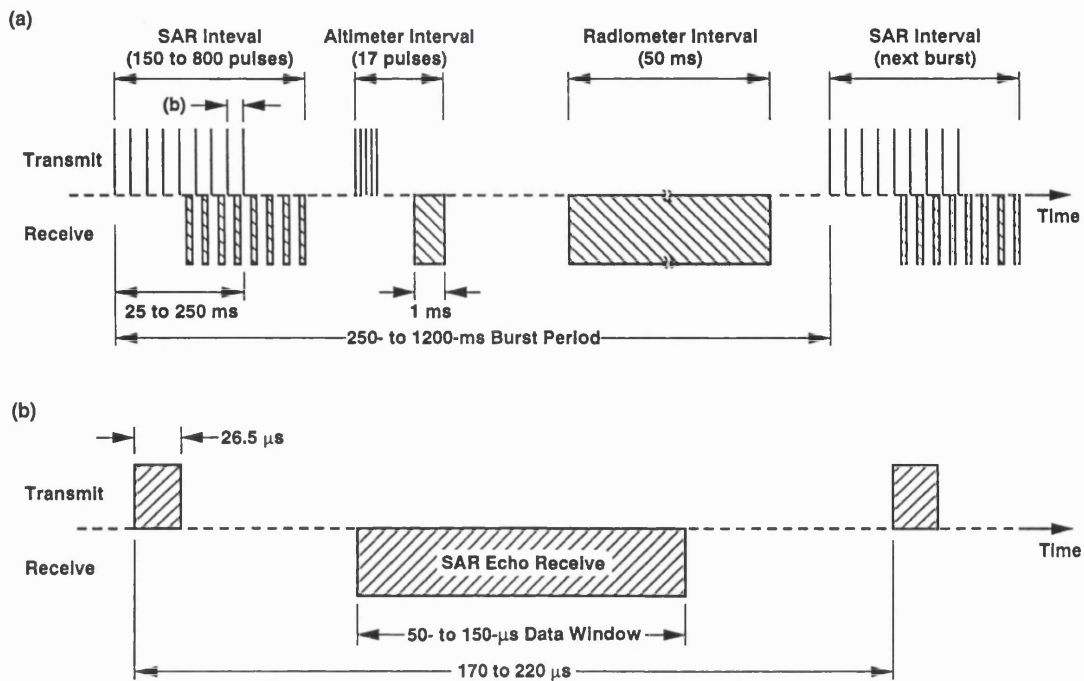


Figure 1 Burst-Mode method of data collection (a) time-domain multiplexing of SAR altimeter, and radiometer intervals; (b) detail of the receive interval between transmitted SAR pulses. After Ford (1993), adapted from Pettengill et al. (1991).

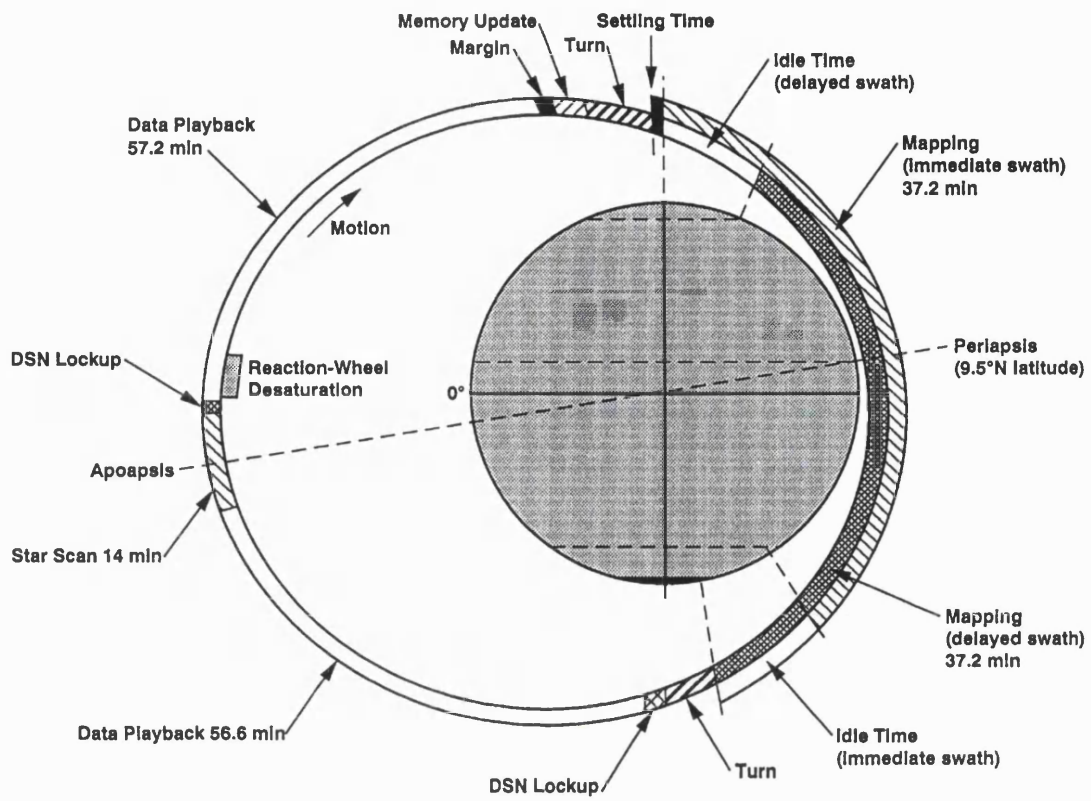


Figure 2 Magellan mapping orbit profile. After Ford, (1993) adapted from Young (1990).

2. SAR Products

SAR data products were obtained by processing the scattering coefficient σ_0 (sigma-0) returned from the surface of the planet. The scattering coefficient is defined as the scattering cross section per surface area (m^2), a dimensionless quantity which can be treated as an intrinsic property of the surface at a given wavelength, polarisation, and incidence angle (*Tyler et al.*, 1991, 1992; *Tanaka et al.*, 1994; *Campbell*, 1995). The value has several terms in the literature: sigma zero, specific backscatter cross section and absolute backscatter cross section. In this thesis, sigma-0 is referred to as radar backscatter. The backscatter values from which the Magellan CD-ROM and photoproducts are produced have been scaled using an empirical model for radar echoes, derived by *Muhleman* (1964). The 'Muhleman law' is a best-fit approximation to the average backscatter as a function of incidence angle which incorporates both the quasi-specular and diffuse components, treated separately by *Hagfors* (1968). The scaling allows the dynamic range of the data to be compressed into 8-bit format of the pixels, regardless of the incidence angle of the observations.

The Muhleman model has been modified for Venus by *Pettengill* (1988). The prescribed reference backscatter coefficient (σ_0) model as a function of incidence angle (θ) is given by:

$$\sigma_0 = \alpha \cos \theta / (\sin \theta + \beta \cos \theta)^3 \quad \text{Eq. 1.1}$$

where the constants $\alpha = 0.111$ and $\beta = 0.0188$ (empirically derived from Pioneer-Venus data) describe the radar scattering behaviour of the 'average' Venus surface.

However, because of a document misprint, the SAR processor was implemented using the following values: $\alpha = 0.111$ and $\beta = 0.0118$. Furthermore, an error was found in the SAR processor such that $\theta + 0.50$ was used instead of the intended value of θ (*Saunders et al.*, 1992). Consequently, the pixel values are based on the following function:

$$\sigma_0 = 0.0118 \cos(\theta + 0.5^\circ) / (\sin(\theta + 0.5^\circ) + 0.111 \cos(\theta + 0.5^\circ))^3$$

Eq. 1.2

The normalising (scaling) of SAR data means the interpretation of radar backscatter over a wide latitudinal range cannot be achieved since the incidence angle for the two areas will be different. In order to compare the true changes in backscatter, the data must be un-normalised (re-scaled) into a linear value before performing arithmetic operations such as averaging (*Saunders et al.*, 1992; *Wall et al.*, 1995). This is an important consideration when interpreting Magellan SAR images. The raw pixel values which are observed relate to Muhleman such that:

$$\text{Pixel value in dB} = 10 \times \log_{10}(\sigma_{\text{obs}} / \sigma_0)$$

Eq. 1.3

The relation between real pixel values and the image brightness is given by:

$$\text{Pixel value in dB} = 0.2 (\text{pixel DN} - 101)$$

Eq. 1.4

The scaling of the data allows a range of backscatter-pixel values from 1 to 252 (0 and 253 to 255 were used as tags) represented within -25 to +25 dB in 0.2 dB steps. Any averaging of pixel within Magellan images must be carried out by finding the backscatter coefficient (σ_0) from the raw image data.

3. Non-SAR Products, Altimetry and Radiometry data.

Data obtained from the altimeter and radiometer modes are important components in the understanding of the venusian surface and give further dimensions to geological mapping. Ancillary data were referred to while mapping the quadrangles, and during the detailed study of coronae and Sif and Gula Montes in V31.

The altimeter, with a nadir-looking geometry, was designed to determine the distance between the spacecraft and the surface directly below. From these data topography was calculated. Knowledge of the orbital position of Magellan relative to the centre of the planet is combined with the spacecraft-to-surface distance determined by the round-trip travel time of the altimeter signals to produce a topographic map of the surface (*Ford and Pettengill, 1992; Ford and Plaut, 1993*). The footprint size depends on the altitude of the spacecraft, which varies with latitude ranging from 10 and 30 km between 10° N and 80° N respectively; best vertical resolution approximates to 80 metres.

The echoes were used to estimate the surface elevation, Fresnel reflectivity and rms slope by fitting data to an echo 'template' for each footprint, of which there were approximately a thousand per orbit. The echo template represents the strength of the received echo as a function of time delay and are based on Hagfors scattering function (*Hagfors, 1964*). This model assumes a gently undulating surface with no wavelength-scale roughness. Natural surfaces generally depart from this assumption, so a correction is made to the reflectivity for diffuse scattering by wavelength-scale rocks. The Hagfors expression (*Hagfors, 1964, 1968*) which predicts the intensity of radar backscatter (σ_0) from planetary surfaces as a function of incidence angle (θ) Fresnel reflectivity coefficient (ρ) and the large scale roughness of the surface (rms slope, C) is:

$$\sigma_0 = 0.5 \rho C (\cos^4 \theta + C \sin^2 \theta)^{-3/2} \quad \text{Eq. 1.5}$$

Where rms slope in radians is $C^{-1/2}$

The function has proven to be appropriate for the majority of surfaces on Venus where the incidence angle for the altimeter is less than 15° , which corresponds to the altimeter system. For smooth areas the results are reasonably accurate, however, on rougher terrains the Hagfors model is no longer applicable and reflectivity estimates should be treated with some caution (*Campbell, 1995*). On Venus a typical value of C is 175 which corresponds to a rms slope of approximately 4° and a Fresnel reflectivity of 0.12.

Fresnel reflectivity is a measure of the efficiency of a surface in reflecting electromagnetic radiation. A Fresnel reflectivity of 1.0 represents perfect, total reflection. Fresnel reflectivity (ρ) is related to the dielectric constant (ϵ) of the surface such that:

$$\rho = (1 - \sqrt{\epsilon} / 1 + \sqrt{\epsilon})^2 \quad \text{Eq. 1.6}$$

Magellan collected measurements of the passive thermal emission from the surface of Venus at the same wavelength (12.6 cm) and viewing geometry as the SAR instrument (*Pettengill et al., 1992*). Surface emissivity was derived from the radiometry measurements made by the HGA in the passive mode. Emissivity is a measure of how well an object approximates to a perfect blackbody radiator, ranging between 0 and 1, with a good emitter needing to be a good absorber to maintain thermal balance. Emissivity increases with increasing temperature and decreases with conductivity and dielectric constant and gives an insight into the dielectric properties of the surface materials. Dielectric properties are controlled partly by the metallic content and density of the materials. Hence, emissivity can be a useful guide to the chemical composition of the surface materials (see *Pettengill et al., 1992*).

To solve for emissivity, the temperature and radiance for any given area is needed. The temperature was assumed to be a well-behaved function of surface elevation, the radiance was measured by the HGA. The energy emitted (the radiance) is recorded as a temperature brightness T_b ; emissivity can then be calculated using Stefan's Law:

$$R = \sigma e T^4 \quad \text{Eq. 1.7}$$

Where R = total radiance in Wm^{-2} (Stefan-Boltzmann constant)
 $\sigma = 5.67 \times 10^{-8} \text{ Wm}^{-2} \text{ K}^{-4}$
 e = emissivity
 T = temperature, K

If a surface is perfectly smooth, the emissivity will be the complement of the Fresnel reflection coefficient for the same polarisation and incidence angle:

$$E = 1 - \rho \quad \text{Eq. 1.8}$$

However, if a surface is rough or tilted (on any scale) a greater surface area is exposed along any surface area of the same angular distance as seen from the antenna. Since the flux is constant but the presented surface area larger, the total amount of energy radiated from the rougher region will be greater from a smoother region.

The radiometry measurements were interleaved with the collection of the SAR data and so the two data sets have the same geometry; the incidence angles of the SAR data are equivalent to the emission angles of the radiometry data. The radiometry footprint size is a function of spacecraft latitude. The dielectric constant ϵ can be found from:

$$\theta = \sin^{-1}(\sin \theta / \sqrt{\epsilon}) \quad \text{Eq. 1.9}$$

Appendix II: DESCRIPTION OF MAP UNITS - V31 SIF MONS QUADRANGLE

PLAINS MATERIALS

- gpr** **Guinevere regional plains material** -- Extensive unit comprising approximately 45 % of quadrangle. Radar backscatter coefficients are locally homogeneous and are comparatively weak. Unit characterised by a pervasive wrinkle ridge fabric of varying orientation, although a dominant trend of NW-SE is observed. Local reticulate pattern of wrinkle ridges is common. Individual flows not resolved. Small volcanic edifices are identified that have a similar radar backscatter to surrounding plains. Majority of unit lies below the planetary radius (MPR) of 6051.8 km. *Type locality*: 17.94⁰ N, 333.28⁰ E. *Interpretation*: Extensive volcanic plains materials erupted as lava with low effective viscosity with a relatively smooth surface later deformed by compressional stresses
- gph** **Guinevere homogeneous plains material** -- Generally has moderate radar backscatter coefficients, giving a homogeneous appearance. Deficient in small edifices. Contains less wrinkle ridges than *gpr*. Boundaries of unit are often diffuse and sometimes difficult to delineate. Embayed by *gpr*. *Type locality*: 01⁰ N, 335⁰ E. *Interpretation*: Volcanic materials (lava flows) with a relatively rough surface texture at cm-scale deformed by compressional stresses
- gplm** **Guinevere lineated and mottled plains material** -- Radar backscatter coefficients variable on a local scale. Contains abundant edifices typically 2 to 5 km in diameter and predominantly of a shield morphology. Unit has a greater elevation than *gpr*. Displays numerous styles of deformation (ridges, graben and fractures). A fine polygonal fabric is common. Embayed by *gpr* and *gph*. *Type locality*: 21.94⁰ N, 337.8⁰ E. *Interpretation*: Numerous small volcanic edifices and associated flows forming volcanic plains cut by ridges and graben

- pd **Deformed plains material** -- Small outcrops of deformed material with strong radar backscatter coefficients. Can display multi-directional deformation. Embayed by *gpr* and *gplm*. *Type locality*: 11.25⁰ N, 336.5⁰ E.
Interpretation: Small outcrops of earlier plains materials embayed by *gpr* and *gplm*

EDIFICE FLOW MATERIALS

- f **Isolated flow material** -- Small irregular outcrops characterised by relatively weak radar backscatter coefficients. Unit has digitate to lobate boundaries which are often topographically controlled. Small pits are frequently observed. Some outcrops appear to have been modified by surficial crater materials. Superposed on all plains units. *Type locality*: 04.80⁰ N, 335.20⁰ E.
Interpretation: Erupted as flows with low effective viscosity; small pits represent vents
- s **Sif Mons material** -- Materials with a flow like form associated with Sif Mons. Individual flows have different morphologies. Radar backscatter coefficients vary from flow to flow and within a particular flow unit. Individual units typically have distinct lobate boundaries and extend up to 400 km from the caldera. Superposed on *gpr* and *gplm*. *Type locality*: 20⁰ N, 351.7⁰ E. *Interpretation*: Large central shield volcano formed from multiple eruptive events. A number of flank eruptive sites are observed
- g **Gula Mons material** -- Materials with a flow like form associated with large edifice Gula Mons. Individual flows have different morphologies, predominantly digitate. Radar backscatter coefficients vary from flow to flow and within a particular flow unit. Individual units often have distinct lobate boundaries. Superposed on *gpr*. The summit is delineated by parallel lineations. *Type locality*: 20⁰ N, 358⁰ E. *Interpretation*: Large central shield volcano formed from multiple eruptive events

vc **Volcanic centre material** -- Typically intermediate sized edifices greater than 15 kilometres in diameter with associated flow materials. A summit pit or caldera may be present surrounded by materials with variable radar backscatter coefficients which may extend to form an apron approximately 100 km wide. Individual flows can be recognised. Superposed on *gpr* and *gplm* materials. *Type locality*: 19⁰ N, 344⁰ E. *Interpretation*: Central volcanoes of either monogenetic or polygenetic origin and associated lavas

ef **Edifice field material** -- Characterised by a concentration of small (normally less than 10 km in diameter) volcanic edifices of variable morphology but dominantly shields. Size, shape and density of the edifices varies considerably; typical dimensions are on the order of 100 kilometres. Some edifice fields have associated compound flow aprons. Backscatter coefficients vary considerably. Unit is seen superposed on both *g*, *gpr*, *gplm*, *bf2* and *gph*. *Type locality*: 18⁰ N, 353⁰ E. *Interpretation*: Local eruptive centre producing collection of small edifices with or without associated flows

CORONAE MATERIALS

Silvia Corona Materials

si **Silvia corona material** -- Upstanding materials with moderate mottled radar backscatter coefficients. Has undergone greater deformation than the surrounding plains, *gpr*, by which it is embayed. Contain a number of small edifices. *Type Locality*: 12.5⁰ N, 356.0⁰ E. *Interpretation*: Earlier volcanic plains materials uplifted and deformed during the formation of Silvia Corona

Benten Corona Materials

bef **Benten corona edifice field material** -- Irregular field of small edifices in interior of Benten Corona. Numerous edifices observed with different morphologies. *Type locality*: 12.5⁰ N, 340.7⁰ E. *Interpretation*: Late stage volcanism associated with Benten Corona

- bf3 **Benten corona flow material 3** -- Digitate flow material, radar backscatter coefficients change from moderate to strong with increasing distance from corona. Flows emanate from western and southern margin of Benten Corona and extend for approximately 180 km. Superposed on *bf2*, *bf1*, and *ef*. *Type locality*: 14° N, 339° E. *Interpretation*: Materials represent the youngest flow apron of lavas, associated with late stage effusive activity of Benten Corona
- bf2 **Benten corona flow material 2** -- More extensive than *bf3*, unit consists of compound flows seen mainly north of corona and display variable radar backscatter coefficients. Flow boundaries have a more lobate morphology than *bf3* and are clearly deformed by the N and NE annulus of Benten Corona. Superposed on *gpr*, *gplm* and *bf1*, embayed by *bf3*. *Type locality*: 16.5° N, 341° E. *Interpretation*: Relatively voluminous volcanism (lava flows) associated with Benten Corona
- bf1 **Benten corona flow material 1** -- Most extensive materials originating from Benten Corona, generally with homogeneous moderate radar backscatter coefficients. Few individual flows can be delineated within unit. *Type locality*: 15.7° N, 337.5° E. *Interpretation*: Early flow material associated with Benten corona, superposed by *bf2* and *bf3*. Early stage flood lavas from Benten Corona

Nissaba Corona Materials

- cnf2 **Nissaba corona flow material 2** -- A minor unit exhibiting weak radar backscatter coefficients; erupted from small edifice situated on rim of corona. *Type locality*: 24.9° N, 356° E. *Interpretation*: Volcanic flow material associated with small edifice
- cnf1 **Nissaba corona flow material 1** -- Materials with digitate morphology drape southern and SW margin of Nissaba corona. Unit exhibits variable radar backscatter coefficients. *Type locality*: 24.8° N, 355.5° E. *Interpretation*: Volcanic lavas associated with the formation of Nissaba Corona

Idem-Kuva Corona Materials

- if **Idem-Kuva corona flow material** -- Characterised by strong radar backscatter coefficients. Typified by digitate boundary. Western materials originate from a small edifice; eastern materials extend from graben. *Type Locality: 29.5⁰ N, 357.2⁰ E. Interpretation: Later stage effusive activity that occurred after the formation of the corona annulus*
- ikpr **Idem-Kuva corona relic plains material** -- Plains materials with moderate radar backscatter coefficients similar to *gph*. Unit is moderately to severely deformed by compressional and extensional fractures. Unit is superposed by *if* materials. *Type Locality: 25.8⁰ N, 358.0⁰ E. Interpretation: Earlier volcanic plains materials having undergone uplift and deformation during the formation of Idem-Kuva Corona.*

Heng-o Corona Materials

- hvc3 **Heng-o corona volcanic centre material 3** -- Materials with moderate radar backscatter coefficients associated with a prominent edifice located at 1.78⁰ N, 352.01⁰ E. Unit post-dates *hpm* and is contained by western annulus of Heng-o Corona. *Type Locality: 2.43⁰ N, 351.80⁰ E Interpretation: Late stage lava flows which postdate the large scale deformation of Heng-o Corona*
- hvc2 **Heng-o corona volcanic centre material 2** -- Materials with moderate radar backscatter coefficients associated with prominent edifice located at -0.62⁰ S, 353.22⁰ E outside the southern boundary of V31. The edifice is cut by NNW trending fractures. *Type Locality: 0. 25⁰ N, 354.0⁰ E. Interpretation: Volcano with radiating lava flow field which predates fracturing superposed by *hvc3**

- hvc1 **Heng-o corona volcanic centre material 1** -- Materials with moderate but variable radar backscatter coefficients associated with a large edifice approximately 50 km in diameter centred at -0.60° S, 356.97° E. The large edifice is circled by numerous smaller edifices and is cut by NW trending fractures. *Type Locality:* 0.5° N, 356° E. *Interpretation:* Early flow materials with a variable surface roughness.
- hpm **Heng-o corona mottled plains material** -- Plains materials within Heng-o Corona with variable backscatter coefficients similar to *gplm*. Unit is moderately deformed and contains a number of small edifices. The age relationship between *gplm* and *hpm* cannot be established. *Type Locality:* 3.5° N, 352° E. *Interpretation:* Volcanic materials that have been deformed by later tectonics associated with the formation of Heng-o Corona

Beltis Corona Materials

- bf **Beltis corona flow material** -- Materials which originate from the centre of Beltis Corona. Unit has weak to moderate radar backscatter coefficients, with a digitate boundary. Interior lobes of materials with strong radar backscatter coefficients are seen. Materials are topographically controlled by the outer rim of Heng-o Corona. Materials superpose *hpm* and *spr*. *Type locality:* 0.0°N, 350.0°E. *Interpretation:* Volcanic flow materials associated with Beltis Corona

TESSERA MATERIALS

- t **Tessera materials** -- Blocks of upstanding materials with strong radar backscatter coefficients. Contains numerous closely spaced fractures oriented in more than one direction. *Type locality:* 20 °N, 355 °E. *Interpretation:* Highly deformed materials which may represent earlier plains materials

CRATER MATERIALS

- ce Crater ejecta material** -- strong backscatter coefficients radiating from craters. Has gradational distal boundaries. Material may be markedly asymmetrical with lobate boundaries. *Type locality*: 14.7⁰ N, 350.7⁰ E. *Interpretation*: Ejecta excavated by cratering. Asymmetrical ejecta provides an indication of entry direction of meteoroid.
- cf Crater floor material** -- Weak radar backscatter coefficient materials within interior floors of larger craters. Embays both crater walls and *cp* unit where present. Small wrinkle ridges are observed in some craters. *Cf* material is only mapped in craters with diameters greater than 35 kilometres. *Type locality*: 14.4⁰ N, 350.8⁰ E. *Interpretation*: Relatively smooth material; either impact melt or volcanic lava or both
- cp Crater peak material** -- Isolated upstanding with strong radar backscatter coefficients, single or multiple peaks embayed by *cf* materials. Only mapped in craters with diameters greater than 35 kilometres. *Type locality*: 14.46⁰ N, 350.97⁰ E. *Interpretation*: Materials deformed and uplifted from beneath crater floor during late stage excavation by meteoroid impact
- cm Crater margin material** -- Weak radar backscatter coefficients. Unit has sharp proximal boundaries which may fade distally and are often topographically controlled. Superposed on plains units but truncated by crater ejecta. *Type locality*: 14.9⁰ N, 351.2⁰ E. *Interpretation*: Smooth deposits produced by atmospheric and ground shockwave interaction with surficial deposits

**Appendix III: DESCRIPTION OF MAP UNITS - V19
SEDNA PLANITIA QUADRANGLE**

PLAINS MATERIALS

- spr** **Sedna regional plains material** -- Extensive unit comprising approximately 40 % of quadrangle. Radar backscatter coefficient is locally homogeneous and is comparatively weak. Large scale weakly defined boundaries are observed within unit in the NW sector of the quadrangle. Unit is deformed by wrinkle ridges. Deficient in small edifices. Majority of unit lies below the planetary radius (MPR) of 6051.8 km. *Type locality*: 40⁰ N, 350⁰ E. *Interpretation*: Extensive plains erupted as lava with low effective viscosity and a with relatively smooth surface showing weakly defined flow fronts, and later deformed by compressional stresses
- sph** **Sedna homogeneous plains material** -- Generally has a moderate radar backscatter coefficients, giving a homogeneous appearance. Deficient in small edifices. Contains wrinkle ridges. Boundaries of unit are often diffuse and sometimes difficult to delineate. While contact with *spr* is not always clear, embayment by *spr* is observed. *Type locality*: 450⁰ N, 333⁰ E. *Interpretation*: volcanic materials (lava flows) with a relatively rough surface texture at cm-scale deformed by compressional stresses
- splm** **Sedna lineated and mottled plains material** -- Radar backscatter coefficient variable on a local scale. Contains abundant edifices typically 2 to 5 km in diameter and predominantly of a shield morphology. The unit has a greater elevation than *spr*. Displays numerous styles of deformation (ridges, graben and fractures). A fine NW-SE trending fabric is pervasive in the SW sector of the quadrangle. Embayed by *spr* and *sph*. *Type locality*: 33⁰ N, 352⁰ E. *Interpretation*: Numerous small volcanic edifices and associated flows forming volcanic plains cut by ridges and graben

pd **Deformed plains material** -- Small outcrops of deformed material with strong radar backscatter coefficients. May display multi-directional deformation. Embayed by *gpr* and *gplm*. *Type locality*: 42⁰ N, 348⁰ E. *Interpretation*: Small outcrops of early plains materials embayed by *gpr* and *gplm*

EDIFICE FLOW MATERIALS

f **Isolated flow material** -- Small irregular outcrops characterised by a relatively weak radar backscatter coefficients. Digitate to lobate boundaries which are often topographically controlled. Small pits are frequently observed. Superposed *splm*. *Type locality*: 26.0⁰ N, 350.4⁰ E. *Interpretation*: Volcanic flow materials with low effective viscosity; small pits represent vents

s **Sif Mons material** -- Small outcrop of materials with a flow like form associated with Sif Mons located to the south of the quadrangle. Individual flows show a pronounced difference different morphologies and radar backscatter coefficients. Superposed on *spr* and *splm* units. *Type locality*: 25.5⁰ N, 353⁰ E. *Interpretation*: Volcanic materials (lava) erupted from large central volcano

g **Gula Mons material** -- Small outcrop of materials associated with large edifice Gula Mons to the south of the quadrangle. Individual flows have different morphologies, predominantly digitate. Radar backscatter coefficients are variable within materials seen. Individual units often have distinct lobate boundaries. Superpose *spr* materials. *Type locality*: 25.8⁰ N, 359.8⁰ E. *Interpretation*: Volcanic materials (lava) erupted from large central volcano

vc **Volcanic centre flow material** -- Typically intermediate sized edifices greater than 15 kilometres in diameter with associated flow materials. A summit pit or caldera may be present surrounded by materials with variable radar backscatter coefficients which may extend to form an apron approximately 100 km wide. Boundaries are often diffuse. Individual flows can be recognised. Superposed on *spr* and *splm* materials. *Type locality*: 37.6⁰ N, 342.5⁰ E. *Interpretation*: Central volcanoes of either monogenetic or polygenetic origin and associated lavas

ef **Edifice field material** -- Characterised by a concentration of small (normally less than 10 km in diameter) volcanic edifices of variable morphology but dominantly shields. Size, shape and density of the edifices varies considerably; typical dimensions are on the order of 100 kilometres. Some edifice fields have associated compound flow aprons. The unit is seen superposed on *spr*, *splm*, *sph* and *vc* but also embayed by *spm* and *vc*. *Type locality*: 35.0⁰ N, 343.0⁰ E. *Interpretation*: Local eruptive centre producing collection of small edifices with or without associated flows

FLOW MATERIALS

fd **Dissociated flow material** -- A NW-SE trending outcrop of materials with moderate radar backscatter coefficients. The unit consists of numerous individual rafts of various sizes with separated by *spr* materials. The majority of the unit appears to originate from a NW-SE trending lineament. *Type locality*: 39.2⁰ N, 355.5⁰ E. *Interpretation*: Volcanic flow whose crust is relatively rough, has been broken into rafts

nf4 **Neago fluctus flow material 4** -- Small outcrop of materials with weak radar backscatter coefficients. Unit has a lobate to dendritic boundary. Source of materials not observed within quadrangle. *Type locality*: 49.7⁰ N, 350.7⁰ E. *Interpretation*: Volcanic flow materials with a relatively smooth surface texture

- nf3 **Neago fluctus flow material 3** -- Extensive unit contained in the north sector of the quadrangle which has strong, homogeneous radar backscatter coefficients. Unit is deformed by wrinkle ridges, however deformation structure is difficult to identify as the wrinkle ridges have a similar radar backscatter as unit. Boundary of the unit is lobate. Source is not seen in quadrangle. *Nf4* materials superpose unit. *Type locality*: 49.0⁰ N, 347.1⁰ E. *Interpretation*: Extensive volcanic flow materials which have a relatively rough surface texture
- nf2 **Neago fluctus flow material 2** -- Unit of moderate homogeneous radar backscatter coefficients. Deformed by wrinkle ridges and superposed by *nf3*. *Type locality*: 48.4⁰ N, 350.5⁰ E. *Interpretation*: Volcanic flow materials
- nf1 **Neago fluctus flow material 1** -- Unit of moderate homogeneous radar backscatter coefficients. Deformed by wrinkle ridges. Superposed by *nf2*, superposed on spr materials. *Type locality* 45⁰ N, 348⁰ E. *Interpretation*: Volcanic flow materials with a relatively rough surface texture
- fs **Sachs patera flow material** -- Small outcrop of materials with moderate to strong radar backscatter coefficients. Unit originates from elliptical depression delineated by arcuate fractures. Greatest dimension of depression is approximately 75 km. Unit boundary is digitate. Materials superpose *sph* and *ef*. *Type locality*: 49.4⁰ N, 334.4⁰ E. *Interpretation*: Volcanic flow associated with caldera

CORONAE MATERIALS

- cu **Unnamed corona flow material** -- Materials which radiate from central area of an unnamed corona. Unit has moderate radar backscatter coefficients similar to *splm* materials which they superpose. Materials deformed by radial graben. *Type locality*: 30⁰ N, 348⁰ E. *Interpretation*: Volcanic flow materials associated with corona

Nissaba Corona Materials

- cnf3 **Nissaba corona flow material 3** -- A minor unit exhibiting weak radar backscatter coefficients; erupted from small edifice situated on rim of corona. *Type locality: 25.2⁰ N, 356⁰ E. Interpretation:* Volcanic flow material associated with small edifice
- cnf2 **Nissaba corona flow material 2** -- Materials with digitate morphology drape southern and SW margin of Nissaba corona. Unit exhibits variable radar backscatter coefficients. *Type locality: 25.5⁰ N, 354.7⁰ E. Interpretation:* Volcanic lavas associated with the formation of Nissaba Corona
- cnf1 **Nissaba corona flow material 1** -- Weak radar backscatter coefficients; erupted from an edifice situated in the NW sector of Nissaba Corona. Unit is embayed by *spr* and superposes *cnf1* and *npr*. *Type locality: 26.1⁰ N, 354.3⁰ E. Interpretation:* Volcanic flow material associated with an edifice
- npr **Nissaba corona relic plains material** -- Plains materials with moderate radar backscatter coefficients similar to *sph*. Unit is weakly to moderately deformed by compressional and extensional fractures. Unit is embayed by *spr* and superposed by *nf1*, *nf2*, and *nf3*. *Type Locality: 25.5⁰ N, 355.5⁰ E. Interpretation:* Earlier volcanic plains materials having undergone uplift and deformation during the formation of Nissaba Corona.

Idem-Kuva Corona Materials

- if **Idem-Kuva corona flow material** -- Characterised by strong radar backscatter coefficients. Typified by digitate boundary. Western materials to emanate from small edifice; eastern materials extend from graben. *Type locality: 26.5⁰ N, 358.5⁰ E. Interpretation:* Later stage effusive activity that occurred after the formation of the corona annulus

ikpr **Idem-Kuva corona relic plains material** -- Plains materials with moderate radar backscatter coefficients similar to *gph*. Unit is moderately deformed by compressional and extensional fractures. Unit is embayed by *spr* and superposed by *if* materials. *Type Locality*: 26.2° N, 358.0° E. *Interpretation*: earlier volcanic plains materials having undergone uplift and deformation during the formation of Idem-Kuva Corona.

TESSERA MATERIALS

t **Tessera materials** -- Blocks of upstanding materials with strong radar backscatter coefficients. Contains numerous closely spaced fractures oriented in more than one direction. *Type locality*: 40.2° N, 356.5° E. *Interpretation*: Highly deformed materials which may represent earlier plains materials

CRATER MATERIALS













ce **Crater ejecta material** -- strong backscatter coefficients radiating from craters. Has gradational distal boundaries. Material may be markedly asymmetrical with lobate boundaries. *Type locality*: 27° N, 336.8° E. *Interpretation*: Ejecta excavated by cratering. Asymmetrical ejecta provides an indication of entry direction of meteoroid.

cf **Crater floor material** -- Weak radar backscatter coefficient materials within interior floors of larger craters. Embays both crater walls and *cp* unit where present. Small wrinkle ridges are observed in some craters. *Cf* material is mapped in craters with diameters greater than 35 kilometres. *Type locality*: 26.8° N, 336.7° E. *Interpretation*: Relatively smooth material; either impact melt or volcanic lava or both

cp

Crater peak material -- Isolated upstanding with strong radar backscatter coefficients, single or multiple peaks embayed by *cf* materials. Only mapped in craters with diameters greater than 35 kilometres. *Type locality:* 26.7° N, 336.7° E. *Interpretation:* Materials deformed and uplifted from beneath crater floor during late stage excavation by meteoroid impact

Key to mapping symbols for USGS V31 and V19 Quadrangles.

	Contact - Dashed where approximately located or arbitrarily located based on edifice densities.
	Wrinkle ridge. <i>Interpretation:</i> compressional deformation analogous to lunar and martian wrinkle ridges
	Lineament/fracture
	Graben - Bar and ball on downthrown side
	Scarp - Line marks top of slope; hatches point downslope
	Ridge - Large scale topographic features often commonly associated with coronae, barbs point downslope from ridge crest
	Trough - Large scale topographic features often associated with coronae, symbol marks the bottom of the troughs
	Channel, narrow and sinuous. <i>Interpretation :</i> Formed by lava erosion
	Volcanic edifice < 15 km
	Volcanic edifice > 15 km
	Volcanic Dome 5 - 40 km
	Inferred flow direction of flow lobe.



Impact crater



Superficial crater material with strong radar backscatter coefficient



Superficial crater material with weak radar backscatter coefficient

Appendix IV

Location data for radar sample areas for V31 - Sif Mons Quadrangle units.

Unit	Lat	Long	N	Δ(m)	Angle	Radius (km)
gpr	14.290, 15.190 N;	347.340, 348.190 E	205,530	225	45.7	6050.766 (6050.630, 6051.022)
gpr	16.240, 17.120 N;	342.300, 343.360 E	192,750	225	45.5	6050.569 (6050.325, 6050.769)
gpr	07.200, 08.110 N;	339.560, 341.700 E	223,512	225	45.9	6050.218 (6050.001, 6050.541)
gpr	16.040, 16.550 N;	330.540, 332.100 E	225,834	225	45.5	6050.493 (6050.349, 6050.696)
gph	01.490, 02.420 N;	333.200, 334.310 E	231,712	225	45.4	6051.093 (6051.017, 6051.192)
gph	03.500, 04.400 N;	334.460, 335.410 E	170,640	225	45.6	6050.982 (6050.771, 6051.223)
gph	03.490, 04.160 N;	345.130, 345.400 E	044,099	225	45.6	6051.288 (6051.120, 6051.415)
gph	04.560, 05.200 N;	345.120, 345.340 E	032,448	225	45.7	6050.904 (6050.729, 6051.068)
gplm	21.150, 22.010 N;	339.180, 340.220 E	172,674	225	44.6	6051.300 (6050.564, 6051.659)
gplm	12.310, 13.220 N;	333.080, 333.480 E	125,955	225	45.8	6050.798 (6049.867, 6051.009)
gplm	16.390, 17.090 N;	345.340, 346.050 E	054,747	225	45.5	6051.185 (6050.745, 6051.587)
gplm	11.070, 11.420 N;	342.520, 343.570 E	134,534	225	45.9	6050.818 (6050.513, 6051.148)
f	04.500, 04.560 N;	335.040, 335.120 E	003,100	225	45.7	6050.911 (6050.909, 6050.915)
f	04.010, 04.050 N;	333.170, 333.230 E	001,734	225	45.6	6051.255 (6051.238, 6051.273)
f	03.350, 03.420 N;	346.260, 346.430 E	008,083	225	45.6	6051.204 (6051.185, 6051.215)
f	04.070, 04.200 N;	344.140, 344.280 E	011,000	225	45.6	6050.982 (6050.970, 6051.010)
vc	07.560, 08.420 N;	347.480, 348.500 E	199,892	225	45.9	6050.985 (6050.774, 6051.286)
vc	21.430, 22.140 N;	344.470, 345.160 E	054,312	225	44.6	6051.948 (6051.591, 6052.641)
vc	19.420, 20.250 N;	339.110, 339.260 E	040,560	225	44.9	6051.236 (6050.927, 6051.451)
vc	01.240, 02.090 N;	332.210, 332.520 E	088,250	225	45.3	6051.329 (6051.243, 6051.564)
ef	17.330, 18.110 N;	353.010, 353.360 E	079,864	225	45.4	6052.618 (6052.382, 6052.755)
ef	12.120, 12.470 N;	340.380, 341.120 E	076,713	225	45.8	6050.877 (6050.708, 6051.120)
ef	21.580, 22.250 N;	336.220, 336.520 E	045,333	225	44.5	6050.779 (6050.712, 6050.865)
ef	18.400, 19.140 N;	341.520, 342.290 E	077,452	225	45.1	6050.970 (6050.722, 6051.342)
t	20.090, 20.150 N;	354.560, 355.070 E	004,150	225	45.0	6052.997 (6052.806, 6053.151)
t	20.060, 20.130 N;	355.410, 355.480 E	002,900	225	45.0	6052.633 (6052.622, 6052.649)

Location data for radar sample areas for V31 - Sif Mons Quadrangle units.

Unit	Lat,	Long	N	Δ (m)	Angle	Radius (km)
pd	19.380, 19.500 N;	343.140, 343.240 E	007,296	225	45.0	6051.412 (6051.356, 6051.462)
pd	10.390, 10.500 N;	338.170, 338.300 E	007,938	225	45.9	6050.584 (6050.422, 6050.722)
bef	13.270, 13.380 N;	339.330, 339.550 E	014,705	225	45.8	6051.291 (6051.154, 6051.338)
bf3	13.180, 13.510 N;	340.460, 341.140 E	059,701	225	45.8	6051.139 (6050.622, 6051.485)
bf3	14.090, 14.570 N;	338.330, 339.010 E	083,276	225	45.7	6050.880 (6050.541, 6051.389)
bf2	14.430, 15.340 N;	341.470, 342.310 E	140,298	225	45.7	6050.528 (6049.918, 6050.938)
bf2	16.220, 17.040 N;	340.370, 341.200 E	110,544	225	45.5	6050.637 (6050.414, 6050.917)
bf1	15.240, 16.010 N;	337.310, 338.130 E	095,016	225	45.6	6050.721 (6050.616, 6050.943)
bf1	11.020, 11.370 N;	339.590, 340.220 E	049,775	225	45.9	6050.340 (6050.129, 6050.562)
cnf2	24.540, 25.010 N;	335.110, 355.420 E	013,320	225	43.9	6051.842 (6050.704, 6052.650)
cnf1	24.490, 24.590 N;	355.560, 356.040 E	004,880	225	43.9	6052.529 (6052.454, 6052.639)
if	26.010, 26.160 N;	358.290, 358.430 E	008,840	225	43.6	6052.416 (6052.387, 6052.442)
if	25.400, 25.530 N;	357.000, 357.110 E	013,750	225	43.6	6052.475 (6052.438, 6052.511)
hmp	02.500, 03.060 N;	350.500, 351.350 E	045,234	225	45.5	6051.106 (6051.000, 6051.431)
hvc1	00.050, 00.430 N;	355.330, 355.530 E	058,435	225	45.1	6051.396 (6051.275, 6051.485)
hvc2	-01.040, 00.380 N;	352.160, 352.560 E	065,508	225	44.9	6051.339 (6051.305, 6051.375)
hvc3	02.070, 02.220 N;	350.390, 351.360 E	053,788	225	45.4	6051.078 (6051.018, 6051.261)
bf	-00.621, 00.274 N;	349.738, 350.475 E	128,412	225	44.9	

Radar data for sample areas for V31 - Sif Mons Quadrangle units.

Unit	σ_0 (dB)	θ_{rms} (deg)	ρ Fresnel	Emissivity	ϵ_s	ϵ_T
gpr	-19.34 (-26.03, -02.04)	1.78 (1.10, 2.40)	0.103 (0.080, 0.130)	0.832 (0.825, 0.839)	3.3,	5.4
gpr	-17.89 (-23.39, -06.99)	2.31 (1.70, 3.30)	0.098 (0.075, 0.125)	0.838 (0.828, 0.866)	3.2,	5.2
gpr	-17.37 (-23.30, -05.10)	2.54 (1.40, 5.10)	0.122 (0.090, 0.185)	0.812 (0.786, 0.843)	3.6,	6.1
gpr	-16.14 (-22.20, -06.01)	1.40 (0.80, 2.60)	0.082 (0.065, 0.105)	0.848 (0.832, 0.858)	3.1,	4.8
gph	-16.11 (-21.99, -07.18)	2.47 (1.30, 3.50)	0.103 (0.075, 0.145)	0.809 (0.781, 0.830)	3.7,	6.2
gph	-15.81 (-21.43, -07.64)	2.35 (1.50, 3.40)	0.112 (0.085, 0.150)	0.802 (0.783, 0.826)	3.8,	6.5
gph	-15.96 (-22.03, -07.83)	1.83 (0.70, 2.80)	0.081 (0.070, 0.095)	0.841 (0.827, 0.850)	3.2,	5.1
gph	-16.15 (-21.06, -08.05)	2.64 (2.00, 3.60)	0.102 (0.090, 0.110)	0.826 (0.821, 0.834)	3.4,	5.6
gplm	-13.54 (-20.54, -02.17)	2.99 (1.60, 6.30)	0.101 (0.070, 0.190)	0.855 (0.848, 0.863)	3.0,	4.7
gplm	-13.71 (-19.88, -04.68)	3.90 (1.90, 5.80)	0.073 (0.060, 0.095)	0.865 (0.849, 0.874)	2.8,	4.3
gplm	-16.78 (-23.38, -03.18)	3.00 (1.50, 6.30)	0.105 (0.075, 0.175)	0.833 (0.820, 0.851)	3.3,	5.3
gplm	-15.25 (-22.50, -05.50)	1.65 (0.80, 3.00)	0.088 (0.060, 0.130)	0.856 (0.834, 0.867)	2.9,	4.6
f	-18.95 (-23.25, -12.85)	2.47 (2.20, 2.80)	0.092 (0.085, 0.095)	0.827 (0.826, 0.827)	3.4,	5.5
f	-20.07 (-24.83, -12.23)	2.00 (1.90, 2.10)	0.122 (0.115, 0.135)	0.803 (0.802, 0.804)	3.8,	6.4
f	-19.74 (-23.82, -10.22)	2.92 (2.80, 3.10)	0.099 (0.095, 0.100)	0.836 (0.834, 0.839)	3.2,	5.2
f	-18.15 (-22.64, -11.83)	2.38 (2.10, 2.80)	0.103 (0.100, 0.105)	0.832 (0.826, 0.836)	3.3,	5.4
vc	-14.43 (-20.90, -05.50)	1.98 (1.00, 3.60)	0.075 (0.060, 0.105)	0.852 (0.846, 0.859)	3.0,	4.7
vc	-15.76 (-20.77, -05.96)	3.07 (1.80, 4.10)	0.091 (0.055, 0.130)	0.848 (0.836, 0.864)	3.1,	4.9
vc	-17.69 (-22.63, -06.63)	2.17 (1.50, 2.90)	0.104 (0.090, 0.120)	0.837 (0.834, 0.842)	3.3,	5.2
vc	-17.25 (-23.57, -03.15)	2.22 (1.60, 2.80)	0.119 (0.105, 0.135)	0.799 (0.795, 0.805)	3.9,	6.6
ef	-14.51 (-21.94, -01.96)	1.78 (1.00, 2.90)	0.155 (0.135, 0.185)	0.761 (0.742, 0.778)	4.7,	8.2
ef	-17.74 (-23.49, -05.88)	1.95 (1.10, 3.10)	0.101 (0.085, 0.130)	0.822 (0.816, 0.829)	3.5,	5.7
ef	-15.61 (-21.53, -06.33)	1.97 (1.30, 2.40)	0.095 (0.080, 0.110)	0.854 (0.846, 0.860)	3.0,	4.7
ef	-14.50 (-20.91, -04.28)	2.46 (1.60, 3.20)	0.083 (0.070, 0.115)	0.860 (0.853, 0.868)	2.9,	4.5
t	-14.49 (-22.44, -02.24)	2.60 (1.70, 3.60)	0.111 (0.075, 0.140)	0.812 (0.808, 0.816)	3.7,	6.1
t	-12.78 (-20.44, -03.64)	1.35 (1.20, 1.60)	0.138 (0.130, 0.150)	0.809 (0.808, 0.809)	3.8,	6.2

Radar data for sample areas for V31 - Sif Mons Quadrangle units.

Unit	σ_0 (dB)	θ_{rms} (deg)	ρ Fresnel	Emissivity	ϵ_s	ϵ_T
pd	-10.88 (-19.26, -01.65)	2.83 (2.30, 3.60)	----	0.856 (0.854, 0.858)	3.0,	4.6
pd	-12.19 (-19.50, -02.70)	2.52 (2.10, 3.00)	0.082 (0.080, 0.085)	0.833 (0.826, 0.843)	3.3,	5.3
bef	-16.65 (-22.27, -05.07)	3.10 (2.40, 4.90)	0.090 (0.070, 0.115)	0.846 (0.840, 0.854)	3.1,	4.9
bf3	-16.38 (-21.87, -09.47)	2.22 (1.30, 2.80)	0.084 (0.070, 0.110)	0.834 (0.826, 0.849)	3.2,	5.3
bf3	-15.83 (-22.25, -08.46)	2.98 (1.70, 4.10)	0.100 (0.080, 0.115)	0.854 (0.843, 0.871)	2.9,	4.6
bf2	-15.84 (-22.04, -01.82)	2.56 (0.70, 9.70)	0.103 (0.080, 0.145)	0.834 (0.818, 0.864)	3.3,	5.3
bf2	-15.42 (-21.19, -03.38)	2.10 (1.40, 3.20)	0.084 (0.055, 0.105)	0.856 (0.832, 0.876)	3.0,	4.6
bf1	-14.82 (-20.22, -06.42)	1.30 (0.70, 2.30)	0.099 (0.080, 0.135)	0.843 (0.838, 0.848)	3.1,	5.0
bf1	-15.25 (-21.09, -04.69)	2.23 (1.40, 3.30)	0.086 (0.065, 0.095)	0.850 (0.831, 0.869)	3.0,	4.8
cnf2	-15.17 (-20.56, -08.17)	2.09 (0.30, 5.40)	0.135 (0.075, 0.250)	0.816 (0.776, 0.849)	3.8,	6.0
cnf1	-17.85 (-23.36, -10.16)	1.92 (1.50, 2.30)	0.147 (0.135, 0.160)	0.809 (0.807, 0.814)	3.9,	6.2
if	-08.94 (-14.91, -04.11)	1.50 (1.20, 2.00)	0.110 (0.085, 0.135)	0.838 (0.834, 0.842)	3.4,	5.2
if	-11.11 (-19.49, -03.48)	2.71 (2.20, 3.10)	0.121 (0.110, 0.125)	0.819 (0.816, 0.821)	3.7,	5.9
hpm	-16.96 (-22.40, -10.20)	3.23 (2.40, 6.30)	0.098 (0.075, 0.170)	0.836 (0.818, 0.858)	3.2,	5.2
hvc1	-16.62 (-22.71, -05.69)	3.00 (2.10, 3.70)	0.107 (0.095, 0.120)	0.819 (0.815, 0.825)	3.6,	5.8
hvc2	-16.85 (-23.24, -00.64)	2.06 (1.30, 2.90)	0.101 (0.080, 0.130)	0.835 (0.828, 0.845)	3.3,	5.3
hvc3	-16.82 (-21.78, -04.18)	3.20 (1.50, 4.70)	0.090 (0.080, 0.100)	0.840 (0.831, 0.849)	3.2,	5.1
bf	-16.95 (-22.87, -07.05)					

Appendix V

Location data for radar sample areas for V19 - Sedna Planitia Quadrangle units.

Unit	Lat	Long	N	Δ (m)	Angle	Radius (km)
spr	31.490, 32.380 N;	357.520, 359.080 E	204,580	225	41.5	6051.291 (6051.163, 6051.479)
spr	36.460, 37.320 N;	350.190, 351.240 E	176,250	225	39.6	6050.465 (6050.351, 6050.638)
spr	39.460, 40.320 N;	350.020, 351.260 E	184,912	225	38.2	6050.501 (6050.366, 6050.571)
spr	44.240, 45.000 N;	351.550, 352.480 E	086,904	225	36.0	6050.818 (6050.713, 6050.890)
sph	48.450, 49.270 N;	336.240, 337.220 E	081,344	225	34.0	6051.525 (6051.487, 6051.600)
sph	44.290, 45.150 N;	332.390, 334.020 E	175,570	225	35.8	6051.210 (6051.097, 6051.344)
sph	48.120, 48.530 N;	335.590, 337.090 E	127,834	225	34.3	6051.546 (6051.484, 6051.612)
sph	37.180, 38.080 N;	330.160, 331.180 E	152,880	225	39.2	6051.103 (6051.060, 6051.197)
gplm	23.360, 24.230 N;	340.400, 341.240 E	125,060	225	44.1	6052.007 (6051.481, 6052.299)
gplm	35.250, 36.150 N;	336.560, 338.140 E	199,136	225	40.1	6051.083 (6050.920, 6051.321)
gplm	27.040, 27.480 N;	338.270, 339.270 E	151,983	225	43.1	6051.185 (6050.992, 6051.298)
splm	39.350, 40.150 N;	359.300, 359.500 E	085,228	225	38.3	6051.129 (6050.941, 6051.329)
splm	40.550, 41.150 N;	357.210, 357.570 E	033,896	225	37.7	6050.886 (6049.137, 6051.674)
vc						
E. N.	37.550, 38.410 N;	341.480, 342.570 E	142,882	225	39.1	6050.787 (6050.602, 6051.486)
E. S.	37.090, 37.250 N;	341.570, 342.560 E	046,860	225	39.5	6050.686 (6050.589, 6050.789)
vc						
T. N.	29.510, 30.200 N;	354.530, 355.510 E	0941,92	225	42.3	6051.810 (6051.442, 6052.208)
T. S.	28.040, 28.250 N;	354.440, 355.130 E	032,074	225	43.0	6052.099 (6052.067, 6052.140)
ef	33.130, 33.500 N;	349.020, 349.410 E	072,790	225	41.0	6051.022 (6050.838, 6051.390)
ef	34.240, 35.110 N;	330.490, 331.510 E	144,279	225	40.5	6051.448 (6051.343, 6051.546)
ef	31.270, 31.580 N;	331.450, 332.210 E	058,072	225	41.6	6051.429 (6051.294, 6051.554)
ef	47.420, 48.030 N;	334.360, 335.060 E	029,754	225	34.7	6051.541 (6051.478, 6051.621)
t	33.130, 33.490 N;	360.080, 360.440 E	072,448	225	41.0	6051.595 (6051.324, 6051.808)
t	40.240, 40.440 N;	356.470, 357.240 E	035,568	225	37.9	6050.774 (6049.180, 6051.540)
t	44.130, 44.260 N;	356.380, 356.540 E	010,395	225	36.0	6051.039 (6050.772, 6051.164)
t	44.110, 44.430 N;	337.140, 337.250 E	022,932	225	36.2	6051.194 (6051.130, 6051.236)

Location data for radar sample areas for V19 - Sedna Planitia Quadrangle units.

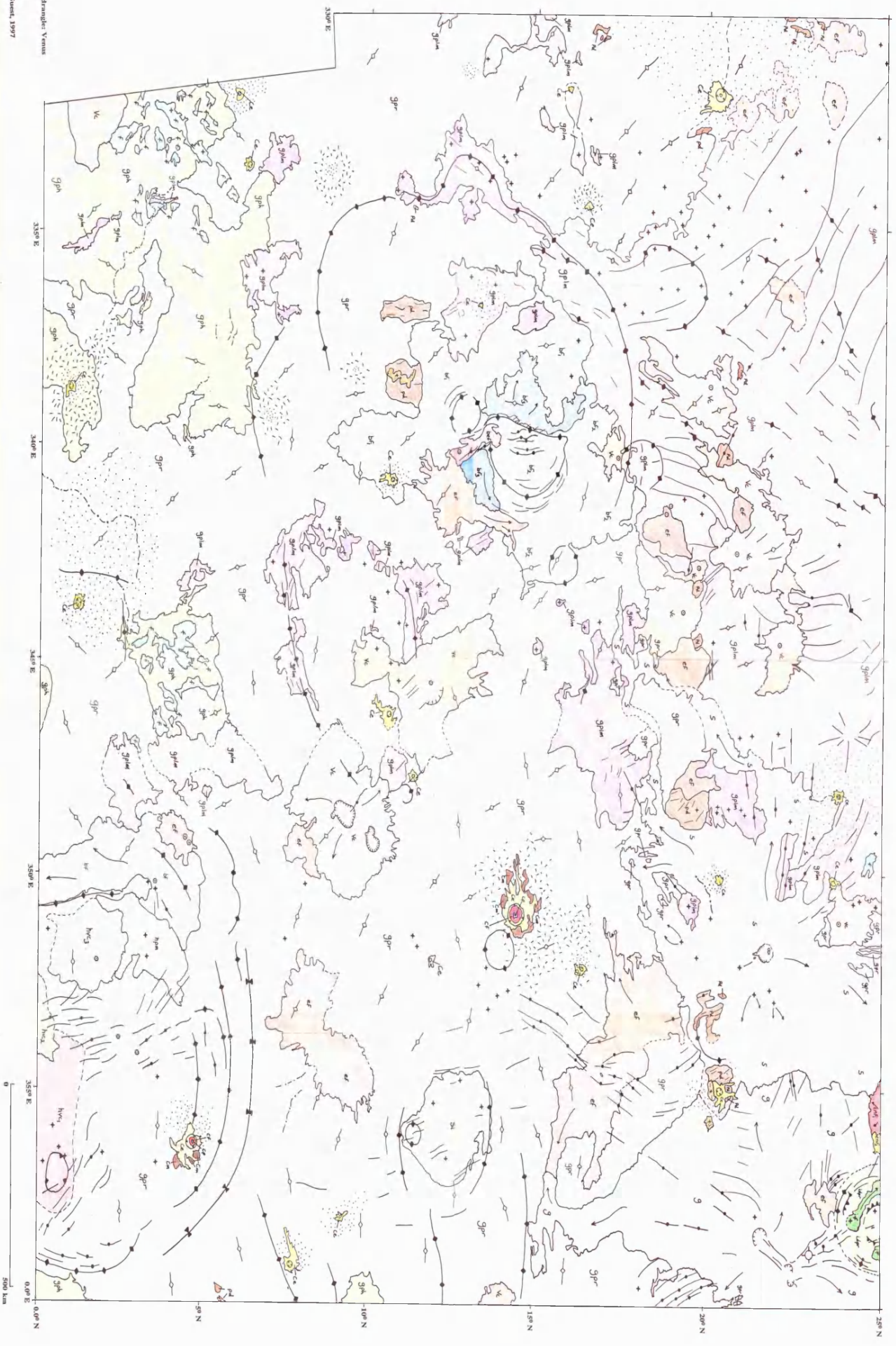
Unit	Lat	Long	N	Δ (m)	Angle	Radius(km)
ik						
West	25.480, 26.090 N;	356.530, 357.030 E	013,182	225	43.6	6052.483 (6052.414, 6052.570)
East	25.590, 26.170 N;	358.270, 358.430 E	017,568	225	43.6	6052.421 (6052.382, 6052.572)
ikpr	25.172, 25.024 N;	358.136, 358.312 E	087,465	075	43.8	
nf1	49.570, 49.530 N;	352.140, 352.210 E	001,116	225	33.3	6051.520 (6051.499, 6051.540)
nf2	48.130, 49.050 N;	347.420, 349.160 E	195,286	225	33.9	6051.332 (6051.201, 6051.490)
nf2	48.300, 49.140 N;	343.120, 345.000 E	183,848	225	33.8	6051.273 (6051.203, 6051.400)
nf3	47.400, 47.270 N;	347.190, 348.060 E	033,565	225	34.6	6051.026 (6050.958, 6051.077)
nf3	48.430, 49.000 N;	350.490, 351.450 E	040,528	225	33.9	6051.406 (6051.336, 6051.486)
nf4	44.180, 45.040 N;	346.470, 348.230 E	190,212	225	36.0	6050.548 (6050.533, 6050.672)
nf4	46.430, 47.020 N;	346.430, 347.490 E	053,808	225	35.0	6050.871 (6050.783, 6050.994)
fd	38.530, 39.070 N;	355.260, 355.430 E	012,650	225	38.7	6050.484 (6050.458, 6050.557)
fd	39.190, 39.160 N;	355.170, 355.230 E	001,184	225	38.7	6050.477 (6050.473, 6050.479)
cnf3	25.142, 25.065 N;	355.670, 355.762 E	087,283	075	43.6	
cnf2	25.612, 25.323 N;	354.766, 354.930 E	144,117	075	43.7	
cnf1	26.011, 25.718 N;	353.940, 354.154 E	087,283	075	43.6	
npr	25.733, 25.453 N;	355.504, 355.839 E	159,470	075	43.7	
cu	30.972, 30.079 N;	347.968, 348.682 E	083,743	225	42.2	
fs	49.643, 49.349 N;	333.945, 334.387 E	016,650	225	33.2	

Radar data for sample areas for V19 - Sedna Planitia Quadrangle units.

Unit	σ_0 (dB)	θ_{rms} (deg)	ρ Fresnel	Emissivity	ϵ_s	ϵ_T
spr	-20.50 (-25.76, -10.57)	2.40 (1.30, 3.20)	0.139 (0.115, 0.165)	0.819 (0.802, 0.831)	3.9,	6.0
spr	-15.82 (-24.55, -08.35)	1.59 (0.90, 2.30)	0.102 (0.080, 0.125)	0.849 (0.844, 0.855)	3.5,	5.0
spr	-16.12 (-20.85, -06.56)	1.22 (0.70, 2.20)	0.117 (0.090, 0.150)	0.846 (0.842, 0.854)	3.7,	5.1
spr	-15.05 (-19.19, -09.19)	1.88 (0.80, 2.70)	0.118 (0.100, 0.140)	0.846 (0.844, 0.849)	3.8,	5.1
sph	-13.03 (-18.56, -08.29)	2.16 (1.40, 3.00)	0.111 (0.090, 0.135)	0.852 (0.847, 0.857)	3.8,	5.0
sph	-13.83 (-18.69, -08.73)	3.60 (2.40, 4.90)	0.112 (0.095, 0.130)	0.862 (0.855, 0.870)	3.5,	4.7
sph	-13.29 (-18.39, -08.47)	2.26 (1.20, 3.20)	0.111 (0.090, 0.140)	0.857 (0.851, 0.861)	3.7,	4.8
sph	-14.16 (-18.91, -06.71)	2.14 (1.20, 2.90)	0.085 (0.070, 0.100)	0.870 (0.861, 0.879)	3.1,	4.4
gplm	-13.05 (-22.83, 02.96)	3.15 (1.20, 9.00)	0.114 (0.085, 0.210)	0.832 (0.820, 0.841)	3.4,	5.4
gplm	-14.34 (-20.08, -04.18)	2.52 (1.60, 3.80)	0.089 (0.075, 0.105)	0.869 (0.861, 0.876)	3.1,	4.4
gplm	-19.56 (-26.16, -04.00)	2.65 (1.70, 3.70)	0.119 (0.095, 0.135)	0.824 (0.821, 0.827)	3.7,	5.7
splm	-13.59 (-20.44, -01.06)	2.73 (1.80, 3.50)	0.132 (0.105, 0.165)	0.829 (0.809, 0.849)	4.0,	5.7
splm	-14.38 (-19.47, -06.06)	2.73 (0.80, 6.20)	0.107 (0.070, 0.170)	0.862 (0.838, 0.896)	3.4,	4.6
vc						
T. N	-19.13 (-24.57, -08.94)	2.90 (1.60, 6.70)	0.120 (0.035, 0.260)	0.827 (0.819, 0.837)	3.7,	5.7
T. S	-19.07 (-23.31, -11.50)	2.00 (1.50, 2.40)	0.127 (0.115, 0.145)	0.829 (0.824, 0.834)	3.6,	5.6
vc						
E. N	-13.39 (-19.19, -00.08)	2.52 (1.20, 3.70)	0.129 (0.105, 0.155)	0.836 (0.826, 0.845)	3.8,	5.4
E. S	-13.07 (-18.55, -02.98)	2.56 (1.90, 3.00)	0.127 (0.110, 0.135)	0.835 (0.831, 0.848)	3.8,	5.4
ef	-12.73 (-20.43, 01.60)	2.47 (1.30, 3.80)	0.116 (0.105, 0.165)	0.854 (0.847, 0.857)	3.3,	4.8
ef	-14.26 (-20.42, -01.82)	2.83 (1.90, 3.80)	0.085 (0.065, 0.095)	0.870 (0.865, 0.881)	3.1,	4.3
ef	-17.48 (-23.78, -03.35)	2.72 (1.70, 3.60)	0.091 (0.080, 0.100)	0.863 (0.857, 0.865)	3.1,	4.5
ef	-14.76 (-20.16, -02.36)	2.35 (1.20, 3.50)	0.125 (0.105, 0.140)	0.865 (0.863, 0.868)	3.5,	4.6
t	-10.26 (-21.58, 01.37)	2.85 (1.50, 8.20)	0.079 (0.065, 0.125)	0.870 (0.840, 0.887)	3.0,	4.3
t	-08.37 (-18.15, 03.07)	3.10 (0.60, 8.90)	0.100 (0.070, 0.170)	0.858 (0.826, 0.889)	3.4,	4.7
t	-07.96 (-16.61, 04.20)	4.02 (2.00, 5.80)	0.121 (0.095, 0.135)	0.872 (0.863, 0.881)	3.3,	4.4
t	-09.17 (-17.82, 01.21)	4.90 (3.30, 7.60)	0.128 (0.105, 0.165)	0.885 (0.879, 0.888)	3.0,	4.0

Radar data for sample areas for V19 - Sedna Planitia Quadrangle units.

Unit	σ_0 (dB)	θ_{rms} (deg)	ρ Fresnel	Emissivity	ϵ_s	ϵ_r
ik						
West	-08.96 (-15.89, -02.91)	2.18 (1.10, 3.10)	0.131 (0.110, 0.155)	0.821 (0.805, 0.832)	3.7,	5.8
East	-11.18 (-19.49, -03.09)	1.37 (1.10, 2.00)	0.115 (0.085, 0.155)	0.837 (0.834, 0.842)	3.4,	5.3
ikpr	-15.57 (-27.76, -05.95)					
nf1	-16.57 (-19.51, -10.31)	2.92 (2.30, 3.40)	0.092 (0.085, 0.100)	0.870 (0.867, 0.873)	3.5,	4.4
nf2	-09.89 (-14.90, -05.19)	3.36 (2.40, 4.60)	0.080 (0.060, 0.115)	0.902 (0.872, 0.907)	2.8,	3.6
nf2	-08.78 (-13.66, -04.83)	3.61 (2.20, 5.20)	0.086 (0.055, 0.115)	0.898 (0.873, 0.907)	2.9,	3.7
nf3	-12.99 (-17.10, -07.51)	1.93 (1.60, 2.60)	0.138 (0.110, 0.160)	0.831 (0.828, 0.837)	4.2,	5.7
nf3	-15.13 (-19.10, -10.29)	1.57 (1.20, 2.60)	0.141 (0.100, 0.165)	0.851 (0.841, 0.871)	3.9,	5.0
nf4	-12.10 (-16.90, -05.38)	1.67 (1.00, 2.60)	0.120 (0.060, 0.160)	0.844 (0.838, 0.853)	3.9,	5.2
nf4	-12.40 (-16.42, -08.43)	1.98 (1.00, 3.80)	0.130 (0.105, 0.160)	0.841 (0.835, 0.857)	4.0,	5.3
fd	-13.35 (-19.56, -08.76)	1.56 (1.00, 2.70)	0.115 (0.090, 0.145)	0.865 (0.860, 0.868)	3.3,	4.5
fd	-13.05 (-18.52, -09.71)	1.90 (1.80, 2.00)	0.125 (0.125, 0.125)	0.861 (0.859, 0.863)	3.3,	4.6
cnf3	-17.56 (-28.74, -07.89)					
cnf2	-15.55 (-27.72, -05.32)					
cnf1	-16.72 (-29.10, -05.50)					
npr	-17.34 (-28.12, -07.92)					
cu	-14.10 (-15.98, -04.98)					
fs	-10.96 (-15.98, -04.98)					





Basemap 2 - Sedna Planitia Quadrangle

